Exploring oxygen diffusion mechanisms in SrFeO3-x and Pr2NiO4+d, followed up on single crystals by in situ synchrotron diffraction

Avishek Maity

▶ To cite this version:

Avishek Maity. Exploring oxygen diffusion mechanisms in SrFeO3-x and Pr2NiO4+d, followed up on single crystals by in situ synchrotron diffraction. Other. Université Montpellier, 2016. English. NNT : 2016MONTT188 . tel-01753384

HAL Id: tel-01753384

https://theses.hal.science/tel-01753384

THÈSE

Pour obtenir le grade de

Docteur

Délivré par l'**Université de Montpellier**

Préparée au sein de l'école doctorale
Science Chimiques Balard

Et de l'unité de recherche
Chimie et Cristallochimie des Matériaux
de l'Institut Charles Gerhardt de Montpellier

Spécialité
Chimie et Physico-Chimie des Matériaux

Présentée par **Avishek MAITY**

Exploring oxygen diffusion mechanisms in $SrFeO_{3-x}$ and $Pr_2NiO_{4+\delta}$, followed up on single crystals by *in situ* synchrotron diffraction

Soutenue le 26.09.2016 devant le jury composé de

Mr Georg ROTH Institut für Kristallographie, RWTH Aachen University Aachen, Allemagne	**Rapporteur**
Mr Dmitry CHERNYSHOV ESRF, Swiss-Norwegian beam lines, BM01A Grenoble, France	**Rapporteur**
Mr Hubert HUPPERTZ Institut für Allgemeine Anorganische und Theoretische Chemie Universität Innsbruck, Innsbruck, Autriche	**Examinateur**
Mme. Angélique LETROUIT-LEBRANCHU ICGM-C2M, Université de Montpellier, France	**Co-encadrante de thèse**
Mr Werner PAULUS ICGM-C2M, Université de Montpellier, France	**Directeur de thèse**

Abstract

Understanding fundamental aspects of oxygen diffusion in solid oxides at moderate temperatures, down to ambient, is an important issue for the development of a variety of technological devices in the near future. This concerns *e.g.* the progress and invention of next generation solid oxygen ion electrolytes and oxygen electrodes for solid oxide fuel cells (SOFC) as well as membrane based air separators, oxygen sensors and catalytic converters to transform *e.g.* NO_x or CO from exhaust emissions into N_2 and CO_2. On the other hand oxygen intercalation reactions carried out at low temperatures present a powerful tool to control hole doping, *i.e.* the oxygen stoichiometry, in electronically correlated transition metal oxides. In this aspect oxides with Brownmillerite ($A_2BB'O_5$) and K_2NiF_4-type frameworks, have attracted much attention, as they surprisingly show oxygen mobility down to ambient temperature.

In this thesis we investigated oxygen intercalation mechanisms in $SrFeO_{2.5+x}$ as well as $Pr_2NiO_{4+\delta}$ by *in situ* diffraction methods, carried out on single crystals in especially designed electrochemical cells, mainly exploring by synchrotron radiation. Following up oxygen intercalation reactions on single crystals is challenging, as it allows to scan the whole reciprocal lattice, enabling to obtain valuable information as diffuse scattering, weak superstructure reflections, as well as information of the volume fractions of different domains during the reaction, to highlight a few examples, difficult or impossible to access by powder diffraction.

Both title systems are able to take up an important amount of oxygen on regular or interstitial lattice sites, inducing structural changes accompanied by long range oxygen ordering. For $SrFeO_{2.5+x}$ the uptake of oxygen carried out by electrochemical oxidation yields $SrFeO_3$ as the final reaction product. The as grown $SrFeO_{2.5}$ single crystals we found to show a complex defect structure, related to the stacking disorder of the octahedral and tetrahedral layers. During the oxygen intercalation we evidenced the formation of two reaction intermediates, $SrFeO_{2.75}$ and $SrFeO_{2.875}$, showing complex and instantly formed long range oxygen vacancies. Due to the specific twinning with up to totally twelve possible twin individuals, we directly followed up the formation and changes of the specific domain and related microstructure. We thus observed a topotactic reaction mechanism from $SrFeO_{2.5}$ to $SrFeO_{2.75}$, while further oxidation lead to important rearrangements in the dimensionality of the oxygen defects in $SrFeO_{2.875}$, implying the formation of an additional twin domain in course of the reaction.

The electrochemical reduction of orthorhombic $Pr_2NiO_{4.25}$ yields stoichiometric $Pr_2NiO_{4.0}$ as the final reaction product with the same symmetry, while tetragonal $Pr_2NiO_{4.12\pm\delta}$ appears as a non-stoichiometric intermediate phase. Using a single crystal with 50 μm diameter, the reaction proceeded under equilibrium conditions in slightly

less than 24 h, implying an unusually high oxygen ion diffusion coefficient of $\geq 10^{-11}$ cm^2s^{-1} at already ambient temperature. From the changes of the associated twin domain structure during the reduction reaction, the formation of macro twin domains was evidenced.

Beside exploring the complex phase diagrams of $SrFeO_{2.5+x}$ and $Pr_2NiO_{4+\delta}$ we were able to investigate detailed changes in the microstructure using *in situ* single crystal diffraction techniques, impossible to access by classical powder diffraction methods. The importance of changes in the domain structure goes far beyond the investigated title compounds and has utmost importance of the performance, stability and lifetime of e.g. battery materials.

Résumé

La compréhension des aspects fondamentaux de la diffusion de l'oxygène dans les oxydes solides à des températures modérées, jusqu'à température ambiante, est un enjeu majeur pour le développement d'une variété de dispositifs technologiques dans un avenir proche. Cela concerne, par exemple, le développement de la prochaine génération d'électrolytes et membranes solides d'oxygène pour les piles à combustible de type SOFC. De plus, les réactions d'intercalation de l'oxygène réalisées à basse température présentent un outil puissant pour contrôler le dopage en oxygène ainsi que des propriétés physiques. Dans ce contexte, les oxydes ayant une structure type brownmillérite ($A_2BB'O_5$) ou type K_2NiF_4, ont attiré beaucoup d'attention, car ils montrent une mobilité de l'oxygène déjà à température ambiante.

Dans cette thèse, nous avons étudié les mécanismes d'intercalation d'oxygène dans $SrFeO_{2.5+x}$, ainsi que $Pr_2NiO_{4+\delta}$ par des méthodes de diffraction *in situ*, réalisées sur des monocristaux dans une cellule électrochimique spécifiquement conçue, explorant principalement le rayonnement synchrotron. Ceci a permis d'explorer en 3D tout le réseau réciproque, et d'obtenir des informations précieuses sur la diffusion diffuse, sur les faibles intensités des raies de surstructure, ainsi que des informations sur la fraction volumique des différents domaines de maclage au cours de la réaction, impossibles à obtainir par diffraction de poudre.

Les deux systèmes montrent des changements structuraux complexes, accompagnés par une mise en ordre de l'oxygène à longue distance. Au cours de l'intercalation d'oxygène nous avons mis en évidence deux phases intermédiaires, $SrFeO_{2.75}$ et $SrFeO_{2.875}$, possédant des lacunes en oxygène ordonnées à longue échelle. En raison du maclage, et avec jusqu'à douze individus possibles, nous avons suivi directement la formation et l'évolution des domaines de maclage ainsi que leur microstructure apparentée. Nous avons ainsi observé un mécanisme de réaction topotactique pour $SrFeO_{2.5}$ vers $SrFeO_{2.75}$, tandis que l'oxydation de $SrFeO_{2.875}$ conduit à d'importants réarrangements de l'oxygène, associés à un changement de nombre de domaines de maclage.

La réduction électrochimique de la phase orthorhombique $Pr_2NiO_{4.25}$ donne $Pr_2NiO_{4.0}$ comme produit final, ayant la même symétrie, tandis que la phase tétragonale $Pr_2NiO_{4.12\pm\delta}$ apparaît comme phase intermédiaire. Utilisant un monocristal d'un diamètre de 50 microns, la réaction se déroule dans des conditions d'équilibre en moins de 24 heures, ce qui implique un coefficient de diffusion de l'oxygène anormalement élevé, supérieur à 10^{-11} cm^{2}s^{-1} à température ambiante. Grâce aux changements de la structure associés aux domaines mâclés pendant la réaction de réduction, la formation de domaines mâclés macroscopiques a été mise en évidence.

Outre l'exploration des diagrammes de phases complexes de $SrFeO_{2.5+x}$ et $Pr_2NiO_{4+\delta}$,

nous avons pu étudier les changements détaillés concernant la microstructure à l'aide de la diffraction sur monocristaux *in situ*, impossible à accéder par des méthodes de diffraction de poudre classique. Les changements de la micro-structure des domaines va bien au-delà des composés étudiés ici et est tres importante pour extrapoler sur la performance, la stabilité et la durée de vie par exemple des matériaux utilisés pour le stockage de l'énergie.

Contents

Preamble

Non-stoichiometric transition metal oxides are at the forefront of research in chemistry, physics and material science. The subtle changes in oxygen stoichiometry in these oxides give rise to chemical reactivity and a range of versatile physical properties which make them very special. Being a part of the family of strongly correlated electronic system, these oxides show complex structural and electronic phenomena such as high temperature superconductivity (HTS), charge and spin ordering, magnetic ordering, magnetoresistance, spin dependent transport properties, multiferroicity and many more which likely to originate from strong correlation of spin, charge and crystal field.

The most investigated transition metal oxides are the Perovskite derivatives. From the parent Perovskite structure AMO_3 several structure types can be easily derived by modifying either the cation or anion stoichiometry, among which the most fundamental two are the Brownmillerite and Ruddlesden-Popper (RP) phases. The Brownmillerite framework is an oxygen deficient Perovskite, with the general formula $A_2M_2O_5$. On the other hand the RP series can be understood as intergrowth phases with the general formula $(AO)\bullet(AMO_3)_n$ where n is an integer.

The high-T_c cuprate superconductors belong to the RP phase with $n = 1$, and basic chemical formula La_2CuO_4, being the most well known and most investigated. The physical properties of these compounds drastically vary from system to system and also with the type of dopants *e.g.* $La_{2-x}Sr_xCuO_4$ and $Nd_{2-x}Ce_xCuO_4$[1]. While substitution of the three valent rare earth (RE) metal by two valent Sr is equivalent to hole-doping, electron doping is achieved by four valent cerium. Depending on the dopant concentration these type of compounds present typically Mott insulators developing to a superconducting state showing different magnetic ordering. Similar electronic behavior is also observed for the homologous cobaltates. While stoichiometric La_2CoO_4 shows long-range antiferromagnetic order with a Néel temperature $T_n = 275$ K, a structural transition accompanied by a Co^{2+} spin flip in the (CoO_2)-plane resulting in a new spin structure is observed with decreasing temperature[2]. Sr-doping in La_2CoO_4 suppresses the commensurate antiferromagnetic ordering and exhibits incommensurate spin ordering with the modulation closely following the amount of Sr. The homologous cuprates and nickelates show the same trends but at already much lower doping concentrations[3]. RP-type manganites have also been investigated importantly after the discovery of HTS. $La_{1-x}Sr_xMnO_3$ and $La_{1-x}Ca_xMnO_3$ show colossal magneto resistance (CMR), where the electrical resistance of these materials changes dramatically with the application of a magnetic field, while the local spin alignment of the Mn^{3+} and Mn^{4+} sites are modified depending on the doping concentration[4]. Theses systems are thus considered as key compounds to design new generation electronic and data storage devices.

In addition to the influence of dopant species and doping concentrations, the presence of inherent inhomogeneities on the microscopic level also modifies the physical properties of these compounds. The presence of quenched disorder in cuprates or manganites is inevitable, when induced by conventional high temperature synthesis which leads to spatial inhomogeneities and even electronic phase separation on a local level, different from the extended defect concept, while the degree of disorder needs to be introduced in macroscopic phase diagrams. This especially concerns the simultaneously presence of AF and FM ordered phases as observed for e.g. in $Nd_{0.5}Ba_{0.5}MnO_3$. Particularly for transition metal oxides, sensitive to electronic changes on a local level, it might become impossible to clearly separate different ground states of the material. In fact, theoretical studies by Burgy *et al.*[5] and Aryanpour *et al.*[6] show, the presence of disorder in very small amount of doping especially in the regime of phase competition results in substantial properties of CMR and superconductivity. Also many other theoretical studies predicted the existence of charge and spin stripes in these compounds which must arise from such spatial inhomogeneity[7,8] and recently have been experimentally observed in the layered nickelate and cuprate compounds $La_{2-x}Sr_xNiO_4$ and $La_{2-x}Ba_xCuO_4$[9–11]. Replacing the RE cation by lower valance cation (*i.e.* hole doping) can lead to a phase segregation into periodically spaced charge stripes separating narrow domains of antiferromagnetic order by forming anti-phase domain wall[12]. A high resolution electron microscopy (HRTEM) study on $LaSrCo_3$ by Caciuffo *et al.*[13] elucidate such example of structural phase segregation into a more or less periodic Sr-rich and La-rich region showing cation substitution and associated changes in the valence states of the transition metal can largely modulate the electronic and structural correlations. In such a context a controlled incorporation of the disorder in strongly correlated electronic system could be a powerful tool to modify the physical properties precisely. The fact that cation doping can only be obtained by high temperature synthesis limits the possibilities to change the degree of disorder at moderate temperatures. At high temperature, while the system stays in thermodynamic regime, the disorder in the system in terms of cation distribution or the formation of anti-phase boundaries (APB) etc. are completely controlled by the thermodynamics of the system in order to minimize its free energy.

On the other hand oxygen intercalation is electronically equivalent to hole doping by lower valance cation substitution, but more advantageous as oxygen intercalation reaction can already proceed at ambient. Several oxides belonging to the Perovskite derivatives are well known today to undergo electrochemical oxygen intercalation at room temperature (*e.g*. Brownmillerite Sr(Fe/Co)$O_{2.5}$ and the RP-phase $A_2MO_{4+\delta}$; A = La, Nd, Pr; M = Cu, Ni, Co). Oxygen intercalation or desintercalation reactions at ambient temperature, being far away from thermodynamical equilibrium, would be an alternative method to control the degree of oxidation of the transition metal and as well the degree of disorder. Additionally, related to the low reaction temperature, it facilitates the formation of oxygen superlattices with high structural correlations up to few hundreds of unit cells, which are difficult or impossible to access at high reaction temperatures. The low reaction temperature becomes in this way a unique synthetic tool allowing to access structural and electronical ordering not available by classical high temperature synthesis methods.

Theoretical models to understand such long-range ordering phenomena are in particular based on the assumption of electronic phase separations at the nano scale[12,14–16]. In that regime it is just a question of the respective coherence lengths whether these phases appear to be homogeneous or inhomogeneous and the domain size becomes a decisive parameter to adjust their physical properties. Exploring the correlation lengths between domain size and the structural and electronic ordering, would allow a better understanding of these materials with great potential for technological applications.

The other important aspect which needs to be mentioned here is the fast oxygen diffusion in some of the above cited compounds. Brownmillerite-type Sr(Fe/Co)$O_{2.5}$ and K_2NiF_4-type $RE_2MO_{4+\delta}$ (RE = La, Pr and M = Ni, Cu, Co), show oxygen mobility via electrochemical reaction even at room temperature. Oxygen is highly mobile in these compounds even at ambient which is in principal unexpected owing to the *2-fold* negative charge and rather big size (diameter 2.8 Å) of oxygen ion. Classical hopping mechanism would require elevated temperatures at least above 600 °C for oxygen to diffuse. This surprising behaviour of oxygen diffusion to take place already near room temperature puts also into question the real microscopic diffusion mechanisms in these families of materials. A phonon assisted diffusion mechanism based on the presence of a low lying phonon modes combined with structural instabilities has been recently proposed by Paulus *et al.*[17] which might explain why the oxygen is highly mobile in the Brownmillerite frameworks alrady at room temperature. A similar mechanism for oxygen diffusion in the $RE_2MO_{4+\delta}$ systems have been reported as a result of a dynamical delocalization of the apical oxygen atoms of the MO_6 octahedra on a diameter of more than 1 Å from its equilibrium position[18]. Such delocalization of oxygen atoms is activated by the structural instability due the presence of excess interstitial oxygen. The delocalized apical oxygen atoms can easily diffuse to the adjacent vacant interstitial sites and thus believed to play an important role on the non-classical oxygen mobility at ambient temperature[19].

It is thus clear that exploring diffusion mechanisms for oxygen mobility at low temperatures is of utmost importance for the R&D of technological devices as oxygen membranes or electrolytes for *e.g.* solid oxide fuel cells (SOFC). On the other hand the non-stoichiometry obtained by electrochemical methods or *“chimie douce”* in a temperature regime around and slightly above ambient temperature, induce phase transitions and associated changes of the physical properties which are not accessible with high temperature reaction pathways. Kinetic aspects become here more dominant, as the reactions proceed far away from thermodynamical equilibrium. At low temperature diffusion processes are no longer governed by the *“standard”* Arrhenius equation. Thus dynamical aspects come in and have already been successfully applied to explain oxygen mobility via a phonon assisted diffusion mechanism[17]. As a consequence not only local structural rearrangements of oxygen atoms becomes accessible, but also long-range ordered superstructures, implying a huge potential for the synthesis of metastable phases.

While oxygen intercalation into transition metal oxides generally proceeds via a *topotactic* electron/ion transfer reaction, the transferred electrons are taken up into the conduction band of the oxide which is electronically equivalent to the formation of holes as discussed earlier. This approach is therefore very complementary to the hole-doping achieved by cation substitution. The difference is that the latter always requires high temperature reaction conditions. The idea to continuously intercalate oxygen into transition metal oxides at ambient allows equally to explore the respective phase diagram as a function of the extra oxygen concentration *i.e.* hole-doping and associated structural changes.

In this thesis two systems have been investigated essentially. The first one is $SrFeO_{3-x}$ which has been intensively studied already for more than five decades. This system can reversibly intercalate oxygen in between $0 \leq x \leq 0.5$[20,21], changing its structure from the cubic Perovskite to the orthorhombic Brownmillerite. While $SrFeO_{2.5}$ shows antiferromagnetic ordering with a Néel temperature $T_N = 670$ K[22], $SrFeO_3$ shows a more complex and a screw-type antiferromagnetic ordering below 134 K[23]. $SrFeO_{2.75}$ and $SrFeO_{2.875}$ synthesized at elevated temperature and specific oxygen partial pressure show long range oxygen vacancy ordering. The particular interest here was to investigate the reaction mechanism and vacancy ordered intermediate phases during the electrochemical intercalation of oxygen in $SrFeO_{2.5}$ up to $SrFeO_3$ by following the structural evolution *in situ* using single crystals. To follow up this complex reaction on single crystals of few micrometer, a specific electrochemical cell has been developed which was particularly adapted for the single crystal diffractometer installed at the Swiss Norwegian beamline BM01A at the European Synchrotron ESRF[24]. The techniques to electrochemically oxidise a tiny crystal of about 50 μm diameter has been developed to follow up this reaction by fast and low-noise data collection, taking advantage on the specific arrangements on BM01A along with the 2M Pilatus detector. The used $SrFeO_{2.5}$ crystal shows a complex twinning behaviour which helped to follow up *"easily"* related changes in the microstructure. Such information is not possible to access by powder diffraction methods. The 3D data collection allows to access almost complete reciprocal space. Beside the evolution of basic and superstructure reflections, quantitative information on diffuse scattering can be also accessed. This turned out to be an important issue, also to better identify the ground state of $SrFeO_{2.5}$, which has been recently discussed to be different than the hitherto accepted Brownmillerite framework with disordered $(FeO_4)_\infty$-chains[25]. This is equally important with respect to the characterization of the $SrFeO_{2.75}$ and $SrFeO_{2.875}$ intermediates, since more than 500 publications concerning $SrFeO_{3-x}$ can be found today in the literature.

The second example studied is $Pr_2NiO_{4+\delta}$ system, which is today one of the most promising compounds to serve as oxygen membrane in SOFCs. Also here oxygen mobility at ambient temperature has been discussed to rely on specific lattice modes. The structure of $Pr_2NiO_{4.25}$ is highly complex and incommensurate due to the presence of a superstructure related to oxygen and charge ordering. Here the oxygen deintercalation reaction has been investigated by *in situ* synchrotron diffraction methods on an oriented $[50 \times 50 \times 400]$ μm^3 single crystal which was continuously reduced. Since from the phase diagram it is known that the symmetry of $Pr_2NiO_{4.25}$ and $Pr_2NiO_{4.0}$ is both orthorhombic while the intermediate phase $Pr_2NiO_{4.12}$ is tetragonal[26], this presents an interesting case to follow up the evolution of the related microstructure in terms of twin domains during the oxygen release. A second aspect concerns the evolution of the incommensurate superstructure of the starting compound, as a continuous change in the incommensurate modulation vector might be expected, together with a respective change in the domain size of the related charge ordered domains. In this way the relation between low temperature oxygen mobility and associated electronic correlations can be easily accessed.

From both systems a better understanding in the evolution of the structure and microstructure with the oxygen intercalation/deintercalation is aimed during this thesis, while the experimental setup, i.e. the *in situ* study to follow up in real time a chemical reaction on a single crystal, is the first of this kind and challenging from both, the experimental and fundamental crystallographic part.

Chapter 1

Oxygen mobility in solids

Oxygen ion mobility in solid oxides is a fundamental and complex phenomenon. Several members belonging to the families of transition metal (TM) oxides and rare earth (RE) oxides show oxygen ion conductivity and find keen interests for important technological applications such as solid oxide fuel cell (SOFC), oxygen separation membranes, lambda sensors, catalysis etc. with potential of ecological and economic benefits. Achieving high efficiency for such applications is an important issue and highly depends on the energetics of oxygen transport in these oxides. A number of parameters such as the material structure, composition, oxygen stoichiometry, doping and elastic strain etc. define the energy barrier for oxygen diffusion and in general needs high temperature ~1000°C to overcome such barrier.

In general, presence of point defects *e.g.* vacancies or interstitials is very important for any kind of ionic transport in the solids[27]. Depending on the type of point defects there exist three generally recognized ion diffusion mechanisms namely *interstitial*, *interstitialcy* and *vacancy* mechanism. In the interstitial mechanism, the ion jumps from one interstitial site to the other without displacing any neghbouring ions where as in the interstitialcy mechanism the interstitial ion displaces the neighbouring ions from their equilibrium positions to move to the next interstitial positon. In the vacancy mechanism the host ion diffuses by hopping through the nearby vacancy sites[28].

Among all the three mechanisms, vacancy mechanism governs the self-diffusion of oxygen ions in some well known under-stoichiometric fluorite type (*e.g.* ZrO_2, CeO_2) and layered Perovskite type (*e.g.* $LaMO_3$; M=Ga, Mn, Co) oxides. Theses compounds are of great interests as conventional SOFC electrolyte and cathode materials. However, in these compounds the energy barrier for oxygen migration is very high especially taking into account the *2-fold* negative charge and the big size of oxygen ions ($r_{O^{2-}}$ = 1.4 Å) and requires elevated temperature even for oxygen diffusion to start. The diffusion rate decreases instantly with the lowering of the temperature. As studied by Steele[29], in

Yttrium Stabilized Zirconia (YSZ) which is one of the most promising SOFC material, the oxygen ion conductivity decreases almost by two orders of magnitude when the operating temperature is lowered from 900 °C to 500 °C.

From the transition state theory, oxygen diffusion rate can be expressed as a function of temperature by Boltzmann relation $N = N_0\ exp(-E_m/k_B T)$; where N is migration rate at temperature T and E_m is the corresponding migration energy barrier. The shape of this energy barrier is mainly determined by the interaction of interstitial oxygen with surrounding cations and dopants along with the configuration of vacancy arrangement surrounding the migration path. A schematic diagram for such migration path is shown in Fig. 1.1.

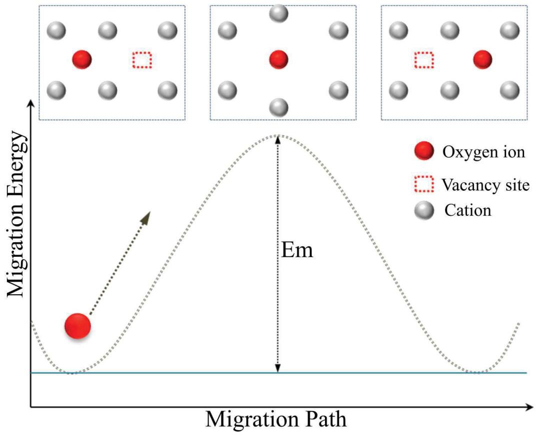

Figure 1.1: Schematic diagram showing migration energy and migration path for oxygen diffusion in solids via vacancy mechanism.

The rates of oxygen diffusion is mostly influenced by oxygen vacancy concentration and operating temperature. But high temperature operation comes with disadvantages. SOFC materials often goes through the challenges of chemical and microstructural degradation which brings high expense for maintenances and replacements. To avoid such problem, we need innovative ideas to design cost effective prototypes for the conventional SOFC materials and as well as we need to find new alternative materials which can operate at intermediate temperatue (IT-SOFC) or at room temperature (RT-SOFC). In this particular regard non-stoichiometric TM and RE oxides are the promising candidates[30–32].

Oxygen mobility at room temperature was a forbidden concept until 25 years ago when electrochemical (EC) oxygen intercalation was realized in $LaCuO_4$ by Rudolf *et al.*[33]. Though the main interest at that time was to observe high temperature superconductivity (HTS) which appears upon oxidation in $LaCuO_{4.07}$; it was evidenced that oxygen diffusion is possible at ambient. The very first trial of EC oxygen intercalation was made by Kudo *et al.*[34] in $Nd_{1-x}Sr_xCoO_x$ system but further it was not interesting due to lack of spectacular properties though the phenomena was itself a sensation. Taking into account the big size of oxygen ion and *2-fold* negative charge, oxygen mobility at ambient is very unusual and unbelievable, and was highly controversial at the early stage of oxygen intercalation history. 90's onwards EC oxygen intercalation became a recognized novel method for preparation of highly oxidized ferrites/cobaltites from the series of ferrates/cobaltates showing Browmillerite type framework *e.g.* $Sr(Fe/Co)O_{2.5}$][20]. Very recently, the combined experimental and theoretical study by Paulus *et al.* suggests a phonon assisted diffusion mechanism based on the presence of a low lying phonon as the origin of non-classical oxygen mobility at ambient temperature[17]. While the *in situ* neutron diffraction study by Le Toquin *et al.*[35] reported that the intercalated oxygen immediately gets ordered in the structure giving rise to long range order. This presents an alternative in terms of synthesis of materials with long range oxygen ordering.

Some of the K_2NiF_4 type oxides also show oxygen mobility at room temperature *e.g.* $Pr_2NiO_{4+\delta}$, $Nd_2NiO_{4+\delta}$ or $La_2CoO_{4+\delta}$. These compound can accommodate interstitial oxygen in a wide range of non-stochiometry ($0 \leq \delta \leq 0.25$) keeping structural stability intact even upto high temperature which makes them potential oxygen ion conductors. Presence of oxygen mobility at ambient gives access to design new generation of IT- or RT-SOFC materials. Experimental and theoretical studies predict that presence of high structural anisotropy and related dynamics plays a key role for oxygen transport down to ambient temperature in these non-traditional oxygen ion conductors. Many theoretical simulation studies have been done using density functional theory (DFT) and molecular dynamics (MD) simulations for proper understanding of oxygen diffusion pathways in these materials[36]. A wide range of parameters such as structures, microstructures, grains and grain boundaries, domain size along with the presence of specific lattice dynamics largely influence the oxygen diffusion. The nature of the oxygen diffusion in terms of dimensionality is different for different systems. Brownmillerite $SrFeO_{2.5}$ shows 1D oxygen diffusion of the oxygen through the vacancy sites along [100] crystallographic direction. In $Pr_2NiO_{4+\delta}$, oxygen diffusion occurs in the *(a,b)*-plane. While the classical ion conductors such as CeO_2 or YSZ present 3D oxygen diffusion. The underlying diffusion mechanism differs from system to system. A detail knowledge about the diffusion mechanism is the prerequisite to develop the desired new generation material for SOFC applications. In the following sections we will summarize the current status of oxygen diffusion in different solids and the related mechanisms.

1.1 Oxygen diffusion mechanisms in solids

Enabling fast oxygen ion transport in electrolyte materials is essential to facilitate the intermediate to room temperature operation of SOFCs for enhanced durability and economics. In the search for high performance oxide ion electrolyte for the IT- or RT-SOFCs various family of oxides has been thoroughly investigated in last decades. The best choice of such oxide ion electrolyte material is still not clarified. In this section different oxygen ion diffusion mechanisms will be briefly discussed as established till date. In the first half of this section, we will be focused to summarize the ionic transport mechanisms in the widely studied conventional electrolyte materials (e.g. YSZ) where vacancy mediated oxygen ion diffusion through hopping mechanism dominates. In the later half, we will discuss the diffusion mechanisms in some non-traditional oxygen ion conductors from recent studies where structural flexibility and dynamics becomes more important.

1.1.1 Oxygen diffusion via classical vacancy mechanism

1.1.1.1 Fluorites

Fluorite type structure with general formula AO_2 has cubic crystal structure where the tetravalent cations are *8-fold* coordinated by oxygen Fig. 1.2(a). Fluorite type ZrO_2 is one of the well known classical oxygen ion conductors. Unlike other fluorite structures with comparatively bigger size of lanthanide cation, Zr^{4+} ion belonging to the transition metal is too small to maintain the fluorite structure. This compound can be stabilized only at high temperature or by substitution with larger cation with lower valance (*e.g.* Y^{3+}) which in turn creates oxygen vacancies. The presence of vacant oxygen sites in the Fluorite framework is essential for high oxygen ionic conductivity Fig. 1.2(b).

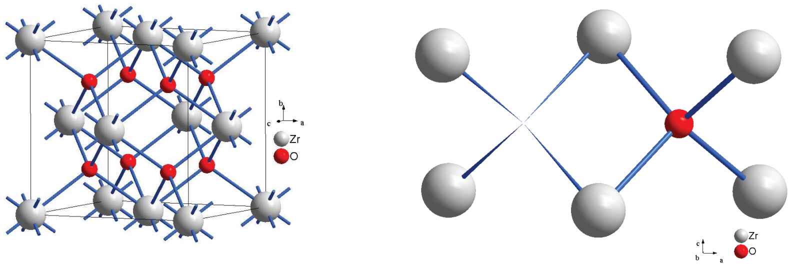

(a)

(b)

Figure 1.2: (a) Fluorite type structure of ZrO_2. (b) Schematic of oxygen diffusion path in ZrO_2 via oxygen vacancy.

Fluorites can maintain high degrees of non-stoichiometry which can be introduced by high doping concentration. Though ionic conductivity increases with increase of doping concentration but that monotonicity is only valid for a very low concentration of Y^{3+} doping Fig.1.3[37]. Atomistic simulations[38–40] show that the strain appearing from lattice mismatch due to the different size of the dopant cause such trend. The best choice would be the similar size of dopant for example Sc^{+3}:ZrO_2 show much higher conductivity compared to Y^{+3}:ZrO_2[41].

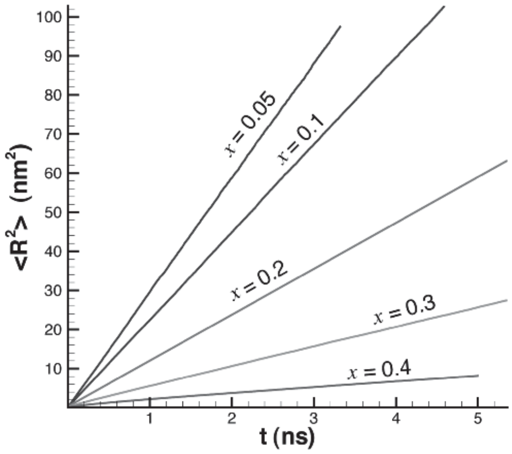

Figure 1.3: Mean square displacement of the oxygen vacancies,$<R^2>$, is shown as a function of time in $(ZrO_2)_{1-x}(Y_2O_3)_{x/2}(V_O)_{x/2}$ for different yttrium ion fractions, x, at 1400 K. **Reproduced from Fig. 1 of ref.[37].**

The other fluorite type material of high technological importance is CeO_2 which finds a lot of applications in SOFC electrolytes, three-way automotive catalytic converter, purification and production of hydrogen and in other catalytic applications[42]. The chemistry of such fluorite type oxides containing RE cations is different from that of containing Transition metal (TM) cations (*e.g.* ZrO_2) because of the electronic configuration. As the energy level of Ce^{3+} with [Xe]4f^1 configuration lies in the energy gap between Ce:5d conduction band and O:2p valance band, at an energy very close to the top of the O:2p valance band, CeO_2 [Ce^{4+}] can be easily reduced to Ce^{3+} giving CeO_{2-x} in the reducing atmosphere of the SOFC anode[28]. It is widely accepted that the oxygen vacancy, with effective charge of 2^+, localize two electrons in the neighbouring Ce^{+3} ions by introducing the [Xe] 4f^1 configuration as shown in Fig. 1.4.

In contradiction to the standard picture of electron localization on neighbouring cerium ions, Shoko *et al.*[43] have recently shown from the bond valance model that the charge distributes itself predominantly in the second coordination shell of cerium ions an even one excess electron can be delocalized over more than one cerium ions. These electrons bound by the oxygen vacancy is called *polarons*. Nakayama *et al.*[44] proposed *polaron*-assisted oxygen diffusion mechanism where the migration energy for oxygen is

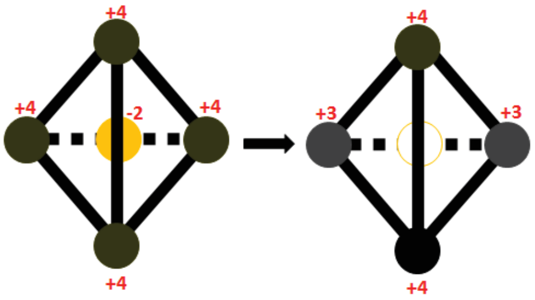

Figure 1.4: Schematic of the standard picture of charge redistribution following the formation of an oxygen vacancy in CeO_{2-x}. The tetrahedron of Ce atoms (black circles) with an O atom at its centre (orange in colour version) is shown along with the charges on these atoms in the simple ionic picture description of CeO_{2-x}. The process of reduction shown by the arrow leads to a neutral O vacancy at the centre of the tetrahedron (empty orange circle) while two of the Ce ions have been reduced to the 3^+ oxidation state. **Reproduced from Fig. 1 of ref.[43].**

considerably decreased resulting in high diffusivity due to local charge compensation around the oxygen vacancy sites. The schematic is given in Fig. 1.5. Though the energy barrier for the oxygen diffusion is reduced by associated polaron migration in reduced CeO_{2-x}, the intrinsic vacancy concentration of oxygen is very low which practically limit oxygen diffusion. Defect concentration can be highly increased by doping with divalent or trivalent cations. With the doping concentration the vacancy increase but with in a low limit of dopant concentration as mention in the case of YSZ in Fig.1.3. The choice of cation is made in such a way that the size mismatch with host lattice is least and the polarons are more free to be delocalized through the neighbouring cations. In this regard Gd doped CeO_{2-x} is very important SOFC electrolyte material operating at much lower temperature (~550 °C) compared to YSZ[45].

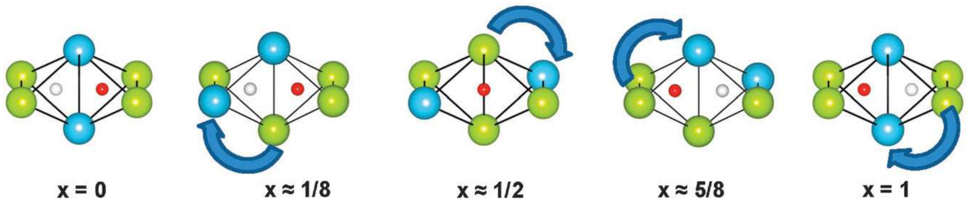

Figure 1.5: Variation in the $e'_{Ce}/Ce^x/V_O^{\bullet\bullet}/O^x$ configuration during oxygen vacancy migration. Arrows indicate the migration of localized electrons, and x denotes the corresponding projected migration distance. **Reproduced from Fig. 5 of ref.[44].**

1.1.1.2 Perovskites

Perovskite structure has a general formula ABO_3 where A is the RE element and B is typically TM element. The TM stays inside BO_6 octahedra and the RE cation is in *12-fold* co-ordination with oxygen Fig. 3.2(a). The possibility of lower valance cation doping into host cation sites (*e.g.* A and B sites) make Perovskite type compounds very interesting for wider range of applications. A and B-site doped $LaGaO_3$ based Perovskite material are well known as intermediate temperature range (~ 650 °C to 800 °C) electrolyte material with purely ionic conductivity. Typical scheme of oxygen diffusion is shown in Fig. 3.2(b) for doped Perovskite system. As pointed out by Goodenough *et al.*[46] and Ishihara *et al.*[47], $La_{10-x}Sr_xGa_{1-y}Mg_yO_{3-d}$ (LSGM) with optimized doping concentration seems to perform with higher efficiency at intermediate temperature compared to conventional ZrO_2 based material operating at much higher temperature ~1000 °C. Further Ishihara *et al.*[48] has studied that Co doping in the b-site as well enhance the performance without introducing electronic conductivity.

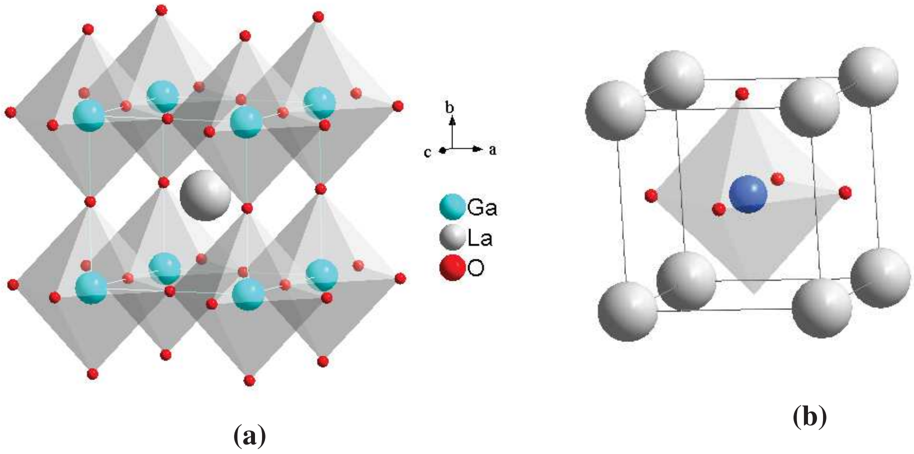

(a) (b)

Figure 1.6: (a) Perovskite type structure of $LaGaO_3$. (b) Schimatic of oxygen diffusion path in $LaGaO_3$ via oxygen vacancy.

1.1.1.3 Double Perovskites

The other important IT-SOFC materials are the ordered Double Perovskite materials with general formula $AA^{'}B_2O_{5+\delta}$, where A = RE; $A^{'}$ = alkaline earth (AE) metal B = TM. Double Peroskite materials are realized by aliovalent substitution of half of the A site cations with $A^{'}$ in conseqeutive layers of the basic Perovskite ABO_3 structure. Due to substitution with a lower valance cation $A^{'}$, oxygen vacancies are created giving a stoichiometry $A_{0.5}A^{'}_{0.5}B_{3-\delta}$. For a notable mismatch between the two A-site cations, the structure adopt a layered arrangement where the A-sites cations are arranged on a lattice which is two time of the basic ABO_3 Perovkite cell and that leads to formula unit rewritten as $AA'B_2O_{5+\delta}$. The oxygen vacancies are ordered as channel in the RE layers along [100]-direction of the lattice as shown in Fig. 1.7. Co and Mn based Double Perovskites are promising for IT-SOFC electrode material as they show electronic conductivity and higher oxygen conductivity compared to the conventional doped Perovskite[49]. $GdBaCo_2O_{5+\delta}$ belongs to the family of Double Perovskite. The study by Taskin *et al.*[50,51] repoted that the chemical diffusion coefficient of the oxygen can be significantly enhanced in the presence of ordered arrangement of A site cations. The homologous compound $PrBaCo_2O_{5+\delta}$ show even higher oxygen diffusivity (almost 2 orders of magnitude higher) compared to $GdBaCo_2O_{5+\delta}$ at 500 °C as studied by Kim *et al.*[52,53].

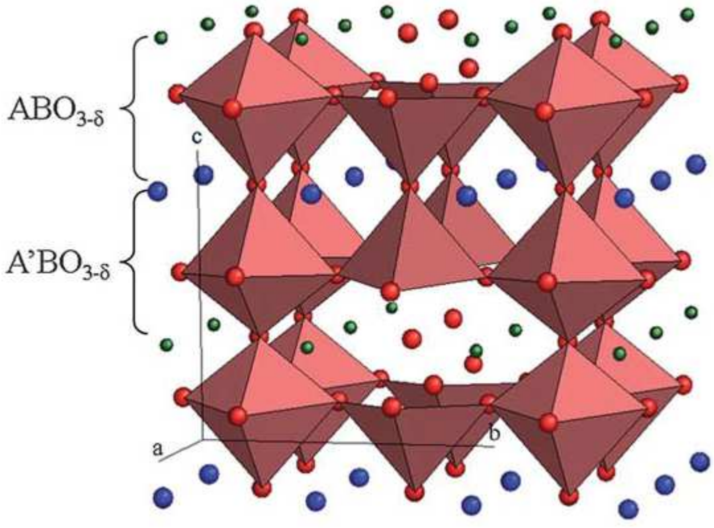

Figure 1.7: Polyhedral view of a Double Perovskite structure, $AA'B_2O_{5+\delta}$. B ions are coordinated in pyramids (BO_5) and octahedras (BO_6) with oxygen vacancies along [1 0 0] direction, in the plane containing RE ions A. **Reproduced from Fig. 1 of ref.[49]**.

1.1.1.4 LAMOX

Apparently a new family of oxides named as LAMOX with parent structure $La_2Mo_2O_9$ draws attention in IT-SOFC material. It was introduce by the group of Lacorre *et al.*[54,55]. This compound present a reversible phase transition from a low temperature slightly distorted structure α-$La_2Mo_2O_9$ to high temperature more cubic structure β-$La_2Mo_2O_9$ around 580 °C similar to that of β-$SnWO_4$ though the oxygen stoichiometry is different due to lower cationic oxidation state. In β-$SnWO_4$, the W atom is coordinated in a tetrahedra with one oxygen atom on the 3-*fold* axis, whereas Sn^{2+} stays in octahedral environment distorted by the lone pair. The lone pair is considered to occupy a volume similar to that of an O^{2-} anion Fig. 1.8(a). Lacorre *et al.* suggested that $La_2Mo_2O_9$ can be viewed as β-$SnWO_4$ ($Sn_2W_2O_8$) substituted by La and Mo. In the case of LAMOX the two Sn lone pairs in β-$SnWO_4$ are replaced by one oxygen ion and one oxygen vacancy giving rise to high oxygen mobility. This is a novel approach namely "lone pair substitution principle" as suggested by Lacorre *et al.*, showing new direction in the search for new generation IT-SOFC material.

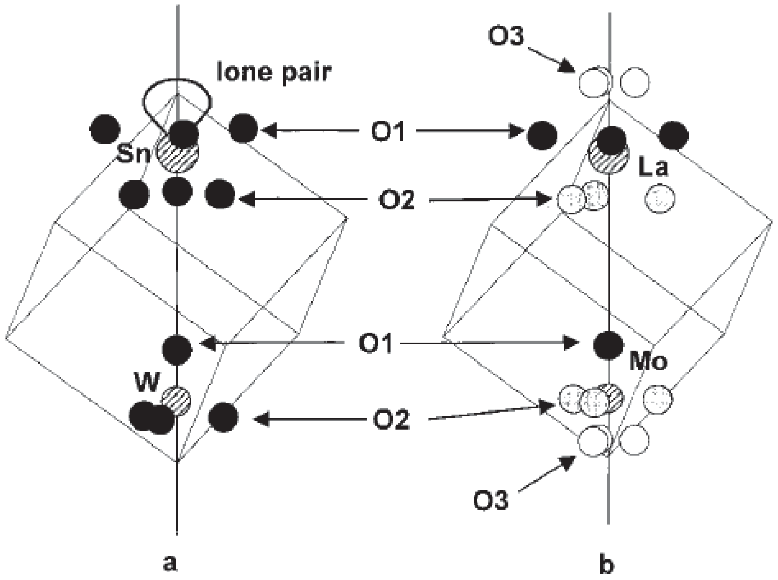

Figure 1.8: (a) Cationic environments in β-$SnWO_4$ and (b) $La_2Mo_2O_9$. The environment of La has been limited to the nearest neighbors for comparison purposes. Gray and open circle represent oxygen sites are partially occupied. **Reproduced from Fig. 4 of ref.[55].**

So far discussed all the classes of material show the oxygen diffusion through vacancy mediated classical hopping mechanism. The other class of materials which show rather a non-traditional ion transport pathways. The presence of high structural anisotropy along with the lattice flexibility and related dynamics play key role for the ionic transport in those systems even at ambient. In the next section we describe few of such materials showing non-classical diffusion mechanisms.

1.1.2 Oxygen diffusion via structural flexibility and dynamics

1.1.2.1 Brownmillerites

Brownmillerite type compounds with general formula $A_2M_2O_5$ (A: AE, M and M':TMs in octahedra and tetrahedra) are well known for oxygen mobility down to room temperature from late 80's[33]. Brownmillerite type frame work can be realized from its underlying AMO_3 Perovskite type parent structure by introducing oxygen vacancy channel along the [110]-Perovskite direction. This leads to a layered arrangement containing the TM ions in octahedral and tetrahedral coordination in the consecutive layers Fig. 1.9(a). The lattice of the vacancy ordered structure can be parameterized as $[\sqrt{2}a_p \times 4a_p \times \sqrt{2}a_p]$ where a_p is the cubic Perovskite lattice parameter. Depending on the chain arrangement in the tetrahedral layers, these compounds crystallize in three different space groups among which two are ordered: *I2mb*, *Pnma* due to regular arrangements of 'L' and 'R' $(FeO_4)_\infty$ chains in the tetrahedral layers where the disordered space group *Imma* represents a completely irregular or statistically random appearance of the 'L' and 'R' chains as shown in Fig. 1.9(b).

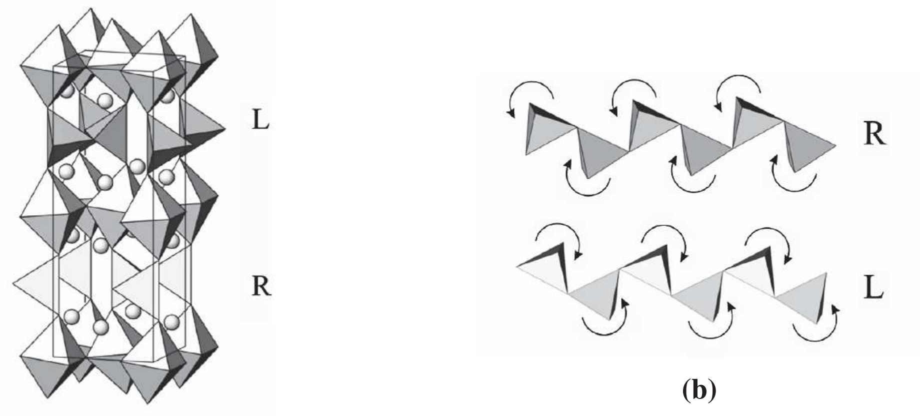

(b)

(a)

Figure 1.9: (a) Brownmillerite type structure with consecutive layers of octahedra and tetrahedra. (b) Schematic representation for 'R' and 'L' $(FeO_4)_\infty$ chain arrangements. **Reproduced and modified from Fig. 2 of ref.[56].**

Several studies[20,21,35,57,58] have shown for a series of Brownmillerite compounds with composition $AMO_{2.5}$ (with A = Sr, Ca and M = Fe, Co), oxygen ion can be intercalated and de-intercalated reversibly at ambient using gentle chemical methods '*chimie douce*' or electrochemical methods which is surprising taking into account the large radius of O^{2-} ions $r_{O^{2-}}$= 1.4 Å. A Classical approach to understand such oxygen diffusion in terms of thermally activated ion hopping process would require rather higher temperature. Study by Paulus *et al.*[17] proposed the presence of specific lattice dynamics is the most important parameters to explain such non-Arrhenius process in Brownmillerite frameworks *e.g.* $SrFeO_{2.5}$ and $SrCoO_{2.5}$.

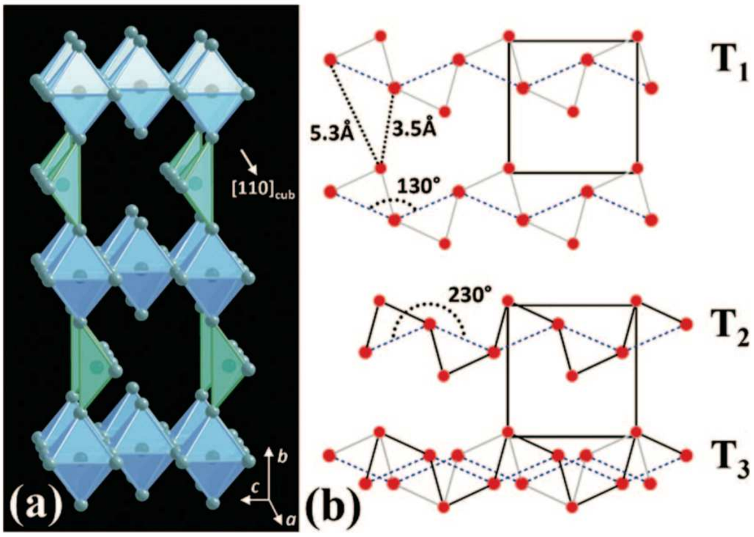

Figure 1.10: Idealized scheme of the Brownmillerite structure with 1D oxygen vacancy channels along $[110]_p$ with respect to the cubic Perovskite phase. FeO_6 octahedra and FeO_4 tetrahedra are reported in blue and green, respectively; Sr or Ca are omitted for clarity. In reality the tetrahedral chains show a *'zig-zag'* arrangement as shown in part (b) (T1 and T2). Dynamical switching between 'R'(T1) and 'L'(T2) configuration can trigger *phonon assisted* oxygen diffusion along the oxygen vacancy channel while the distances from the 'apical O' to 'equatorial O' atoms vary between 3.5 and 5.3 Å. This disorder scenario is schematically represented as T3 ('R'+'L'). The coordinate system (a, b, c) refers to the Brownmillerite structure in *Pnma*. **Reproduced from Fig. 1 of ref.[17].**

The study suggested RT oxygen diffusion is essentially *'phonon assisted'* involving specific low energy lattice modes. The presence of dynamically disordered $(FeO_4)_\infty$ chains enhances the oxygen diffusion acting as internal interfaces to push the oxygen through the vacancy channel (Fig. 1.10). Due to the presence of shallow level lattice modes (see Fig. 1.11), when the apical oxygen atoms being sufficiently far away from their equilibrium positions, they can escape into the vacancy channels and migrate through formation of reoriented tetrahedra leaving behind a square pyramid via *'two-step diffusion'* process as shown in Fig. 1.12. A pronounced lattice dynamics exists also for the tetrahedral chains, showing a marked *'zig-zag'* switching behavior.

The easy escape of the apical oxygen atoms into the vacancy channel and also the switching behaviour of the tetrahedra is mainly determined by the Fe–O bond strength and length along the *c*-axis; the longer the bond, the easier is to displace the oxygen atom. Therefore *c*-axis length influence the fast oxygen diffusion. As reported by the same study the diffusion path for homologous $CaFeO_{2.5}$ found be much slower and only gets activated at higher temperature ($\geq$ 1070 K) compared to $SrFeO_{2.5}$ ($\sim$ 600 K) where they have the respective *c*-lattice parameters of c_{CFO} =14.77 Å and c_{SFO} =15.85 Å.

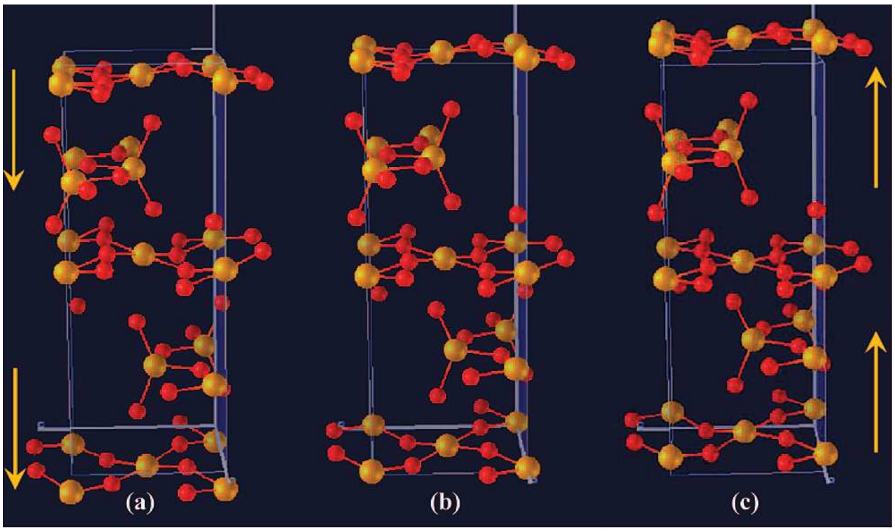

Figure 1.11: Representation of the lattice mode leading to the instability of the apical oxygen position. This mode involves an unidirectional shift, as indicated by the orange arrows of the upper and lower octahedra (at y = 0) and tetrahedra layers (at y = 1/4), while the position of the octahedra layer situated at y = 1/2 remains almost constant. Part (b) corresponds to the equilibrium position, while parts (a) and (c) show the extreme positions of the dynamically displaced layers. **Reproduced from Fig. 4 of ref.[17].**

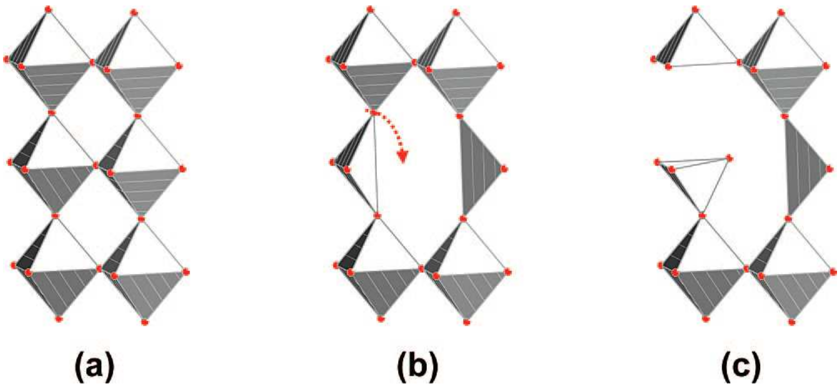

Figure 1.12: Structure schemes of (a) the Perovskite and (b) the Brownmillerite framework. Part (c) presents the intermediate state after the diffusion of an apical oxygen atom to a vacant lattice site in the tetrahedral layer (see red arrow), yielding locally a FeO_5 square pyramid and a newly formed FeO_4 tetrahedron. **Reproduced from Fig. 6 of ref.[17].**

Microstructural modification can alternatively enhance dynamics. The HRTEM study by Gupta *et al.*[59] suggests nanostructured $CaFeO_{2.5}$ synthesized by sol-gel route show lower onset temperature for oxygen mobility compared to bulk $CaFeO_{2.5}$. The presence of much higher defect density in nano-$CaFeO_{2.5}$, especially in the form anti-phase boundary (APB)[56,59], locally affects the ordered (*intra*- and *inter*- layer) arrangements of tetrahedral $(FeO_4)_\infty$ chains in *Pnma*. This local disorder (≤ 50 nm) in nano-$CaFeO_{2.5}$

energetically favors the switching between the 'L' and 'R' chains compared to bulk-$CaFeO_{2.5}$ and results into decrease of onset temperature.

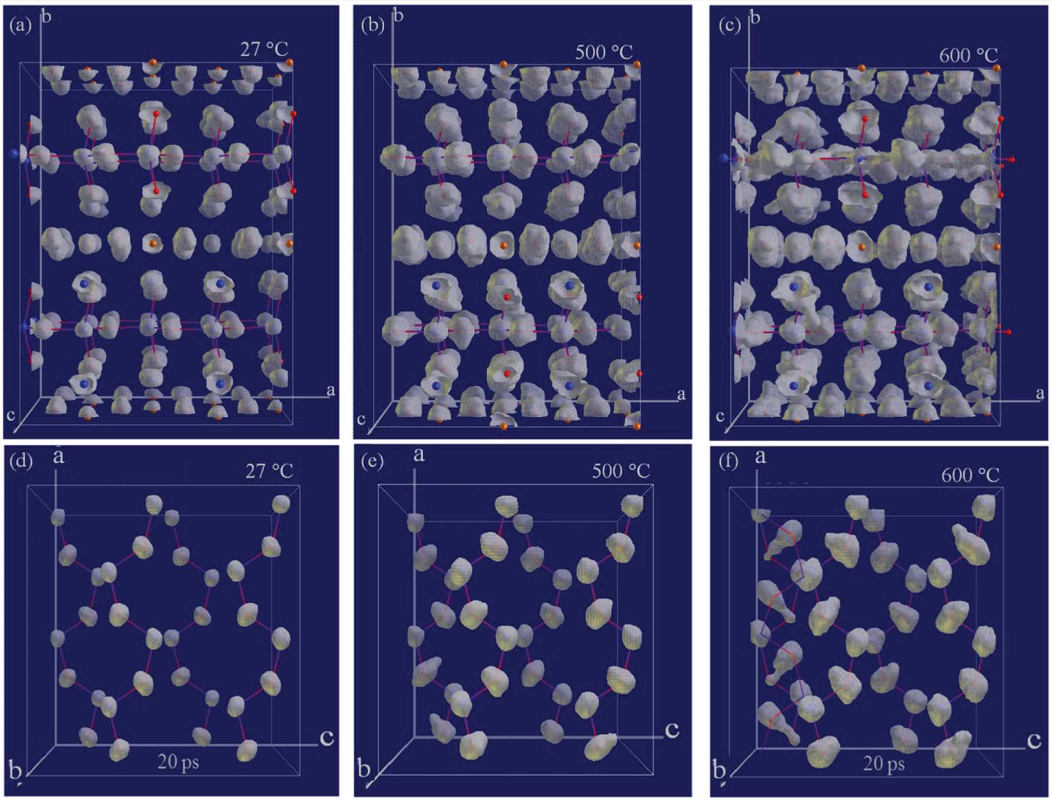

Figure 1.13: Envelopes of O atoms obtained during a 20 ns *ab initio* molecular dynamics simulation for Sr_2ScGaO_5, at different temperatures. While at RT (a,d), only small envelopes are encountered; the Debye-Waller displacements increase to almost twice this value at 500 °C (b,e), and the outer diameter reaching about 2 Å in diameter. The envelopes show a slight anisotropic elongation along the *b*-axis. However, the dynamics at 600 °C (c,f) does not lead to a *wormhole* scenario, involving the apical oxygen atoms jumping toward the 1D-vacancy chains, but to a direct switching of the $(GaO_4)_\infty$-tetrahedral chains from the R to L configuration and vice versa, allowing the amplification of oxygen diffusion along the vacancy channels. **Reproduced from Fig. 12 of ref.[60].**

The other class of Brownmillerite compounds (*e.g.* Sr_2ScGaO_5, Ba_2InGaO_5) with d^0/d^{10} electronic configuration are special as they maintain the oxygen stoichiometry rendering fixed valance state of the cations. Unlike the case of $Sr_2Fe_2O_5$ or $Ca_2Fe_2O_5$ where Fe or Co goes through changes of valance states and coordination, the (MO_x) polyhedra of the TM with $[d^0/d^{10}]$ electronic configurations are rigid in nature. In Sr_2ScGaO_5, Sc^{3+} ions occupy all the octahedral sites, Ga^{3+} ions stay in the tetrahedral sites. Sr_2ScGaO_5 adapts *I2mb* space group with ordered arrangement of $(GaO_4)_\infty$ chain either all in the 'L' or in 'R' configurations. The study by Corallini *et al.*[60] has shown that pure ionic conductor Sr_2ScGaO_5 does not follow *two-step diffusion* process as proposed for $CaFeO_{2.5}$ or $SrFeO_{2.5}$ systems and needs much higher temperature (~ 600

°C) to initiate oxygen diffusion. Molecular dynamics simulation does not evidence any *'wormhole'* type envelop (see Fig. 1.13) representing oxygen migration even upto high temperature (600 °C) where Debye-Waller displacement factor significantly increases except for the equatorial oxygen of the (ScO_6) octahedra. As proposed by the study, $(GaO_4)_\infty$ tetrahedral chains seemingly exhibit an independent dynamics to switch in between 'R' and 'L' configuration reversibly by without involving the (ScO_4) square planar unit of the (ScO_6) octahedra unlike $CaFeO_{2.5}$/$SrFeO_{2.5}$ where the apical oxygen is involved via a *two-step diffusion* process. Structural instabilities along with the dynamic fluctuations of the tetrahedral chains may therefore be an important prerequisite to allow low temperature oxygen ion mobility in solids, at least for those with Brownmillerite type structure.

1.1.2.2 Ruddlseden-Popper phases

Compounds belonging to the RP phase, *e.g.* $RE_2MO_{4+\delta}$ with RE = La, Nd, Pr and M = Cu, Ni, Co, are also well known to show oxygen mobility at ambient[33,61,62]. The structure is similar to K_2NiF_4-type structure consisting of (RE)MO_3 Perovskite layers interspersed by M_2O_2 rock-salt type layers (Fig. 1.14). The non-stoichimetry in this framework arises because of the excess oxygen accommodated in the interstitial sites. The stress inside the structure, related to the considerable mismatch of the two different types of layers as mentioned, is released by insertion of interstitial oxygen inside the rock-salt layer[63]. Smaller the size of the RE atom, more the amount of the interstitial oxygen gets accommodated in the structure.

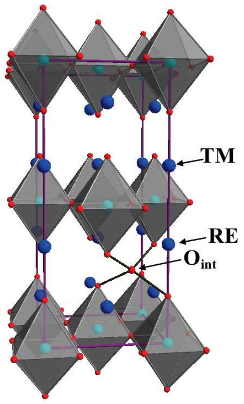

Figure 1.14: $RE_2MO_{4+\delta}$ type structure model with RE = Pr, Nd, La and TM = Ni, Cu, Co. The non-stoichiometric oxygen is related to the oxygen interstitial O_{int} which occupies one of the 8 possible (1⁄4, 1⁄4, z) with z ~ 0.25 position in the *Fmmm* cell.

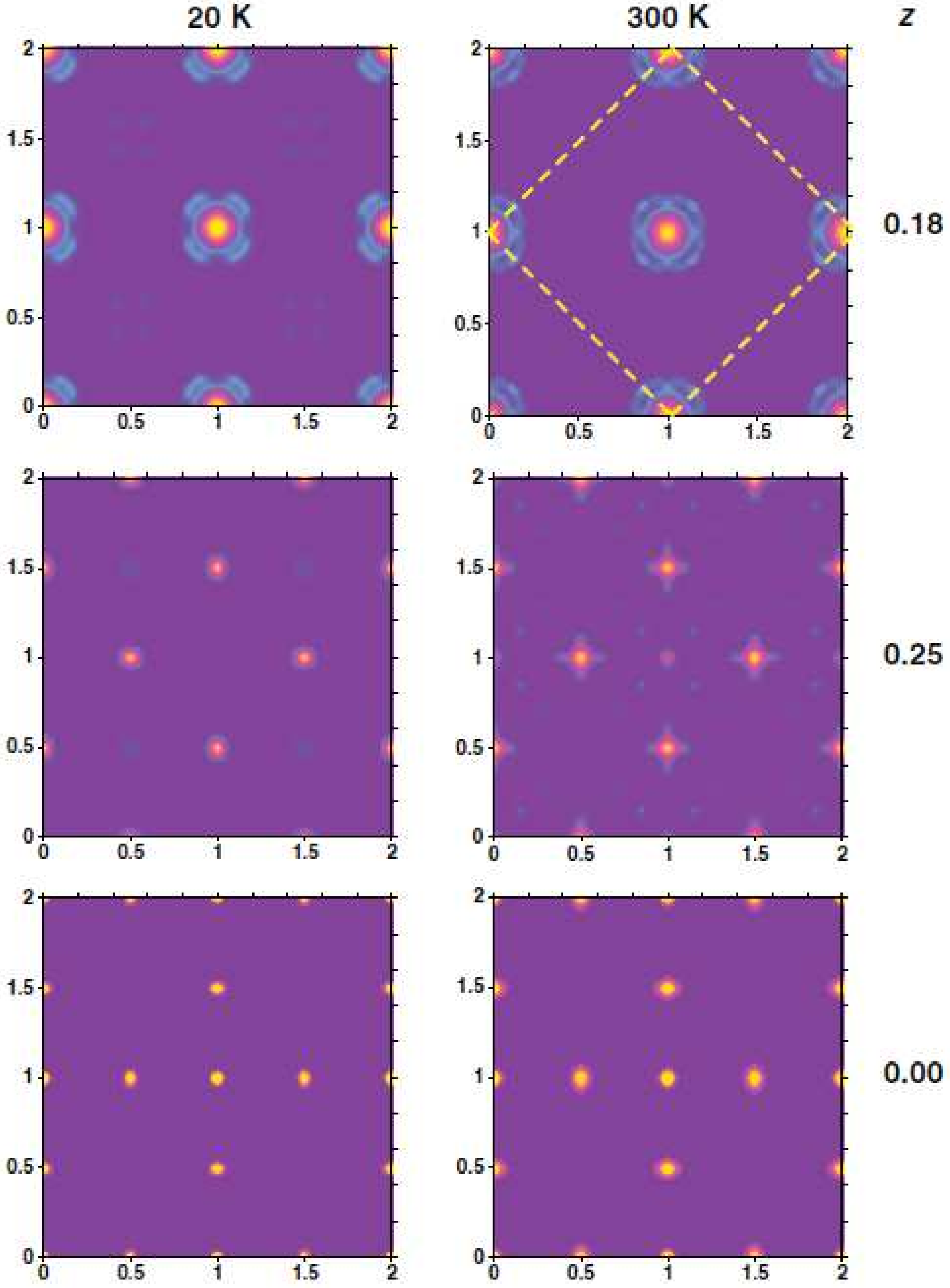

Figure 1.15: Nuclear scattering densities obtained from a $La_2CuO_{4.07}$ twinned single crystal by neutron diffraction study and subsequent reconstruction using the maximum entropy method at 20 K and room temperature. Sections of the apical oxygen layer in z = 0.18 and the interstitial oxygen section in z = 0.25 are given. The F-centered unit cell is outlined for the figure at z = 0.18 and 300 K. **Reproduced from Fig. 2 of ref.[64].**

In order to understand the diffusion mechanisms at ambient temperature, a series of compounds $La_2CuO_{4+\delta}$[64], $La_2Co_{4+\delta}$[65], $Pr_2NiO_{4+\delta}$[18,66], $Nd_2NiO_{4+\delta}$[19], with different size of the RE and TM ions have been investigated experimentally using neutron and X-ray diffraction techniques and as well as theoretically by DFT based *ab-initio* MD simulations. The study by Villesuzanne *et al.*[64] suggests the origin of low temperature oxygen mobility for $La_2CuO_{4.07}$ can be explained by the concept of low energy phonon modes. The strong anisotropic delocalization of the apical oxygen atoms was evidenced from neutron single crystal diffraction data using a maximum entropy method (MEM) (see Fig. 1.15). While at 20 K the atomic displacements of the of the apical oxygen (z = 0.18) is limited to maxima pointing towards the [100]-directions with respect to the *F*-centered unit cell due to the steric hindrance effect of the interstitial oxygen, at RT the displacements are simultaneously present along [100]- and [110]-directions showing the displacements of the apical oxygen atoms on a sphere of 1 Å in diameter from their average positions. This dynamic disorder scenario can explain the migration of apical oxygen atoms towards interstitial lattice sites (and *vice versa*). Closer inspection of the associated lattice modes using DFT calculation shows that in the presence of interstitial oxygen the displacements of apical oxygen along [110]-direction is energetically favored (~ -4.1 meV) compared to the case of stoichiometric La_2CuO_4 (~20 meV). At low temperature the apical oxygen atoms are mobile species but presence of interstitial oxygen is a mandatory requirement. These results strongly evidence the concept of lattice dynamics to be at the origin of low temperature oxygen mobility, with specific requirements depending on the underlying structural framework.

Homologous $Pr_2NiO_{4.25}$, $La_2CoO_{4.25}$ and also $Nd_2NiO_{4.25}$ are more interesting since they can accommodate much higher amount of interstitial oxygen compared to $La_2CuO_{4.07}$ which makes them promising oxygen ion conductors for membrane application in SOFC. Ceretti *et al.*[18] very recently have shown by single crystal neutron diffraction and subsequently by MEM analysis of $Pr_2NiO_{4.25}$ at ambient and 400 °C, a much more pronounced displacement of the apical oxygen atoms towards the interstitial lattice sites in the [110]-direction of the *F*-cell compared to the case of $La_2CuO_{4.07}$. The stability of $Pr_2NiO_{4.25}$ with respect to interstitial oxygen content even above 500 °C, makes it a key model compound to study the effect of anharmonicity which appears in the lattice dynamics at such high temperature. Also it helps to understand influence of the presence of interstitial oxygen to initiate anisotropic oxygen mobility triggered by lattice dynamics. Slightly above the orthorhombic–tetragonal phase transition (~400 °C), the anharmonic apical oxygen displacements occur towards [110]-direction of in the *F*-cell ([100]-direction in original *I4/mmm* cell) of the commensurate tetragonal parent structure under a double-well potential creating a quasi continuous shallow energy diffusion pathway between apical and interstitial oxygen sites Fig. 1.16.

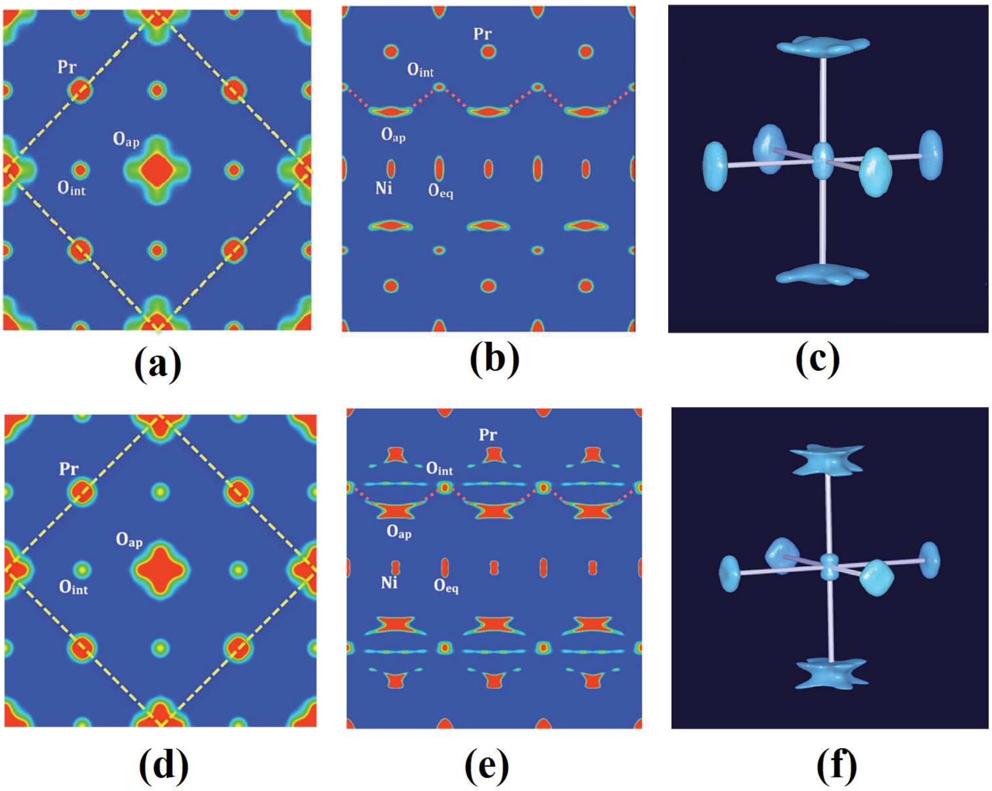

Figure 1.16: (a, b, d, e) Neuclear density maps of $Pr_2NiO_{4.25}$ obtained from neutron single crystal diffraction data by MEM analysis; (a) and (d) represents respectively the scattering densities of Pr (z = 0.14), O_{ap} (z = 0.17) and O_{int} (z = 0.25) integrated in the range $0.12 \leq z \leq 0.25$ in the $2a \times 2a$ projection of the *I4/mmm* unit cell at RT and 400 °C. Note that the F-centred cell is outlined by yellow dashed bars. Similarly (b) and (e) represents respectively the scattering densities of Pr, O_{ap} and O_{int} integrated in the range $0.452 \leq y \leq 0.55$ in the $3a \times c$ projection of the *I4/mmm* unit cell at RT and 400 °C. The red dashed lines indicates the oxygen diffusion pathways along the a-axis in the I-cell, equivalent to [110]-direction in the F-cell, between apical and interstitial sites. (c) and (f) represents the isosurface of the NiO_6 octahedra at RT and 400 °C respectively. **Figures are taken from ref.[18].**

.

Perrichon *et al.*[19] investigated the effect of the oxygen interstitial and length of the stacking axis ('c' lattice parameter) on the lattice dynamics for $Nd_2NiO_{4+\delta}$ framework by the DFT based MD simulation and by neutron TOF spectroscopy. It has been shown by position recurrence map (PRM)[67], calculated from molecular dynamics trajectories at RT, that with the increasing amount of interstitial oxygen and c-axis length, the displacements of the apical oxygen atoms get enhanced along the [110]-direction thus favouring diffusion towards interstitial sites (see Fig. 1.17(a)). On a first look PRM may look similar to nuclear density maps obtained by MEM analysis from diffraction data, but there is a subtle difference between these two kind of maps. In PRM, only the dynamical contribution specific to the single particle motion is taken into account, as the atomic displacement is calculated from center-of-mass of the atom. Unlike maximum entropy method, the static deformations are not taken into account.

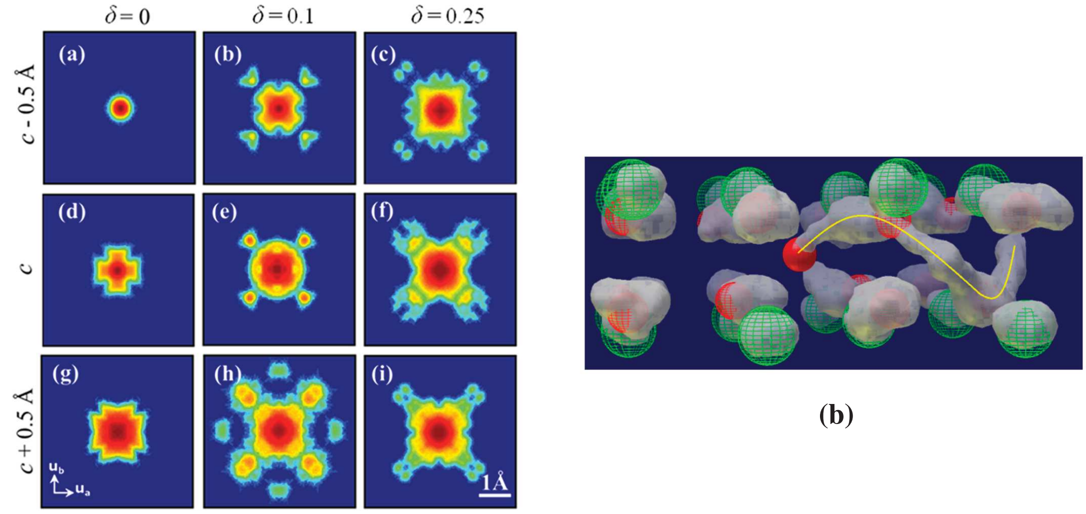

(a)

(b)

Figure 1.17: (a) Positional recurrence maps: displacement vectors of apical oxygen atoms in the Nd_2O_2 rock-salt layer from center-of-mass positions projected on unitary vectors (a,b), with respect to the conventional F-cell. PRMs are calculated from *ab initio* molecular dynamics at 310 K, of (Fig. 3a, d, g) Nd_2NiO_4, (Fig. 3b, e, h) $Nd_2NiO_{4.10}$, and (Fig. 3c, f, i) $Nd_2NiO_{4.25}$, with (Fig. 3a–c) reduced c-axis parameter by 0.5 Å, (Fig. 3d–f) optimal c-axis parameter, and (Fig. 3g–i) elongated c-axis parameter by 0.5 Å. The color scale is logarithmic. Each PRM is cut in space to the conventional F-cell (black border). **(b)** Detail of the rock-salt layer of the $Nd_2NiO_{4.10}$ supercell in the T = 310 K molecular dynamics. Wired green spheres represent Nd^{3+} ions, wired red spheres O^{2-} ions in apical sites, and plain red spheres O^{2-} ions in the interstitial site. Atoms are drawn at their initial positions. Gray clouds represent the ensemble of positions occupied by the atoms over 40 ps of the molecular dynamics. Connected clouds from apical to interstitial sites are marked with a yellow line and evidence oxygen mobility. **Reproduced from Fig. 5 and Fig. 6 of ref.[19].**

The diffusion pathway of mobile oxygen extracted from MD calculations show that in non-stoichiometric $Nd_2NiO_{4+\delta}$ the envelop of the oxygen diffusion passes through the interstitial sites (see Fig. 1.17(b)), similar to the one reported for isostructural $La_2CoO_{4+\delta}$ and $Pr_2NiO_{4+\delta}$. The mechanism of diffusion involves both apical and interstitial oxygen atoms with a defined scheme. In the *1st Step*: one of the apical oxygen atoms, closest to the interstitial oxygen, diffuses away to a nearby vacant interstitial site followed by *2nd step*: the former interstitial oxygen diffuses to the newly vacant apical site. Such diffusion is confined in the rock-salt layer with jump only along [110]-direction. In the absence of excess oxygen in the interstitial sites no diffusion events occur as reported by Perrichon *et al.*[19].

1.1.2.3 Apatites

Another family of compounds which show high oxygen conductivity belong to Apatite with general formula $La_{10-x}Ge_6O_{26+y}$ and $La_{10-x}Si_6O_{26+y}$ [68–70] . At lower temperature these compounds show high level of ionic conductivity compared to YSZ. The structure of the silicate apatite $La_{9.33}(SiO_4)_6O_2$ is shown in Fig. 1.18(a). The arrangement of isolated (SiO_4) tetrahedra in this structure give rise to two distinct channels parallel to c-direction of the lattice. Lanthanide cation occupies both of these channels whereas the oxygen occupies only the big channels. The mechanism of oxygen diffusion in appatites is different compared to the vacancy hopping mechanism as in the case of YSZ or CGO. It has been shown experimentally and theoretically the presence interstitial oxygen is crucial for the diffusion to occur[71–74]. In fact, the detail atomic scale simulation by Tolchard *et al.* [75] suggested that the interstitial oxygen resides in the periphery of the larger channel instead of its center favouring the displacement of the neighbouring (SiO_4) tetrahedron towards the La-channels. The presence of channel restricts the oxygen diffusion along c-direction giving a very anisotropic nature. The atomistic simulation by Kendric *et al.* [71] reveales that co-operative tilting of (SiO_4) tetrahedra push the interstitial oxygen through the vacancy channel in a *sinusoidal* path as shown in Fig. 1.18(b). Thus flexibility and dynamics of the (SiO_4) tetrahedral moieties play an important role for oxygen diffusion at low temperature.

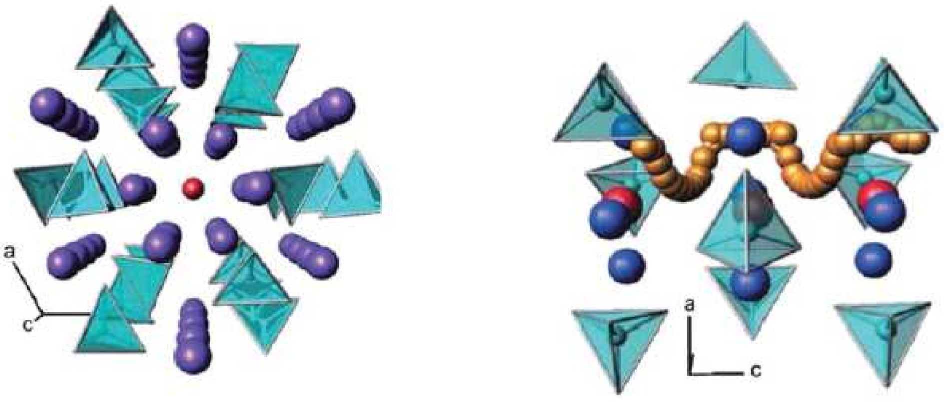

(a) **(b)**

Figure 1.18: (a) Structure of the silicate apatite $La_{9.33}(SiO_4)_6O_2$ and (b) oxygen migration path (yellow) perpendicular to the crystallographic c-axis. Oxygen ions in the channels are in red, SiO_4 tetrahedra in light blue and La cations in purple. **Reproduced from Fig. 11 of ref.[36].**

In the last two subsections few well established oxygen diffusion mechanisms have been briefly discussed, importantly showing that completely different mechanisms exist explaining oxygen diffusion at low temperature compared to high temperature.

1.2 Oxygen ordering at ambient

In the last section a few well established oxygen diffusion mechanisms have been discussed in short showing that completely different mechanisms can explain the oxygen diffusion at low temperature. Lattice dynamics plays a crucial role in non-Arrhenius regime of oxygen mobility. Even more importantly it has been shown that at low temperature not only oxygen can diffuse through the lattice but also get ordered in long range giving rise to different oxygen ordered metastable phases which are in general difficult to obtain by conventional high temperature synthesis.

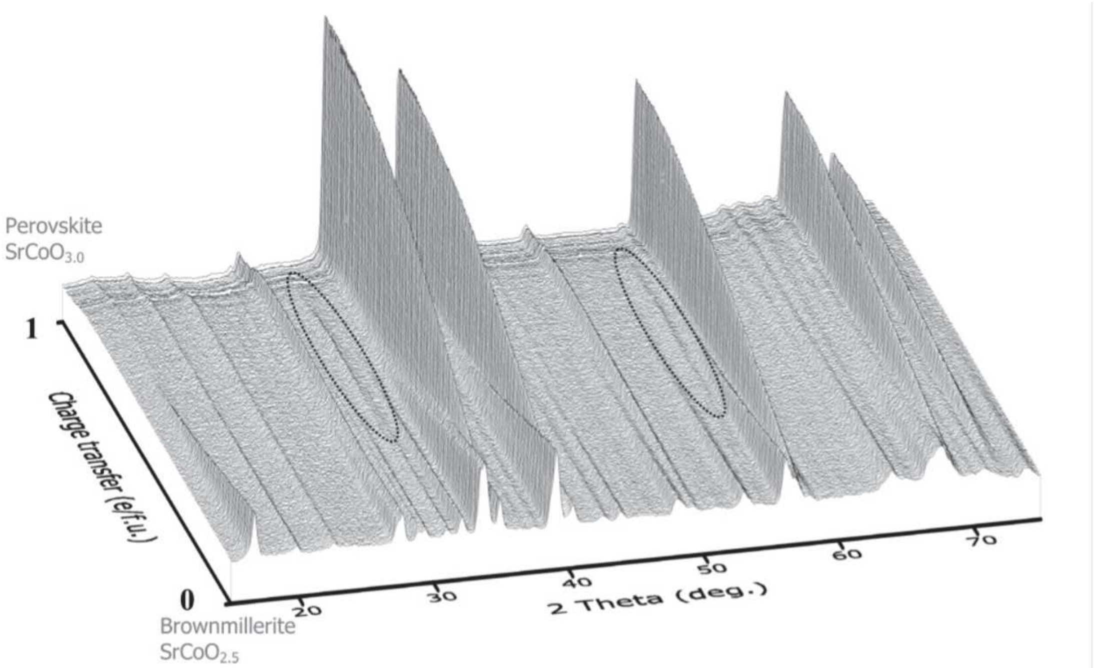

Figure 1.19: Evolution of the NPD pattern obtained *in situ* during the electrochemical oxidation of $SrCoO_{2.5}$ as a function of charge transfer. The diffractogram of the Brownmillerite $SrCoO_{2.5}$ is represented at the bottom, whereas that of the Perovskite $SrCoO_{3.00}$ is shown at the top. The dotted ellipsoids show the positions of the superstructure reflections corresponding to the long range oxygen order. **Reproduced from the Fig. 4 of ref.[35].**

The study by Le Toquin *et al.*[35] show evidence of such oxygen ordering at ambient. The Study reported the electrochemical oxygen intercalation in Brownmillerite type $SrCoO_{2.5}$. On the course of the electrochemical oxygen intercalation $SrCo_{2.5} \rightarrow SrCo_3$, new superstructure reflection were observed as shown in Fig. 1.19. Which clearly suggests that oxygen is not only mobile inside the structure even at ambient, but instantly gets ordered in long range.

1.3 Summary

In this chapter we have discussed different classical and non-classical oxygen diffusion mechanisms. In the classical high temperature oxygen diffusion, oxygen mainly diffuse through the vacancy mediated hopping mechanism. In low temperature oxygen diffusion, lattice instability along with the associated dynamics become very important. Also we have discussed at ambient not only oxygen diffuses through the structure but also gets ordered in long range. As a consequence of the long-range ordering it gives a possibility to obtain some metastable phases which are very difficult to synthesize at high temperature.

Chapter 2

Experimental Techniques

In this thesis work we have investigated single crystals of mainly two compounds, Brownmillerite $SrFeO_{2.5}$ and Ruddlesden-Popper $Pr_2NiO_{4.25}$. High-quality single crystals of these compounds were prepared by Image Furnace using Travelling Solvent Floating Zone (TSFZ) technique[76]. One particular aim of this thesis work was to follow the structural evolution of theses compounds *in situ* during electrochemical (EC) oxygen intercalation/deintercaltion in these single crystals, in order to understand the reaction mechanism on the course of oxygen intercaltion and to draw important differences with reaction mechanisms at high temperature. During the oxygen intercaltion, the oxygen gets immediately ordered inside the structure via formation of stable or metastable intermediate phases. But the problem to identify such oxygen ordereding is the related intensities which are too weak to detect with the normal laboratory X-ray. The high brilliance synchrotron X-ray gives the opportunity to see such superstructures taking advantage of the high-resolution detectors available in the beamlines.

Electrochemistry on single crystal is challenging related to the limited reactivity and takes almost a year to oxidise a $[5\times5\times5]$ mm^3 single crystal. This is the reason that solid-state reactivity followed up on single crystals is almost unreported in literature and is generally limited to surface reactions or defined starting and final reaction products[77] [78]. In order to investigate the *'complete'* intercalation reaction in a feasible time scale (few days), we used single crystals of approximately $[50\times50\times400]$ μm^3 size. Performing EC intercalation on such tiny crystals with diameter less than human hair thickness comes with a lot of challenges. We had to develop a special electrochemical cell dedicated only for such purpose also taking care of the proper adaptation of the cell on the diffractometer of BM01A at SNBL, ESRF where the *in situ* investigations were performed.

In this chapter we will discuss at first the method of single crystal growth by Floating Zone (FZ) technique in the optical image furnace. Afterwards we present in details the construction of the EC cell which was perfectly adapted on the beamline for investigating EC intercalation on micrometer size single crystals followed by the particular experimental strategy and setup used for the diffraction on BM01A diffractometer.

2.1 Crystal growth by FZ technique in Image Furnace

High quality single crystals of $SrFeO_{2.5}$ and $Pr_2NiO_{4.25}$ were obtained by FZ technique in an image furnace (NEC, Japan) (see Fig. 2.1). Synthesis of good quality single crystals is very important and crucial in order to investigate the structural and physical properties. More importantly physical properties drastically change with the presence of impurity or undefined stoichiometry. Especially good quality single crystal growth of the non-stochiometric oxides is very challenging, as very precise control of temperature and the oxygen partial pressure is important to keep the oxygen stoichiometry fixed. A less controlled synthesis most of the time leads to unwanted crystals with inhomogeneity, phase-mixture or undefined oxygen stoichiometry.

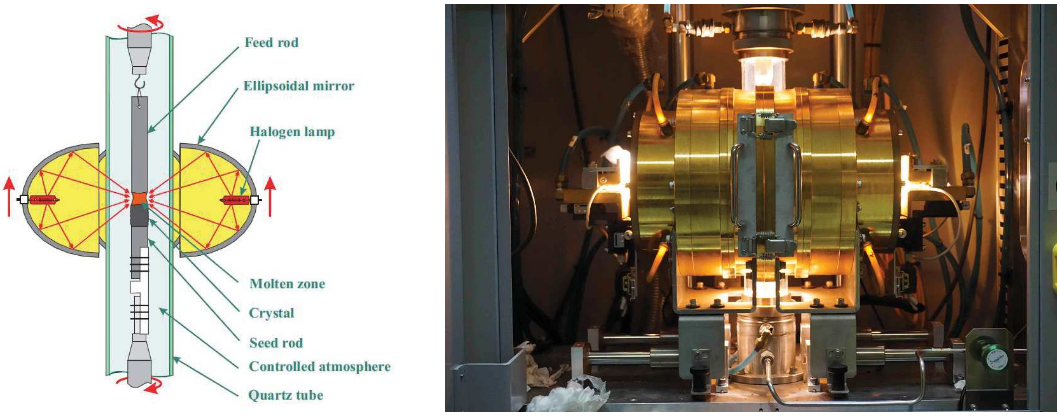

Figure 2.1: (left) Schematic diagram of an Image Furnace apparatus. (right) A picture of inside of the Image Furnace (from NEC Machinery Corporation, Japan), during single crystal growth.

Though there are many techniques available to grow big size single crystal (*e.g.* Bridgman and Czochralski method), the most common technique yielding large single crystals (approximately 10 cm in length and 8 mm in diameter) of transition metal oxides and insulating compounds remains the floating zone method with optical Image Furnace. In addition, this is the only method that allows to grow single crystals of compounds which melt incongruently.

Among the different zone melting techniques, the vertical floating zone configuration is recognized as the "*cleanest*" method as the molten zone inbetween two solid rods, *i.e.* seed and feed rods, is formed by contact-less heating and held by its own surface tension (see Fig. 2.1(left)). Being a crucible free method it avoids contamination and generally used for materials which are highly reactive or having high-melting temperatures. For the oxide materials which are mostly insulating, infrared image furnaces are used in which the radiation is focused by gold-coated ellipsoidal mirrors in the desired floating point. Powerful halogen or xenon lamps are used as the power source and a temperature of approximately 3000 °C can be easily reached. To keep the floating zone stable for an extended time is extremely difficult. The mirror and lamp positions need to be optimized to produce the optimum temperature gradient in the axial direction. The seed and feed rods are held inside a quartz tube (see Fig. 2.1(right)) where the single crystal growth takes place. It allows different gas atmosphere and also gas pressure almost up to 5 bars. Image Furnace are in general equipped with infrared camera in order to examine the molten zone and to do necessary adjustment of the lamp positions in order to keep the molten zone stable throughout the single crystal growth.

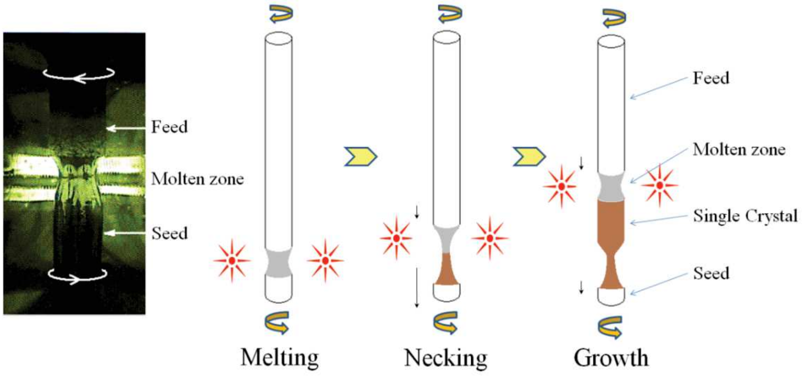

Figure 2.2: General process for single crystal growth with Image Furnace; the "*necking*" allows to form a single grain which is the starting point of the single crystal growth.

The principle for single crystal growth is rather simple. First the dense feed and seed rods of the desired compound are made by hydrostatic pressing the powder in a cylindrical latex tube of size typically 8 mm in diameter and 150 mm in length followed by annealing afterwards. The feed rod is hanged from an iron shaft and placed coaxially on the top of the seed rod inside the quartz tube. At first the junction is adjusted at the focal point of the mirror in order to melt. Once the junction starts melting, the seed and feed rods are rotated in opposite directions continuously. After reaching a suitable condition, when the molten zone (solvent) is almost stable, the whole assembly 'seed–solvent–feed" is moved downwards very slowly. Because of the temperature gradient the solvent solidifies on the seed. Usually to grow the crystalline phase, at the beginning the seed is pulled downward faster than the feed which produce a slim neck in the molten zone. This process is called "*necking*" (see Fig. 2.2). Necking is very crucial to obtain single crystals. Necking is done to reduce the number of grains from the polycrystalline sample. In this way the grains are eliminated until only one large grain, the desired single crystal, remains. Afterwards, the diminution of the rotation speed of the seed rod allows the single crystal to grow in diameter to the final size, typically 5-10 mm and then onwards the crystal of such diameter continues to grow in length as long as "*fresh*" feeding material, the upper rod, is available.

2.1.1 $SrFeO_{2.5}$: single crystal growth

Single crystals of $SrFeO_{2.5}$ have been grown by the floating zone method in an Image Furnace (NEC SC2, Japan) equipped with two 500 W halogen lamps as described before. At first the polycrystalline feed and seed rods of $SrFeO_{2.5}$ were prepared using standard solid-state synthesis methods. High purity $SrCO_3$ (99.95%) and Fe_2O_3 (99.99%) were thoroughly mixed in appropriate molar ratios and heated in air at 900 °C for 24 h. After being furnace cooled to room temperature, the obtained product was ground and pressed into pellets of about 1 gm each. The pellets were then sintered at 1200 °C for 24 h followed by quenching in air down to ambient. Seed and feed rods for crystal growth were obtained by hydrostatic pressing of $SrFeO_{2.5}$ powder obtained from grounded pellets at 10 bars in a cylindrical latex tube of 8 mm in diameter and 150 mm in length. The as obtained rods were then sintered in air at 1200 °C for 24 h to obtain dense polycrystalline rods. Crystal growth was performed in high-purity Ar-atmosphere (99.999%). The seed and feed rods were rotated in opposite directions at 25 rpm with a travelling rate of 1 mm/h through the melting zone. The obtained as grown crystals had a typical length of up to 10 cm and 8 mm in diameter with shiny metallic lustre. A photo of the parts of such as grown crystal is shown in Fig. 2.3.

Figure 2.3: Sections of the as grown single crystal of $SrFeO_{2.5}$.

2.2 Electrochemical Cell

The detail construction of EC cell designed for the *in situ* experiment is shown in the schematic diagram in Fig. 2.4. All the necessary components are labeled. As can be seen from the diagram, the design of the cell is very compact. The hight and the diameter of the cylindrical shaped cell are 45 mm and 30 mm respectively. The main body of the cell is made up of hard plastic cylinders (white part with black stripes) encapsulated with a metal cap and a metal base with 3 metal screws (only one is shown). All this blocks are connected by the co-axial central channel. In perpendicular to the central channel, two more channels are made through the upper and lower plastic blocks which are essentially connected to each other via the central channel. Through the central channel two debye-scherrer capillaries telescoped (one inside the other) to each other are placed. The outer capillary is colored in sky blue and the inner capillary is colored in light green. The single crystal used as electrode ('-ve' or '+ve' depending on the reduction or oxidation reaction) is placed inside the inner capillary on the top of a gold wire ϕ = 50 μm (shown as red line) by silver paste and carefully fixed on the wall of the capillary. Please note that the inner capillary of diameter (ϕ = 300 μm) is cut at the upper end and the base of the capillary is connected to the lower channel (inlet). While the upper capillary of diameter (ϕ = 700 μm) is closed at the top end and the lower end is connected to the upper channel (outlet). This gives a closed circulation for the electrolyte flow. The counter electrode can be inserted anywhere in the electrolyte (here we put in the outlet channel). 1N KOH electrolyte was steadily pumped by a peristaltic pump through the inner capillary while flowing back through the outer one. A permanent electrolyte flow guaranties constant reaction conditions and also assures the transport of gas (O_2 or H_2) bubbles, which are always produced as a by-product during the electrolysis, away from the crystal. A constant current of 10 μA was applied by a KEITHLEY current source during the whole intercalation reaction. The biggest advantage of this particular design of the EC cell was its liberties of movements. It gives same degrees of freedom for single crystal diffraction as same as that of a standard goniometer head. Fig. 2.5 shows the installation of the electrochemical cell on the BM01A diffractometer at ESRF with all necessary connections for electrolyte flow and current. The cell allows free rotation of 360 °. This helps to access the changes in the whole reciprocal space through out the EC intercalation while the system stays under chemical equilibrium. Particular lattice planes of interest can be easily reconstructed from such 3D data.

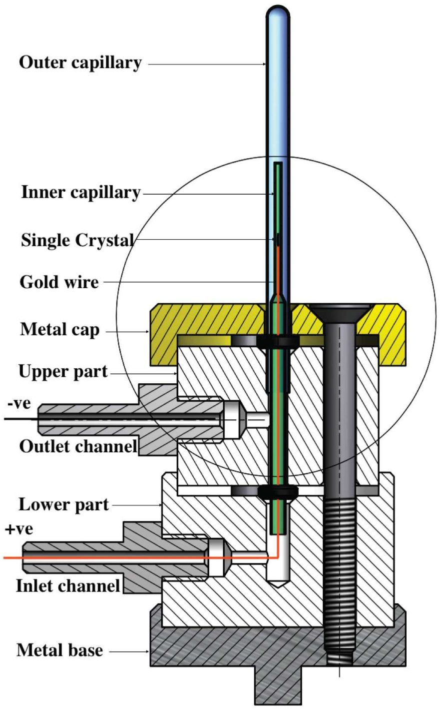

Figure 2.4: Electrochemical cell dedicated for the *in situ* oxygen intercalation investigation in very small micron size single crystals and perfectly adapted on the BM01A diffractometer at SNBL, ESRF.

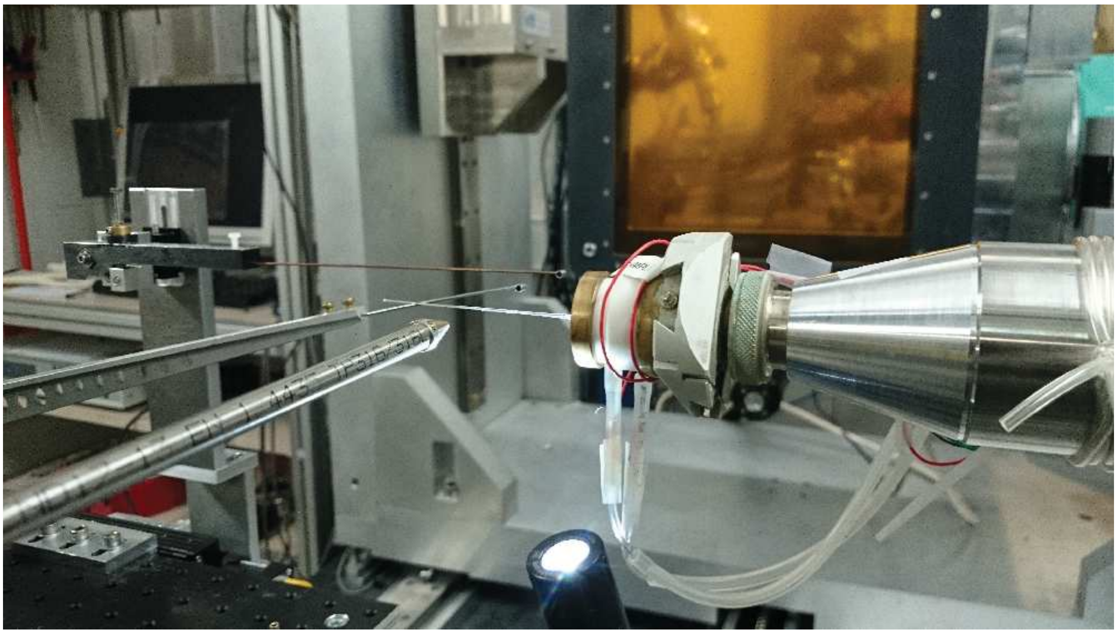

Figure 2.5: Installation of the electrochemical cell, used for *in situ* single crystal diffraction studies, on BM01A diffractometer. The whole cell allows free rotation of 360°, enabling to scan almost whole reciprocal space, suitable for reconstruction of specific lattice planes.

2.3 Diffraction on BM01A at SNBL, ESRF

In this thesis work most of the *in situ* investigations reported have been performed on the multipurpose diffractometer BM01A[79] at Swiss–Norwegian Beamlines (SNBL) in The European Synchrotron, ESRF. The multifunctional diffractometer, combined with a high resolution, fast and low-noise area detector 2M Pilatus, opens up the opportunity for very fast and good quality data collection, especially important for the experiments with fast kinetics. The possibility to tilt or to move horizontally/vertically the detector together with flexible goniometry for sample positioning and orientation is advantageous for installing range of experimental setups (several heating and cooling devices, *in situ* cells and complimentary spectroscopic tools) and also to access particular section of the reciprocal space with high resolution (see Fig. 2.6).

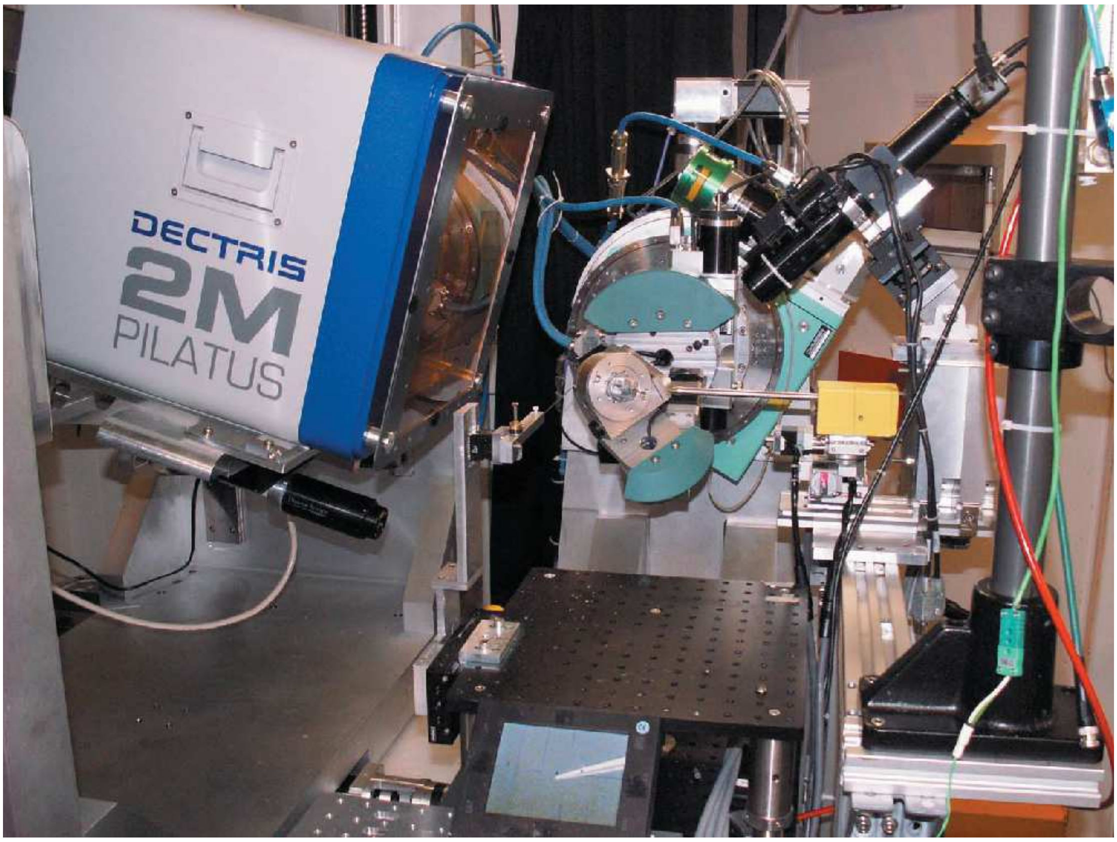

Figure 2.6: The diffractometer PILATUS at BM01A, SNBL with the tilted 2M Pilatus detector and the Huber mini-kappa goniometer. **Reproduced from Fig. 1 of ref.[24].**

Monitoring the on-going intercalation reaction on the single crystals of $SrFeO_{2.5}$ and $Pr_2NiO_{4+\delta}$ on BM01A diffractometer, strongly benefits the fast and almost zero noise data collection, which is possibly due to the combination of a sufficiently high beam intensity together with the use of a 2M Pilatus detector, having a readout time of 2.5 ms only.

The possibility to tune the energy of the SX-ray beam and also the thresold energy of the Pilatus detector (no photon detection below 12 keV), helps to suppress widely any fluorescence below 12.00 keV. To illustrate, during the EC on single crystal of $SrFeO_{2.5}$ as will be discussed in chapter 5, the fluoresence originating from Fe K-absorption edge at 7.112 keV (with K_α at 6.403 keV and K_β at 7.06 keV) was suppressd by tuning the threshold energy of the detector. While the fluorescence from Sr K-absorption edge (16.104 keV) was suppressed by tuning the energy of SX-ray beam to exactly 16.00 keV corresponding to $\lambda = 0.7750$ Å. Similar precautions were taken also for the measurement on $Pr_2NiO_{4+\delta}$ single crystals.

An important advantage of BM01A in terms of unambiguous data interpretation, is the absence of contamination by harmonics and its very narrow energy resolution, achieved via a combination of focusing beam optics with a double crystal monochromator. Data collection in BM01A is done by a user friendly and GUI-based software *Pylatus*. All the data were collected for different measurements in a timescale of ≤ 0.5 s per frame while rotating the electrochemical cell with a 0.1° angular step.

For example, during the EC oxidation on $SrFeO_{2.5}$, a full sphere data collection takes 18 min for 3600 frames (0.3 s per frame). During the constant data collection of 5 days, a total no of 1188000 frames were collected, presenting a data size of 2.7 TB. This huge amount of data was pre-processed with an in-house-developed package SNBL ToolBox[24] at SNBL beamlines containing different utilities to convert the data for different platform. Final data analysis and reconstruction of the reciprocal planes was done using CrysAlis^{Pro} software[80](version 171.36.28).

Chapter 3

Phase diagram of $SrFeO_{3-x}$ system

$SrFeO_{3-x}$ is a very well investigated system at least for last six decades but still it does not lose its interest as it shows many fascinating physical and chemical properties. In this chapter we will discuss the as established phase diagram of this compound and related structure models obtained from high temperature synthesis and also at ambient by EC, in order to emphasize the important differences in terms of reaction mechanisms and intermediate phases at these two different synthesis regime. We will discuss the oxygen vacancy ordering scheme for the different phases including their physical properties. Also we will highlight the recently proposed structure model for the $SrFeO_{2.5}$ with ordered tetrahedral chain arrangement in comparison to the one with disordered tetrahedral chain arrangement and the related effects on the oxygen diffusion.

$SrFeO_{3-x}$ possesses a small portion of the wide pseudo-binary phase diagram[81] in the SrO-Fe_2O_3 in air (Fig. 3.1). Till now established phases of this solid solution series are $SrFeO_{3-x}$; with $x = 0.5, 0.25, 0.125, 0$ as established in literatures. These phases are difficult to prepare and even difficult to characterize as one has to necessarily deal with defect structures (i.e. oxygen vacancy) which eventually depend on the sample history. Gallagher *et al.*[82] and MacChesney *et al.*[83] were the first ones to investigate these phases and characterize them by Mössbauer spectroscopy and X-ray diffraction. The aim was to study the different environment of Fe-coordination and valance states for different oxygen stoichiometry of $SrFeO_{3-x}$. Thenceforth successive studies by Toefield *et al.*[84], Greaves *et al.*[85], Gibb *et al.*[86], Takeda *et al.*[87] and Takano *et al.*[88] significantly contributed to predict the oxygen vacancy ordered structures and also magnetic alignment of the series $SrFeO_{3-x}$ ($0 < x < 2.5$). However important limitations exit for each studies regarding synthesis conditions and associated difficulties of near cubic defect structure which were subsequently resolved from later studies. The summary of the above studies imply that beyond a composition dependent transition temperature, $SrFeO_{3-x}$ form a continuous oxygen vacancy disordered solid solution with cubic Perovskite structure.

On cooling three miscibility gaps arise which divide the $SrFeO_{3-x}$ system into four distinct phases. These phases are line phases as they are formed in a very narrow region of oxygen stoichiometry and can be considered as a member of the ideal line phase series $Sr_nFe_nO_{3n-1}$ with n = 2, 4, 8, ∞. Each of these phases has distinct oxygen vacancy ordering scheme and shows different electronic and magnetic properties. The study by Hodges *et al.*[89] is the first elaborative study showing systematically all possible oxygen vacancy ordering scheme for all the phases synthesized by high temperature (HT) synthesis.

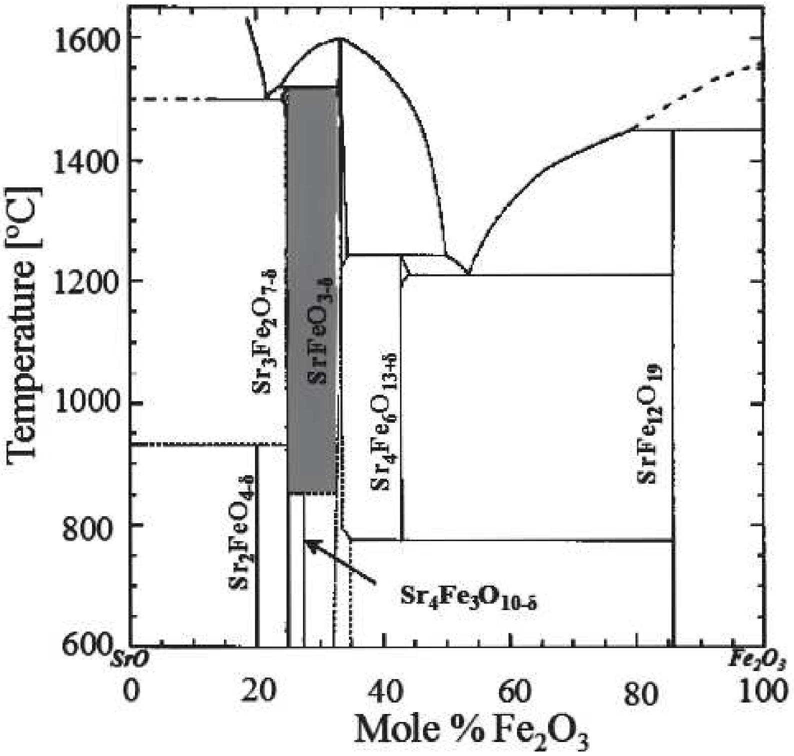

Figure 3.1: Pseudo-Binary phase diagram in the system SrO-Fe_2O_3 in air. The high temperature (> 1000 °C) region was measured in O_2 atmosphere. **Reproduced from ref.[81].**

3.1 Phase diagram obtained by HT synthesis

3.1.1 $SrFeO_3 (n = \infty)$

$SrFeO_3$ is the end member with highest oxygen content of this series $Sr_nFe_nO_{3n-1}$ with $n = \infty$. At room temperature $SrFeO_3$ possesses a cubic Perovskite structure adapting in $Pm\bar{3}m$ space group with three dimensional network of corner sharing FeO_6 octahedra Fig. 3.2(a). Idially the fully oxidized phase of $SrFeO_3$ is without any oxygen vacancy in comparison to the other oxygen-vacancy ordered members. Fe atoms in $SrFeO_3$ are in the (+IV) valence state giving a strong covalent character to the 'Fe–O' bond[90]. The stronger covalency increase the width of the conduction band, which is formed from the σ*(Fe:3d – O:2p) antibonding e_g orbitals. In contrast to the other transition metal oxides with high spin state of transition metal, $SrFeO_3$ and related compounds do not show *Jahn–Teller* effect because of the increased delocalization of the e_g electrons driven by extended band width[90]. The compound exhibits metallic conductivity ~103 S cm^{-1} [83,91] and undergoes phase transition from paramagnetic to helicoidal magnetic state (i.e. screw-type antiferromagnetic ordering) near to T_N = 130 K[91] Fig. 3.3. This unusual combination of metallic conductivity and antiferromagnetism in $SrFeO_3$ is related to the enhanced 'Fe–O' bond covalency and O:2p to Fe:3d electron itinerancy.

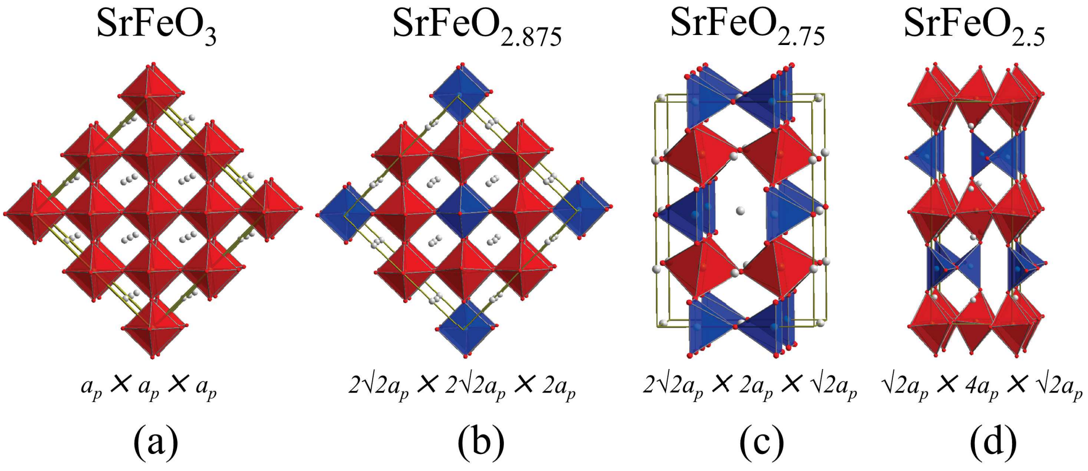

Figure 3.2: (a) Cubic Perovskite structure of $SrFeO_3$ with three dimensional network of corner sharing FeO_6 octahedra. (b) Tetragonal structure of $SrFeO_{2.875}$ with Fe atoms in square pyramidal FeO_5 and octahedral FeO_6 configurations. (c) Orthorhombic structure of $SrFeO_{2.75}$ with Fe atoms in the similar square pyramidal and octahedral configurations. (d) Orthorhombic $SrFeO_{2.5}$ with Fe atoms in FeO_6 octahedra and FeO_4 tetrahedra. All the cells are parameterized with respect to the pseudocubic cell $[a_p \times a_p \times a_p]$.

3.1.2 $SrFeO_{2.875}$ and $SrFeO_{2.75}$

$SrFeO_{2.875}$ (n = 8) and $SrFeO_{2.75}$ (n = 4) are the two vacancy ordered intermediate phases of the series $Sr_nFe_nO_{3n-1}$ (Fig. 3.2(b) and (c)). Oxygen vacancies are ordered in the supercells with lattice parameters $[2\sqrt{2}a_p \times 2\sqrt{2}a_p \times 2a_p]$ and $[2\sqrt{2}a_p \times 2a_p \times \sqrt{2}a_p]$ for the respective phases where a_p is the lattice parameter of the pseudocubic cell. Ideally $SrFeO_{2.875}$ can be realized by incorporating one oxygen vacancy along $[101]_p$ Perovskite direction for each 8 unit cells of $SrFeO_3$, while for $SrFeO_{2.75}$ each 4 unit cells of $SrFeO_3$ contain one oxygen vacancy. The structural complexity arises from the

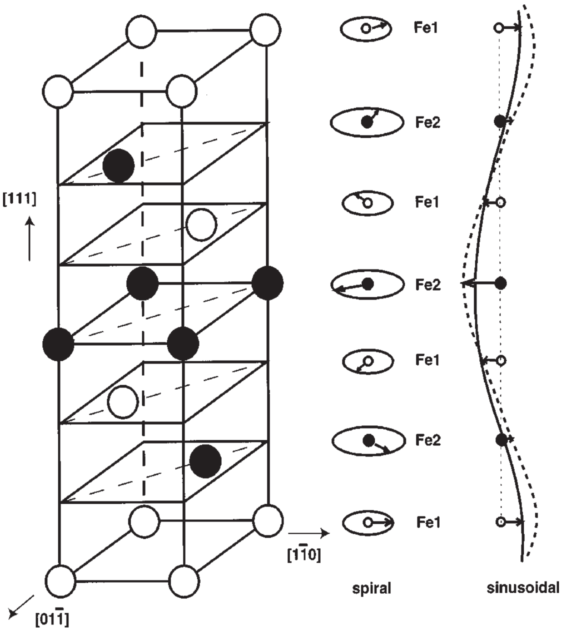

Figure 3.3: Schematic illustration of the helicoidal magnetic structures as seen in homologous CaFeO3 system at low temperature below ~200 K where it goes through a phase transition from cubic (3.8 Å) to monoclinic (5.31 Å, 5.34 Å, 7.52 Å) structure. **Reproduced from Fig. 13 of ref.**[92]

alternative possibilities to arrange these vacancies inside the SrO_3 unit, which lead to different space groups proposed to these compounds. Both these intermediate phases contains Fe in FeO_6 octahedral and FeO_5 square pyramid coordination. The structure can be presented as one-dimensional chains of vertex-linked FeO_6 octahedra cross-linked by $(FeO_5)_2$ vertex linked square-pyramidal dimer units (⋈ "*bow-tie*") as shown in Fig. 3.4. From a closure look on the Fig. 3.4, it can be realized that $SrFeO_{2.875}$ can be obtained from $SrFeO_{2.75}$ by converting alternate lines of $(FeO_5)_2$ bow-tie units along $[001]_p$ into chains of FeO_6 octahedra by selectively filling oxygen vacancies.

Recent neutron diffraction study by Hodges *et al.*[89] suggested that the vacancy ordered structure of $SrFeO_{2.75}$ and $SrFeO_{2.875}$ can be best described in the orthorhombic *Cmmm* and tetragonal *I4/mmm* space groups respectively. Though previous study by Takano *et al.*[88] suggested the respective vacancy ordered phases in monoclinic *C12/m1* and $I112/m$ structure models. Fig. 3.5 shows the scheme of oxygen ordering as reported by both studies for $SrFeO_{2.75}$ and $SrFeO_{2.875}$.

The magnetic and electronic properties in these phases are even more complex. The complexity arises from the different coordination environment of the Fe cations. Both of theses phases are mixed valent with Fe^{4+} and Fe^{3+}. A correct assignment of the charge to the different Fe sites is very important to understand the complicated magnetic and electronic ordering that occurs in these compounds. In $SrFeO_{2.75}$, Fe^{3+} occupies the square pyramidal sites and Fe^{4+} stays in the distorted octahedral sites as proposed

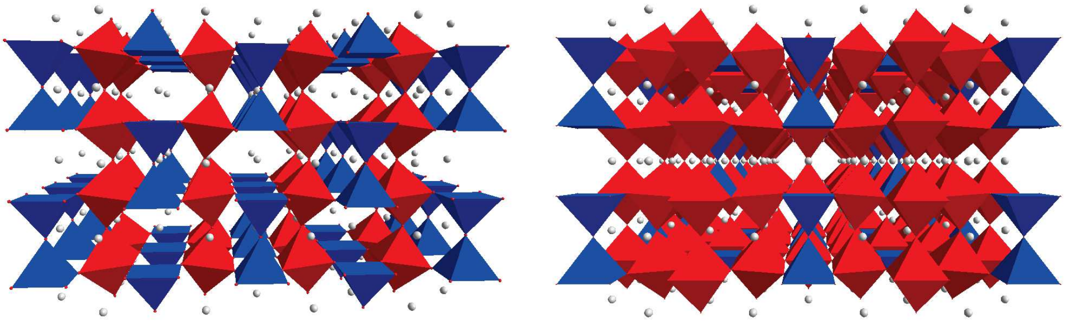

(a) **(b)**

Figure 3.4: Supercell of (a) $SrFeO_{2.75}$ and (b) $SrFeO_{2.875}$ in the bow-tie representation. $SrFeO_{2.875}$ can be obtained from $SrFeO_{2.75}$ by converting alternate lines of $(FeO_5)_2$ bow-tie units (blue) along $[001]_p$ into chains of FeO_6 octahedra (red) by selectively filling the oxygen vacancies.

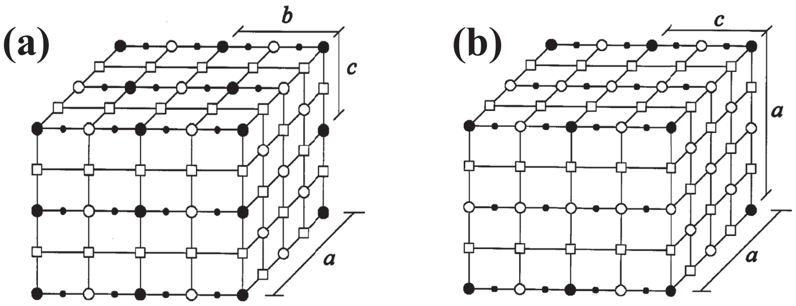

$SrFeO_{2.75}$ (Hodges et. al.) **$SrFeO_{2.875}$ (Hodges et. al.)**

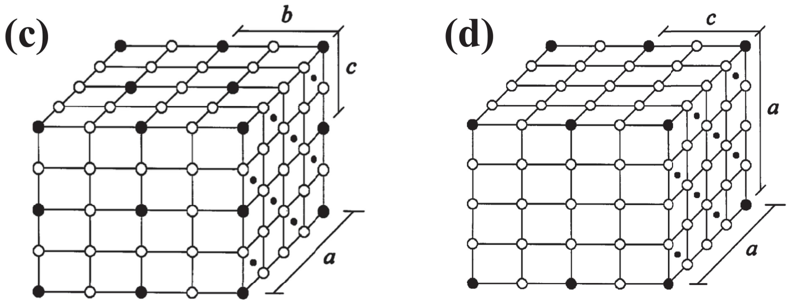

$SrFeO_{2.75}$ (Takano et. al.) **$SrFeO_{2.875}$ (Takano et. al.)**

Figure 3.5: Propose models for oxygen-vacancy ordering $SrFeO_{2.75}$ and $SrFeO_{2.875}$. Big open circles → O^{2-} anions; big filled circles → oxygen vacancies; small filled circles → Fe cations; open squares → Sr^{2+} cations. **Taken from Fig. 1 of ref.[89].**

by Hodges *et al.* from the 'bond-strength' calculation using "Zeolkowski" method, where in contray the study by Schmidt *et al.*[93] proposed '*Vice-Versa*'. The anisotropic distribution of the Fe^{3+} and Fe^{4+} ions in the nearest neighbor coordination distorts the orientation of the octahedras. As proposed by Hodges *et al.*, below the transition temperature ($T_N = 230$ K) the spins on the Fe^{3+} sublattice show a strong antiferromagnetic ordering along the crystallographic *b*-axis (Fig. 3.6), while the spins on the Fe^{4+} sites remain nearly disordered due to the frustration arising from the neighbours giving rise to a spin-glass or a very week paramagnetic state.

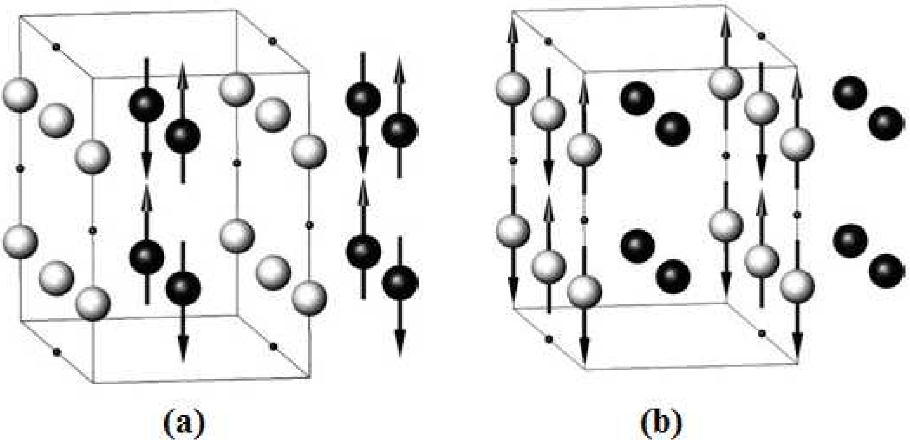

Figure 3.6: The magnetic structure of $SrFeO_{2.75}$ in (a) model proposed by Hodge *et al.*[89] (b) model proposed by Schmidt *et al.*[93]. The grey and black spheres represent the Fe in the square-pyramidal and octahedral coordination. The orthorhombic *c*- and *b*- axes are horizontal and vertical in the pictures respectively. The solid line outlines the unit cell. **Reproduced from Fig. 6 of ref.[93].**

Unlike the metallic $SrFeO_3$, $SrFeO_{2.75}$ shows a semiconducting behavior with E_a = 0.053 ev and $\sigma \sim 10^{-1}$– 10^3 S cm^{-1} [89]. Unlike $SrFeO_3$ which show metallic conductivity because of the increased O:2p to Fe:3d charge transfer, in $SrFeO_{2.75}$ the electrical conductivity is highly affected by the incorporation of the oxygen vacancy creating non-continuous octahedral chains interspersed by the vertex connected square-pyramidal dimer units. Instead of O:2p to Fe:3d charge transfer, nearest neighbour charge hopping fluctuation dominates to manifest the semiconducting behavior of $SrFeO_{2.75}$.

$SrFeO_{2.875}$ also show similar semiconducting behavior with E_a = 0.02 ev and σ = 10^3 S cm^{-1} [89]. In case of $SrFeO_{2.875}$ the assignment of the Fe^{4+} and Fe^{3+} is even more complex as this compound occupies three distinct Fe sites. The neutron diffraction study on the single crystals of $SrFeO_{2.875}$ by Reehuis *et al.*[23] suggests helical magnetic ordering along $[111]_p$-direction around T_N = 75 K similar to the $SrFeO_3$ but the powder $SrFeO_{2.875}$ show a sine wave modulated magnetic ordering along the same direction. This implies subtle microstructural difference with different distribution of the vacancy can lead to different degenerated magnetic state.

3.1.3 $SrFeO_{2.5}$ $(n = 2)$

$SrFeO_{2.5}$ is the oxygen vacant end member of pseudocubic perovskite series $Sr_nFe_nO_{3n-1}$ with $(n = 2)$. This compound possesses Brownmillerite type structure. The lattice parameters can be expressed as $(\sqrt{2}a_p \times 4a_p \times \sqrt{2}a_p)$ where a_p is the cubic Perovskite lattice parameter. For each two unit cells of $SrFeO_3$ one out of six oxygen is missing and these vacant oxygen sites are ordered in the $[101]_p$ direction of the parent Perovskite cell which leads to a layered structure containing Fe^{4+} atoms in the octahedra and Fe^{3+} in the tetrahedra configuration in the consecutive layers (Fig. 3.2(d)). The structure can be best expressed by body centered space group *Icmm*, as proposed by Greaves *et al.*[85], with the presence of disorder in the tetrahedral sites. The disorder is related to the random appearance of $\bar{1}$ symmetry element in between 'R' and 'L' configuration of $(FeO_4)_\infty$ chains (see *Chapter* 1. *Oxygen mobility in solids, Subsection: Brownmillerite*). $SrFeO_{2.5}$ is a Mott-type insulator. It shows a G-type antiferromagnetic ordering along the crystallographic *c*-direction with a Néel temperature $T_N = 673$ K[22].

Table 3.1: Symmetries and lattice parameters for $SrFeO_{3-x}$ system as reported by Hodges *et al.*[89] from neutron powder diffraction.

Phase	Space Group	Lattice Parameters (Å)
$SrFeO_{2.5}$	*Icmm*	*a*: 5.527(1) *b*: 15.59(2) *c*: 5.672(1)
$SrFeO_{2.75}$	*Cmmm*	*a*: 10.974(1) *b*: 7.702(1) *c*: 5.473 (1)
$SrFeO_{2.875}$	*I4/mmm*	*a*: 10.929(1) *c*: 7.698(1)
$SrFeO_3$	$Pm\bar{3}m$	*a*: 3.851(1)

Although, all the structure models of $Sr_nFe_nO_{3n-1}$ series as presented in Table. 3.1 are well established, some of them are still under discussion. Recently $SrFeO_{2.5}$ has been described with an ordered structure model in *Pbma* by Auckett *et al.*[25] with an ordered arrangement of $(FeO_4)_\infty$ chains. In detail the structure has been described in the (3 + 1)-dimensional superspace group *I2/m(0βγ)0s*, $q = \beta b^* + \gamma c^*, 0 \leq \beta \leq 1/2$ and $0 \leq \gamma \leq 1$. This turned out to be an important issue in terms of oxygen mobility, which is present in $SrFeO_{2.5}$ down to ambient, as it can not be successfully explained without the presence of specific disorder of the tetrahedral chains $(FeO4)_\infty$ chains[17]. This implies the necessity to better identify the actual ground state of $SrFeO_{2.5}$ which is very complicated to characterize especially in single crystal because of the presence of twin domains and diffuse rods. There could be many pitfalls leading to describe a wrong structure model. We will discuss more critically the newly proposed structure model[25] of $SrFeO_{2.5}$ and the probable pitfalls which lead to assign such structure model in chapter 5.

3.2 Summary

This chapter essentially summarizes all the established structure models for the different phases of $SrFeO_{3-x}$ ($0 \leq x \leq 0.5$) synthesized at high temperature. The other aspect is the low temperature phase diagram. There is almost no study reporting successfully the phase sequence at low temperature. In this thesis work we tried to investigate the phase diagram at RT by *in situ* synchrotron diffraction on a single crystal of $SrFeO_{2.5}$ during EC oxygen intercalation. In order to describe the experimental outcomes of the *in situ* investigation, the knowledge of the high temperature phase sequence, which has been described in this chapter, was a prerequisite. As almost all the single crystals of $SrFeO_{3-x}$ are highly twinned in three dimension, a solid knowledge of twinning in the $SrFeO_{3-x}$ system is necessary to understand the single crystal diffraction patters. We will discuss the twinning in the next chapter 4 followed by a discussion on the ground state of the as grown single crystal of $SrFeO_{2.5}$ in the chapter 5 as it has been put into question recently. Also we will discuss the microstructure of the as grown single crystal to follow the structural evolution in during the EC oxygen intercalation as will be discussed in the chapter 6.

Chapter 4

Twinning in $SrFeO_{3-x}$ system

Presence of twinning is almost unavoidable in $SrFeO_{3-x}$ system. The high temperature parent structure of $SrFeO_{3-x}$ during crystal growth condition is cubic above 900 °C[94], while cooling down below this temperature, it transforms to tetragonal and subsequently orthorhombic phases. Phase transition towards lower symmetry is generally accompanied by the formation of twin domains in order to minimize the crystal energy. The presence of different twin domains with their respective orientations and volume fractions strongly affects the diffraction patterns. Detail knowledge of the twin laws relating one twin individual to another is very crucial and of utmost importance in order to assign each of the reflections properly to the corresponding twin individuals. The volume fractions for the twin domains can be determined from the integrated intensities by applying twin laws. All twin crystals mostly fall into two categories. In the first category whole diffraction patterns is affected by the overlap of reflections from different twin domains (*i.e. merohedral*, *pseudo-merohedral* twinning) whereas in the second category only part of the diffraction pattern is affected by such overlap (*non-merohedral* twinning)[95].

Twinning in $SrFeO_{3-x}$ can be realized by considering the well known *pseudo-merohedral* twinning scheme in K_2NiF_4-type oxides. During the crystal growth, the K_2NiF_4-type oxides undergoes a phase transition from high temperature tetragonal to low temperature orthorhombic structure, induced by the cooperative tilting of the octahedra creating slight difference in a and b lattice parameters. This symmetry reduction is accompanied by the loss of (110) or ($\bar{1}$10) mirror planes. Loss of each mirror plane contributes to the generation of two twin domains. In case both mirror symmetries related to (110) and ($\bar{1}$10) planes are lost, four twin individuals are created with common c axis.

In the presence of only two individuals due to the loss of (110) mirror plane all Bragg reflections show splitting in $(\omega - 2\theta)$ except the ($\bar{h}$*h0*) and (*00l*) type reflections. An ideal (*hk0*) diffraction pattern in such case is presented in Fig. 4.1(c). Similarly

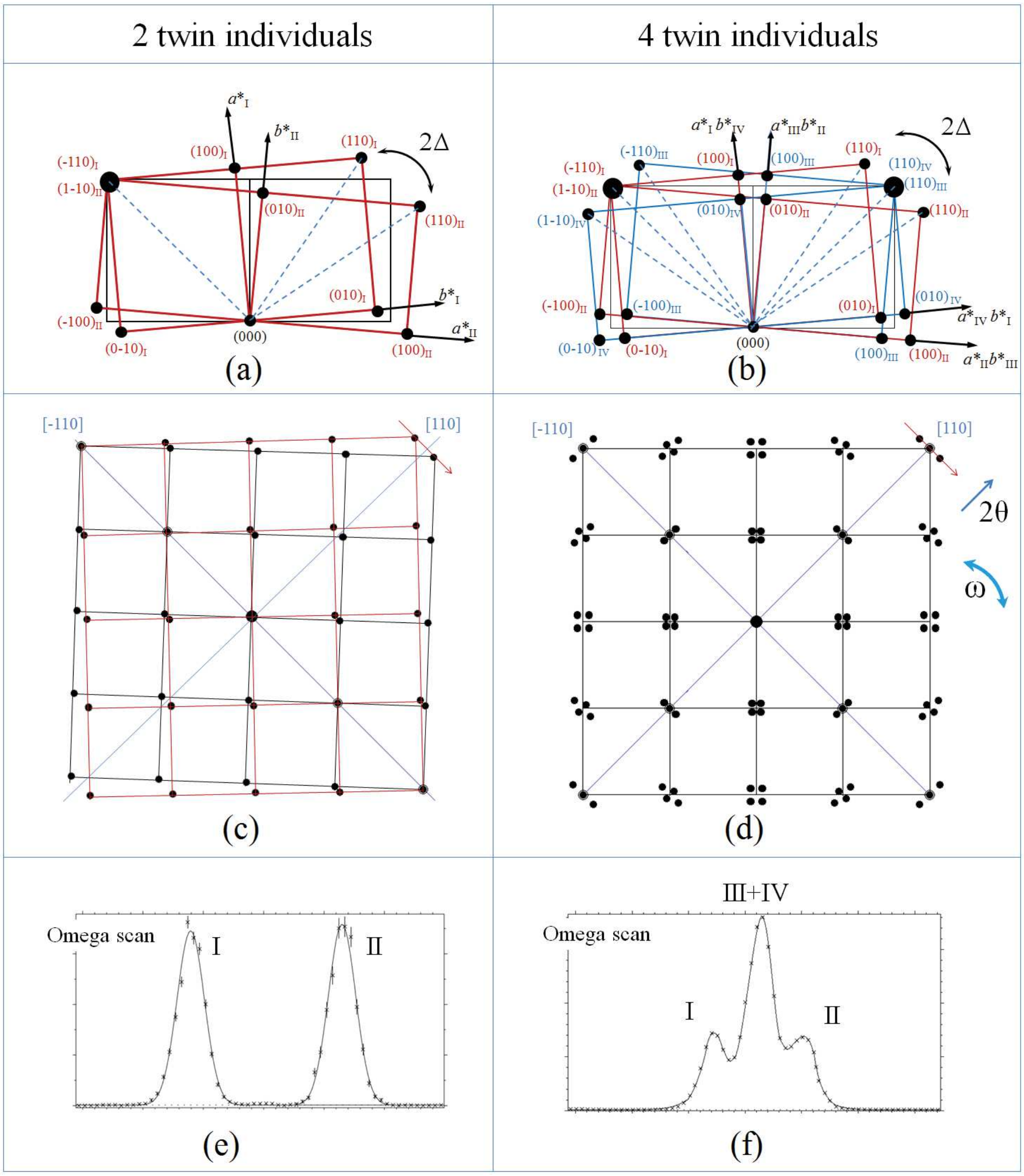

Figure 4.1: Scheme of twinning in La$_2$MO$_{4+\delta}$ single crystals, with the loss of either (110) or both (110) and ($\bar{1}$10) mirror planes, resulting respectively in 2 or 4 twins individuals. (a,b) Twin law in reciprocal space view perpendicular to [001] direction which is the axis common to the two twin twin individuals. (c,d) Simulated (*hk0*) diffraction patterns showing how reflections are affected by twinning. Reflections are splitted into ($\omega - 2\theta$) plane. (e,f) Typical ω-scan of the (*hh0*) type Bragg reflection representing the volume fraction of each domain. **Reproduced from Fig. 3.3 of ref.[96].**

(*hh0*) type reflections are not splitted when ($\bar{1}$10) mirror symmetry plane is lost. The splitted reflection can be completely separated or partially overlapped depending on the 2θ position and the orthorhombicity Δ as given by Eq. 4.1. In the presence of the four twin domains all Bragg reflections split into four in ω and 2θ except the (*hh0*) and

($\bar{h}h0$) type reflections which split into three in ω, while the ($00l$) type reflections do not split. In the ($hh0$) and ($\bar{h}h0$) type reflections, the central peak is overlap of two peaks corresponding two one set of twin individuals whereas the two outer peaks correspond to the other set of individuals. All the 4 twin domains can be related with respect to the first domain by the *twin laws* as expressed by following matrices in Eq. 4.3.

$$\Delta = tan^{-1}(a/b) - tan^{-1}(b/a); \qquad a,\, b : \text{ lattice parameters} \tag{4.1}$$

$$I_{total} = \sum_{n} \alpha_n \times I_n \tag{4.2}$$

$$T1 = \begin{pmatrix} 1 & 0 & 0 \\ 0 & 1 & 0 \\ 0 & 0 & 1 \end{pmatrix};\; T2 = \begin{pmatrix} 0 & 1 & 0 \\ 1 & 0 & 0 \\ 0 & 0 & -1 \end{pmatrix};\; T3 = \begin{pmatrix} -1 & 0 & 0 \\ 0 & 1 & 0 \\ 0 & 0 & -1 \end{pmatrix};\; T4 = \begin{pmatrix} 0 & -1 & 0 \\ 1 & 0 & 0 \\ 0 & 0 & 1 \end{pmatrix} \tag{4.3}$$

The total intensity of a particular reflection in the presence of n twin domains is the weighted sum of individual intensities (I_n) by their volume fractions (α_n) as expressed by Eq. 4.2. Fig. 4.1(e) and (f) show the typical ω scan in the case of 2 twin and 4 twin individuals with a point detector. In the presence of equal volume fraction of the twin domains the central peak intensity in Fig. 4.1(e) will be twice than that of the side peaks.

The twinning scheme in pseudocubic SrFeO$_{3-x}$ is much more complex. The difficulty is related to the presence of higher symmetric supercell in which all the members in this series can be accommodated. Twin laws are not only determined by the lost symmetry elements of the lattice but also by the relation to the cubic supercell. In Table 4.1, we have presented the relations in between different phases of SrFeO$_{3-x}$ in terms of the pseudocubic lattice parameter a_p.

Table 4.1: The symmetry relation of SrFeO$_{3-x}$ phases with the pseudocubic cell. Lattice parameters and space groups are taken from Hodges *et al.* [89].

Phase	Space Gr.	Latt. Param. (Å)	Latt. param. (a_p)	Orthorhombicity
SrFeO$_{2.5}$	*Imma*	a = 5.527(1) b = 15.59(2) c = 5.672(1)	$a \approx \sqrt{2}a_p$ $b \approx 4a_p$ $c \approx \sqrt{2}a_p$	$\Delta \sim 1.48°$
SrFeO$_{2.75}$	*Cmmm*	a = 10.974(1) b = 7.702(1) c = 5.473 (1)	$a \approx 2\sqrt{2}a_p$ $b \approx 2a_p$ $c \approx \sqrt{2}a_p$	$\Delta \sim 0.15°$
SrFeO$_{2.875}$	*I4/mmm*	a = 10.929(1) c = 7.698(1)	$a = b \approx 2\sqrt{2}a_p$ $c \approx 2a_p$	$\Delta = 0°$
SrFeO$_3$	*Pm-3m*	a: 3.851(1)	$a = b = c = a_p$	$\Delta = 0°$

From the relations it is clear that all the phases $SrFeO_{3-x}$; $x = 0.5$, 0.25, 0.125 can be accommodated in a supercell of dimension $[4a_p \times 4a_p \times 4a_p]$(see Fig. 4.2). To understand the twinnig behaviour our approach will be very simple. We will describe all the twin laws in each phase with respect to the supercell $[4a_p \times 4a_p \times 4a_p]$ and simulate the corresponding principle planes (*hk0*), (*0kl*) and (*h0l*) in each case to see the effect of twinnig.

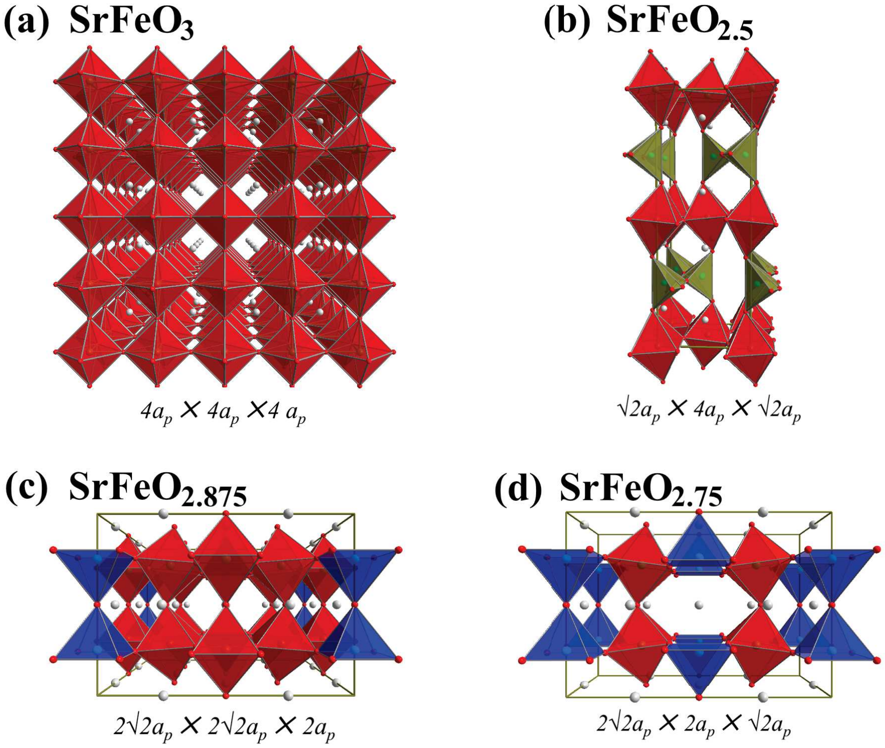

Figure 4.2: Representation of different phases of $SrFeO_{3-x}$ with respect to the $[4a_p \times 4a_p \times 4a_p]$ supercell. Notice the stacking of the octahedra is in the *b*-direction for $SrFeO_{2.5}$ and $SrFeO_{2.75}$ and in the *c* direction for $SrFeO_{2.875}$. (a) $SrFeO_3$ in the 4 times supercell. (b) $SrFeO_{2.5}$ in $[\sqrt{2}a_p \times 4a_p \times \sqrt{2}a_p]$, octahedrons are in red and tetrahedrons are in green. (c) $SrFeO_{2.875}$ in $[2\sqrt{2}a_p \times 2\sqrt{2}a_p \times 2a_p]$ and (d) $SrFeO_{2.75}$ in $[2\sqrt{2}a_p \times 2a_p \times \sqrt{2}a_p]$, square pyramids are shown in blue.

4.1 Twinning in $SrFeO_{2.5}$

In $SrFeO_{2.5}$ the long axis *b* which is the stacking axis of the octahedra (see Fig. 4.2). The lattice parameters can be expressed as $[a \approx \sqrt{2}a_p, b \approx 4a_p, c \approx \sqrt{2}a_p]$ where a_p is the pseudocubic cell parameter. In general, the stacking axis can run along three principle directions a_p, b_p and c_p of the cubic supercell $[4a_p \times 4a_p \times 4a_p]$ as shown in the Fig. 4.3. The orthorhombicity arising from the slight mismatch of the *a* and *c* lattice parameter is accompanied by the loss of two mirror planes along (101) and $(\overline{1}01)$ direction and gives rise to 4 twin individuals in plane perpendicular to the stacking axis b. Three possible orientations of the b stacking axis (*henceforth* ‘variants’) inside the supercell result into maximum of 12 individuals (3 variants × 4 individuals for each variant).

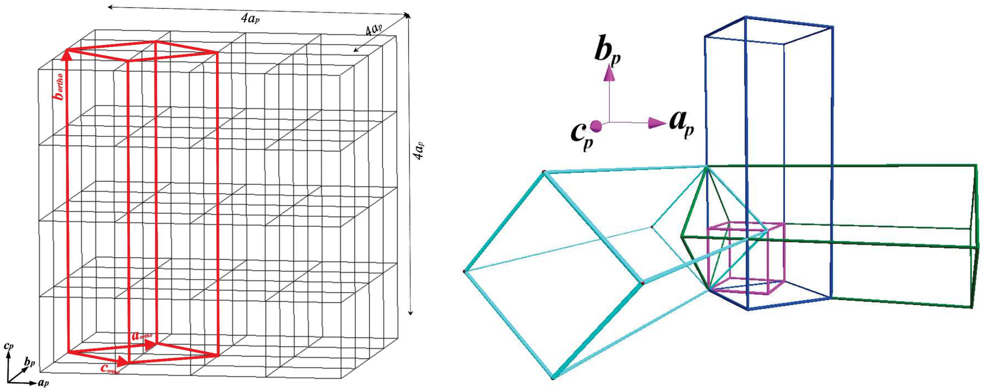

(a) **(b)**

Figure 4.3: (a) Orientation of the orthorhombic SrFeO$_{2.5}$ cell within cubic supercell. (b) All three possible orientation variants along three cubic axes.

$$T1=\begin{pmatrix}1&0&-1\\0&4&0\\1&0&1\end{pmatrix}\quad T2=\begin{pmatrix}1&0&1\\0&-4&0\\1&0&-1\end{pmatrix}\quad T3=\begin{pmatrix}1&0&-1\\0&-4&0\\1&0&1\end{pmatrix}\quad T4=\begin{pmatrix}1&0&1\\0&4&0\\1&0&-1\end{pmatrix}\tag{4.4}$$

$$T5=\begin{pmatrix}0&-1&1\\4&0&0\\0&1&1\end{pmatrix}\quad T6=\begin{pmatrix}0&1&1\\-4&0&0\\0&-1&1\end{pmatrix}\quad T7=\begin{pmatrix}0&-1&1\\-4&0&0\\0&1&1\end{pmatrix}\quad T8=\begin{pmatrix}0&-1&1\\4&0&0\\0&-1&1\end{pmatrix}\tag{4.5}$$

$$T9=\begin{pmatrix}-1&1&0\\0&0&4\\1&1&0\end{pmatrix}\quad T10=\begin{pmatrix}1&1&0\\0&0&-4\\-1&1&0\end{pmatrix}\quad T11=\begin{pmatrix}-1&1&0\\0&0&-4\\1&1&0\end{pmatrix}\quad T12=\begin{pmatrix}1&1&0\\0&0&4\\-1&1&0\end{pmatrix}\tag{4.6}$$

The matrices relating these 12 individuals with the supercell are listed in the Eqs. 4.4–4.6. The first set of matrices Eq. 4.4 represents 4 twin individuals with common b axis (variant) along the pseudo cubic b_p direction, while the second set in Eq. 4.5 and the third set in Eq. 4.6 represent the individuals with variants running along a_p and c_p respectively.

SrFeO$_{2.5}$

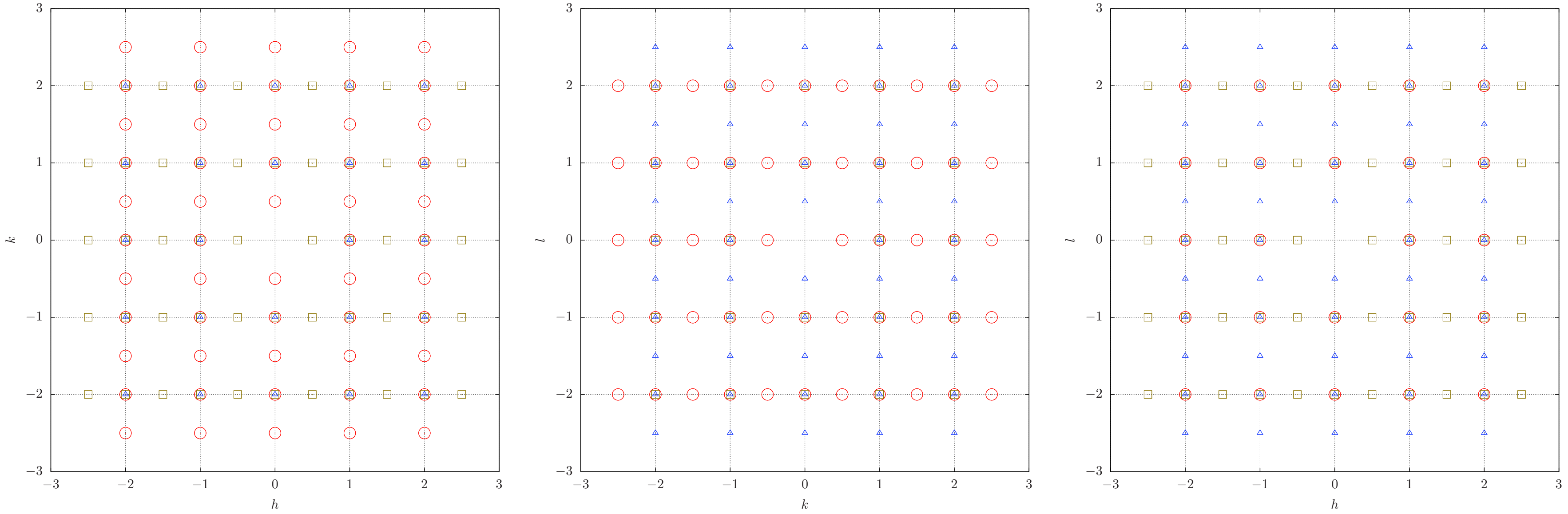

(a) (*hk0*) **(b)** (*0kl*) **(c)** (*h0l*)

Figure 4.4: Simulated reflection patterns of **SrFeO$_{2.5}$** for three principle planes (a) (*hk0*), (b) (*0kl*) and (c) (*h0l*) in the pseudocubic cell. Only the extinction conditions from *Imma* space group have been applied for calculating such reflection positions. Intensity is not taken into account. Red circle, olive square and blue triangledown represents the reflections from the individuals with variants along cubic b_p, a_p and c_p axes of the pseudocubic cell respectively.

In order to realize the complexity of such twin scenario in $SrFeO_{2.5}$, simulated patterns of the three principle planes (*hk0*), (*0kl*) and (*h0l*) are presented in Fig. 4.4. The patterns are indexed in pseudocubic cell. Three different sets of reflections as presented in different colors, belong to the individuals with three possible variants. The in plane splitting (similar to Fig. 4.1) corresponding to each variant is ignored to avoid complexity. As it can be noted most of the reflection positions are overlapped by the reflections from different variants except few which uniquely belong to one variant (*e.g.* the $(0{}^1/{}_2 0)_p$ type reflections in the cubic cell, equivalent to (020) in the orthorhombic $SrFeO_{2.5}$ cell with *d–value* ~ 7.795 Å.

4.2 Twinning in $SrFeO_{2.75}$

The twinning scheme is similar in orthorhombic $SrFeO_{2.75}$. Lattice parameters can be expressed equivalently as $[a \approx 2\sqrt{2}a_p,\ b \approx 2a_p,\ c \approx \sqrt{2}a_p]$ in terms of cubic cell parameter a_p. The b axis in this case as well can run along three principle directions of the supercell giving maximum of 12 individuals (Fig. 4.5). Orthorhombicity in $SrFeO_{2.75}$ (see Table 4.1) can be calculated by considering the equivalent axes length (*i.e.* ${}^a/{}_2$ and c) using the equation Eq. 4.1. It is noted the orthorhombicity in the case of $SrFeO_{2.75}$ ($2\Delta_{2.75} \sim 0.3°$) much less compared to $SrFeO_{2.5}$ ($2\Delta_{2.5} \sim 2.96°$) showing much less splitting in reflections compared to $SrFeO_{2.5}$.

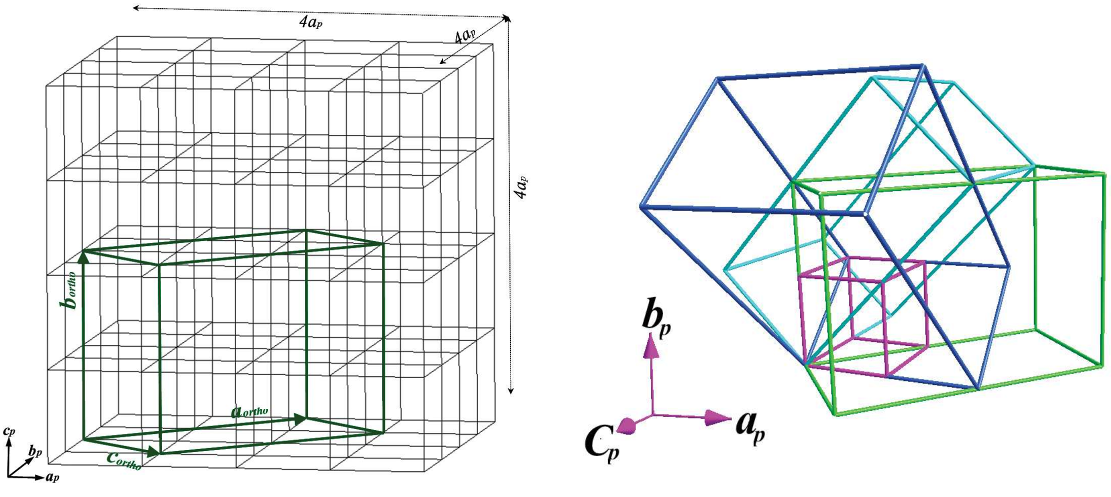

(a)

(b)

Figure 4.5: (a) Orientation of the orthorhombic $SrFeO_{2.75}$ cell within cubic supercell. (b) All three possible orientation variants along three cubic axes.

The matrices relating these 12 individuals with the supercell are listed in the Eqs. 4.7–4.9. The first set of matrices Eq. 4.7 represents 4 twin individuals with common variant along the pseudo cubic b_p direction, while the second set in Eq. 4.8 and the third set in Eq. 4.9 represent the individuals having common variants running along a_p and c_p respectively.

$$T1=\begin{pmatrix}2&0&-2\\0&2&0\\1&0&1\end{pmatrix}\quad T2=\begin{pmatrix}2&0&2\\0&-2&0\\1&0&-1\end{pmatrix}\quad T3=\begin{pmatrix}2&0&-2\\0&-2&0\\1&0&1\end{pmatrix}\quad T4=\begin{pmatrix}2&0&2\\0&2&0\\1&0&-1\end{pmatrix}\tag{4.7}$$

$$T5=\begin{pmatrix}0&-2&2\\2&0&0\\0&1&1\end{pmatrix}\quad T6=\begin{pmatrix}0&2&2\\-2&0&0\\0&-1&1\end{pmatrix}\quad T7=\begin{pmatrix}0&-2&2\\-2&0&0\\0&1&1\end{pmatrix}\quad T8=\begin{pmatrix}0&2&2\\2&0&0\\0&-1&1\end{pmatrix}\tag{4.8}$$

$$T9=\begin{pmatrix}-2&2&0\\0&0&2\\1&1&0\end{pmatrix}\quad T10=\begin{pmatrix}2&2&0\\0&0&-2\\-1&1&0\end{pmatrix}\quad T11=\begin{pmatrix}-2&2&0\\0&0&-2\\1&1&0\end{pmatrix}\quad T12=\begin{pmatrix}2&2&0\\0&0&2\\-1&1&0\end{pmatrix}\tag{4.9}$$

Three principle reflection patterns (*hk0*), (*0kl*) and (*h0l*) in the case of $SrFeO_{2.75}$ as shown in the Fig. 4.6. All the planes are indexed in the pseudocubic cell. Different color (also symbols) have been used to distinguish contribution from domains belonging to 3 different variants. Only few reflection position are uniquely contributed by single variant *e.g.* $(0{}^1/{}_2{}^1/{}_2)_p$ type reflections in the cubic cell which are equivalent to (001)/(200) type reflections of $SrFeO_{2.75}$ with *d-value* ~ 5.47 Å.

$SrFeO_{2.75}$

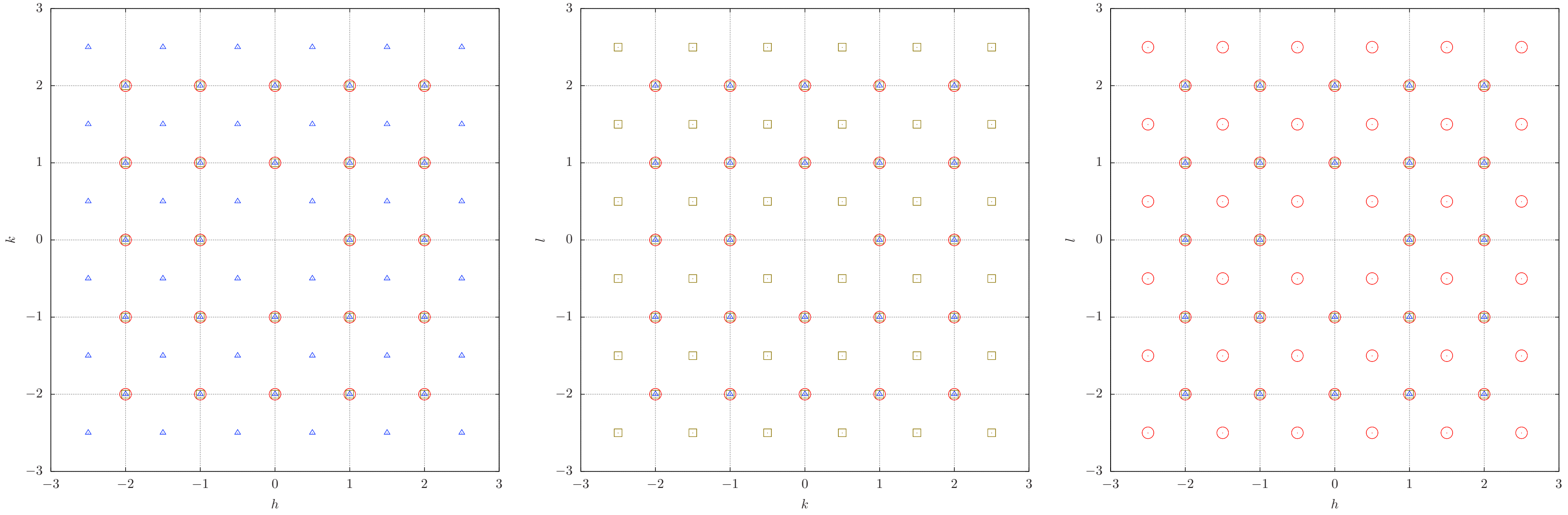

(a) (*hk0*) **(b)** (*0kl*) **(c)** (*h0l*)

Figure 4.6: Simulated reflection patterns of **$SrFeO_{2.75}$** for three principle planes (a) (*hk0*), (b) (*0kl*) and (c) (*h0l*) in the pseudocubic cell. Only the extinction conditions from *Cmmm* space group have been applied for calculating such reflection positions. Intensity is not taken into account. Red circle, olive square and blue triangledown represents the reflections from the individuals with variants along cubic b_p, a_p and c_p axes of the pseudocubic cell respectively.

SrFeO$_{2.875}$

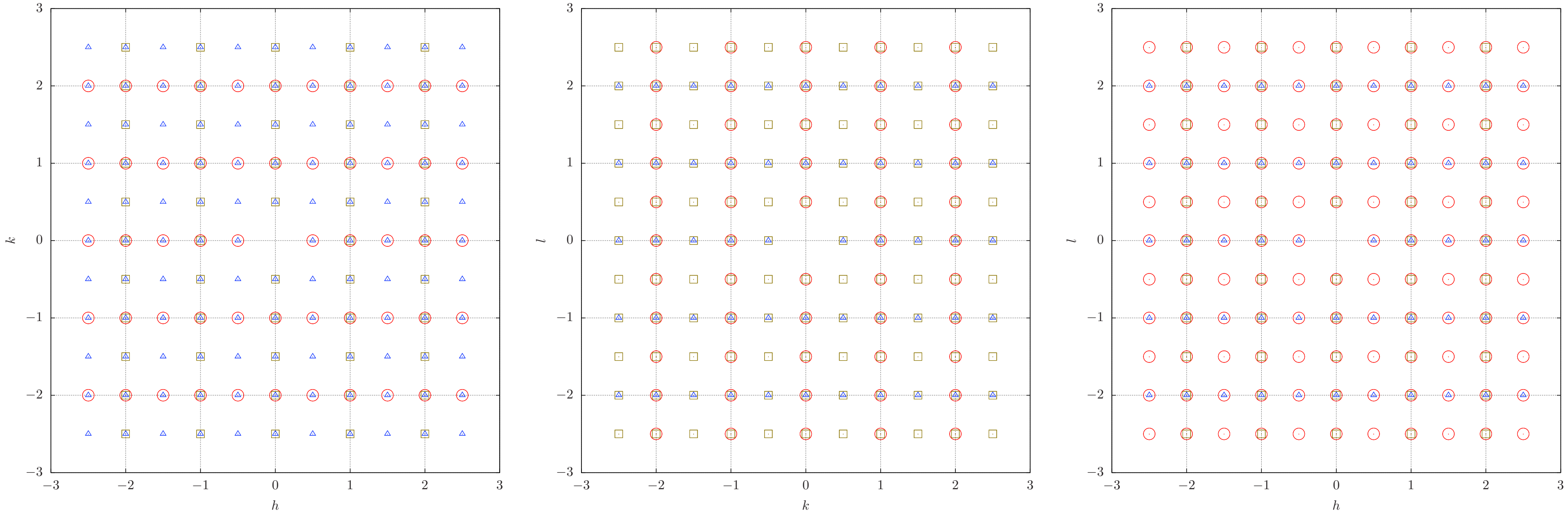

(a) (*hk0*) **(b)** (*0kl*) **(c)** (*h0l*)

Figure 4.7: Simulated reflection patterns of **SrFeO$_{2.875}$** for three principle planes (a) (*hk0*), (b) (*0kl*) and (c) (*h0l*) in the pseudocubic cell. Only the extinction conditions from *I4/mmm* space group have been applied for calculating such reflection positions. Intensity is not taken into account. Red circle, olive square and blue triangledown represents the reflections from the individuals with variants along cubic b_p, a_p and c_p axes of the pseudocubic cell respectively.

4.3 Twinning in $SrFeO_{2.875}$

Twinning scheme in $SrFeO_{2.875}$ is comparatively simpler as this compound crystallizes in more symmetric tetragonal (a=b) structure adapting *I4/mmm* space group. In $SrFeO_{2.875}$, the stacking direction of the octahedrons is along the c axis (Fig. 4.2) which is the variant is this case. The cell parameters can be expressed as $[a = b \approx 2\sqrt{2}a_p, c \approx 2a_p]$. Maximum six individuals are possible for $SrFeO_{2.875}$ and they are related to the three possible orientations of the c axis in the supercell as shown in the Fig. 4.8.

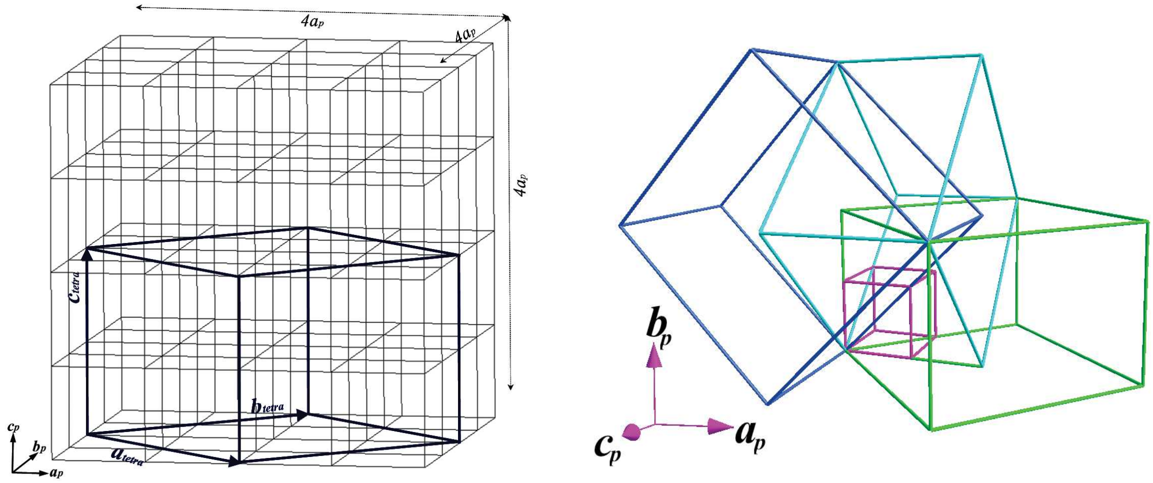

(a) (b)

Figure 4.8: (a) Relation between the orthorhombic $SrFeO_{2.875}$ cell with cubic supercell. (b) Three possible orientation variants along three cubic axes.

$$T5 = \begin{pmatrix} 2 & 0 & 2 \\ 2 & 0 & -2 \\ 0 & 2 & 0 \end{pmatrix} \qquad T6 = \begin{pmatrix} 2 & 0 & 2 \\ 2 & 0 & -2 \\ 0 & -2 & 0 \end{pmatrix} \tag{4.10}$$

$$T3 = \begin{pmatrix} 0 & 2 & 2 \\ 0 & -2 & 2 \\ 2 & 0 & 0 \end{pmatrix} \qquad T4 = \begin{pmatrix} 0 & 2 & 2 \\ 0 & -2 & 2 \\ -2 & 0 & 0 \end{pmatrix} \tag{4.11}$$

$$T1 = \begin{pmatrix} 2 & 2 & 0 \\ -2 & 2 & 0 \\ 0 & 0 & 2 \end{pmatrix} \qquad T2 = \begin{pmatrix} 2 & 2 & 0 \\ -2 & 2 & 0 \\ 0 & 0 & -2 \end{pmatrix} \tag{4.12}$$

The matrices relating these 6 individuals with the supercell are listed in the Eqs. 4.10–4.12. The first set of matrices Eq. 4.10 represents 2 twin individuals with common c axis (variant) along the pseudo cubic b_p direction, while the second set in Eq. 4.11 and the third set in Eq. 4.12 represent the individuals with variants running along a_p and c_p respectively.

The reflection patterns for SrFeO$_{2.875}$ are shown in the Fig. 4.7. The reflection patterns are much more crowded by reflection in comparison to previous two phases, and most of the reflections are contaminated by the presence of other domains belonging to other variants due to higher symmetry. Only reflections of $(0{}^1\!/\!{}_2{}^1\!/\!{}_2)_p$ type in the pseudocubic cell which are equivalent to (200) type reflections with a *d–value* ~ 5.462 Å in SrFeO$_{2.875}$ cell, uniquely belong to one variant.

4.4 Summary

In this chapter we have summarised the twinning behaviour of different phases of SrFeO$_{3-x}$ system with a very simple approach (twin colouring) without taking any in plane splitting of reflections. In reality the diffraction patterns are much more complicated. But this chapter gives an important introduction to twinning which is required to understand the results obtained from the single crystals Syncrotron diffraction on the as grown SrFeO$_{2.5}$ single crystal (chapter 5) and also to analyze the results obtained from the *in situ* electrochemistry (chapter 6) and *in situ* temperature (chapter 7) measurements on the single crystal of SrFeO$_{2.5}$.

Chapter 5

The ground state of $SrFeO_{2.5}$

All the basic structure frameworks as established in the literature for the $SrFeO_{3-x}$ have been discussed previously in chapter 3. Although most of the structure models are well accepted for a long time, some of them are still under question. $SrFeO_{2.5}$ was well known to adopt *Icmm*[89] structure model with the presence of disordered $(FeO_4)_\infty$ tetrahedral chain arrangement until recently when the RT structure has been described by Auckett *et al.*[25] in *Pbma* structure model with ordered $(FeO_4)_\infty$ tetrahedral chain arrangement together with a doubling of the *a* axis (See Fig. 5.1).

The real ground state of $SrFeO_{2.5}$ presents an important issue not only concerning its structure and symmetry but equally for the lattice dynamical aspects as we have discussed in chapter 1. This compound is known to uptake oxygen even at ambient by electrochemical oxygen intercalation as have been described in the literatures[20,21]. This surprising behaviour of oxygen mobility through the lattice at close to RT has been successfully described by Paulus *et al.*[17] in terms of '*phonon–assisted*' oxygen diffusion. The presence of particular dynamic disorder along with the specific lattice dynamics plays important role for such non-classical oxygen diffusion mechanism. Whereas in contray, the presence of an ordered arrangement of the $(FeO_4)_\infty$ chains as described by Auckett *et al.*[97] needs much higher temperature for oxygen to pass through the solids. This study[97] reports the oxygen mobility to set in only at 530 °C because of confined local rotations of the FeO_4 tetrahedra which leads to a *Pbma* to *Icmm* (*order-disorder*) phase transition.

In this chapter we want to reinvestigate the ground state of $SrFeO_{2.5}$ as the study by Auckett *et al.* leaves some inconsistency to explain the experimentally observed fact of oxygen mobility at RT. We will discuss the results of the structural investigations as obtained from complimentary techniques *e.g.* X-ray/SX-ray, neutron diffractions on the powder and single crystals of $SrFeO_{2.5}$ in both the structure model *Imma* and *Pbma*, and critically look at the issues with such characterization techniques which might lead to an incorrect description of the structure model. Please note *Icmm* is equivalent to *Imma* while interchanging the *a* and *c* lattice parameters. In *Imma*, the tetrahedral chains are perpendicular to the *c* axis while in *Icmm* they are perperdicular to the *a* axis. Here onwards in our discussion, we will use the *Imma* structure model insted of equivalent *Icmm* model.

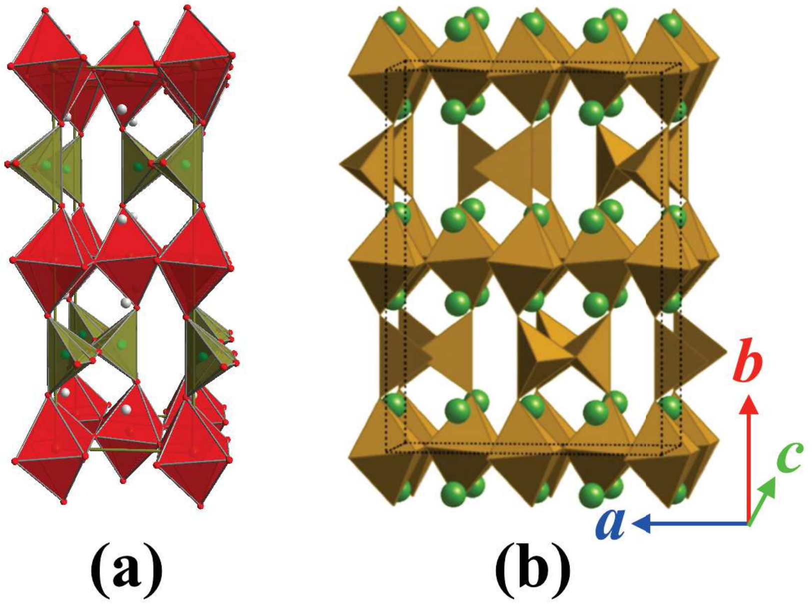

Figure 5.1: The brownmillerite structure of $SrFeO_{2.5}$. (a) The conventional *Icmm* subcell with the disordered $(FeO_4)_\infty$ tetrahedral chain arrangement. (b) The recently prposed *Pbma* supercell by Auckett *et al.*[97] resulting from a doubling of the *a* axis and additional interlayer chain ordering.

5.1 X-ray powder diffraction

Single crystal of $SrFeO_{2.5}$ was grown by floating zone technique using Image Furnace as described in chapter 2. The as grown single crystal of $SrFeO_{2.5}$ was groung and characterized by laboratory X-ray powder diffraction on a PHILIPS X'Pert powder diffractometer. The diffraction pattern was taken in the range $0^\circ \leq 2\theta \leq 80^\circ$ using Cu $K_{\alpha_{1,2}}$ wavelength in *'Bragg-Brentano'* geometry. Rietveld analysis on the obtained diffraction pattern (Fig. 5.2) was carried out using FullPROF[98] program and the details of the Rietveld refinement is listed in the Table 5.1. Form the diffraction pattern no evidence of *P*-type reflections (expected in *Pbma* model) was found. The refinement suggests the best agreement with *Imma* structure model with the disorder $(FeO_4)_\infty$ tetrahedral chains even compared to the other possible body centered model *I2mb* with ordered arrangement of the interlayer $(FeO4)_\infty$ chains.

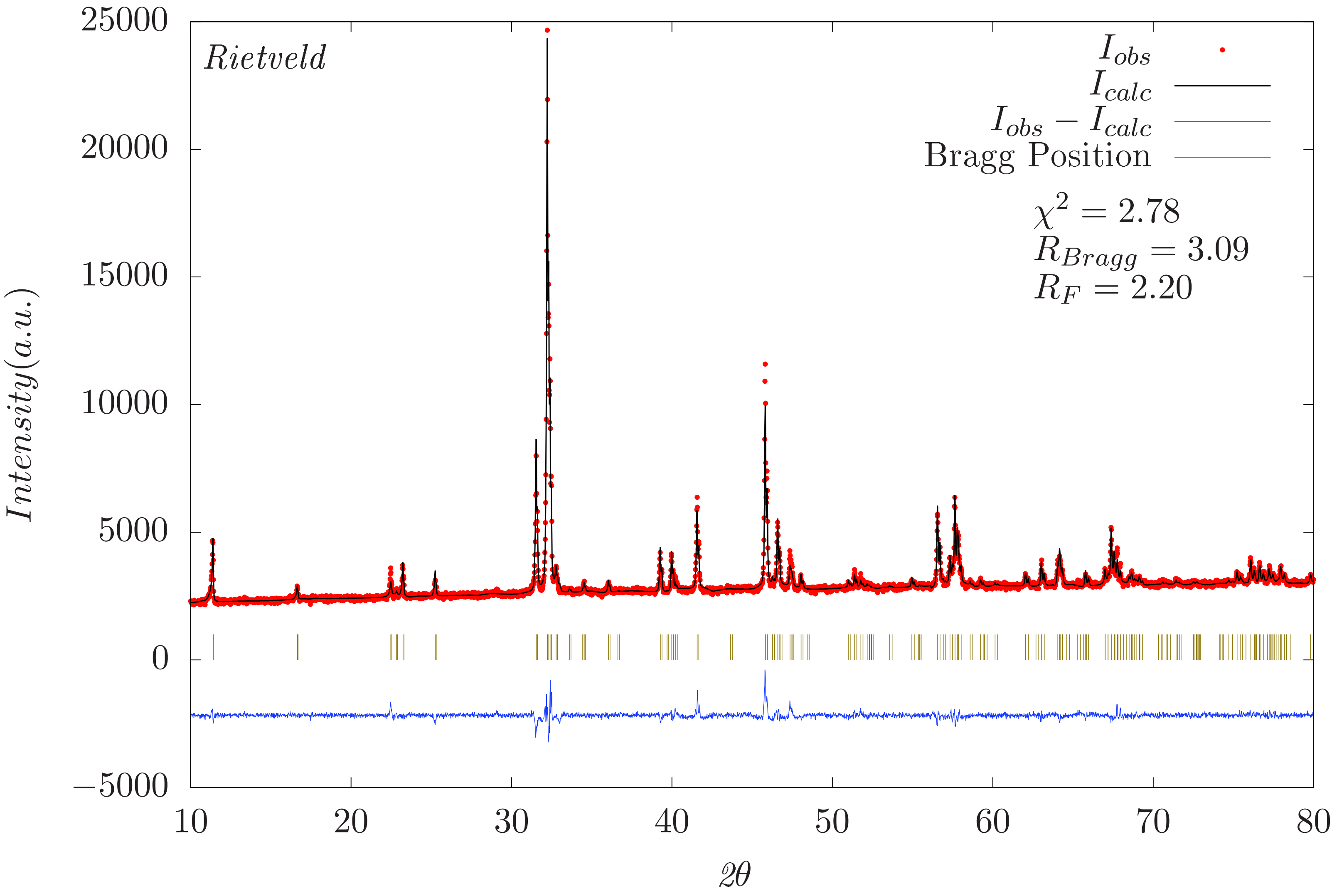

Figure 5.2: Rietveld refinement on X-ray powder diffraction data obtained from ground as grown $SrFeO_{2.5}$ single crystal in *Imma* structure model.

Table 5.1: Structural parameters of $SrFeO_{2.5}$ obtained from Rietveld refinement of the X-ray powder diffraction data obtained on the crushed single crystal of $SeFeO_{2.5}$.

Atom	x/a	y/b	z/c	Occ.	$B_{iso} = 8 \times \pi^2 \times U_{iso}$
Sr	1/2	0.107(8)	0.016(4)	0.5	0.5(2)
Fe1	0	0	0	0.25	0.1(7)
Fe2	0.966(3)	1/4	0.935(2)	0.25	0.1(2)
O1	1/4	0.989(7)	1/4	0.5	0.3(8)
O2	0	0.144(2)	0.054(6)	0.5	0.7(7)
O3	0.67(5)	1/4	0.79(7)	0.25	0.6(3)

λ = Cu $K_{\alpha_{1,2}}$ Å; $a = 5.530(9)$ Å, $b = 15.59(8)$ Å, $c = 5.678(3)$ Å,
$\alpha = \beta = \gamma = 90°$;Space group *Imma*; $R_{Bragg} = 3.27$, $R_F = 2.32$, $\chi^2 = 2.78$

Table 5.2: Refinement results and structural parameters of $SrFeO_{2.5}$ as proposed in *Pbma* structure model by Auckett *et al.* [25]

.

Atom	x/a	y/b	z/c	Occ.	$100 \times U_{iso}$
Sr1a	0.2414(6)	0.1090(4)	0.9993(6)	1.00000	1.00(2)
Sr1b	0.4931(7)	0.6085(4)	0.5013(6)	1.00000	1.00(2)
Fe1a	0.00000	0.00000	0.00000	0.50000	0.47(4)
Fe1b	0.25000	0.50000	0.4996(13)	0.50000	0.47(4)
Fe2a	0.9650(11)	0.25000	0.0319(14)	0.50000	0.84(7)
Fe2b	0.7169(11)	0.75000	0.5339(14)	0.50000	0.84(7)
O1a	0.883(3)	0.0065(10)	0.257(6)	1.00000	0.86(18)
O1b	0.378(3)	0.4922(10)	0.253(7)	1.00000	0.86(18)
O2a	0.028(4)	0.142(3)	0.996(4)	1.00000	1.63(18)
O2b	0.272(4)	0.641(3)	0.491(4)	1.00000	1.63(18)
O3a	0.676(3)	0.75000	0.871(6)	0.50000	4.1(5)
O3b	0.582(3)	0.75000	0.377(6)	0.50000	4.1(5)

$\lambda = 0.574460$ Å; $a = 11.35052(6)$ Å, $b = 15.58875(8)$ Å, $c = 5.52881(3)$ Å,
$\alpha = \beta = \gamma = 90°$; Space group *Pbma*; $R_p = 0.1047$, $wR_p = 0.1432$, $\chi^2 = 9.404$

To understand the agreement with the newly reported structure model *Pbma* (see Table 5.2), we performed Rietveld refinement on the same powder diffraction data obtained on the ground single crystal of $SrFeO_{2.5}$ taking the structural parameters as published in this study[25]. The refinement (see Fig. 5.3(a)) shows a quite good agreement also with the *Pbma* structure model. This was not surprising because the only difference what is expected in the diffraction patterns for these two structure models is the presence of extra superstructure reflections which originate from the structural modulation imposed by the ordering of the tetrahedral chains. But as the intensities of such reflections are very weak they do not affect significantly χ^2 value. These weak superstructure reflections are very difficult to distinguish from background if the statistics are not of extremely good quality. Fig. 5.3(b) shows the intensity of the superstructure reflections (marked by blue stars) are hidden in the background of the diffraction patterns obtained from the standard laboratory X-ray diffractometer.

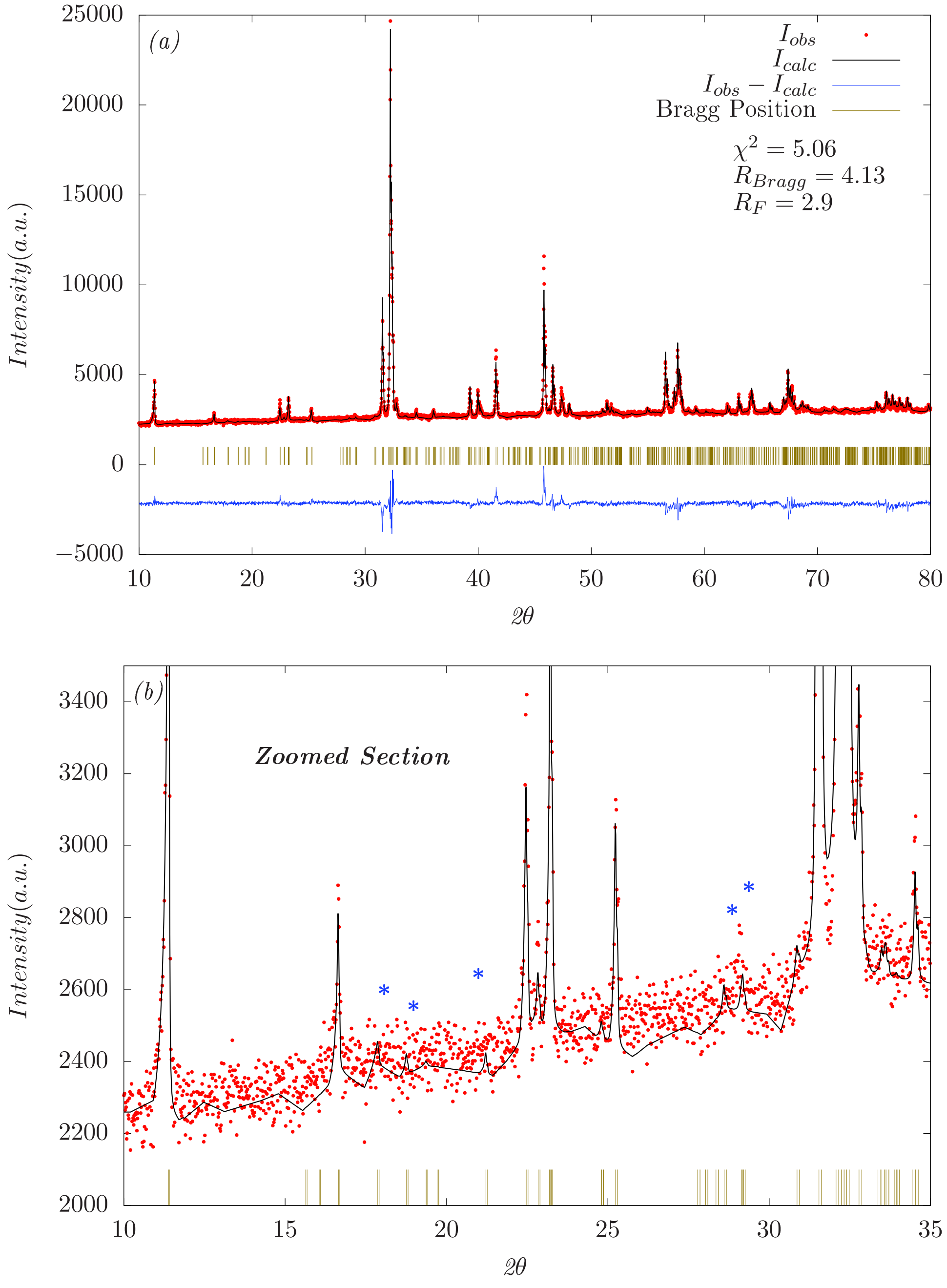

Figure 5.3: (a) Rietveld analysis of X-ray powder diffraction pattern obtained from crushed as grown $SrFeO_{2.5}$ single crystal in *Pbma* structure model. (b) Representation of the weak superstructure intensities from the calculated pattern as pointed by the asteriks *. The superstructure intensities expected from *Pbma* structure models are hidden in the background.

It is clear that the statistics of the collected data on the laboratory X-ray diffractometer as presented in the Fig. 5.3(b) is not sufficient to validate the *Pbma* model. Even in the synchrotron X-ray diffraction pattern as published in the ref.[25] does not have enough statistics to infer the *Pbma* structure model, as the superstructure reflections in the expected reflection positions do not even come out from the background of the diffraction pattern (see inset of the Fig. 5.4). Single crystal X-ray diffraction with area detector is more evident to resolve such problems as the reflections appear spatially separated in the 3D reciprocal space. In order to verify the existence of the *Pbma* related superstructure we have also performed single crystal diffraction on a standard laboratory diffractometer equipped with 2D area detector as shown in Fig. 5.5.

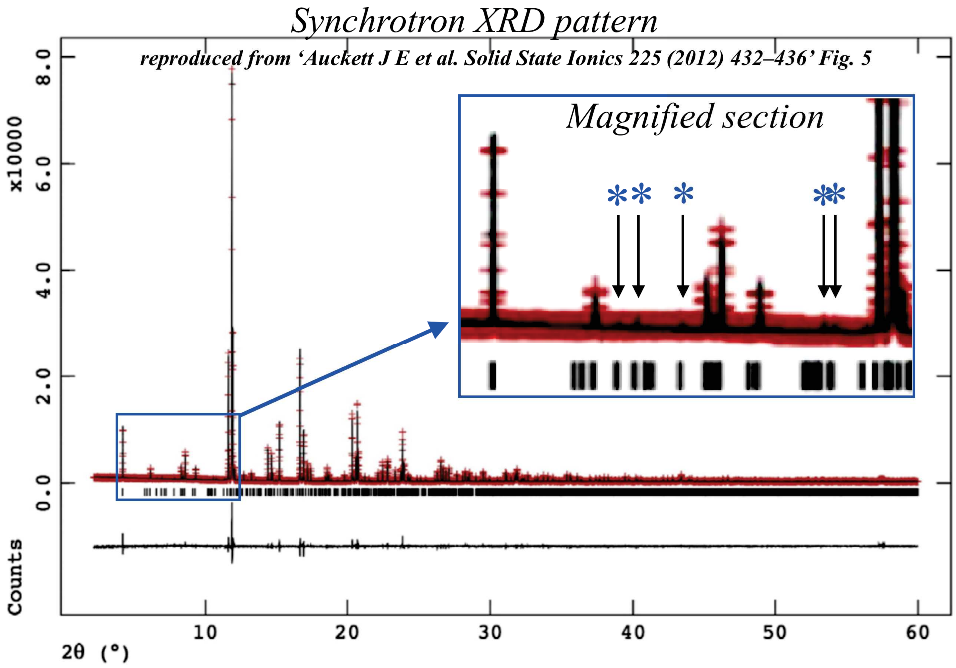

Figure 5.4: Rietveld refinement of Synchrotron XRD (λ = 0.574460 Å) pattern of $Sr_2Fe_2O_5$ as published in the ref.[25] (reproduced and modified from Fig. 5 of ref.[25]). Observed data is presented in red crosses, calculated data in solid black lines and differences are presented below. S-XRD profiles from the final Rietveld refinement of $Sr_2Fe_2O_5$ (*Pbma* supercell). (INSET) The superstructure reflections are indicated by blue stars which are hidden inside the background of the data.

5.2 X-ray single crystal diffraction

Single crystal X-ray diffraction of $SrFeO_{2.5}$ was carried out on Xcalibur diffractometer (oxford diffraction) equipped with 4-circle kappa goniometer and a CCD area detector using laboratory X-ray source (Mo: 0.7107 Å). Fig. 5.5 represents the (*hk0*) reciprocal plane as obtained from the 3D diffraction data. The plane is reconstructed in the pseudocubic cell ($a_p \sim 3.89$ Å) in order to conveniently index the twin domains as discussed in chapter 4. All the reflections present in the plane can be indexed in the *Imma* structure model with lattice parameters $[a \approx \sqrt{2}a_p, b \approx 4a_p, c \approx \sqrt{2}a_p]$ by taking into account two orientation variants of the *b* axis in the pseudocubic supercell (please consult chapter 4 : Twinning in $SrFeO_{3-x}$ system). The presence of $(1/200)_p$ type reflections in the pseudocubic cell uniquely represent the direction of the variants. As can be seen from the diffraction pattern, this type of reflections were not accessible by the particular set up we used which was a big limitation. As these are the only reflections belonging to one variant only they are mandatory for the analysis of orientation variants of different twin domains. Simulated diffraction pattern as shown in Fig. 5.6(a), indicates atleast two variants in the pseudocubic a_p and b_p direction needed to index all the reflection position.

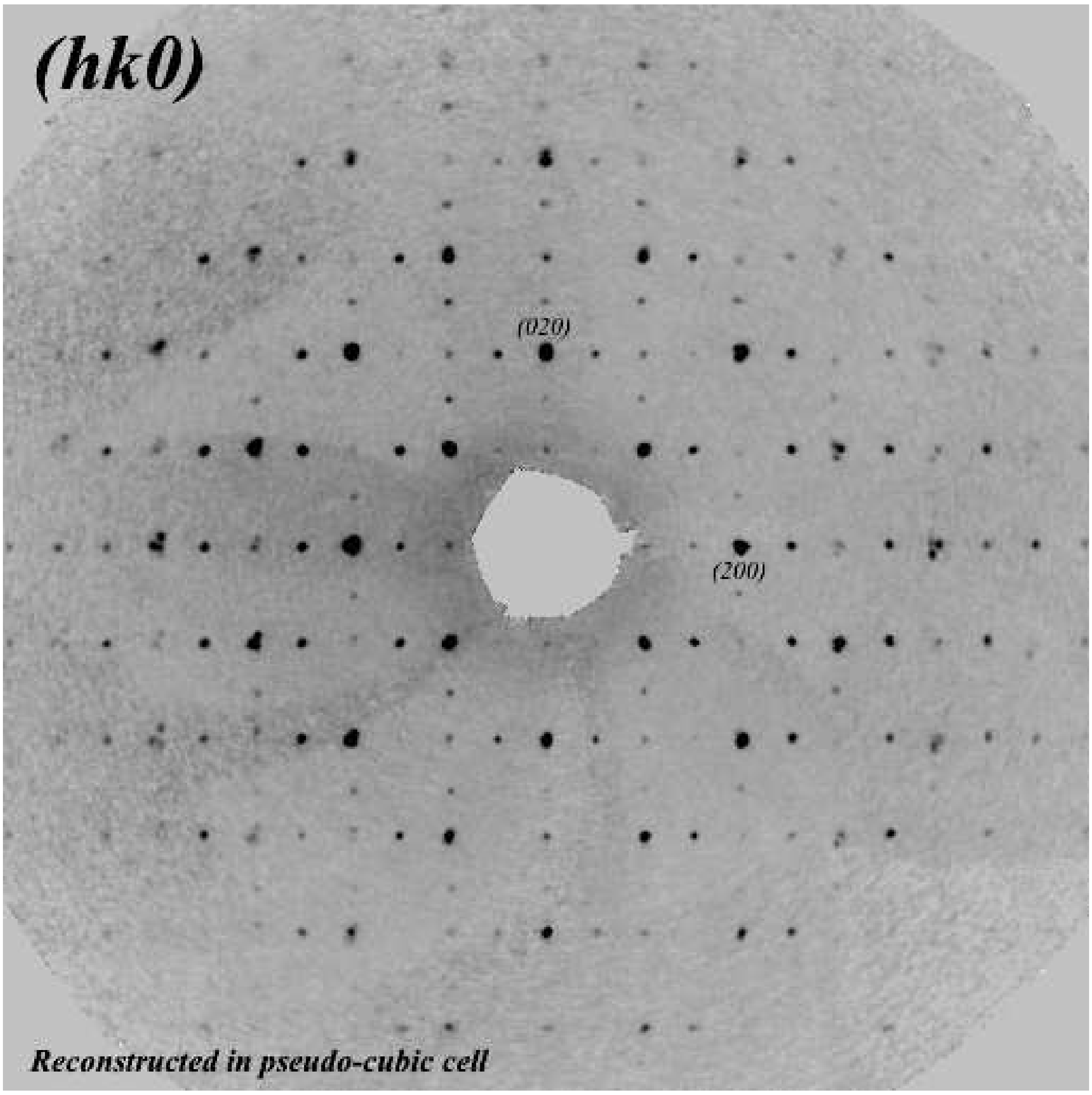

Figure 5.5: Reconstructed (*hk0*) plane in the pseudocubic cell from the data obtained from laboratory single crystal X-ray diffraction on $SrFeO_{2.5}$.

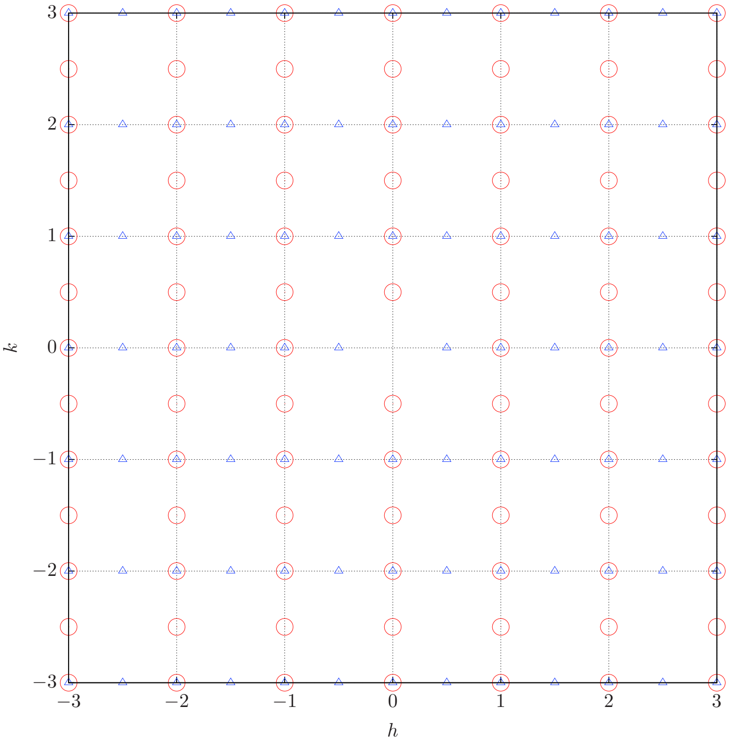

(a)

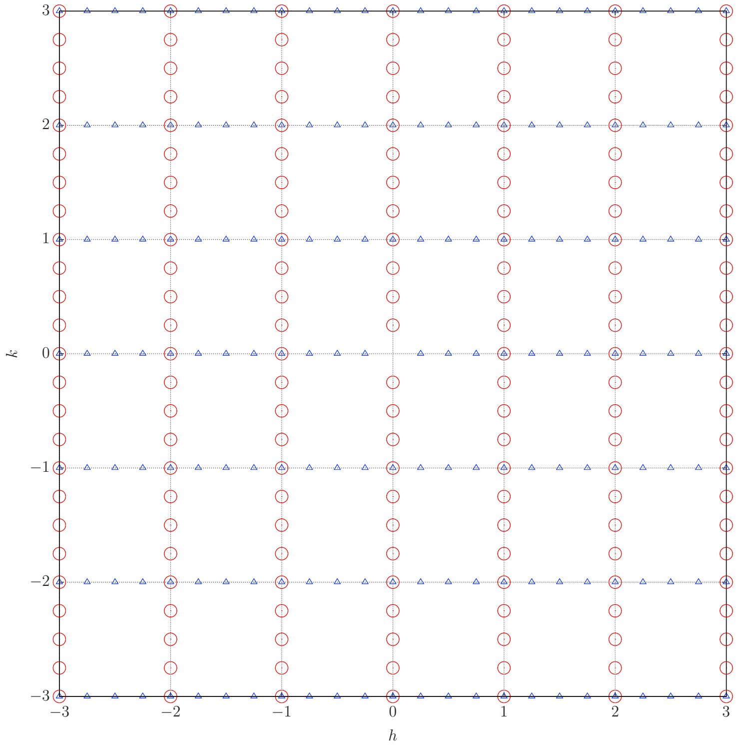

(b)

Figure 5.6: Simulated diffraction patterns of (*hk0*) plane (a) in *Imma* structure model (b) in *Pbma* structure model with the presence of 2-variants, blue triangles and red circles indicate respectively the reflections corresponding to the variants along a_p and b_p.

In order to realize the same scenario in the *Pbma* structure model with equivalent orientation variants we have simulated the (*hk0*) diffraction pattern as shown in Fig. 5.6(b). As expected for the structure model in *Pbma* space group with lattice parameters [$a \approx 2\sqrt{2}a_p, b \approx 4a_p, c \approx \sqrt{2}a_p$], the calculated patterns shows appearance of significantly more superstructure reflections. It is evident that no such reflections are visible on the experimental diffraction pattern. As we have discussed already in the earlier section in Fig. 5.3(b) that the superstructure intensities expected for the *Pbma* model are really weak compared to the ones in the *Imma* structure model, there might be a possibility, even in the case of single crystal diffraction with 2D detector that the weak reflections disappear in the electronic background or by the unwanted fluorescence from the Fe K-edge as collected by CCD detector. A longer exposure time would give the possibility for getting higher intensities for the weak reflections but does not help as the CCD detector collects more and more background with time. The other limitation presents the resolution of the CCD detector used. The splitting of the reflections due to the twinning is almost invisible which lacks important information in order to analyse the number of twin domains corresponding to each variant.

However, interpretation of the newly proposed structure model was still not evident on the ground of such limited data quality as affected by the detector efficiency and relatively weak flux of laboratory X-ray. The only possible alternative to avoid such limitations was to perform synchrotron X-ray diffraction using high brilliance source along with the high resolution noise free 2D detector as Pilatus 2M. The advantage of such high dynamic range detector is the equal efficiency for detection of weakest and strongest reflections at the same time with no electronic background.

Table 5.3: Technical specfication showing the advantage of PILATUS 2M over the CCD detectors.

Technical specifications	PILATUS 2M	Sapphire 3 CCD Detector
Sensitive area (width × height)	253.7×288.8 mm^2	90 – 92 mm diagonal
Pixel size	172×172 μm^2	31 μm on scintillator
Readout time	2.03 ms	2.8 s (4×4 binning) 4.4 s (2×2 binning)
Maximum count rate [phts/s/pixel]	10^7	
Threshold energy [keV]	2.7–18	

5.3 Synchrotron X-ray single crystal diffraction

Single crystal synchrotron X-ray diffraction was performed on the high-flux beamline BM01A at The European Synchrotron–ESRF using high resolution 2D area detector Pilatus 2M as described in chapter 2. The advantage of such detector is that it has almost zero electronic background. Special care was taken to reduce the background from fluorescence. The wavelength of the harmonics free SX-ray beam was fixed at 0.7750 Å (16.00 keV) just below the Sr-absorption edge (16.104 keV). The detector threshold for photon detection was set at 12.000 keV to suppress the fluorescence from Fe-K edge (7.112 keV). Also at this wavelength the X-ray transmission through a sample of 50 μm was almost 30% which was much less (5%) for the Mo-wavelength ($\lambda = 0.7170$ Å). Data were collected in a timescale of 0.3 s per frame obtained for each $\Delta\phi$ rotation of 0.1° upto $\phi = 360°$. A full sphere data collection took 18 min for 3600 frames. Fig. 5.7 shows such reciprocal space obtained from 3D volume reconstruction of the diffraction data obtained on beamline BM01A at ESRF. The intensities are represented by the volume of each reflection position. The highest intense reflections are shown in red while other lower intensity reflections are in black. The presence of enormous number of weak reflections becomes easily visible from such volume representation.

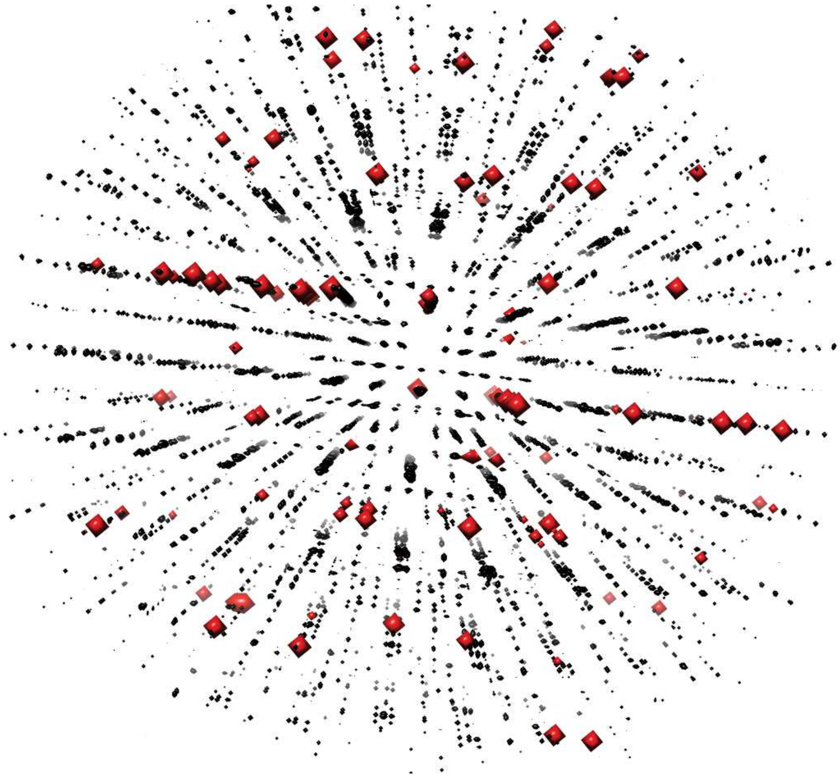

Figure 5.7: 3D reciprocal volume representation of the diffraction data obtained on beamline BM01A at ESRF

The 3D data was preprocessed by SNBLToolBox[24] and the data analysis and receprocal plane reconstruction was performed using Crysalis^{Pro}[80] diffraction software. Using proper orientation matrix (UB), the principle planes have been reconstructed in the pseudocubic cell and presented in Fig. 5.9 and Fig. 5.10. The strong reflections are corresponding to the basic Perovskite type framework while the weak superstructure reflections are related to the vacancy ordering in $SrFeO_{2.5}$ and these are the most important reflections. The splitting of many reflections is related to the twinning. The non-equivalent appearance of the three diffraction planes (*0kl*), (*h0l*) and (*hk0*) indicate all three possible variants were not present in the particular crystal. The $(0{}^{1}/_{2}0)_p$ type reflections (*i.e.* (020) type in Brownmillerite) are the most crucial ones to determine the number of the variants present in a particular crystal as they represent *uniquely* the long b axis of a particular domain. In Fig. 5.8 we have presented the scheme of different orientations of the all possible variants (V1 along b_p, V2 along a_p and V3 along c_p; Please note, this convention will be followed throughout).

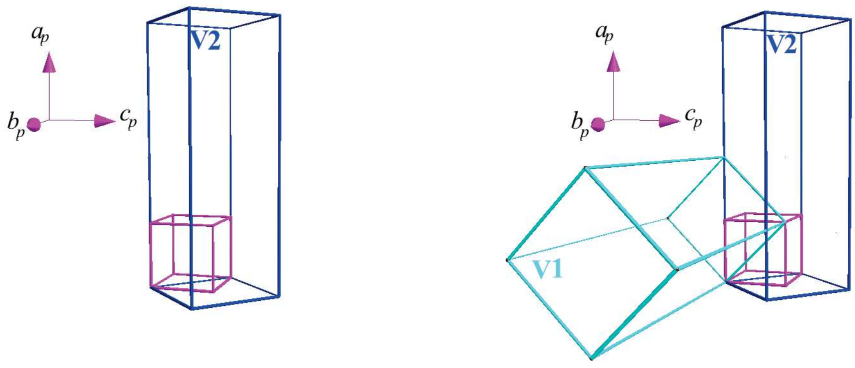

(a) 1 variant

(b) 2 variants

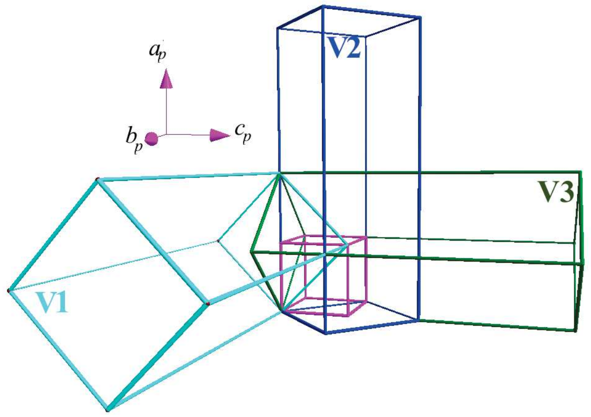

(c) 3 variants

Figure 5.8: Orientation of the variants (b axis of $SrFeO_{2.5}$ in with respect to the pseudocubic cell $[a_p \times b_p \times c_p]$ for the presence of (a) one variant (V1) (b) 2 variants (V1 & V2) and (c) 3 variants (V1, V2 & V3); the directions of the cubic cell are arbitrary.

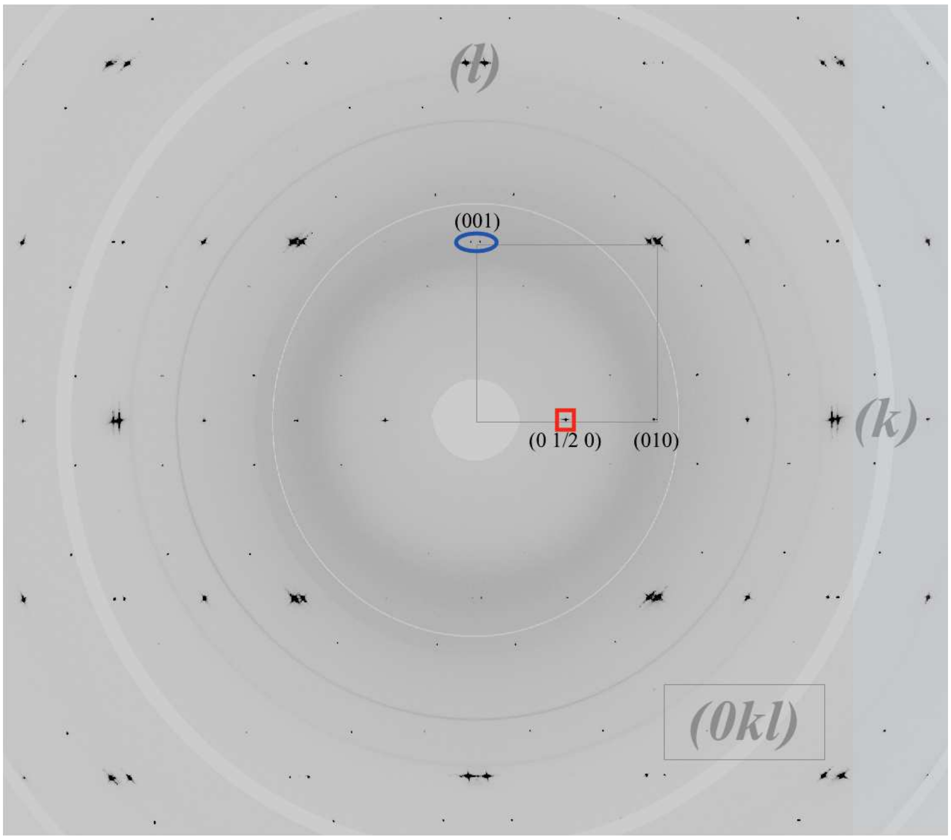

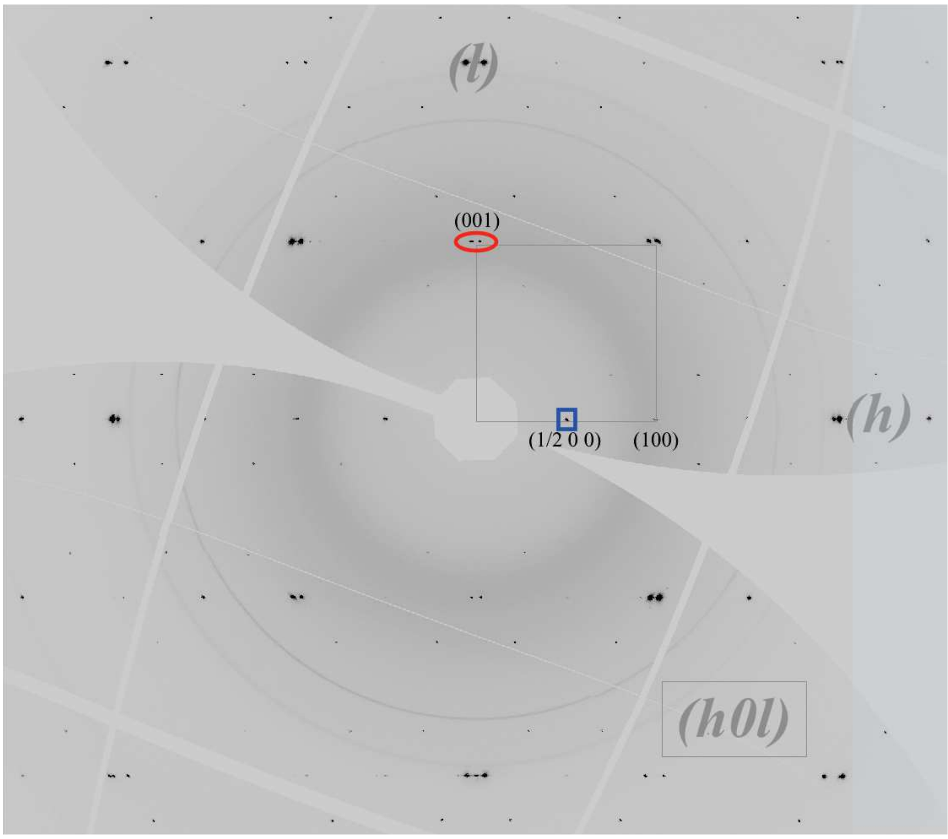

Figure 5.9: Reconstructed (*0kl*) and (*h0l*) planes in the psudocubic cell from the diffraction data obtained on BM01A diffractometer, ESRF. The pseudocubic cell is marked by the black square and little shifted to see the reflections properly.

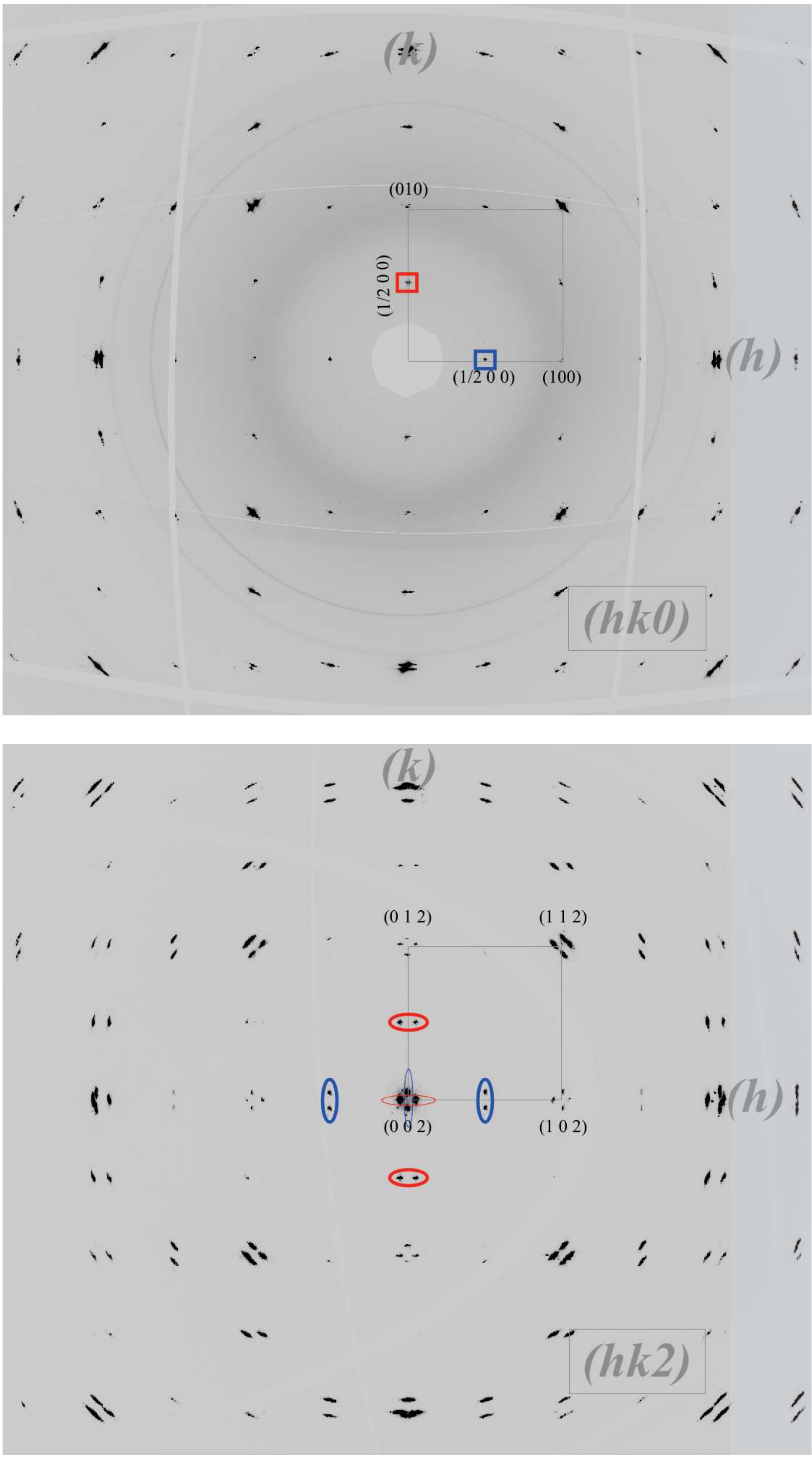

Figure 5.10: Reconstructed (*hk0*) and (*hk2*) planes in the psudocubic cell from the diffraction data obtained on BM01A diffractometer, ESRF. The pseudocubic cell is marked by the black square and little shifted downwards to see the reflections properly.

In order to attribute the reflections corresponding to particular twin domains the information regarding orientation variants and number of twin domains is very important to determine. Here onwards, the reflections corresponding to the psedocubic cell will be written with subscript $(hkl)_p$ and the corresponding orthorhombic reflection in the $SrFeO_{2.5}$ will be written without any subscript.

The $(0\,{}^1\!/\!_2\,0)_p$ type reflections in the cubic cell are unique corresponding to each variant. They are related to the (020) type reflection in the orthorhombic cell of $SrFeO_{2.5}$. As can be seen from the *(0kl)* plane in Fig. 5.9, the presence of $(0\,{}^1\!/\!_2\,0)_p$ reflection which indicate the presence of the twin domains with variant (V1) along the b_p axis of the pseudocubic cell. Similarly, in the *(h0l)* plane the presence of $({}^1\!/\!_2\,00)_p$ reflection confirms the presence of other twin domains with variant (V2) running along a_p pseudocubic axis. In both planes the absence of $(00\,{}^1\!/\!_2)_p$ reflection refers that no twin domain exist with variant along c_p axis. The presence of both, $(0\,{}^1\!/\!_2\,0)_p$ and $({}^1\!/\!_2\,00)_p$ reflections can be realized in the *(hk0)* plane. In summary, in the present crystal we have two variants V1 and V2 running along b_p and a_p direction of the pseudocubic cell as shown in Fig. 5.8(b).

The next important information which is necessary to know is the number of twin domains corresponding to each variant. As discusses in chapter 4, corresponding to each there can be at maximum 4 twin individual and results into in plane splitting of the reflection perpendicular to the variant (*b*-axis). In the present single crystal we had 2 twin individuals corresponding to each variants (V1 and V2) as can be understood from a closure look to the $(001)_p$ reflection in *(0kl)* and *(h0l)* showing splitting. The splitting in the $(001)_p$ reflection (equivalent to (-101) in $SrFeO_{2.5}$) in *(0kl)* plane is related to presence of 2 twin individuals having the common variant along the a_p direction (V2). Similarly the splitting of $(001)_p$ reflection in the *(h0l)* plane indicates the other two twin individuals having a common variant along along b_p direction (V1) of the pseudocubic cell. To clarify the relation with the variants, we used squares and ellipses for the reflections belonging to variant V2 in blue colour and for variant V1 in red colour. The splitting is similar $2\Delta \sim 3^\circ$ as expected from the orthorhombicity for (101) type reflection in $SrFeO_{2.5}$.

To summarize, the present sample had 2 variants along b_p (V1) and a_p (V2) direction and for each of the variants there were two twin individuals splitted along c_p direction giving in total 4 twin individuals. The splitting of the twins corresponding to the two variants are in perpendicular to each other as can be clearly visible from the reconstructed *(hk2)* plane Fig. 5.10. In the center of the plane, the 4 contributions of the $(002)_p$ reflection are related to the 4 individuals. The top and bottom ones as indicated by the *thin blue ellipse*, are related to the twin domains with variant along a_p axis whereas the left and right ones indicated by the *thin red ellipse* having the variant along the b_p axis.

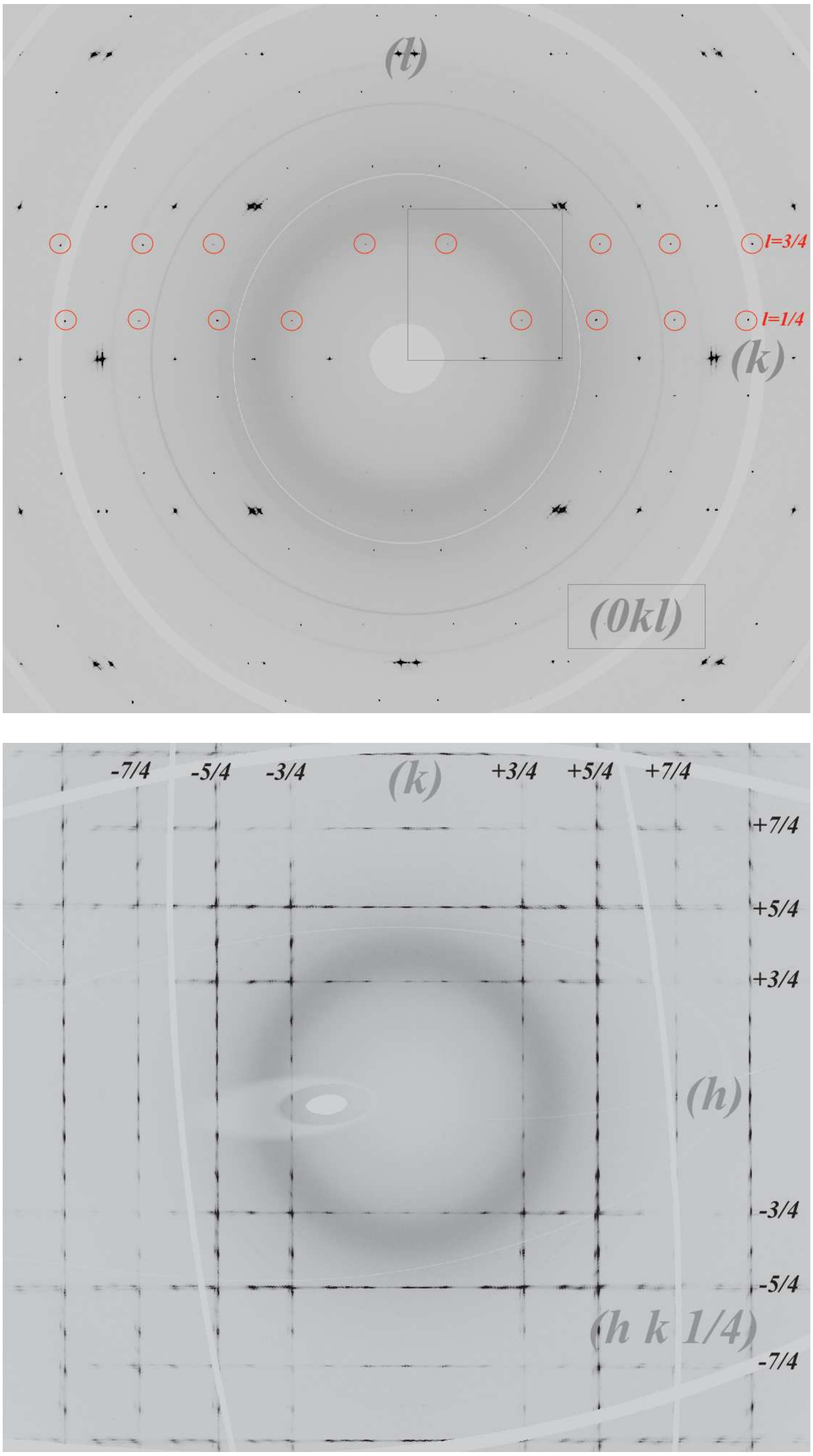

Figure 5.11: (a) Reconstructed ($0kl$) plane showing apparently sharp reflection which can not be indexed in *Imma* structure model. They are basically the diffuse rods appear as sharp reflections when passing through the ($0kl$) plane at $l = {}^1\!/_4, {}^3\!/_4$ etc. (b) The reconstructed ($hk\,{}^1\!/_4$) plane showing the diffuse rods along the two variants a_p and b_p.

With the discussed twin model almost all the reflection can be indexed except a few very small reflections in the (*0kl*) and (*h0l*) planes. Fig. 5.11(a) show such reflections in the (*0kl*) as encircled by the red circle at $l = 1/4, 3/4$ etc. At first glance, these reflection position can be perfectly indexed with the newly proposed *Pbma* structure model with twice the *a* lattice parameter in the presence of 3 variants, as can be seen from the blue triangles in the simulated pattern in Fig. 5.12, but in such case more reflections are expected to appear in the reciprocal plane.

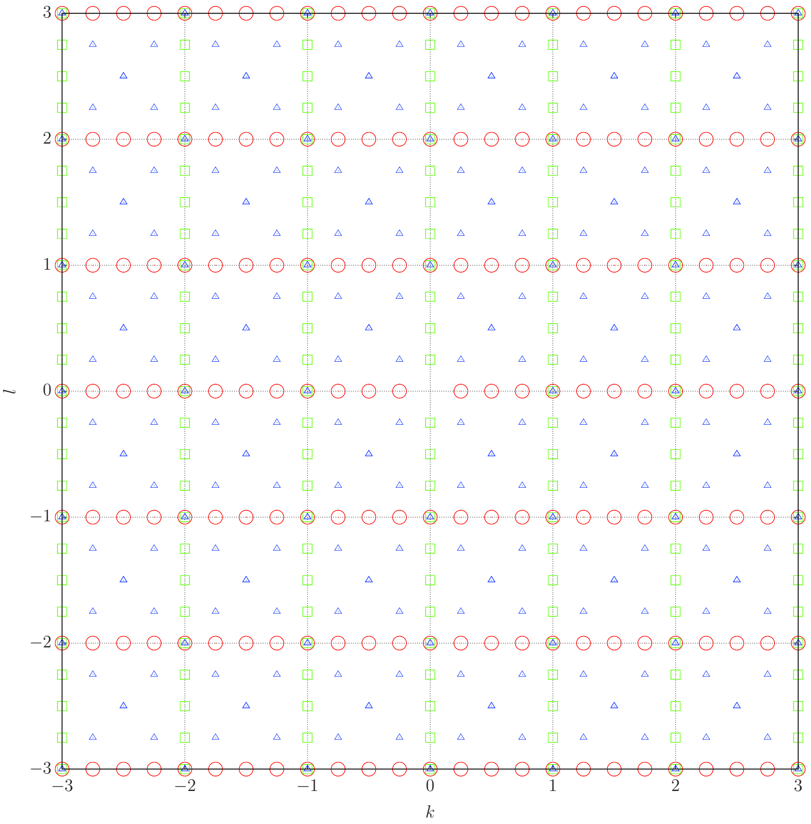

Figure 5.12: Simulated (*0kl*) plane of SrFeO$_{2.5}$ in newly proposed *Pbma* structure model showing the reflection positions for the contribution from 3 variants. Reflection related to V1 (along b_p), V2 (along a_p) and V3 (along c_p) are represented respectively in red circles, green squares and blue triangles.

Careful inspection of the 3D reciprocal space, as obtained from the diffraction, reveals those apparently sharp reflections are not reflections but diffuse rods passing perpendicularly through the (*0kl*) and (*h0l*) planes. Presence of such diffuse rods along the two variants is shown in the reconstructed ($hk1/4$) plane in Fig. 5.11(b). It is noteworthy that such modulated intensity distribution of the diffuse scattering can be only obtained from high quality 3D diffraction data as obtained from single crystal diffraction using high resolution detector like Pilatus-2M on BM01A diffractometer in ESRF. Such information is almost impossible to get from polycrystalline samples.

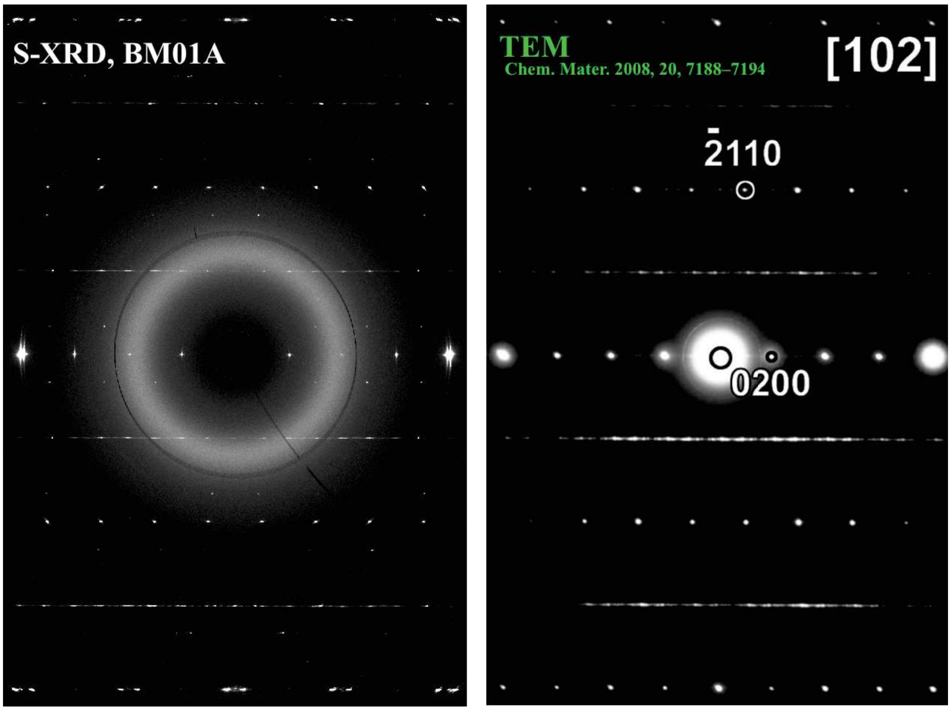

Figure 5.13: Comparison of the scattering planes with the zone axis [102] obtained for (right) TEM study by D'Hondt *et al.*[99] on SrFeO$_{2.5}$ (left) reconstructed receprocal plane from 3D diffraction data obtained on BM01A. The extra reflections in the S-XRD patterns are from the twin domains of the second variant in the present sample. while the TEM pattern indicates the corresponding sample had only one variant.

The TEM investigation on SrFeO$_{2.5}$ by D'Hondt *et al.*[99] also confirms the presence of such diffuse rods as shown Fig. 5.13 and compared with the reconstructed plane with the same zone axis [102] from the synchrotron diffraction data obtained on the single crystal in this work. The study by D'Hondt *et al.* revealed instead of a perfect ordering, the adjacent tetrahedral (FeO$_4$)$_\infty$ chains are arranged completely randomly giving rise to different stacking faults of the (FeO$_4$)$_\infty$ tetrahedral layers along the *b* axis as shown in Fig. 5.14. The underlying space group still remains *Imma* but with the presence of defects related to the random stacking of (FeO$_4$)$_\infty$ chains in the "R" and "L" configuration. In detail the structure has been described in the (3 + 1)-dimensional superspace group $I2/m(0\beta\gamma)0s$, $q = \beta b^* + \gamma c^*, 0 \leq \beta \leq 1/2$ and $0 \leq \gamma \leq 1$. The stacking disorder has been simulated successfully by D'Hondt *et al.* and intergrowth phases related to a stacking sequence with *C2/m* or *Pbma* space group have been identified. The degree of stacking disorder has been interpreted to depend on the history of the crystallites. In this regards TEM appears to be an esteem tool to quantitatively describe stacking disorder in solids. As shown in Fig. 5.11, these diffuse rods which appear as regular reflections for special projections are misleading as it suggests one to believe the compound to be multiphase or to propose new structure models.

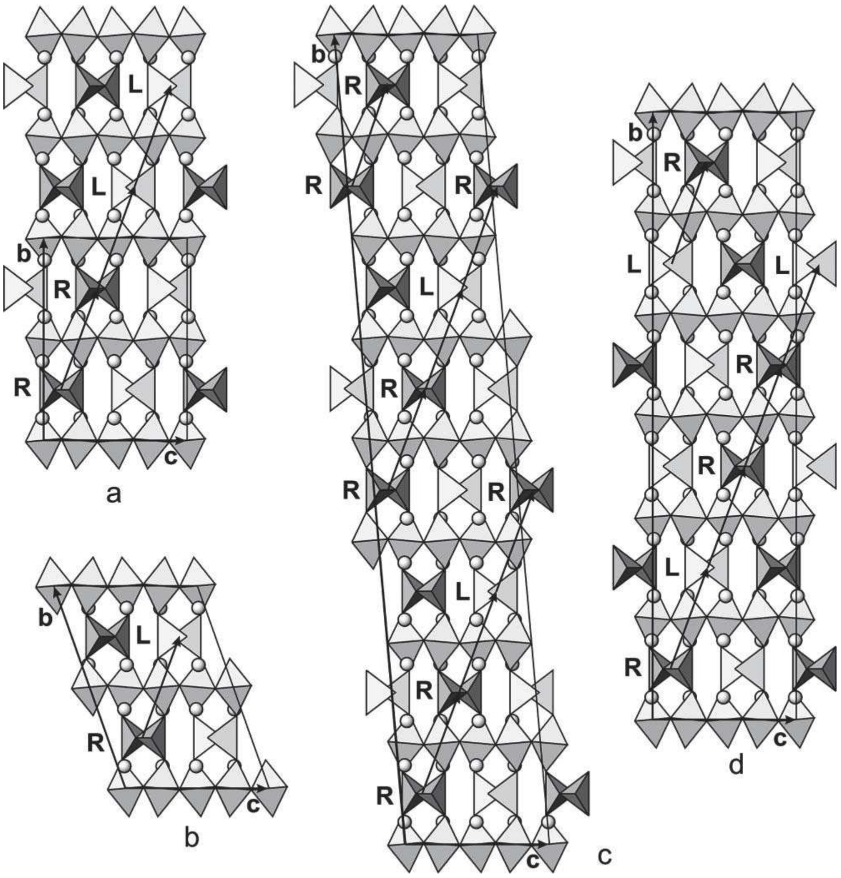

Figure 5.14: Commensurate structures with the stacking sequences of tetrahedral layers for $\beta = 0$ (a), 1/2 (b), 1/8 (c), 1/3 (d). The 1/2[111] vector of the brownmillerite subcell is shown by arrows with the structure model described in the (3 + 1)-dimensional superspace group $I2/m(0\beta\gamma)0s$, $q = \beta b^* + \gamma c^*, 0 \leq \beta \leq 1/2$ and $0 \leq \gamma \leq 1$. **Reproduced from Fig. 8 of ref.[99].**

The structure is already complicated with the presence of twinning and diffuse scattering and neutron diffraction adds another dimension of complexity because of the related magnetic reflections appearing from each twins. One can easily fall into one of the several pitfalls present in the case of such a complicated structure. The next section will be mainly focused on neutron diffraction studies on $SrFeO_{2.5}$.

5.4 Neutron powder diffraction

Neutron powder diffraction was performed on the crushed single crystal of SrFeO$_{2.5}$ on the high resolution two axis instrument 3T2 at Laboratoire Léon Brillouin (LLB) using the wavelength λ = 1.2252 Å. SrFeO$_{2.5}$ shows a G-type antiferromagnetic ordering with a Néel temperature around 690 K[22,85]. The magnetic moments on the Fe atoms align parallel to c axis in the *Imma* structure model (parallel to a in *Icmm* structure model[100]). Reflections with $h+k+l=2n+1$ where n is an integer, are only contributed by magnetic intensity in the *Imma* structure model where as the body centered reflections with $h+k+l=2n$ show neuclear contribution only. Rietveld refinement (nuclear and magnetic) on the diffraction data in *Imma* structure model is shown in Fig. 5.15 (top). To see the agreement with the newly proposed structure model by Auckett *et al.*[25,97] we have also refined the diffraction data in the *Pbma* structure model Fig. 5.15 (bottom). The corresponding refinement results in the respective space groups are given in Table 5.5 and 5.6.

Fig. 5.16 shows a magnified portion of the diffraction data refined in the *Pbma* structure model. The refinement results clearly show the intensities of the (2*k*1) type reflections, where k is odd, are mainly contributed by the magnetic intensities in the *Pbma* structure model (see Table 5.4), though the single crystal neutron diffraction study by Auckett *et. al.* reports these intensities are purely nuclear and they are related to the ordered arrangement of the (FeO$_4$)$_\infty$ chains (Fig. 5.17). And most importantly on the basis of such superstructure reflections, which are mainly magnetic in origin the study by Auckett *et al.* misinterpreted the nuclear structure of SrFeO$_{2.5}$ to be *Pbma*.

Table 5.4: Nuclear and magnetic intensity as obtained from the Rietveld refinement of the SrFeO$_{2.5}$ neutron powder diffraction data in *Pbma* structure model.

Pbma structure model				
Reflection in *Pbma*	Nuclear Intensity		Magnetic intensity	
(*hkl*)	I$_{Cal.}$	I$_{Obs.}$	I$_{Cal.}$	I$_{Obs.}$
(201)	3139.4	3136.2	0.0	0.0
(211)	1.2	1.2	202.7	196.3
(221)	56.4	56.8	0.0	0.0
(231)	3.6	2.2	162.4	103.9
(241)	6564.0	6393.6	0.0	0.0

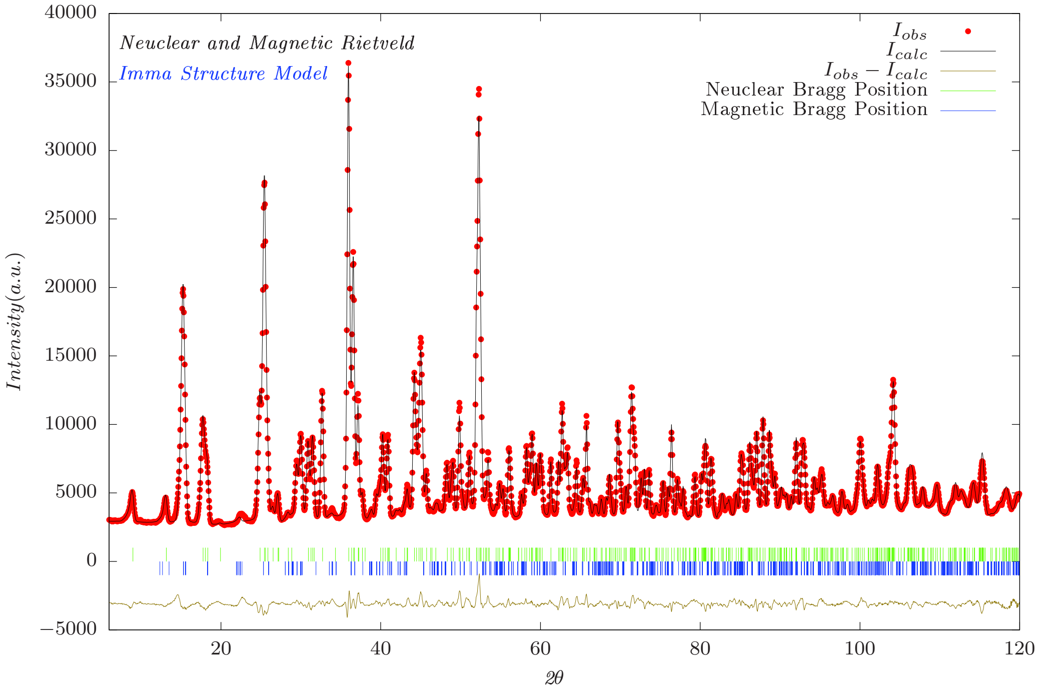

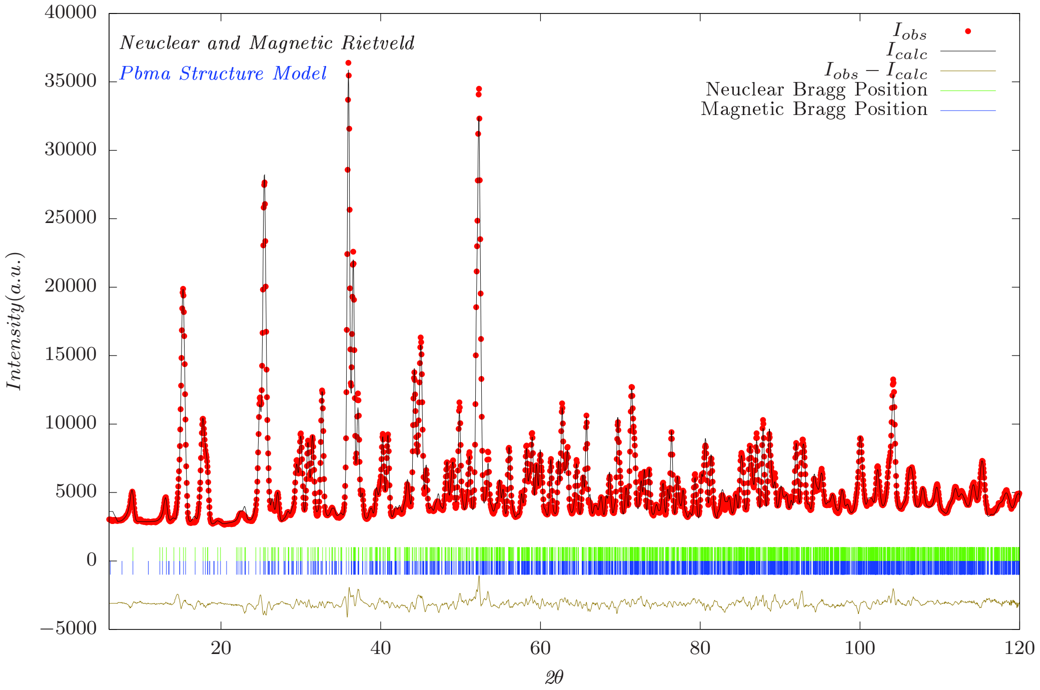

Figure 5.15: Nuclear and magnetic Rietveld refinement of the neutron powder diffraction (λ = 1.2252 Å) data obtained on 3T2, LLB (top) in *Imma* structure model (bottom) in *Pbma* structure model. The experimental data in red points, calculated pattern in black solid line and the difference in between the experimental and calculated patterns is presented below with olive solid line.

Table 5.5: Results of the Rietveld (nuclear and magnetic) refinement on the neutron powder diffraction data obtained on SrFeO$_{2.5}$ in the *Imma* structure model.

Atom	*x/a*	*y/b*	*z/c*	*Occ.*	B_{iso}
Sr	1/2	0.890(9)	0.015(1)	0.50	0.6(6)
Fe1	0	0	0	0.25	0.6(9)
Fe2	1.041(5)	1/4	0.679(1)	0.25	0.4(2)
O1	1/4	0.00(7)	1/4	0.50	0.5(2)
O2	0	0.859(4)	0.049(9)	0.50	1.0(1)
O3	0.126(9)	3/4	0.638(2)	0.25	0.5(7)

λ = 1.2252; a = 5.529(8) Å, b = 15.58(9) Å, c = 5.674(2) Å; $\alpha = \beta = \gamma = 90°$;
Space group $Imma$; Neuclear R$_{Bragg}$ = 3.84, R$_F$ = 2.50

Magnetic moment along c-axis; M(FE1)= $3.7(7)\mu_B$, M(FE2)= $-3.3(7)\mu_B$;
Magnetic R-factor = 5.17

Table 5.6: Results of the Rietveld (nuclear and magnetic) refinement on the neutron powder diffraction data obtained on SrFeO$_{2.5}$ in the newly proposed *Pbma* structure model.

Atom	x/a	y/b	z/c	Occ.	B_{iso}
Sr1a	0.240(3)	0.109(7)	1.001(2)	1.00000	0.6(5)
Sr1b	0.494(2)	0.607(7)	0.507(6)	1.00000	0.6(1)
Fe1a	0.00000	0.00000	0.00000	0.50000	0.5(9)
Fe1b	0.25000	0.50000	0.501(1)	0.50000	1.0(1)
Fe2a	0.965(6)	0.25000	0.021(3)	0.50000	1.1(8)
Fe2b	0.717(1)	0.75000	0.546(9)	0.50000	0.7(2)
O1a	0.8752(8)	0.008(3)	0.249(4)	1.00000	0.7(5)
O1b	0.373(3)	0.492(5)	0.250(3)	1.00000	0.3(5)
O2a	0.026(1)	0.140(2)	0.995(4)	1.00000	1.6(2)
O2b	0.275(2)	0.640(5)	0.50450	1.00000	1.6(1)
O3a	0.680(1)	0.75000	0.869(8)	0.50000	0.6(1)
O3b	0.570(5)4	0.75000	0.377(9)	0.50000	1.6(4)

λ = 1.2252 Å; a = 11.347(6) Å, b = 15.588(5) Å, c = 5.529(3) Å; $\alpha = \beta = \gamma = 90°$;
Space group $Imma$; Neuclear R$_{Bragg}$ = 6.20, R$_F$ = 4.43

Magnetic moment along c-axis; M(FE1)= $3.6(1)\mu_B$, M(FE2)= $-3.3(7)\mu_B$;
Magnetic R-factor = 5.99

From the temperature dependent measurement, the same study reported the intensities of the (*2k1*) type reflections with *k* odd (which were misinterpreted as superstructure reflection from oxygen ordering) drops down with temperature and vanishes around 813 K (Fig. 5.16). Such intensity drops has been explained by Auckett *et al.* as the transition from an ordered *Pbma* to disordered *Imma* model due to local tetrahedral rotation at such high temperature. This *order–disorder* transition suggests that oxygen mobility is feasible only above 800 K which is a contradiction by itself as this compound is well know to undergo oxygen intercalation at ambient[20,21].

The intensity drop at 813 K as investigated in ref.[97] can be best explained by considering the magnetic ordering which has been completely ignored in this study. Fig. 5.17(a) shows the diffraction pattern obtained by Auckett *et al.* by the single crystal neutron diffraction of SrFeO$_{2.5}$. The diffraction pattern at 25°C can be easily realized by superimposing the nuclear and magnetic structure obtained in the *Imma* structure model as shown by the Fig. 5.18c. All reflections can be indexed by the *Imma* structure model taking into account both nuclear and magnetic ordering. Fig. 5.18(a) and (b) represents the nuclear and magnetic reflection positions separately as simulated in the *Imma* structure model with two variants. From the superposition of these two patterns as in Fig. 5.18(a), it is quite clear that all reflection can be indexed as obtained in the diffraction pattern Fig. 5.17(a)II. There is absolutely no need to propose any supercell to index all the reflection. But in case the magnetic reflections are mistaken as nuclear reflections, this would lead to a new supercell.

At elevated temperature it is self-evident that at high temperature (beyond the Néel temperature $T_N \sim 693$ K) there will be no reflections corresponding to magnetic ordering. Only the nuclear reflection will be persist and still the underlying structure remains in *Imma* model. So it is very transparent that the phase transition at high temperature must be taken as the magnetic transition (antiferromagnetic to paramagnetic) and not related to any structural *order-disorder* phenomena. The underlying structure of SrFeO$_{2.5}$ can still be explained in the *Imma* model below and above the magnetic phase transition. As discussed in the ref.[97], the phase transition observed at 813 K instead of 693 K, might then be related to an improper calibration of the temperature sensor.

However, the structure model in *Pbma* is associated with 4 different Fe sites: 2 octahedral sites in *4a* and *4c* and 2 sets of tetrahedral sites in *4d* wyckoff positions. In comparison, *Imma* structure model has only 2 different Fe sites: one octahedral site in *4a* and one tetrahedral site in *8i* wyckoff position. To understatd the local environment of Fe atoms, plenty of Mössbauer studies[20,31,82,86] have been done. There is no literature on Mössbauer study of SrFeO$_{2.5}$, reporting more than two different type of Fe sites.

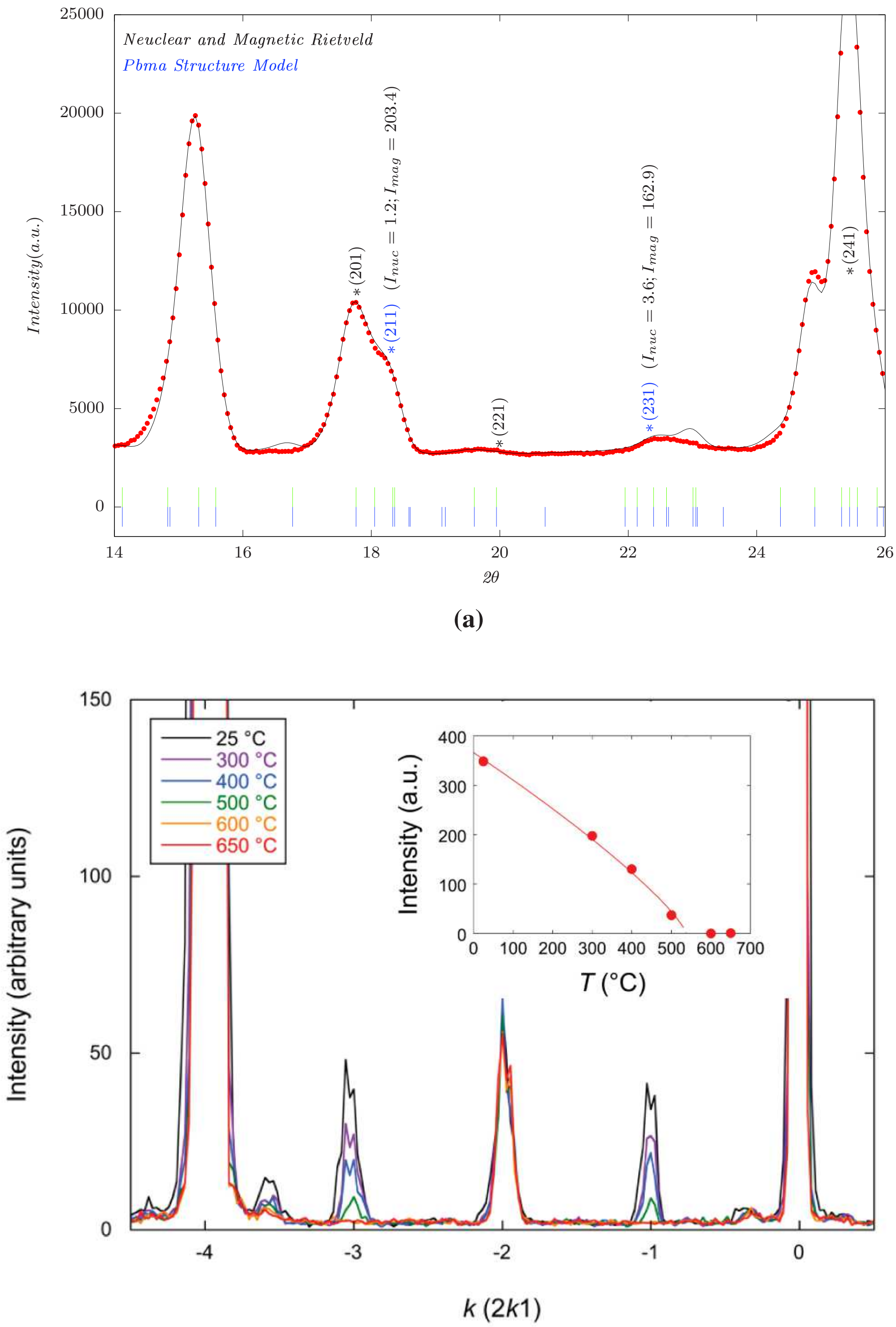

(a)

(b)

Figure 5.16: (a) Magnified section of the Rietveld refined diffraction pattern showing the nuclear and magnetic intensity (this work). (b) Integrated intensities of reflections along the ($2k1$) row, showing the decrease in relative intensity of the superstructure (k odd) reflections with increasing temperature. The inset shows an order parameter fit to the average intensity of the two satellites shown. **Reproduced from figure 3 of ref.[97].**

* Reproduced from "Chem. Mater. 2013, 25, 3080−3087" Figure. 2

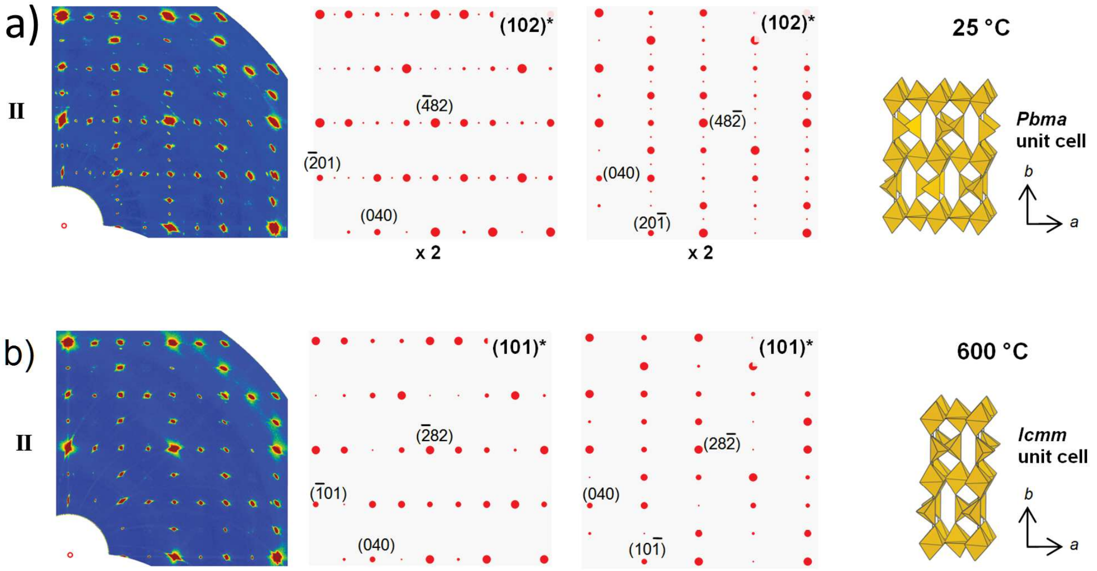

Figure 5.17: Taken from figure 2 of ref.[97] as published. Single-crystal neutron diffraction data collected on the FZ-grown crystal of $Sr_2Fe_2O_5$ in $[100]_P$-type plane. Experimental data (solid blue images, left) are composed of several overlaid patterns corresponding to the twin components present; simulated patterns for contributing twins are shown to the right of each pattern. The label "×2" indicates that the pattern arises from two nonequivalent twins. (a) Data collected at 25 °C, indexed to the *a*-doubled *Pbma* brownmillerite unit cell with fully ordered G-type antiferromagnetic structure. (b) Data collected at 600 °C, indexed to the chain-disordered *Icmm* unit cell.

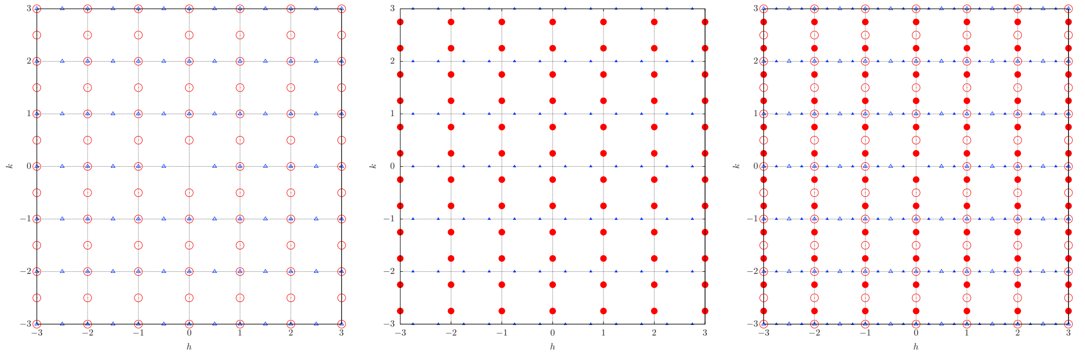

(a) **(b)** **(c)**

Figure 5.18: Simulated patterns in the *Imma* structure model with 2 variants (a) nuclear reflection positions (b) magnetic reflection positions and (c) superposition of nuclear and magnetic reflections.

Recently Waerenborgh *et al.*[101] studied the possible different Fe sites on the single crystal of $SrFeO_{2.5}$ by Mössbauer spectroscopy, taking into account the *Pbma* structure model. Also here the study reports only two different iron position as shown in Fig. 5.19.

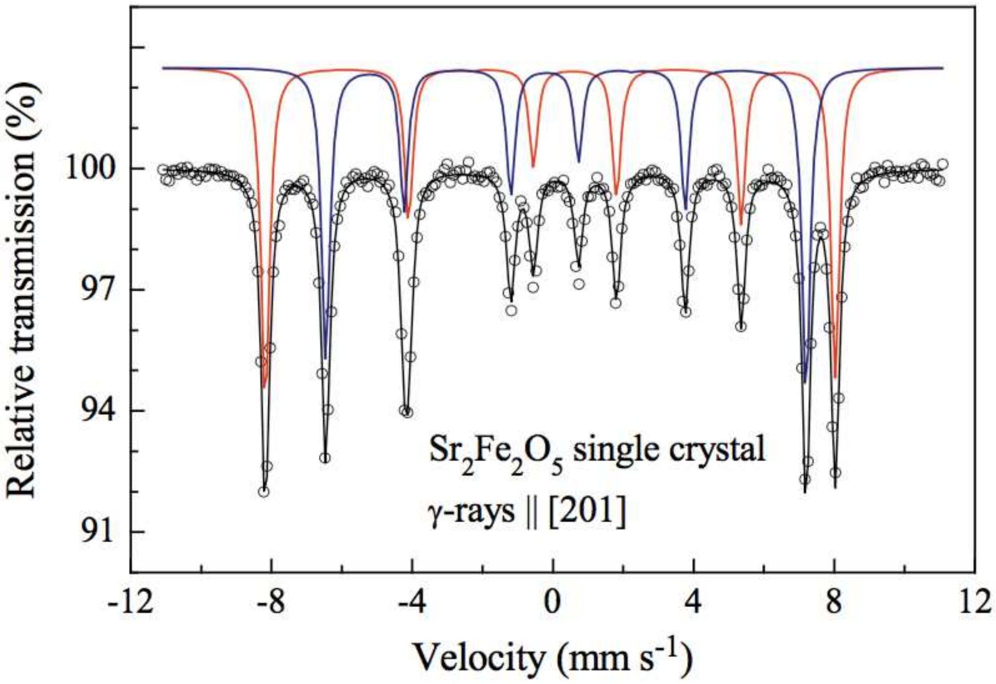

Figure 5.19: Room-temperature Mössbauer spectrum of $Sr_2Fe_2O_5$ single crystal, with the [201] crystallographic direction parallel to γ-rays. Solid lines correspond to the fitting results obtained by solving the complete Hamiltonian for the hyperfine interactions in both the excited and ground nuclear states of the ^{57}Fe nuclei. **Taken from the figure 4 of ref[101].**

5.5 Summary

In this chapter we have discussed in details the ground state of $SrFeO_{2.5}$. Through different complimentary techniques and comparison with the other studies we have justified the structure of $SrFeO_{2.5}$ to be explained in the *Imma* structure model with the presence of particular disorder of the $(FeO_4)_\infty$ chains ordering. We have also shown in the single crystal SX-ray diffraction, with the presence twinning and diffuse rods related to the stacking faults of the tetrahedral layers, the structure validation is very complex which gets more complicated with neutron diffraction due to the associated magnetic structure. Having the structural knowledge of the as grown single crystal as discussed in details in this chapter, we performed electrochemical oxygen intercalation study on single crystal of $SrFeO_{2.5}$ to investigate the phase diagram of $SrFeO_{3-x}$ at ambient and will be discussed in chapter 6. Especially we were interested to investigate the intermediate phases to explore the reaction pathways at low temperature in comparison to the conventional high temperature synthesis.

Chapter 6

In situ electrochemical oxygen intercalation: From $SrFeO_{2.5}$ to $SrFeO_3$

The high temperature phase diagram of $SrFeO_{3-x}$ has been highly investigated in the last 50 years. In chapter 3 we have discussed in detail the complex structures of different vacancy ordered phases of $SrFeO_{3-x}$ as established in the literature. Even the ground state of $SrFeO_{2.5}$ is very complex as we have discussed in details the ground state of $SrFeO_{2.5}$ in chapter 5. This is due to the presence of disordered tetrahedral chain arrangement which plays an important role for low temperature oxygen mobility in this compound[17].

The $SrFeO_{3-x}$ system is also well known to undergo eletrochemical (EC) oxygen intercalation in the range of ($0 \leq x \leq 0.5$). This is surprising taking into account the big size of the $r_{O^{2-}}$. The reaction mechanism is expected to be different at low temperature compared to high temperature synthesis as the system stays in kinetic equilibrium rather than thermodynamic equilibrium. In this consequence it is meaningful to investigate the reaction mechanism for EC oxygen intercalation at ambient. Especially it is important to scrutinize the essential difference in oxygen ordering scheme at low temperature compared to the ones at elevated temperature. The primary goal of the *in situ* investigation presented in this chapter is to identify the intermediate phases and related changes in the microstructures during EC intercalation of $SrFeO_{2.5}$.

Nemudry *et al.*[21] investigated the *in situ* oxygen intercalation on the polycrystalline sample of $SrFeO_{2.5}$. The reaction was carried out in a galvanosatic mode (constant current) in order to relate the oxygen content to charge transfer by following the Eq. 6.1.

$$SrFeO_{2.5} + xO^{2-} \rightleftharpoons SrFeO_{2.5+x} + 2xe^{-} \tag{6.1}$$

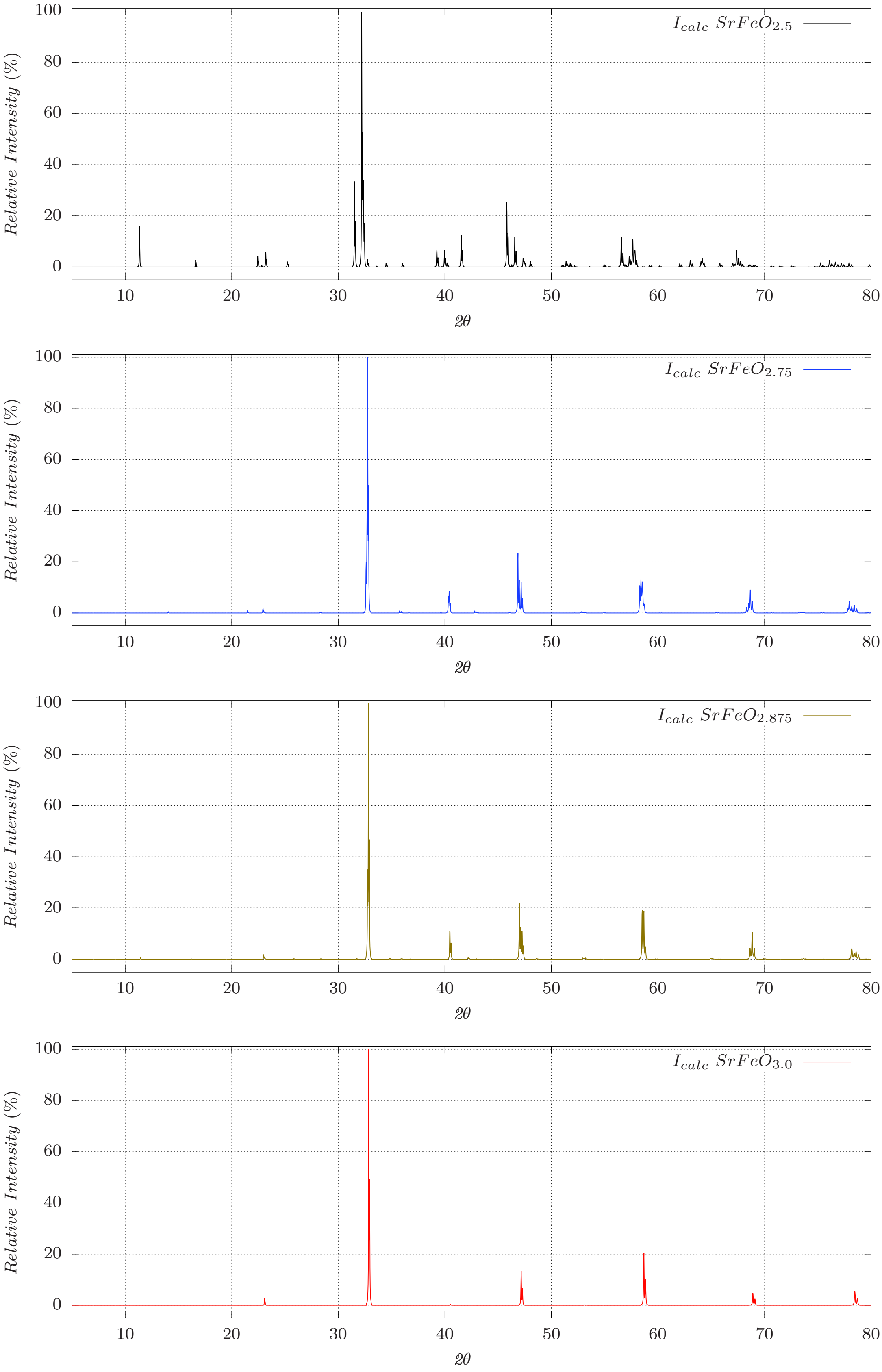

Figure 6.1: The simulated diffraction patterns for $SrFeO_{3-x}$ phases in the range ($5° \leq 2\theta \leq 80°$) with best possible instrument resolution assuming the FWHM to be 0.03° in 2θ. The intensity is plotted as relative to highest intensity of the corresponding phase in %.

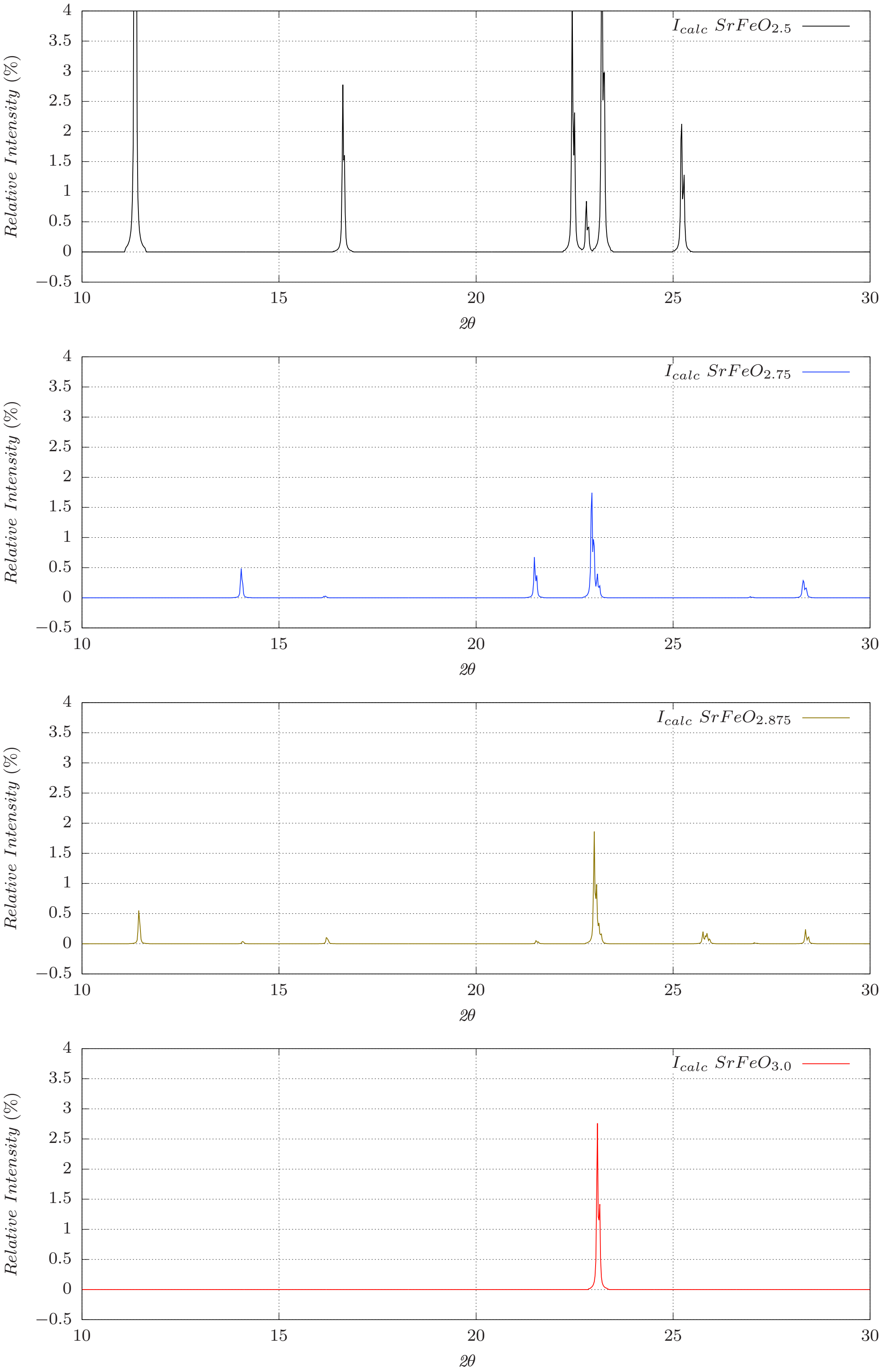

Figure 6.2: The simulated diffraction patterns for $SrFeO_{3-x}$ phases in the range ($10° \leq 2\theta \leq 30°$) with best possible instrument resolution assuming the FWHM to be 0.03° in 2θ. The intensity is plotted as relative to highest intensity of the corresponding phase in %.

Presuming that oxygen intercalation will follow through the formation of intermediate phases $SrFeO_{2.75}$ and $SrFeO_{2.875}$ as obtained in the high temperature synthesis one can in principle follow the oxygen intercalation on the polycrystalline sample by *in situ* X-ray powder diffraction. From the simulated powder X-ray diffraction patterns with best possible instrumental resolution available for the laboratory X-ray diffractometer (Cu K_α), the small but distinct differences in the patterns can be realized from the Fig. 6.1. The intermediate phases show presence of few but unique superstructure reflections representing the phases in the range $10° \leq 2\theta \leq 30°$ Fig. 6.2.

One must notice that the intensities of such weak superstructure reflection (related to the oxygen ordering) in the Fig. 6.2 is less that 1% of the highest intensities (related to the underlying Perovskite framework). Though the weak reflections are differentiable, the study by Nemudry *et al.*[21] was not able to distinguish the intermediate phases by X-ray powder diffraction (Cu K_α). The reflection profiles were too broad to distinctively identify the intermediate phases. As the shape of the reflection profile is mainly determined by the convolution of the instrumental resolution and the crystal mosaicity, the increase in the mosaicity on the course of oxygen intercalation essentially broaden the peak shape even with the best possible instrumental resolution. Nemudry *et al.* reported in the study[21], *' The high value of the line width full width at half-maximum (fwhm) and the compound in this range is in agreement with orthorhombic splitting of $SrFeO_{2.75}$ lattice, which can not be resolved, however, because of the imperfection of the crystal lattice of the intermediate and lower resolution of the Cu K_α radiation which has been used'* (see Fig. 6.3). The study was mainly relying on the observation of splitting or non-splitting appearance of the higher intense peaks in the range ($30° \leq 2\theta \leq 60°$) to identify the phases. But the unique signature of such phases depend on weak superstructure reflections as can be seen from the Fig. 6.2 in the range ($10° \leq 2\theta \leq 30°$).

Neutron diffraction is more sensitive to investigate oxygen ordering. In the thesis work of Tanguy Berthier[102], the oxygen intercalation on $SrFeO_{2.5}$ has been investigated by *in situ* neutron powder diffraction study. The study was also unable to resolve the intermediate phases. One has to also take into account the complexity in the neutron diffraction pattern due to the presence of magnetic intensity from different phases. In order to identify the intermediate phases, *in situ* synchrotron diffraction on the single crystal of $SrFeO_{2.5}$ seems to appear as most justified strategy because of high superstructure to main-structure reflection intensity ratio. Also the reflections are spatially separated in the reciprocal space which is important to distinguish reflections with same *d-value*. But single crystal comes with extreme complexity because of the presence of several twin individuals. The reflection from several twin domains overlaps and make the diffraction pattern very complex.

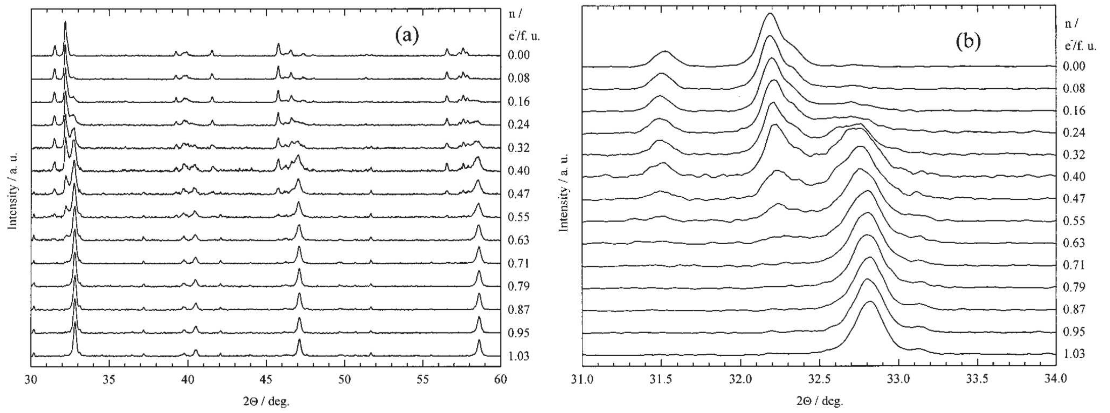

Figure 6.3: *In situ* measurement of the anodic oxidation of $SrFeO_{2.5}$: (a) X-ray patterns for selected charge-transfer values; (b) enlarged section showing the transition for the strongest reflection. **Reproduced from Nemudry *et al.*[21] Chem. Mater. 1998, 10, 2403-2411**

.

6.1 Data collection strategy

The EC oxidation of was performed on a 70 μm size almost single crystal of $SrFeO_{2.5}$ in a specially designed electrochemical cell as described in details in chapter 2. Diffraction was performed with a beam orientation perpendicular to the axis of the capillary using wavelength 0.7750 Å. For each rotation of 0.1° of the single crystal, the diffraction pattern was framed using the high resolution area detector Pilatus 2M. Each frame was collected with an exposure time of 0.3 s. In total 3600 frames were collected for 360° rotation in 18 min for each data set implying that the changes in the structure during the electrochemical reduction has been temporarily averaged over a time window of 18 min. The detail of the experimental setup for the for data collection on BM01A diffractometer at The European Synchrotron has been described in the chapter 2.

For electrochemistry 1N KOH was used. In principle the current required to reduce such micrometer size crystal in 3 days is about to $\sim$10 nA . But we noticed the sample starts reacting only after applying a current load of $\gtrsim$ 10 μA. This could be related to considerable amount of parasitic reactions. In that context the reaction is no longer galvanostatic where the oxygen content can be related to the electron transfer following the Eq. 6.1 but governed by its self controlled kinetics which does not correspond to the applied current once activated. Hence the reaction will be described in terms of the reaction time rather than the oxygen stoichiometry.

6.2 Methodology used for data analysis

The single crystal of $SrFeO_{2.5}$ used for EC had two orientation variants (b axis) along the pseudocubic a_p (V2) and b_p (V1) as explained in the Fig. 5.10 in chapter 5. Though the directions in the pseudocubic cell are arbitrary, for the sake of consistency of the discussion with the previous chapters, these particular directions of the variants will be followed throughout. For each variants two twin individuals were splitted along the pseudocubic c_p direction giving in total 4 individuals. The absence of the third variant was very helpful to investigate the evolution of phases and the reason will be elaborated shortly after.

Before proceeding to the details of the results obtained from the EC *in situ* investigation, it will be thoughtful and supportive to understand how the diffraction patterns should look like from simulation. We will first discuss the expected diffraction patterns for different phases taking only one variant (V1) into account and then we will extend the idea to two variants V1 and V2. For the sake of completeness of the discussion, we will also explain how the presence of all three variants V1, V2 and V3 would complicate the phase identification. All the patterns have been simulated with respect to the pseudocubic cell and in plane splitting corresponding to the variant has not been taken into account. From the distinctive appearance of the particular reflections corresponding to each phases, we can follow how the evolution of the phases occurs.

6.2.1 Expected diffraction patterns for one variant

All the principle diffraction patterns (*0kl*), (*h0l*) and (*hk0*) for all different phases are summarized in the Fig. 6.4. The reflection at $(0\,^1\!/_2\,0)_p$ in the (*0kl*) plane and (*h0l*) plane of the cubic cell as shown in Fig. 6.4(a) is very unique. This reflection is equivalent to (020) with *d–value* 7.79 Å in the Brownmillerite phase $SrFeO_{2.5}$ with lattice $a = \sqrt{2}a_p$, $b = 4b_p$, $c = \sqrt{2}c_p$ [5.527 Å, 15.59 Å, 5.672 Å]. From the presence of $(0\,^1\!/_2\,0)_p$ reflection representing the stacking axis of the Brownmillerite phase, it is obvious the variant is running along the b_p direction.

This particular reflection is absent for the orthorhombic phase $SrFeO_{2.75}$ with lattice $a = 2\sqrt{2}a_p$, $b = 2b_p$, $c = \sqrt{2}c_p$ [10.974 Å, 7.702 Å, 5.473 Å] provided the structure model proposed by Hodges *et al.*[89] in *Cmmm* space group is correct (see Fig. 6.4(b)). No reflection in this structure model is allowed with *d–value* of ~7.7 Å.

Reflections with similar *d–value* 7.698 Å are present in the tetragonal $SrFeO_{2.875}$ with the lattice $a = 2\sqrt{2}a_p$, $c = 2c_p$ [10.929 Å, 7.698 Å] in the structure model *I4/mmm*. This reflection corresponds to the (110) type reflection in the tetragonal cell. Provided

---

The subscript 'p' in $(hkl)_p$ indicates the indexation in pseudocubic cell.

that the variant (V1) in not altered on the course of the phase transformation, this (011) type reflection would appear in the $(00\frac{1}{2})_p$ reflection position in the (*0kl*) and (*h0l*) planes instead of the $(0\frac{1}{2}0)_p$ reflection positions as in the case of $SrFeO_{2.5}$ (compare Fig. 6.4(a) and (c)). In the final cubic phase $SrFeO_3$ no such $(0\frac{1}{2}0)_p$ type superstructure reflections are present, only the reflections from the Perovskite framework are present.

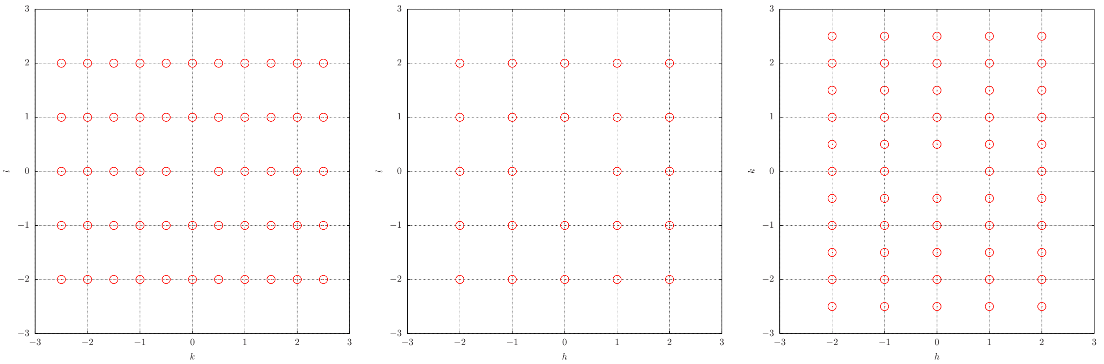

(a) *(0kl), (h0l)* and (*hk0*) planes for $SrFeO_{2.5}$.

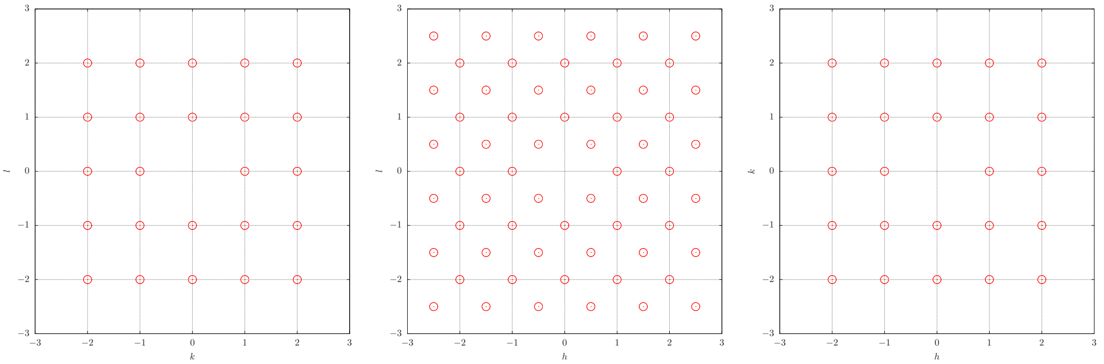

(b) *(0kl), (h0l)* and (*hk0*) planes for $SrFeO_{2.75}$.

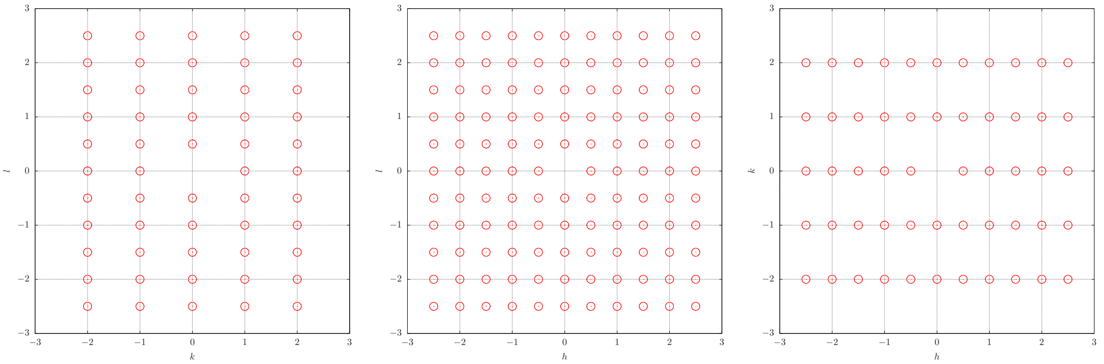

(c) *(0kl), (h0l)* and (*hk0*) planes for $SrFeO_{2.875}$.

Figure 6.4: Principle planes for $SrFeO_{3-x}$ phases with only **one variant** V2.

6.2.2 Expected diffraction patterns for two variants

The idea of the diffraction patterns for the presence of only one variant (V1) can be easily extended to the two variants (V1 & V2). For the presence of two variants running along the b_p (V1) and a_p (V2) of the pseudocubic cell, the diffraction patterns have been simulated and presented in the Fig. 6.5. As the single crystal used for EC oxygen intercalation have similar twin structure, these simulated patterns will help to understand how the patters are expected to evolve on the course of the reaction.

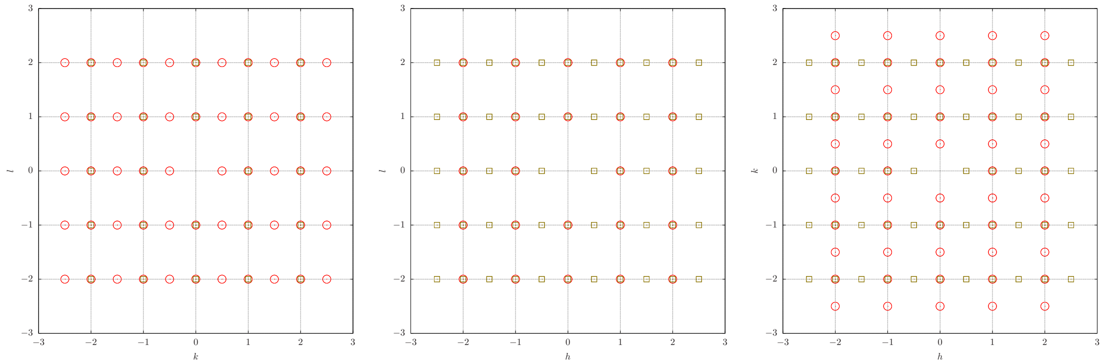

(a) *(0kl), (h0l)* and (*hk0*) planes for SrFeO$_{2.5}$.

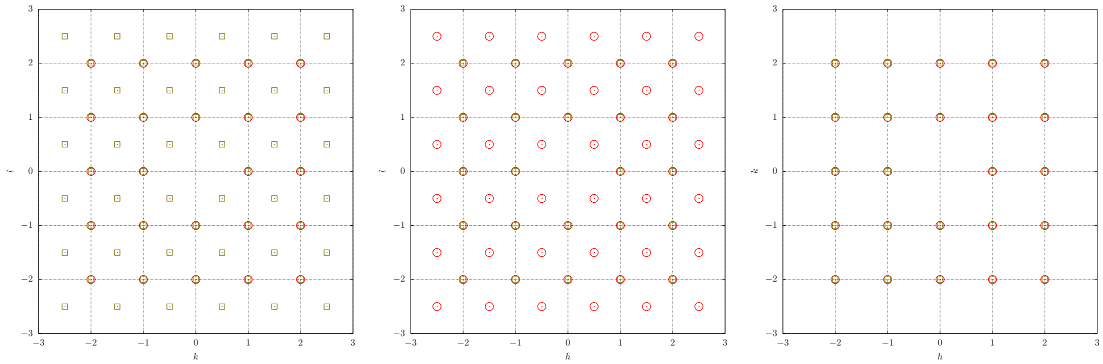

(b) *(0kl), (h0l)* and (*hk0*) planes for SrFeO$_{2.75}$.

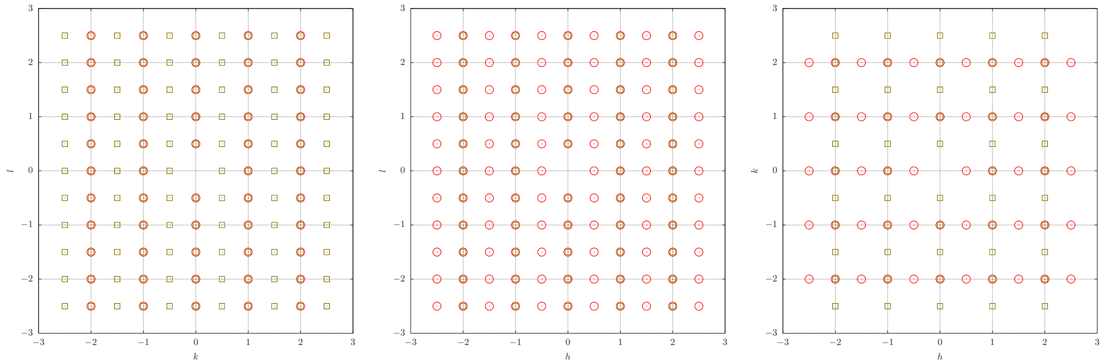

(c) *(0kl), (h0l)* and (*hk0*) planes for SrFeO$_{2.875}$.

Figure 6.5: Principle planes for SrFeO$_{3-x}$ phases with **two variants** V2 & V1. The reflections corresponding to V2 are in red circles and for V1 in olive squares.

The patterns become more populated with superstructure reflections and more complicated due to the overlapping from the contribution of two domains related to two variants (V1 & V2). Looking at the (*0kl*) and (*h0l*) plane in the Fig. 6.5(a), it is clear that the $(0\frac{1}{2}0)_p$ type reflections keep their unique identities and not affected by the overlapping of the reflections from the other variant. The presence of two variants can be realized by the presence of $(0\frac{1}{2}0)_p$ and $(\frac{1}{2}00)_p$ reflections in the (*hk0*) plane running along b_p and a_p respectively.

$SrFeO_{2.75}$ does not have any such $(0\frac{1}{2}0)_p$ type reflection as discussed earlier while they are present for $SrFeO_{2.875}$ phase in each of the principle planes (*hk0*), (*0kl*) and (*h0l*). Note that already with the presence of just two variants the (*hk0*) plane of $SrFeO_{2.5}$ and $SrFeO_{2.875}$ look exactly similar as can be realized compare Fig. 6.5(a) and (c). In the presence of more than one variant, choice of reciprocal planes to follow the evolution of phases is an important issue especially in the presence of the non-reacted residue from the primary phase of $SrFeO_{2.5}$ during EC oxygen intercalation.

In the presence of two variants V1 & V2, (*hk0*) plane is not preferable to follow the phase evolution assuming the residue from the primary phase will remains through out the reaction. Whereas (*0kl*) and (*h0l*) planes are much more convenient to follow the reaction. As the (*0kl*) plane in Fig. 6.5(a) does not contain any reflection at $(00\frac{1}{2})_p$ position, appearance of new reflection at $(00\frac{1}{2})_p$ will indicate the formation of $SrFeO_{2.875}$ (compare Fig. 6.5(a) and (c)). The presence of residue highly hinders the phase identification. For example, ideally on the course of oxidation from $SrFeO_{2.5}$ to $SrFeO_{2.75}$ the reflection at $(0\frac{1}{2}0)_p$ must vanish but in reality it may not be the case due to the presence of the residual phase. The formation of $SrFeO_{2.75}$ has to be justified from other perspective (*e.g.* orthorhombicity) which will be discussed later. The less is the number of variants the more it is convenient to distinctively identify the phases.

6.2.3 Expected diffraction patterns for three variants

The small differences in between the patterns corresponding to a particular phase, which can be still realized in the presence of two variants, almost vanishes in the presence of all three variants as shown in the Fig. 6.6. For the completeness of the discussion let us clarify the difficulty with the presence of all three variants. Assuming the presence of non-reacted residual phases in addition to the presence of all three variants V1, V2 and V3, the phase separation is almost impossible. Looking at the (*0kl*) planes in Fig. 6.6 one can realize that the newly grown $(0\frac{1}{2}\frac{1}{2})_p$ type reflections of $SrFeO_{2.75}$ on the top of the already present reflections from $SrFeO_{2.5}$ residual phase will already give a pattern which exactly corresponding to $SrFeO_{2.875}$. It might mislead one to overlook the formation of the phase $SrFeO_{2.75}$.

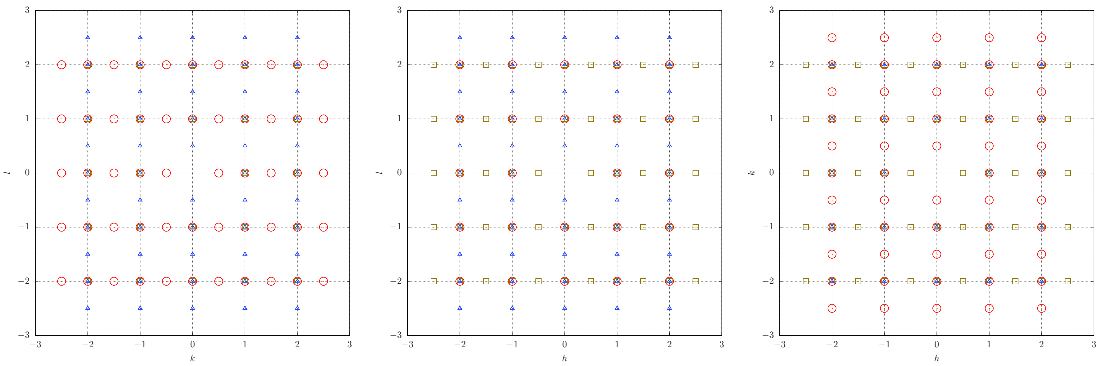

(a) *(0kl), (h0l)* and (*hk0*) planes for SrFeO$_{2.5}$.

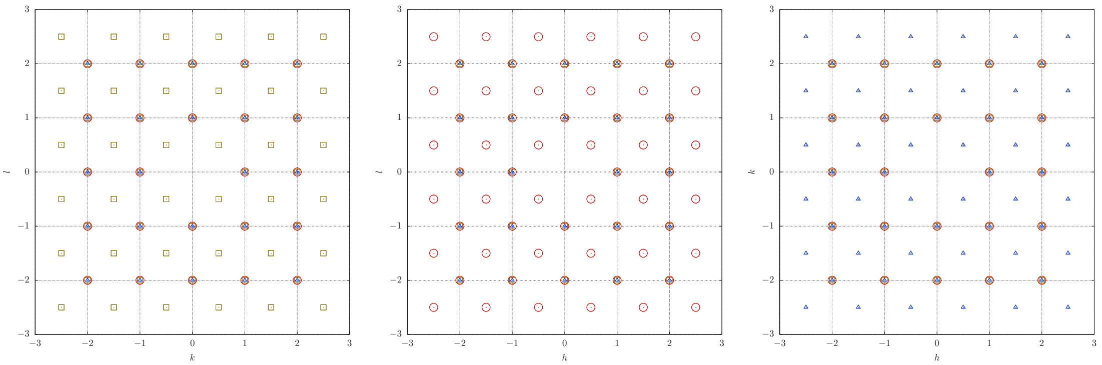

(b) *(0kl), (h0l)* and (*hk0*) planes for SrFeO$_{2.75}$.

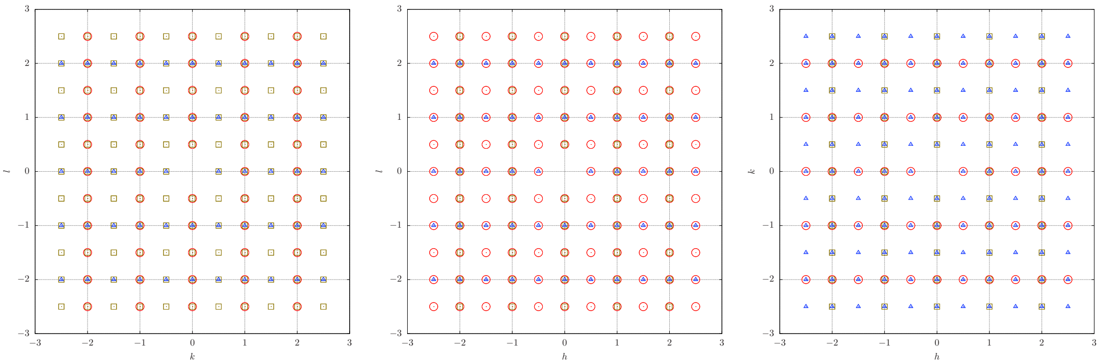

(c) *(0kl), (h0l)* and (*hk0*) planes for SrFeO$_{2.875}$.

Figure 6.6: Principle planes for SrFeO$_{3-x}$ phases with **three variants** V2, V1 & V3. The reflections corresponding to V2 are in red circles, for V1 in olive squares and for V3 in blue triangles.

At least in the present twin configuration with two twin variants V1 and V2 for the single crystal used in EC, identification of different phases are comparatively less difficult compared to the one with presence of all three variants. Although the presence of residual phases always provides a big obstacle. To make the phase identification more percipient in such case consideration of particular type of planes *e.g.* ($hk1/4$) is recommended. Direct observation of the ($hk1/4$) plane indicates for the present configuration of the two variants V1 & V2 (as in the present single crystal), this plane must not posses any reflections of $SrFeO_{2.5}$ where as $SrFeO_{2.75}$ and $SrFeO_{2.875}$ have reflections from both the variants. In the same time it is impossible to distinguish these two phases $SrFeO_{2.75}$ and $SrFeO_{2.875}$ as the patterns are exactly equivalent. So it is still difficult to differentiate the $SrFeO_{2.75}$ and $SrFeO_{2.875}$ by considering only $(hk\frac{1}{4})$ plane though $SrFeO_{2.5}$ can be identified.

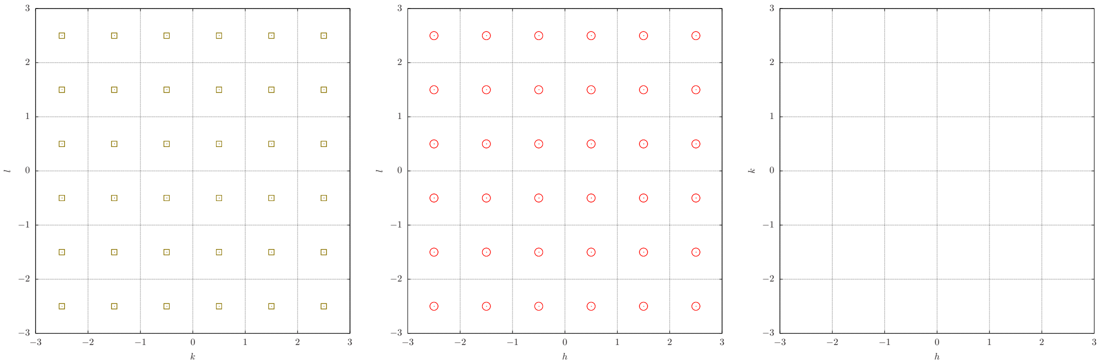

(a) $(\frac{1}{4}kl)$, $(h\frac{1}{4}l)$ and $(hk\frac{1}{4})$ planes for $SrFeO_{2.5}$.

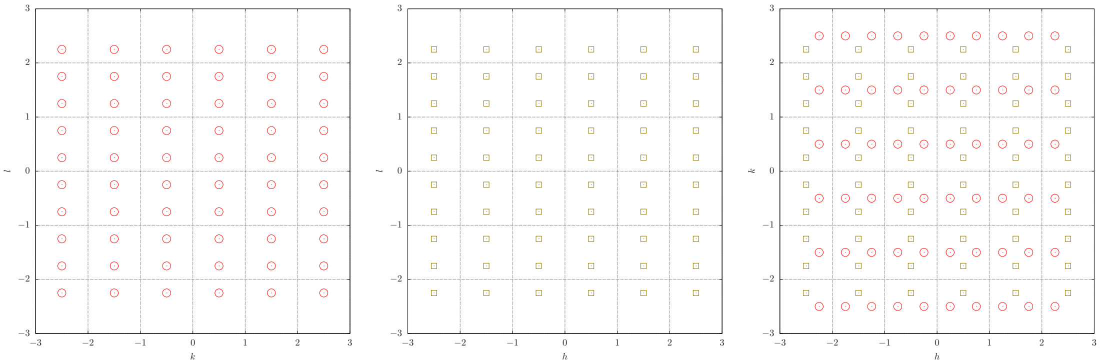

(b) $(\frac{1}{4}kl)$, $(h\frac{1}{4}l)$ and $(hk\frac{1}{4})$ planes for $SrFeO_{2.75}$.

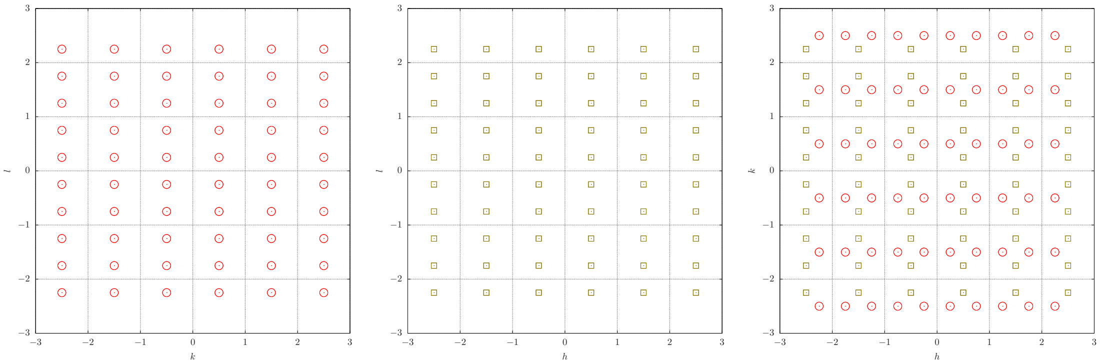

(c) $(\frac{1}{4}kl)$, $(h\frac{1}{4}l)$ and $(hk\frac{1}{4})$ planes for $SrFeO_{2.875}$.

Figure 6.7: $(hk\frac{1}{4})$-type planes for reconstructed in pseudo-cubic cell with for **two variants** V2 & V1. The reflections corresponding to V2 are in red circles and for V1 in olive squares.

A combined observation of the $(hk\frac{1}{4})$ type and $(hk0)$ type planes could help to resolve the difficulties in the present case of twin structure as described below. Though the $(hk\frac{1}{4})$ type planes are exactly similar with respect to the reflection positions for

$SrFeO_{2.75}$ and $SrFeO_{2.875}$, the difference can be seen in the (*hk0*) type planes. Specially looking at (*0kl*) in Fig. 6.5(b), the $SrFeO_{2.75}$ does not have any reflections $(0\frac{1}{2}0)_p$ corresponding to *d–value* of ~ 7.79 Å whereas $SrFeO_{2.875}$ have such reflections Fig. 6.5(c). It is very clear that particularly the $(0\frac{1}{2}0)_p$ reflection is very crucial to identify phases especially in this case of the present twin structure with 2 variants V1 & V2.

6.3 Results of the *in situ* EC oxygen intercalation

6.3.1 Structural evolution

The *in situ* diffraction data obtained during the EC oxygen intercalation was reconstructed in the pseudocubic cell. Fig. 6.8 summarises all essential changes occurring in the (*0kl*) planes in course of the EC oxidation of $SrFeO_{2.5}$ with a = 5.527(1) Å, b = 15.59(2) Å and c = 5.672(1) Å in the *Imma* space group. The choice of (*0kl*) plane was done on purpose to follow the evolution of the diffraction patterns. From the detailed discussion in the previous section, explaining how the diffraction patterns must evolve as shown by the simulated patterns, the very crucial role of $(0\frac{1}{2}0)_p$ type reflection has been pointed out. The single crystal of $SrFeO_{2.5}$, used for EC oxygen intercalation, had only two variants V1 & V2. The (*0kl*) diffraction pattern does not contain any $(00\frac{1}{2})_p$ reflection corresponding to the third variant (V3). As this reflection also belongs to the other phase $SrFeO_{2.875}$, the newly appearance of $(00\frac{1}{2})_p$ on the course of the reaction will help us to identify directly $SrFeO_{2.875}$. The selection of the (*0kl*) (equivalently (*h0l*) is particularly helpful in case the non-reactive residual phase of $SrFeO_{2.5}$ remains until the end of the EC, as discussed before. In the (*hk0*) plane the presence of both the $(0\frac{1}{2}0)_p$ and $(\frac{1}{2}00)_p$ hinders the new appearance of any such type of reflection from the newly grown phase in case there exists non-reacted $SrFeO_{2.5}$.

Fig. 6.8(a) represents the (*0kl*) plane of $SrFeO_{2.5}$ phase. The characteristic $(0\frac{1}{2}0)_p$ reflection represent one of the 2 variants along the pseudocubic b_p direction (V1). The $(001)_p$ reflection which is equivalent to (101) type reflections in the Brownmillerite phase show a splitting of around 3.1°. This splitting is related to the two twin individuals belonging to the variant running along pseudocubic b_p direction. The splitting can be calculated as from the slight difference between a = 5.527 Å and c = 5.672 Å using the Eq. 6.2 and it is in close match with the experimentally observed value 2.96°. The as appeared sharp reflections encircled in red are not reflections but diffuse rods passing as discussed in details in the Fig. 5.11 in chapter 5 and also shown in the Fig. 6.9(a).

$$2\Delta_{SFO_{2.5}} = 2[tan^{-1}(c/a) - tan^{-1}(a/c)] = 2.96° \qquad (6.2)$$

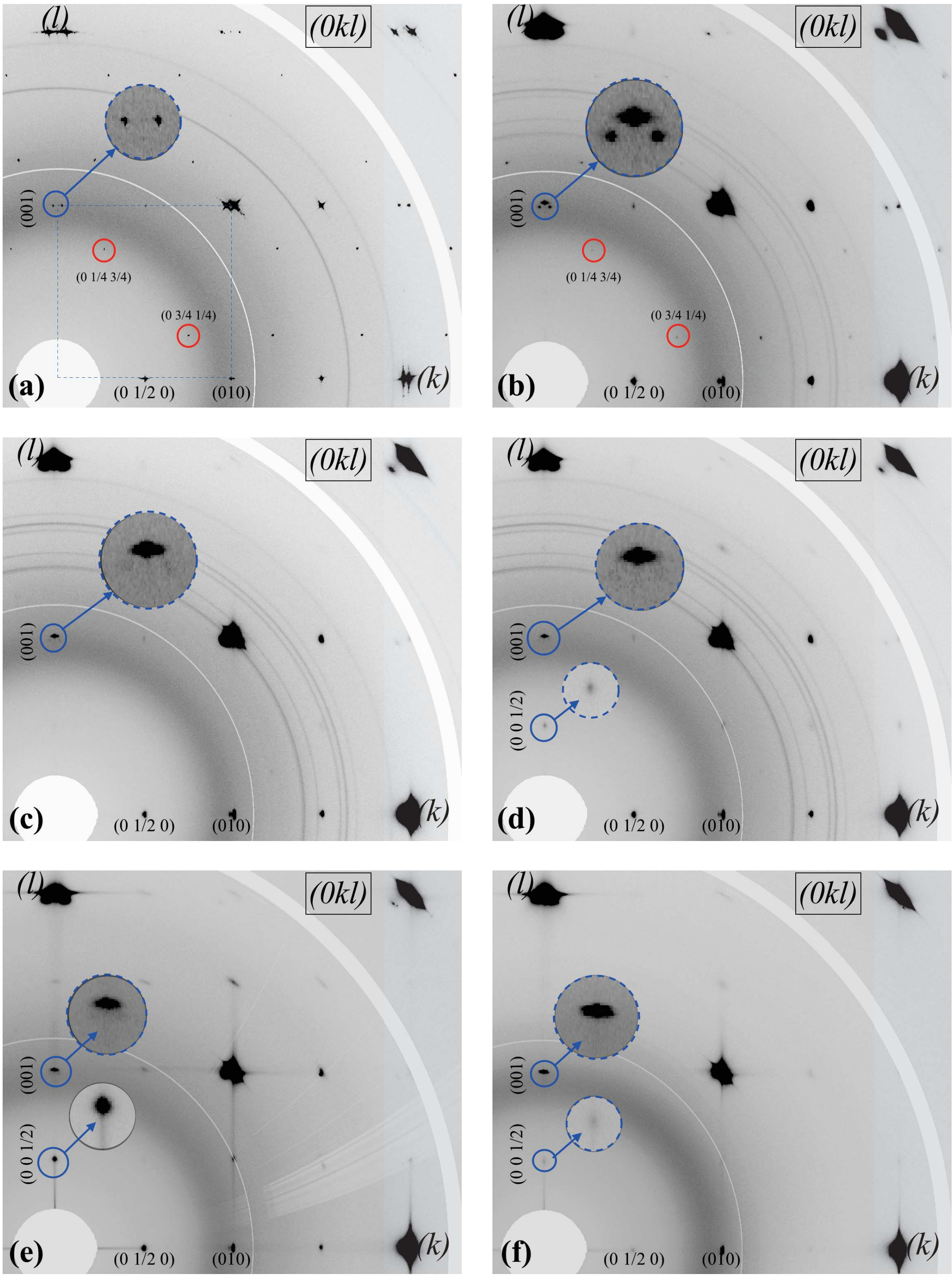

Figure 6.8: Evolution of the (*0kl*) plane during the electrochemical oxygen intercalation in $SrFeO_{2.5}$. Starting from (a) Brownmillerite $SrFeO_{2.5}$ to (f) cubic $SrFeO_3$ phase. The Perovskite unit cell is outlined to guide the diffraction patterns. The insert in (a) shows the (001) reflection of the Perovskite cell corresponding to the (101) type reflections of two twin individuals of the $SrFeO_{2.5}$. The insert in (b) shows the appearance of the new reflection belonging to $SrFeO_{2.75}$. The red circles point to the diffuse rods passing through plane. (e) shows the appearance of the new $(00{}^1/_2)_p$ reflection corresponding to (110) reflection of $SrFeO_{2.875}$. (f) represents the final cubic phase obtained where all the $(00{}^1/_2)_p$ type reflections disappear.

Fig. 6.8(b) represents the biphasic region in between $SrFeO_{2.5}$ and $SrFeO_{2.75}$. The appearance of the new phase $SrFeO_{2.75}$ with a = 10.974(1) Å, b = 7.702(1) Å and c = 5.473(1) Å can be realized from the insert in the Fig. 6.8(b). At the $(001)_p$ reflection position the appearance of the new reflection at slightly lower *d–value* corresponding, to the (201) type reflection of $SrFeO_{2.75}$ with a *d–value* 3.8749 Å, *i.e* less than the *d-value* of the (101) type reflection of $SrFeO_{2.5}$ with *d-value* 3.96 Å. Taking the effective lattice parameters $a_{eff} = {}^{10.974}/_{2} = 5.487$ Å and $c_{eff} = 5.473$ Å the expected twin splitting for $SrFeO_{2.75}$ related to the two twin individual belonging to the variant along a_p is 0.146° only very small. The splitting from the other 2 individuals for the variant along b_p is out of plane. It is noted that the intensity of the diffuse lines become weaker as shown in the Fig. 6.9(b).

$$2\Delta_{SFO_{2.75}} = 2(tan^{-1}({}^{c}/_{a_{eff}}) - tan^{-1}({}^{a_{eff}}/_{c})) = 0.146^{\circ} \tag{6.3}$$

Table 6.1: The intensity of the reflection in $SrFeO_{2.75}$ phase for the present two orientation variants represented by V1 and V2

(hkl)$_p$	*(hkl)*$_{SrFeO_{2.75}}$	*d–value*(Å)	*Relative Intensity(%)*
(001)	(201) (V1/V2)	3.8749 Å	1.97
(010)	(020) (V1)	3.8510 Å	0.35
	(201) (V2)	3.8749 Å	1.97
(0½½)	(001) (V2)	5.4730 Å	0.02
	(200) (V2)	5.4870 Å	0.02
(011)	(221)(V1)	2.7315 Å	100.00
	(002)(V2)	2.7365 Å	22.10
	(400)(V2)	2.7435 Å	21.40

Further oxidation leads to pure $SrFeO_{2.75}$ as presented in the Fig. 6.8(c), confirmed by the absence of the satellite reflections from the $SrFeO_{2.5}$ phase at $(001)_p$ reflection position in the pseudocubic cell and by the presence of (201) type reflections from $SrFeO_{2.75}$ phase only. However the disappearance of all Brownmillerite reflections is not fully complete, as one can still observe in Fig. 6.8(c) a small amount of Brownmillerite contributions such as the $(0½0)_p$ reflection while the presence of reflections with *d–value* 7.796 Å can be completely ruled out for $SrFeO_{2.75}$ in agreement with the fact that no corresponding *d–value* exist for this phase. As is obvious from the Fig. 6.9(c) the diffuse rods related to $SrFeO_{2.5}$ completely vanished as evidenced from the $(0¼¾)_p$ and $(0¾¼)_p$ reflection positions.

Looking at the Fig. 6.10 it becomes evident that the oxidation towards $SrFeO_{2.75}$ phase would require the rearrangement of half of the former octahedra and all tetrahedra of $SrFeO_{2.5}$. In such a case the integrity of the twin structure is conserved *i.e.* the 2

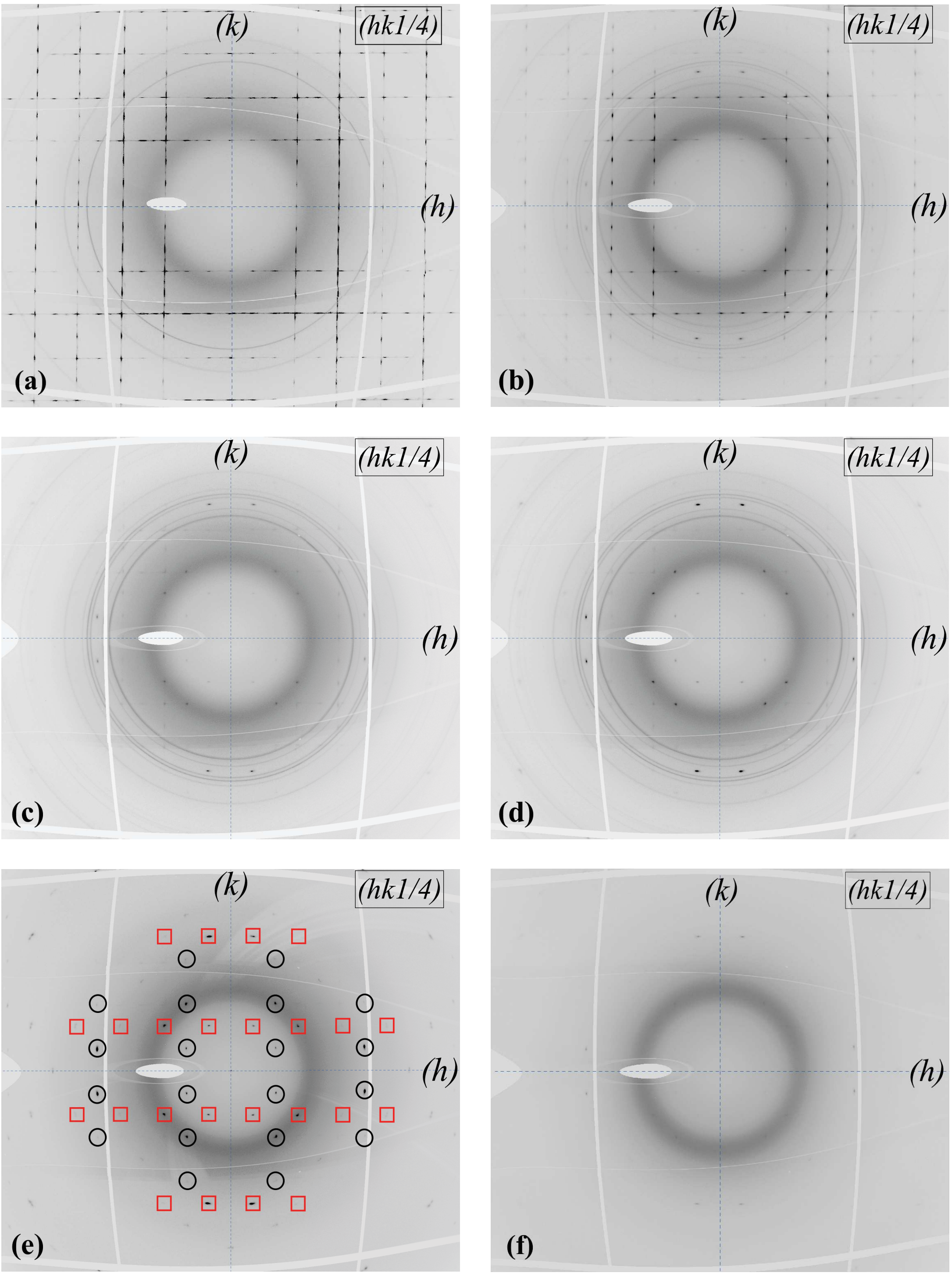

Figure 6.9: Evolution in the *(hk¼)* planes during the electrochemical oxygen intercalation in $SrFeO_{2.5}$ corresponding to the Fig. 6.8(a)-(f). Fig. 6.9(a) shows the only the diffuse rods related to $SrFeO_{2.5}$ which vanishes on the course of electrochemical oxygen intercalation towards $SrFeO_{2.75}$. Fig. 6.9(d) and (e) shows the newly grown reflections belonging to $SrFeO_{2.875}$ out of which only the encircled reflections in black can be indexed with the present twin scheme. The red squared reflections suggest the growth of the new variant along c_p. (f) belongs to the fully oxidised $SrFeO_3$ phase where all superstructure reflections in the $(hk^1/_4)$ plane vanish.

variants along pseudocubic a_p and b_p directions each having two twins totally giving 4 individuals remain. For such twin arrangement with 2 variants for $SrFeO_{2.75}$ one would expect the appearance of $(0\frac{1}{2}\frac{1}{2})_p$ type reflections as shown in the simulated pattern Fig. 6.5(b). These reflections are, however, almost invisible because of their very week intensity (0.02% of the strongest reflections) as given in Table. 6.1 and in addition the background of the quartz capillary used for the electrochemical cell is very high in this *d–value* range.

The oxidation of $SrFeO_{2.75}$ towards $SrFeO_{2.875}$ can be noticed from the growth of the $(00\frac{1}{2})_p$ reflection in the pseudocubic cell as shown in the Fig. 6.8(d) and Fig. 6.8(e). While the first one represents a biphasic region between $SrFeO_{2.75}$ and $SrFeO_{2.875}$, the later essentially represent pure $SrFeO_{2.875}$.

6.3.2 Microstructural evolution

The changes in the corresponding $(hk\frac{1}{4})_p$ plane in the course of the oxidation as shown in the Fig. 6.9(e) is remarkable. The plane shows the growth of new generated reflections during the transition to $SrFeO_{2.875}$ none of which were present at an earlier stage. Direct comparison with the simulated patterns in Fig. 6.7(c) for the present twin structure refers only half of the newly grown reflections can be indexed with the present twin structure as shown by the encircled reflections in black. The other half of the reflection with in the red square boxes can be only indexed if and only if a new variant grows along the pseudocubic c_p direction during the oxidation from $SrFeO_{2.75}$ towards $SrFeO_{2.875}$. The reason behind such 3D-microstructural evolution can be understood by structural relation of $SrFeO_{2.75}$ and $SrFeO_{2.875}$ as shown in the Fig. 6.11. Starting from $SrFeO_{2.75}$ selective filling up the oxygen in each next vacant sites give $SrFeO_{2.875}$ with a 3D-oxygen ordering with an isotropic arrangement of oxygen vacancies.

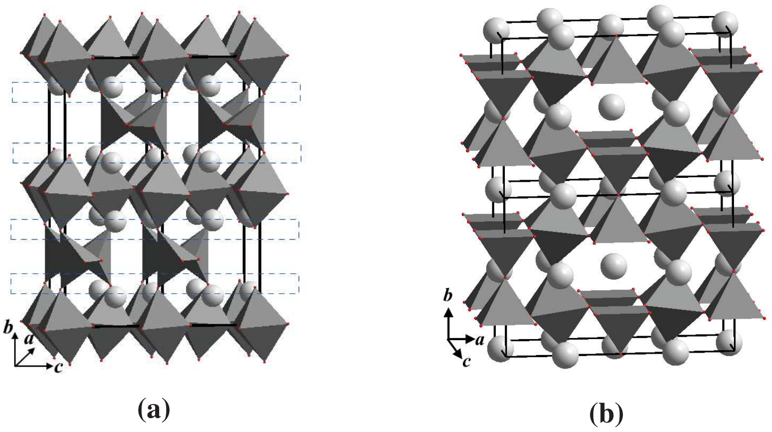

(a) **(b)**

Figure 6.10: (a) Representation of octahedra and tetrahedra in $SrFeO_{2.5}$ supercell with $2a \times b \times c$ (b) Representation of octahedra and square pyramid in $SrFeO_{2.75}$ supercell with $a \times 2b \times c$

The appearance of new diffuse intensities is noticeable in Fig. 6.8(e). These new diffuse rods run along $[010]_p/[001]_p$ direction around the $(011)_p$ and $(0\frac{1}{2}0)_p$ type reflections and reach quite low scattering angles, *i.e.* fairly high *d–value* for the latter one. This type of diffuse scattering might be attributed to a correlation of planar defects (*e.g.* twin boundaries) which is probably related to the change in the twin structure by the appearance of the new variants upon oxidation from $SrFeO_{2.75}$ to $SrFeO_{2.875}$. The uniform distribution of equivalent reflections in $SrFeO_{2.875}$ as will be discussed in more details afterwards might be taken as a hint to assume the presence of micro twinning. The small domain size for the different twin individuals together with an associated correlation length problem might be responsible for the formation of the diffuse streaks.

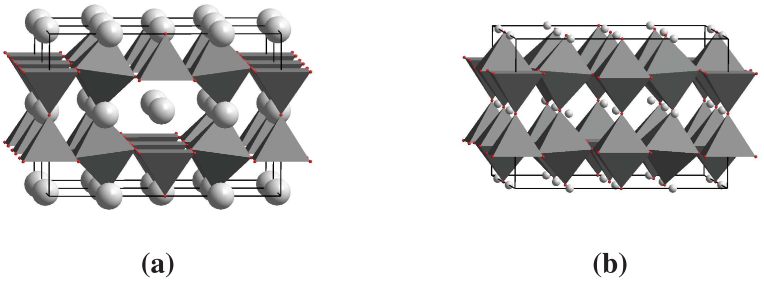
(a) (b)

Figure 6.11: (a) Representation of octahedra and square pyramid in $SrFeO_{2.75}$ supercell with $a \times b \times 2c$ (b) Representation of octahedra and square pyramid in $SrFeO_{2.875}$

The contribution from all three domains can be followed in Fig. 6.12 by comparing all three equivalent $(hk\frac{1}{4})_p$ type planes. The reflections are indexed in the tetragonal cell of $SrFeO_{2.875}$ and the variants (*c* axis in the case of $SrFeO_{2.875}$) contributing them are indicated by I(V1), II (V2) and III (V3). For guidelines simulated patterns are presented corresponding to each planes. While the red circles (V1) and olive squares (V2) represent the reflections from the already present variants, the blue triangles represent the reflection from the new variant (V3).

The yellow circles in $(\frac{1}{4}kl)_p$, $(h\frac{1}{4}l)_p$ planes correspond to Brownmillerite reflections which did not completely disappear during the reaction and which can be indexed as (011)/(110) type with a *d–value* of 5.19 Å in the Brownmillerite unit cell. The absence of these contributions in $(hk\frac{1}{4})_p$ plane can be explained by the fact that the domain III related to the new variant was absent in the starting phase. Note that the symmetry is not *4–fold* because the zone axes of these planes correspond to the [110] type directions of the tetragonal $SrFeO_{2.875}$ phase instead of [001] direction. The reflections are related by *2/m* symmetry as can be easily understood from the simulated patterns from different colored reflections. The intensity appearing in the center of each planes is not a real reflection but it is the cross section of the diffuse lines passing through this planes as can be seen from the (*0kl*) plane in Fig. 6.8(e).

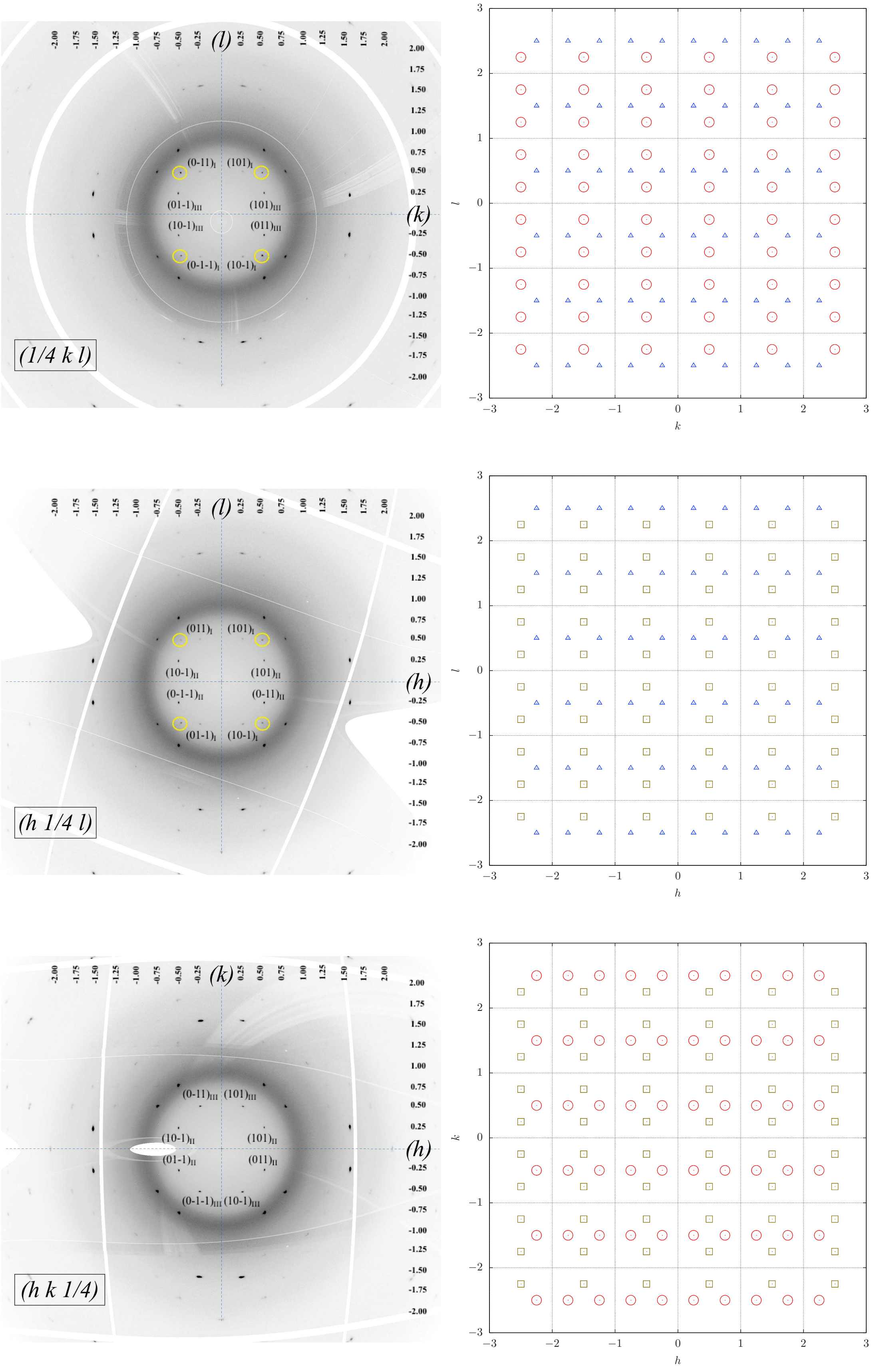

Figure 6.12: *(¼kl)* (top), *(h¼l)* (middle) and *(hk¼)* (bottom) planes reconstructed (left) and simulated (right). The reflections encircled in yellow are contributed from residual SrFeO$_{2.5}$.

6.3.3 Evolution of the volume fractions of different phases

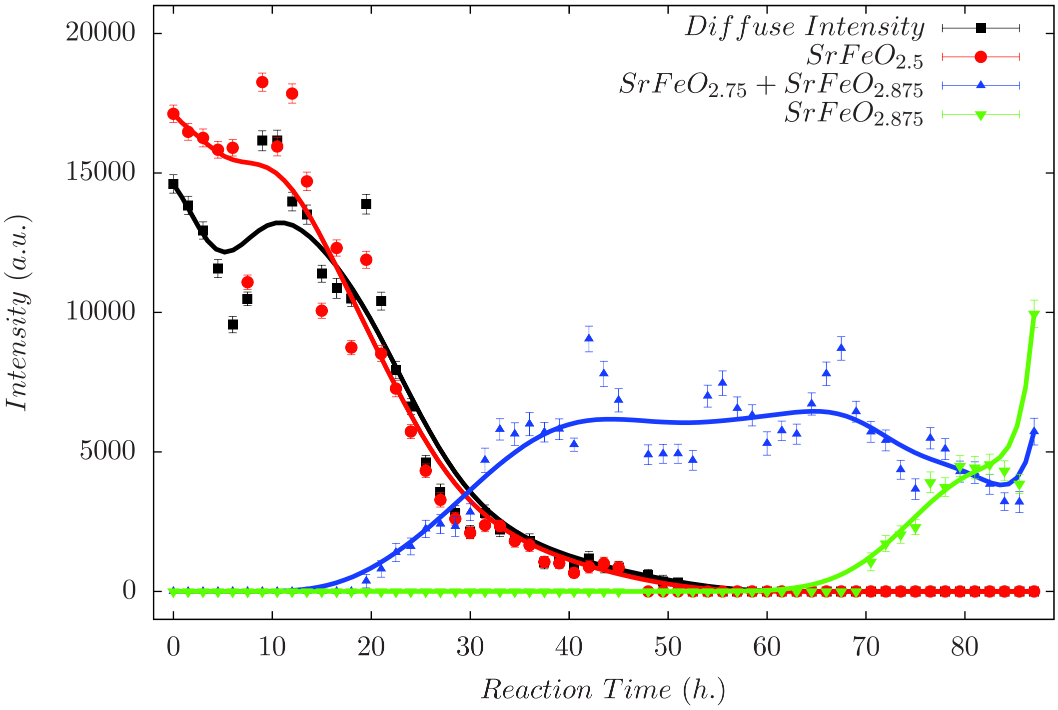

Figure 6.13: Evolution of the fractions of the different phases with time.

Fig. 6.13 gives the intensity evolution of different reflections representing the volume fractions related to the specific phases encountered in course of the EC oxidation of $SrFeO_{2.5}$. The intensity of the diffuse rods present in $SrFeO_{2.5}$ decrease in the same way as the regular (101) type satellite reflections of the Brownmillerite phase at $(001)_p$ reflection position. Simultaneously the new $SrFeO_{2.75}$ phase grows and can be identified from the new (201) type reflection of the orthorhombic $SrFeO_{2.75}$ at $(001)_p$ reflection position as shown in Fig. 6.8(b). The present twin structure with two variants was very helpful as the growth of $SrFeO_{2.875}$ from $SrFeO_{2.75}$ was indicated by the newly grown reflection at $(00\frac{1}{2})_p$. The phase evolution as summarized in Fig. 6.13 represent the phase sequence of $SrFeO_{2.5} \rightarrow SrFeO_{2.75} \rightarrow SrFeO_{2.875} \rightarrow$ final cubic phase. The fact that the $(001)_p$ reflection of $SrFeO_{2.75}$ does not go down to zero is related to the fact that the contribution from $SrFeO_{2.875}$ is undiscernibly overlaid. For both intermediate phases $SrFeO_{2.75}$ and $SrFeO_{2.875}$, the corresponding superstructure reflections have been found as expected from the structural models reported in study by Hodges *et al.*[89]. This shows that complex oxygen ordering is possible in solid oxides already at ambient temperature.

6.4 Summary

In this chapter we discussed the electrochemical oxygen intercalation reaction into $SrFeO_{2.5}$ by *in situ* synchrotron diffraction on a single crystal, in a specially designed electrochemical cell. While this type of study carried out on polycrystalline samples has become a matter of routine, it is still a novelty when using single crystals. To the best of our knowledge this is the first case where a complete solid-state reaction has been investigated to obtain 3D diffraction data obtained under i*n situ* conditions. We have successfully demonstrated the feasibility of these types of experiments on single crystals and also investigated microstructural aspects which almost impossible to obtain from powder diffraction methods. An important factor in the success of this experiment is the high performance diffractometer on BM01A at ESRF in terms of its primary beam quality and essentially the fast readout time of the quasi zero-noise detector.

The strongly enhanced sensitivity as can be obtained from this high resolution detectors for weak superstructure reflections helped for the reflection separation, *e.g.* for twin domains. We could consequently confirm that long range oxygen ordering is established during the electrochemical oxygen intercalation reaction already at ambient temperature for the two reaction intermediates $SrFeO_{2.75}$ and $SrFeO_{2.875}$. Also the analysis of the evolution of twin domain structure evidenced a topotactic reaction mechanism from $SrFeO_{2.5}$ to $SrFeO_{2.75}$, while the subsequent transition to $SrFeO_{2.875}$ yields surprisingly to a substantial modification of the microstructure, growing a third twin domain orientation along $[001]_p$, which was absent before.

Chapter 7

Temperature dependent phase transition of $SrFeO_{2.5}$ in air atmosphere

$SrFeO_{2.5}$ is promising material for oxygen conducting membrane. It can take up spontaneously oxygen already below 300 $°C$. Complementary to the EC oxygen intercalation, as described in chapter 6, we were interested to study this fast oxygen uptake reaction *in situ* on the single crystal of $SrFeO_{2.5}$, in order to follow up the associated phase sequence. This needs fast data collection which is available at the Synchrotron with the advantage of high brilliance source and high resolution area detectors. Also we wanted to compare the possible defect structure as observed with EC at RT. The single crystal diffraction was performed on the diffractometer of BM01A at ESRF which was perfectly suitable to investigate the structural changes associated with such fast reaction. We have also performed thermogravitometric analysis (TGA) in order to correlate the oxygen stoichiometry with the structural changes.

7.1 Data collection strategy

The *in situ* temperature study in air was followed up on a cylindrical shaped $SrFeO_{2.5}$ single crystal of diameter ~ 100μm from the same batch of single crystal used for EC oxygen intercalation as described in chapter 6. The single crystal was mounted on the goniometer of BM01A diffractometer at ESRF. The sample was hold inside an open ended quartz capillary of 300 μm inner diameter, supported by two other quartz capillaries of 100 μm inner diameter from two open sides as shown in the Fig. 7.1 making sure that the air can pass through. The sample was heated with a nitrogen stream focussed locally on the sample from room temperature 30 °C to 360 °C with a temperature ramp of 5 °C/min upto 230 °C and from this temperature relatively slowly with 0.5 °C/min upto 360 °C.

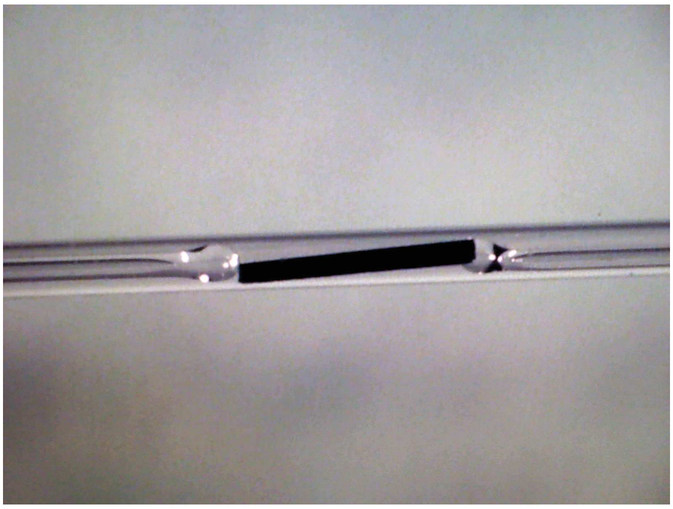

Figure 7.1: Cylindrical shaped single crystal of $SrFeO_{2.5}$ of ~100 μm in diameter inside a 300 μm quartz capillary supported by other two quartz capillaries from the two ends. The choice of such cylindrical shaped crystal was preferential for absorption related problems.

The diffraction was performed on BM01A diffractometer at ESRF with a beam orientation perpendicular to the axis of the cylindrical crystal using a wavelength of $\lambda = 0.7750$ Å. For each rotation of 0.1° of the single crystal along its axis, the diffraction pattern was collected using the high resolution Pilatus 2M area detector. In total 1800 frames were collected for 180° rotation in 9 minutes for each data set implying that the changes in the structure during the heating has been temporarily averaged over a time window of 9 min. In order to correlate the oxygen stoichiometry with temperature, TGA was performed on a thin disk like single crystal of $SrFeO_{2.5}$ in air atmosphere (20% O_2 : 80% N_2) using a PerkinElmer TGA-8000 (precession on sample weight ≈ 0.1 μg).

7.2 Results of the T-dependent *in situ* investigation

Figs. 7.2 & 7.3 represent the diffraction patterns of SrFeO$_{2.5}$ single crystal obtained at room temperature. All the reciprocal planes are indexed with respect to the pseudocubic cell [$a_p = 3.85$ Å] as discussed in the earlier chapters. The twin structure (microstructure) of the present single crystal was found to be exactly the same as the one used for EC (see Fig. 5.10 in chapter 5) and has been described in short as follows.

The presence of $(0\,{}^1\!/\!_2\,0)_p$ type reflections are most crucial to determine the orientation of the *b* axis (variant) of SrFeO$_{2.5}$ [$a = \sqrt{2}a_p = 5.527$ Å, $b = 4 \times a_p = 15.59$ Å, $c = \sqrt{2}a_p = 5.672$ Å] with in the psedocubic supercell [$4a_p \times 4a_p \times 4a_p$]. The presence of $(0\,{}^1\!/\!_2\,0)_p$ and $({}^1\!/\!_2\,00)_p$ reflections in the (*0kl*) and (*h0l*) plane indicates the two variants running along the pseudocubic b_p (variant: V1) and a_p (variant: V2) directions respectively. The presence of both variants can be evidenced in the (*hk0*) plane from the appearance of $(0\,{}^1\!/\!_2\,0)_p$ and $({}^1\!/\!_2\,00)_p$ reflections.

Each of the (*00l*) type reflections in the (*0kl*) and (*h0l*) planes splits in plane into two which are related to the two twin individuals corresponding to each variants. The splitting of the (001) reflection in the (*0kl*) plane is related to the two twins belonging to the variant: V2 along the a_p direction and similarly the splitting of the corresponding reflection in the (*h0l*) plane represents two twins belonging to the variant: V1 along b_p. The splitting corresponding to theses two variants occurs in perpendicular to each other. In total the splitting related to the two sets of two individuals can be visualized from the (002) reflection in the center of the (*hk2*) plane in Fig. 7.3. It gives a comparable situation with the crystal used for EC.

The only difference in the present crystal was the higher mosaicity as can be realized by comparing the relatively broad $(0\,{}^1\!/\!_2\,0)_p$ type reflections. Please notice that the intensity appearing in between the two splitted reflections at (001) in (*h0l*) plane in Fig. 7.2, is attributed to the tails of the other two splitted reflections perpendicular to this plane at the same *d–values* of 3.898 Å, related to the the increased mosaicity.

The subscript '*p*' in $(hkl)_p$ indicates the indexation in pseudocubic cell.

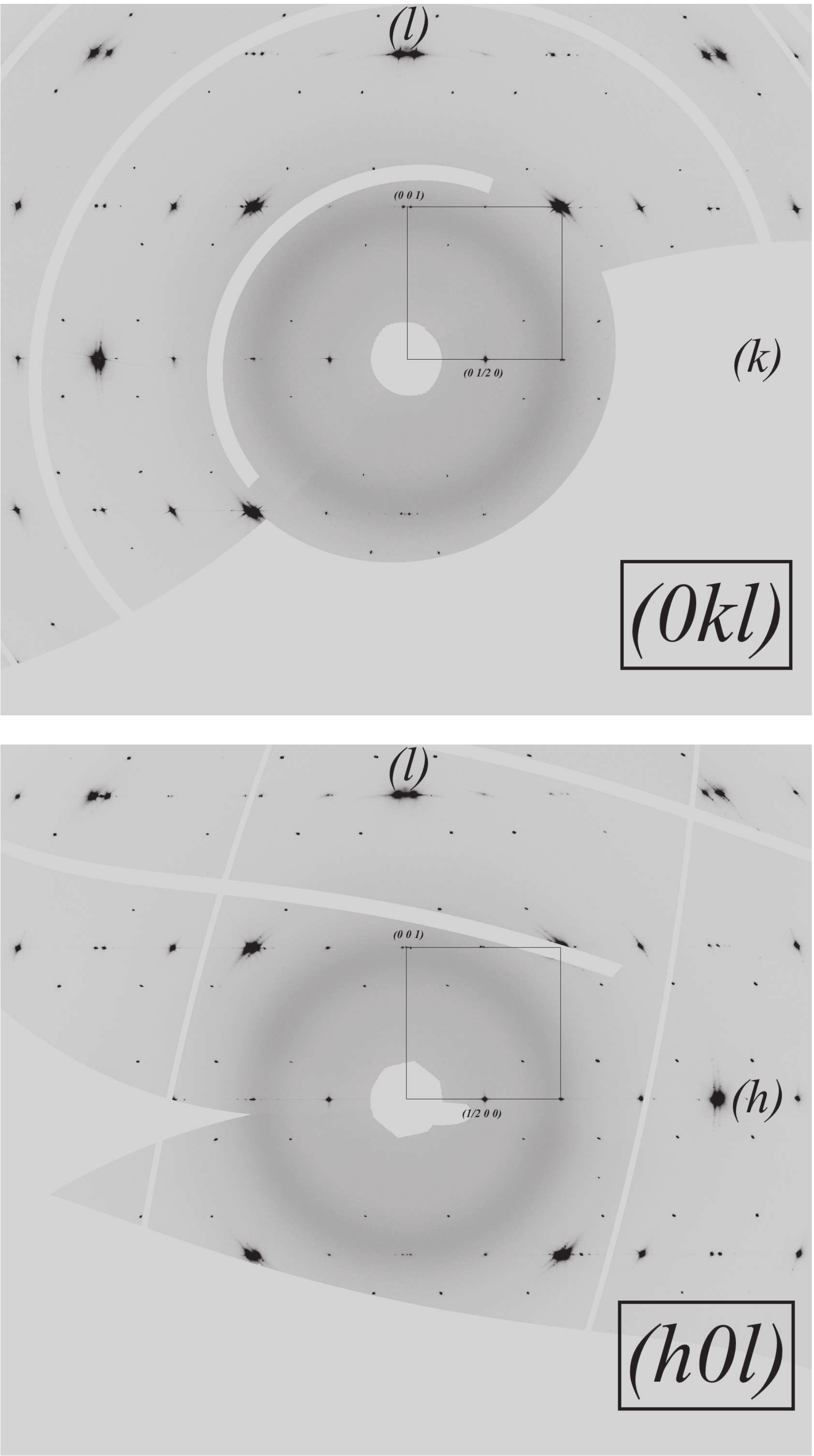

Figure 7.2: Reconstructed reciprocal planes (*0kl*) and (*h0l*) in the pseudocubic cell from the diffraction data obtained on the single crystal of $SrFeO_{2.5}$ at room temperature. The pseudocubic cell has been marked with the black square.

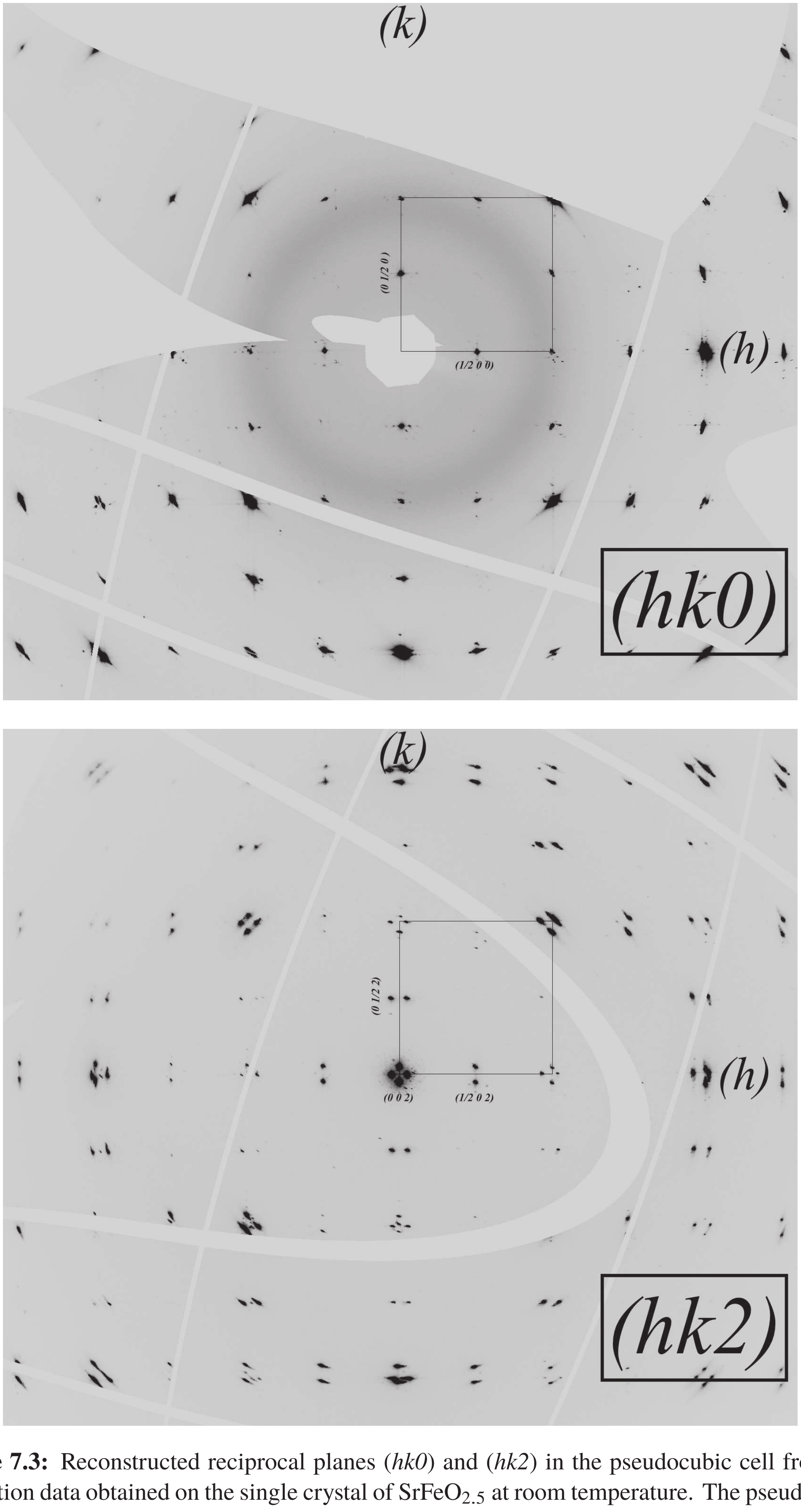

Figure 7.3: Reconstructed reciprocal planes (*hk0*) and (*hk2*) in the pseudocubic cell from the diffraction data obtained on the single crystal of $SrFeO_{2.5}$ at room temperature. The pseudocubic cell has been marked with the black square.

7.2.1 Structural evolution during heating in air

The structural evolution during the heating in air was investigated by *in situ* synchrotron diffraction on BM01A. Fig. 7.4 and Fig. 7.5 summarize all the essential changes occurring during the increase of temperature in air. The presence of only 2 out of 3 maximum possible variants was highly beneficial as mentioned also in chapter 6. In particular, the (*0kl*) or (*h0l*) planes (reconstructed in the pseudocubic cell) are ideally suited to follow up the changes in the structure because of the absence of $(00\frac{1}{2})_p$ reflection. Since this reflection also belongs to the tetragonal SrFeO$_{2.875}$ in *I4/mmm* (but forbidden in SrFe$_{2.75}$ in *Cmmm*), it can serve as a key reflection to evidence the formation of the tetragonal SrFeO$_{2.875}$ phase directly. The formation of SrFeO$_{2.75}$ can be identified from the appearance of $(001)_p$ reflection with almost no splitting (less orthorhombicity) at slightly lower *d–value* while $(00\frac{1}{2})_p$ reflection stays absent, due to systematic extinction.

Some important informations useful for this discussion:

SrFeO$_{2.5}$:: $a = \sqrt{2}a_p = 5.527$ Å, $b = 4 \times a_p = 15.59$ Å, $c = \sqrt{2}a_p = 5.672$ Å; s.g. *Imma*
SrFeO$_{2.875}$:: $a = b = 2\sqrt{2}a_p = 10.974$ Å, $c = 2 \times a_p$=7.698 Å, s.g. *I4/mmm*.
SrFeO$_{2.75}$:: $a = 2\sqrt{2}a_p = 10.974(1)$ Å, $b = 2 \times a_p = 7.702(1)$ Å, $c = \sqrt{2}a_p = 5.473(1)$ Å; s.g. *Cmmm*.
$(00\frac{1}{2})_p \Rightarrow$ (020) type in SrFeO$_{2.5}$; (110) type in SrFeO$_{2.875}$; forbidden in SrFeO$_{2.75}$
$(001)_p \Rightarrow$ (040)/(101) type in SrFeO$_{2.5}$; (220) type in SrFeO$_{2.875}$; (201) type in SrFeO$_{2.75}$

Figs. 7.4(a)(b)–7.5(c)(d) represent the (*0kl*) diffraction patterns at four different temperatures **T = 30 °C, 280 °C, 310 °C and 325 °C** respectively where the system pass through different structural changes. The diffraction patterns are reconstructed in the pseudocubic cell. At room temperature T = 30 °C the (*0kl*) diffraction pattern has been already discussed in the previous section. The insert in blue in Fig. 7.4(a) show the splitting related to two twin domains with common variant along a_p(V2). The splitting of the $(100)_p$ reflection, which is equivalent to (101) type reflection in the Browmillerite phase, was measured to be around 3 ° as expected from the orthorhombicity in SrFeO$_{2.5}$. Also we note that the intensities at $(0\frac{3}{4}\frac{1}{4})_p$ type reflection positions are not related to any reflections from this phase but corresponds to the cross section of diffuse rods passing through the (*0kl*) plane (see Fig. 5.11 in chapter 5). All the reflections can be indexed in the Brownmillerite phase with the cell parameters $\sqrt{2}a_p = 5.527$ Å, $4 \times a_p = 15.59$ Å, $\sqrt{2}a_p = 5.672$ Å in the *Imma* structure model with 4 twin individuals.

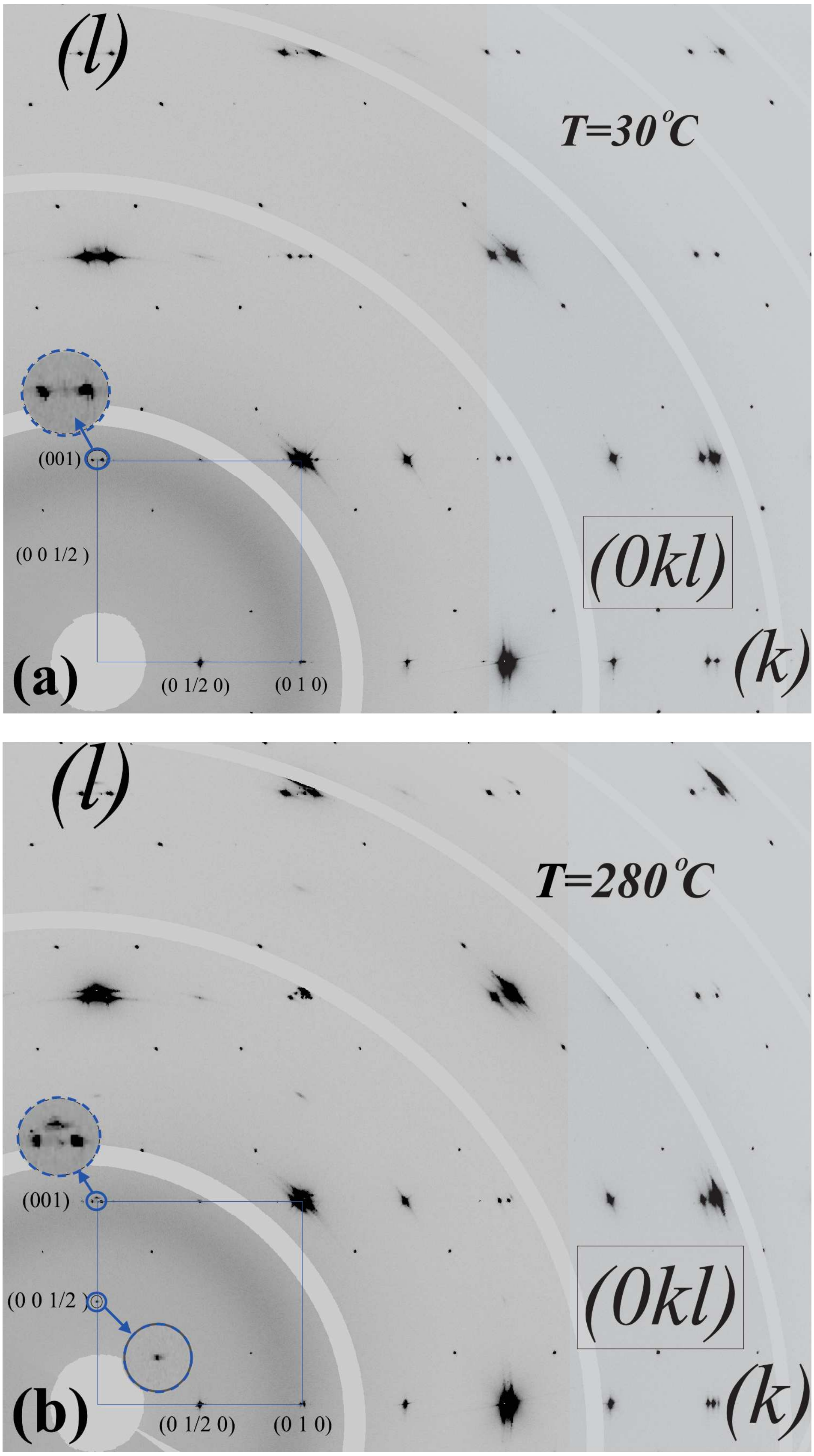

Figure 7.4: Evolution of the (*0kl*) plane during heating of $SrFeO_{2.5}$ single crystal in air. (a) at 30 °C (b) 280 °C. The pseudocubic cell is outlined in the blue square.

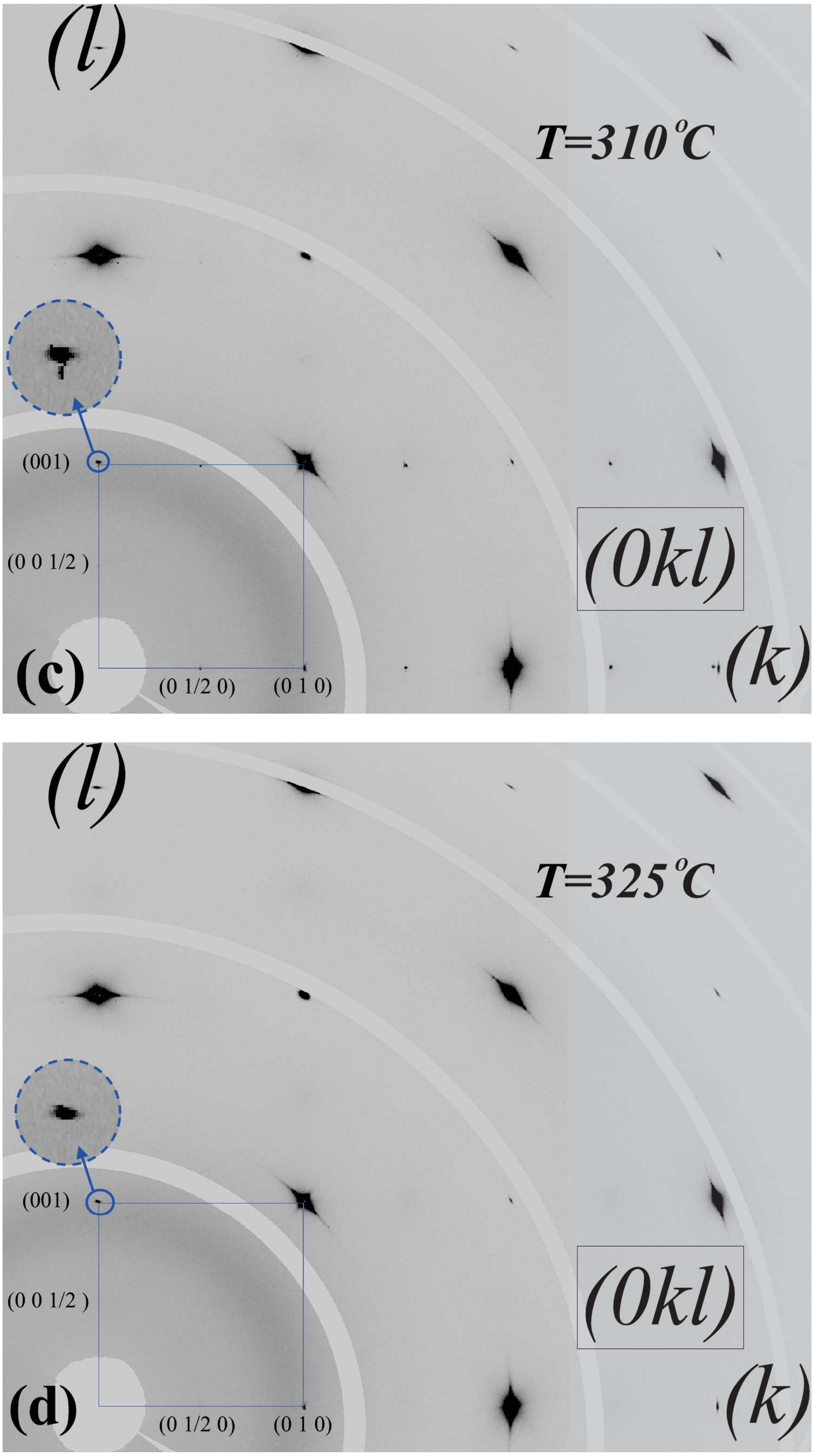

Figure 7.5: Evolution of the (*0kl*) plane during heating of $SrFeO_{2.5}$ single crystal in air (c) at 310 °C and (d) 325 °C. The pseudocubic cell is outlined in the blue square.

With the raise of temperature to T = 280 °C new reflections start appearing in the (*0kl*) plane corresponding to the new phases, *e.g.* at $(001)_p$ and $(00{}^{1}/_{2})_p$ positions as shown by the inserts in blue in Fig. 7.4(b). While the newly appeared $(001)_p$ reflection in the (*0kl*) plane can belong to both $SrFeO_{2.75}$ and $SrFeO_{2.875}$, $(00{}^{1}/_{2})_p$ can only belong to $SrFeO_{2.875}$ as it is systematically forbidden in $SrFeO_{2.75}$.

In this regard, it was quite important to follow the appearance of these two reflections in order to understand the phase sequence of the reaction. While the appearance of the $(001)_p$ reflection, and subsequently followed by $(00{}^{1}/_{2})_p$ would suggest a phase sequence of $SrFeO_{2.5} \rightarrow SrFeO_{2.75} \rightarrow SrFeO_{2.875}$, a simultaneous appearance of both reflections would suggest a sequence of $SrFeO_{2.5} \rightarrow SrFeO_{2.875}$ without passing through the intermediate phase $SrFeO_{2.75}$.

The integrated intensities of these two reflections followed over the whole temperature range are shown in the Fig. 7.6. The intensity has been integrated over a fixed reciprocal volume (fixed number of voxels) using SNBL ToolBox[24](in-house-developed software package of BM01A, ESRF).

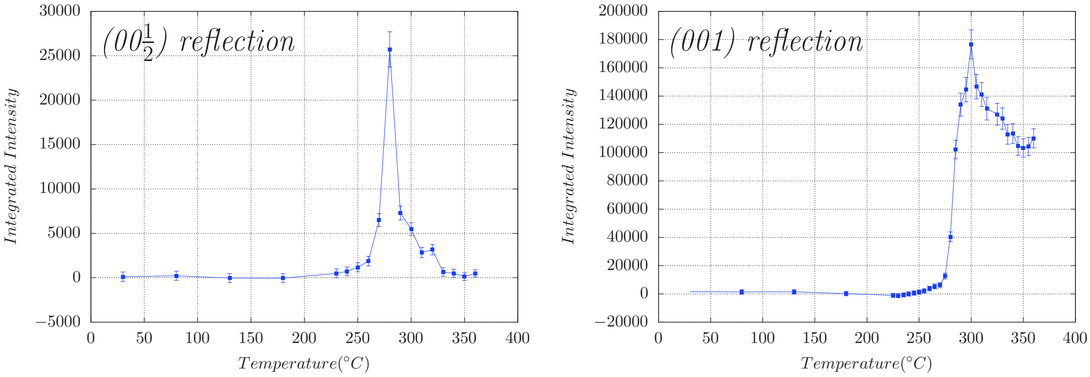

(a) **(b)**

Figure 7.6: Integrated intensity followed on the newly grown (a) $(00{}^{1}/_{2})_p$ reflection and (b) $(001)_p$ reflection in the temperature range 35 °C – 360 °C.

As can be seen from the Fig. 7.6(a) and (b) respectively the intensities of $(00{}^{1}/_{2})_p$ and $(001)_p$ reflections start growing simultaneously above T = 260 °C and peaking to the maximum very fast around T = 275 °C. The simultaneous appearance of both the reflections indicates the direct transition from $SrFeO_{2.5}$ to $SrFeO_{2.875}$ without formation of the orthorhombic intermediate phase $SrFeO_{2.75}$. $SrFeO_{2.875}$ was formed in a very narrow temperature range (260 °C – 275 °C) (in less than 30 min with the temperature ramp provided). To characterize such phase transition associated with fast reaction kinetics, while relying on the superstructure intensities, synchrotron diffraction with fast detector was the only possible choice.

The formation of SrFeO$_{2.875}$ was very difficult to identify from the other two equivalent reflection position i.e. $(0\tfrac{1}{2}0)_p$ and $(\tfrac{1}{2}00)_p$ as can be realized from the Fig. 7.5(a) and (b) because of the presence of the residual SrFeO2.5 phase. Fig. 7.7(a) and (b) show the intensity evolution of $(0\tfrac{1}{2}0)_p$ and $(\tfrac{1}{2}00)_p$ reflections respectively. As corresponding to these reflections the related structure factor for SrFeO$_{2.5}$ is much higher compared to SrFeO$_{2.875}$, the reminiscent SrFeO$_{2.5}$ shows a very high intensity (3 orders of magnitude) even at 275 °C). The intensity contribution of the newly formed SrFeO$_{2.875}$ thus appears as a small hump on the shoulder of the huge intensity from residual SrFeO$_{2.5}$.

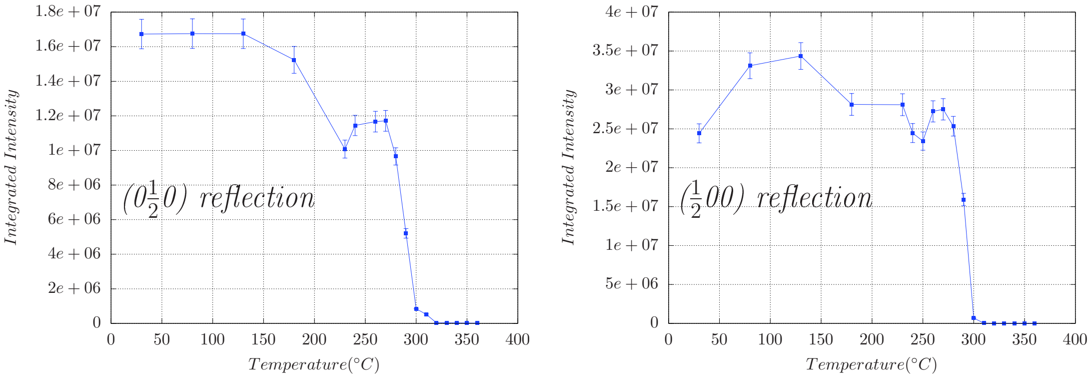

(a) **(b)**

Figure 7.7: (a) and (b) The variation of the integrated intensity of the already existing $(0\tfrac{1}{2}0)_p$ and $(\tfrac{1}{2}00)_p$ reflections from the SrFeO$_{2.5}$ phase related to two variants (V1 and V2). Due to the already present strong intensity of the residual SrFeO$_{2.5}$ phase at $(0\tfrac{1}{2}0)_p$ and $(\tfrac{1}{2}00)_p$ positions, the growth of new phase was less transparent from the intensity variation of such reflections. The expected intensity from the tetragonal phase for such reflection almost 3 orders of magnitude less than the corresponding reflection in the Brownmillerite phase (from the structure factor consideration) and appears as a small hump on the shoulder of the strong reflection of reminiscent SrFeO$_{2.5}$.

Further heating leads to the cubic phase beyond 325° and the corresponding diffraction pattern is shown in the Fig. 7.5(d) with the presence of only Perovskite type reflections. Fig. 7.5(c) represents situation at 310 °C where the system was going through the transition from the tetragonal SrFeO$_{2.875}$ to the nest phase cubic symmetry where all $(00\tfrac{1}{2})_p$ type reflections disappear. The decrease of the integrated intensity of (001) reflection upto a certain value, as can be seen form the Fig. 7.6(b), is related to the structure factor of the final cubic phase.

7.2.2 TGA on single crystal $SrFeO_{2.5}$ in air

In order to correlate the approximate temperature of oxygen uptake and determine the oxygen content of the finally obtained cubic phase, TGA was performed in 80% N_2 : 20% O_2 gas mixture (atmosphere is similar to air) on a very thin disk like $SrFeO_{2.5}$ single crystal (5.5 mg) using PerkinElmer TGA-8000. The temperature ramp was followed similar to the *in situ* diffraction. From room temperature upto 230 °C the single crystal was heated with a rate of 5 °C/min followed by an isothermal plateau of 15 min and afterwards 0.5 °C/min to 360 °C followed by another isothermal plateau of 15 min and then cooled down to room temperature with 0.5 °C/min.

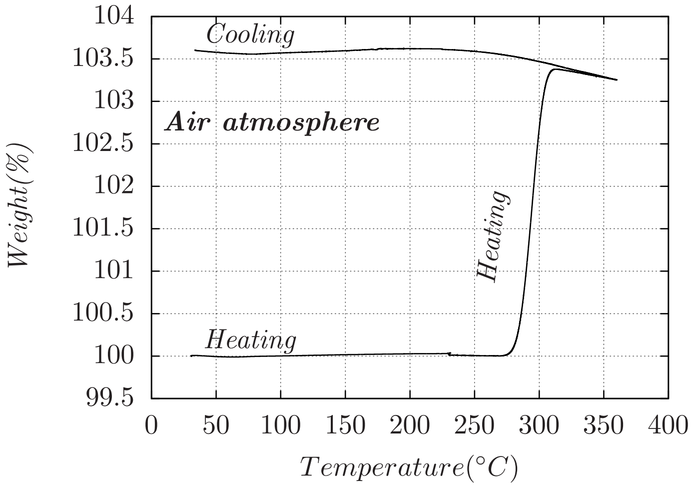

(a)

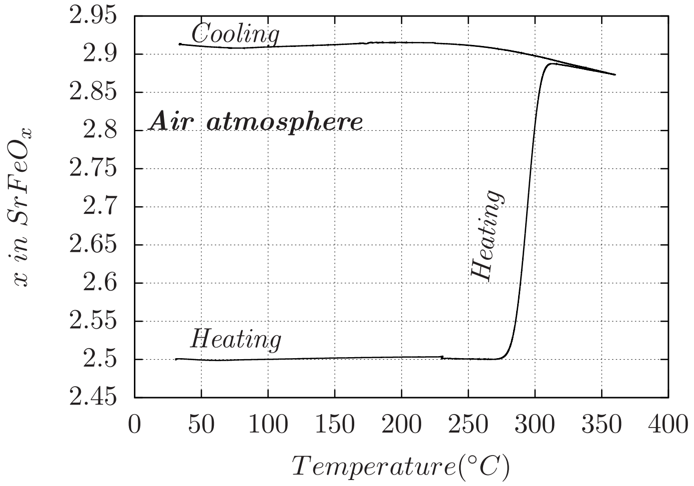

(b)

Figure 7.8: (a) The weight(%) on the course of elevation and diminution of temperature in the air atmosphere taking the intial mass to be 100 %. (b) Plot in terms of oxygen stoichiometry 'x' in $SrFeO_x$ considering the initial compound to be $SrFeO_{2.5}$ and following the Eq.7.1

$$x\, in\, SrFeO_x = \frac{183.4625 \times W_r - 143.465}{15.999};\ where\, W_r = \frac{Sample\, weight\, at\, T}{Initial\, sample\, weight} \quad (7.1)$$

In the Eq. 7.1 the oxygen stoichiometry 'x' in $SrFeO_x$ has been calculated from the weight ratio of the sample at temperature T with the initial sample weight as obtained from the TGA, using the molar mass of $M_{[SrFeO_{2.5}]} = 183.4625$ and $M_{[SrFe]} = 143.465$.

Fig. 7.4(a) shows the oxygen uptake starts around 275 °C and saturates around 315 °C. This result refers an extremely good agreement in between what has been observed in terms of the diffraction. The reflections of the tetragonal phase $SrFeO_{2.875}$ start appearing around ~ 280 °C and the intensities of such reflections starts disappearing around ~ 310 °C where the system passes into the cubic phase. From Fig. 7.8(b) it can be followed easily that the oxygen stoichiometry stays around $x \sim 2.875$ upto 360 °C which suggest the final cubic phase had very similar oxygen content to the tetragonal phase but lacking the ordering of the oxygen vacancies and can be interpreted in terms of high oxygen mobility in such temperature. The most astonishing is to see the very similar response in terms of oxygen uptake and saturation temperature from a 100 μm crystal used in *in situ* diffraction and a much much bigger single crystal used ($\phi \sim 3$ mm and thickness 1 mm) used for TGA. During the cooling the the oxygen content more or less stays constant around $x = 2.92$ until the room temperature.

7.2.3 HT vs. EC oxidation of $SrFeO_{2.5}$ crystal

Comparison of the results discussed in this chapter regarding the oxidation of $SrFeO_{2.5}$ single crystal in the air with the results obtained in EC oxidation as discussed in chapter 6 immediately points out few clear differences in terms of the reaction mechanisms, intermediate phases and oxygen stoichiometry which are following.

The first difference is regarding the formation of intermediate phases. While during the EC oxidation the system passes through both intermediate phases $SrFeO_{2.75}$ and $SrFeO_{2.875}$ with a phase sequence of $SrFeO_{2.5} \rightarrow SrFeO_{2.75} \rightarrow SrFeO_{2.875}$, the HT oxidation in air shows only the formation of $SrFeO_{2.875}$ with phase sequence $SrFeO_{2.5} \rightarrow SrFeO_{2.875}$. The identification of such phases has been done depending on the well established structure models for the both phases using the $(001)_p$ type and $(00½)_p$ type reflections in the Perovskite frameworks. Essentially by following the appearance and disappearance of the combination of such reflections, the phases are identified on the context. In EC the oxygen intercalation occurs under kinetic equilibrium in a *topotactic* fashion by selectively filling up the oxygen in the vacancies channels. The underlying frame work and the anisotropic nature of the arrangement of oxygen vacancies in Brownmillerite phase are kept almost unchanged which probably gives the possibility to access intermediate phases like $SrFeO_{2.75}$ and very difficult to synthesize at high temperature in an uncontrolled environment as open air. A precise control over the oxygen partial-pressure and temperature to synthesize such metastable phase like $SrFeO_{2.75}$ is crucial. In the present case of uncontrolled oxidation of $SrFeO_{2.5}$ at HT in air does not show oxygen ordering correspond to the $SrFeO_{2.75}$ phase.

The other very clear difference is the absence of the diffuse intensities during the formation of the tetragonal phase $SrFeO_{2.875}$. The diffuse intensities as observed in case of EC obtained $SrFeO_{2.875}$ are quite strong and reaching very high *d–values* (see Fig. 6.8 in chapter 6). At high temperature such diffuse lines are completely absent, as the system does not pass through the intermediate $SrFe_{2.75}$, for which the related domain structure remains intact. Also at high temperature the defects have a chance to heal out quickly due to high oxygen mobility.

The third important difference concernes the maximum oxygen content that can be achieved in the $SrFeO_{2.5+x}$ in the two different reaction pathways. In the HT oxidation of the $SrFeO_{2.5}$ single crystal under the uncontrolled atmosphere, the maximum oxygen content achieved was $x \sim 2.92$ as can be seen from the TGA in Fig.7.8. The maximum oxygen content in the EC oxidation can reach almost x~3 in $SrFeO_x$. To obtain such oxygen content at HT synthesis the compound needs to be annealed for long time under extreme oxygen pressure around 30 MPa[89].

7.2.4 Structural evolution during cooling

The structural evolution was also followed by *in situ* diffraction while cooling the crystal from 360 °C to RT 35 °C with a continuous ramp of 0.5 °C/min. Fig. 7.9–7.10 summarize all the essential changes in the structure and has been described by the four situations at different temperatures. All the reciprocal planes have been investigated in detail and for the sake of discussion on the structural evolution only the (*0kl*) planes has been presented.

The diffraction pattern at 360 °C as shown in the Fig. 7.9(a) represents the cubic phase $SrFeO_x$ with oxygen content $x \sim 2.9$ as obtained by the TGA Fig. 7.8(b). In the course of cooling down to room temperature at around 240 °C, very feeble intensities start to appear at $(0\frac{1}{2}\frac{1}{2})_p$ type reflection positions as shown by the encircled reflections. The new reflection can be seen clearly at higher 2θ value because of the less background from capillary. These newly appeared reflections grow to their maximum intensity around 235 °C. The temperature range for the transition was very sharp with in the range 240 °C to 230 °C and afterwards the structure remains constant until the room temperature. Here again it should be emphasized that synchrotron diffraction using the fast detector is the only way to detect such fast phase transitions.

A detailed analysis of the diffraction patterns including the principle (*hk0*)type planes in Fig. 7.14, ($hk\frac{1}{2}$) type planes in Fig. 7.15 and also ($hk\frac{1}{4}$) type planes in Fig. 7.16 confirms all the reflections can be indexed in the $SrFeO_{2.75}$ phase in the *Cmmm* structure model with cell parameters $2\sqrt{2}a_p = 10.974(1)$ Å, $2\times a_p = 7.702(1)$ Å, $\sqrt{2}a_p = 5.473(1)$ Å. The Fig. 7.11 shows the three principle planes (*0kl*), (*h0l*) and (*hk0*) indicating the newly grown $(0\frac{1}{2}\frac{1}{2})_p$ type reflections of $SrFeO_{2.75}$. The pseudocubic cell is outlined by the grey square. These reflections are equivalent to (200)/(001) reflection in the orthorhombic $SrFeO_{2.75}$ phase. The appearance of $(0\frac{1}{2}\frac{1}{2})_p$ type reflections encircled in all the three principle planes refers the fact that during the phase transformation from HT cubic phase to the $SrFeO_{2.75}$, all three variants i.e. the b axis were present in the newly grown phase and they are running along all three pseudocubic axes b_p (V2), a_p (V1) and c_p (V3).

The integrated intensities of $(0\frac{1}{2}\frac{1}{2})_p$-type reflections have been followed upto the RT as can be seen from the Fig. 7.11(b), (d) and (f). In principle from the integrated intensities, information regarding the volume fractions of the domains related to the three variants can be obtained and also it is possible to comment on the type of twin domains *e.g. microdomain* or *macrodomain*. In the presence of microdomains the intensities of all the three $(0\frac{1}{2}\frac{1}{2})_p$-type reflection are expected to be equal.

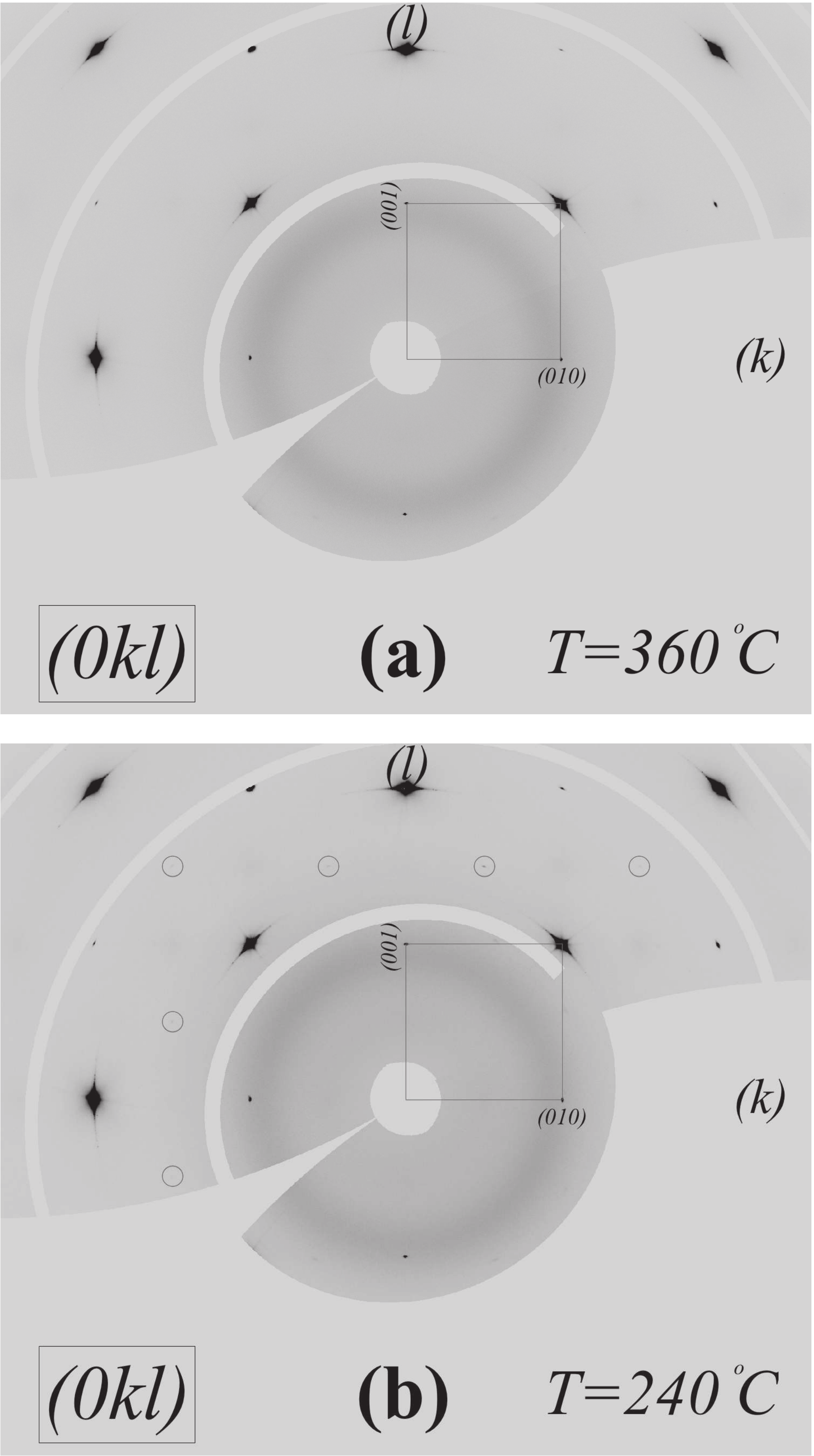

Figure 7.9: Evolution of the (*0kl*) plane (reconstructed in the pseudocubic cell) during cooling of $SrFeO_{2.5}$ single crystal (a) 360 °C and (b) 240 °C. The pseudocubic cell is marked in grey square. The encircled reflections indicate the newly growing reflection .

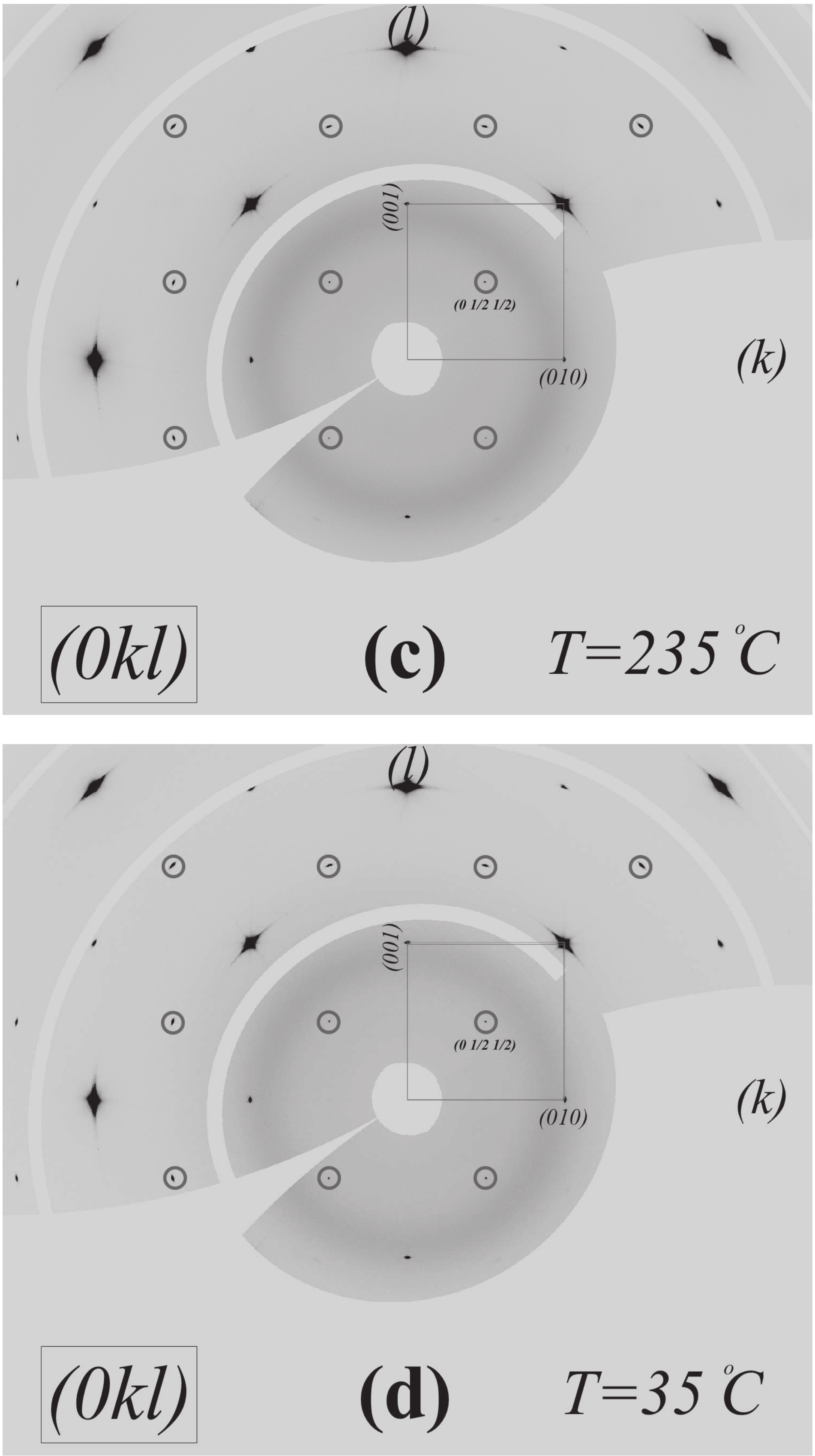

Figure 7.10: Evolution of the (*0kl*) plane (reconstructed in the pseudocubic cell) during cooling of SrFeO$_{2.5}$ single crystal (c) 235 °C and (d) 35 °C. The pseudocubic cell is marked in grey square. The encircled reflections indicate the newly growing reflection.

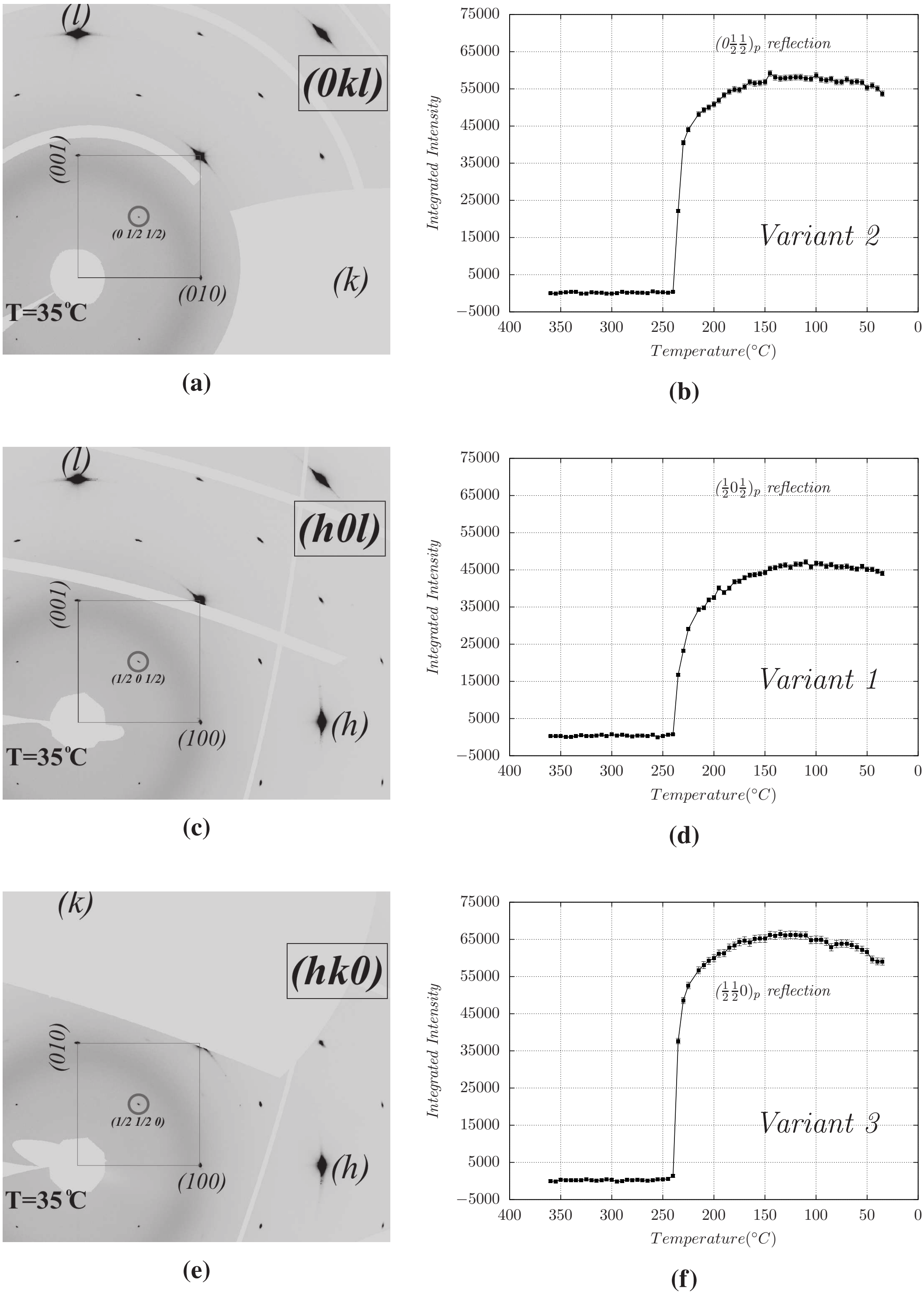

Figure 7.11: Reconstructed reciprocal planes (a) (*0kl*), (b) (*h0l*) and (c) (*hk0*) of $SrFeO_{2.75}$ obtained on the course of cooling from HT cubic phase. The pseudocubic cell has been marked with the grey square. The integrated intensities has been followed on the the encircled reflections i.e. (b) $(0\frac{1}{2}\frac{1}{2})_p$ (d) $(\frac{1}{2}0\frac{1}{2})_p$ and (f) $(\frac{1}{2}\frac{1}{2}0)_p$ over the temperature 360 °C to 35 °C. These presence of all three reflections uniquely indicate the growth of all three possible orientation variants i.e. the b axis of $SrFeO_{2.75}$ phase which are running along all three pseudocubic axes b_p, a_p and c_p respectively. See Fig. 4.5 in chapter 4 for more details.

From the ratios of the maximum intensities the estimated volume fractions for the three domains are respectively V1 : 27%, V2 : 34% and V3 : 38% which is very approximate because of the high absorption of the sample $SrFeO_x$ at the wavelength used 0.7750 Å. Only 30% of the incident intensity transmits through the crystal of 100 μm diameter. In addition to such high absorption, the other most difficult part is to get the information regarding the position of the three domains inside the crystal whic needs to be taken into account to apply absorption correction properly. This was the main difficulty to interpret the domain type *e.g.* macroscopic or microscopic.

What was astonishing is the appearance of $SrFeO_{2.75}$ during the cooling from 360 °C to room temperature whereas the TGA performed in air atmosphere (Fig. 7.8) shows the oxygen stoichiometry in $SrFeO_x$ stays around $x = 2.9$ while cooling down upto RT. The possible reason could be creation of lower oxygen partial pressure inside the capillary during the experiment. The phase diagram of the $SrFeO_x$ system (see Fig. 7.12) suggests at an oxygen partial pressure 10^{-2} bar, below the 360 °C it is in principle possible to form $SrFeO_{2.75}$ phase.

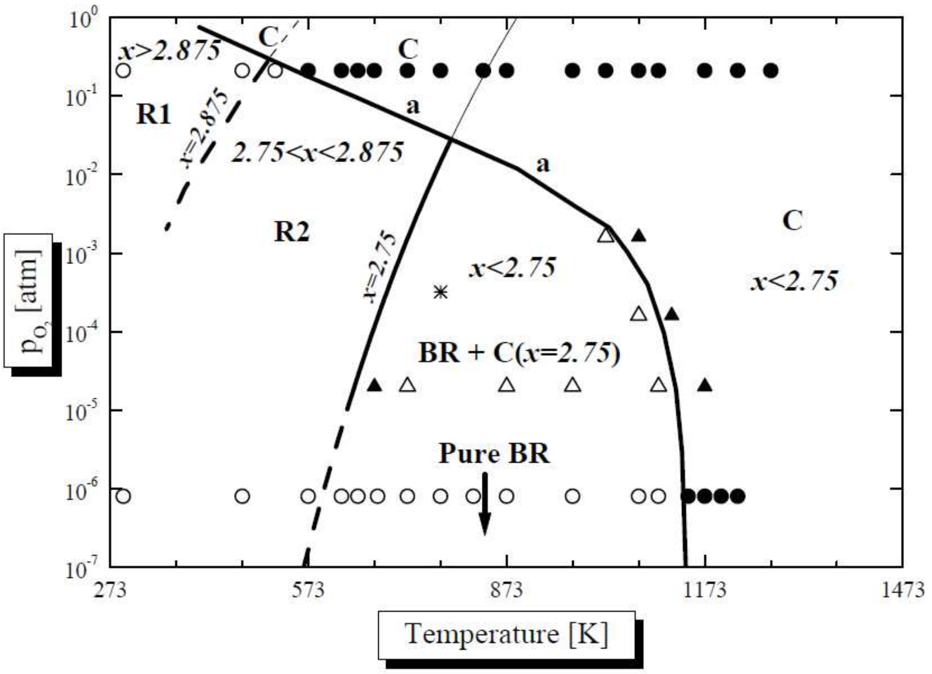

Figure 7.12: Reproduced form the Figure 7.22 of ref.[103]. A phase diagram of the $SrFeO_x$ system. Solid and empty symbols represent the cubic and lower symmetries respectively. The circles and triangles represent the experimental points collected by the M Schmidt[103] and Mizusaki *et al.*[104] respectively. The star represents the result of a Mössbauer experiment of Wißmann and Becker[105]. C and BR refer to the cubic phase and the orthorhombic $Sr_2Fe_2O_5$ (brownmillerite, $x = 2.5$) respectively. The x parameter is the oxygen content of the ferrite and the a- line separates the cubic phase area from the low symmetry parts.

To confirm at such oxygen partial pressure of $ppO_2 = 10^{-2}$ bar, what would be the oxygen composition in $SrFeO_x$, TGA has been performed on the single crystal of $SrFeO_{2.5}$. The single crystal was heated upto 360 °C in air atmosphere where it was having an oxygen stoichiometry of $x = 2.875$ and then cooled down in room temperature under industrial quality nitrogen atmosphere ($\sim ppO_2 = 10^{-2}$bar).

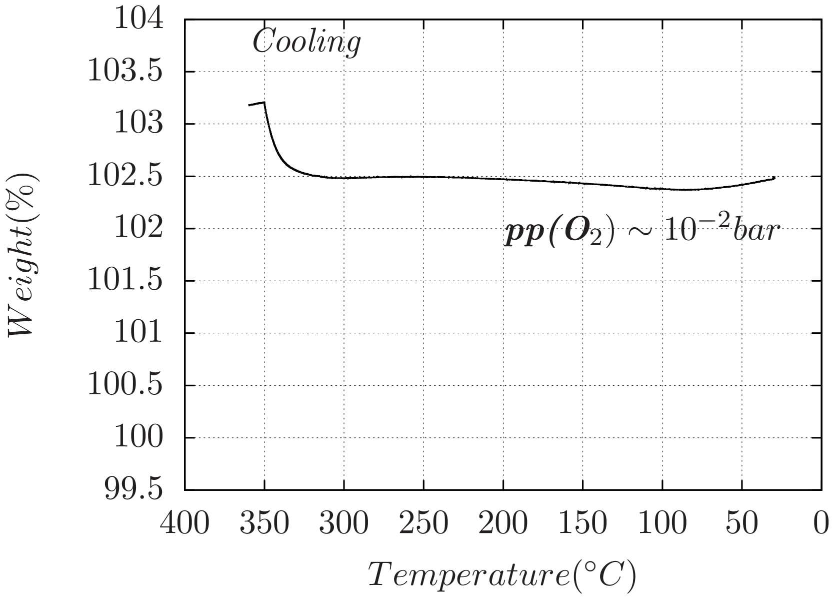

(a)

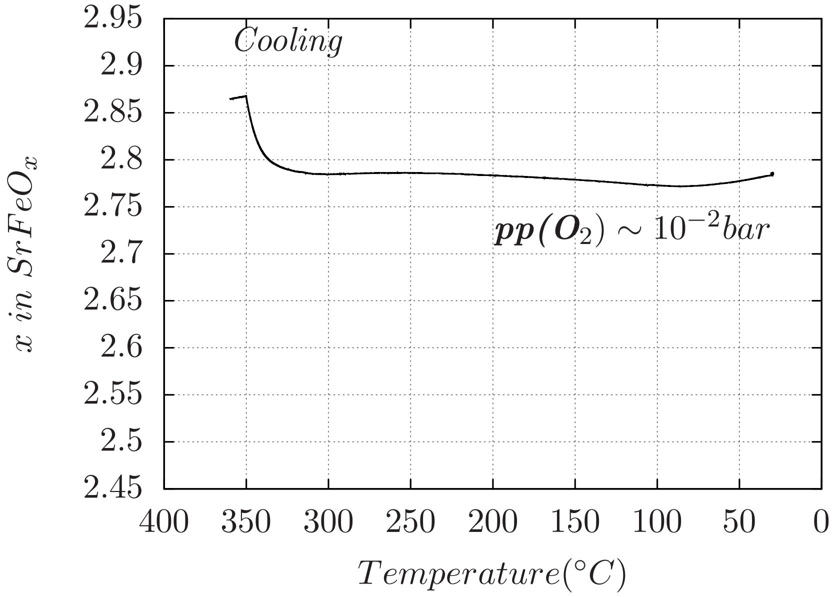

(b)

Figure 7.13: (a) Change in oxygen composition x in $SrFeO_x$ as a function of Temperature obtained from TGA. (b) Change in oxygen composition x in $SrFeO_x$ as a function of Temperature obtained from TGA.

The oxygen stoichiometry x quickly drops down from $x = 2.88$ to $x = 2.75$ and stays until the room temperature as can be seen from the Fig. 7.13. At least this gives an idea what might have happened during the *in situ* diffraction study while cooling down the $SrFeO_x$ single crystal from HT cubic phase to the RT.

Different reciprocal planes of $SrFeO_{2.75}$ has been reconstructed in the pseudocubic cell to compare with the corresponding simulated patterns as shown in the figures Figs. 7.14–7.16. The comparison verifies the correctness of the phase to be pure $SrFeO_{2.75}$ in *Cmmm* structure model as proposed by Hodges *et al.* [89]. The interesting by product of the TGA experiment during the cooling down of $SrFeO_x$ single crystal under industrial quality nitrogen atmosphere was the formation of pure $SrFeO_{2.75}$. This gives an easy way to prepare high quality single crystal of $SrFeO_{2.75}$.

7.3 Summary

In this chapter we have investigated oxygen uptake of $SrFeO_{2.5}$ single crystal at high temperature in air atmosphere. We have discussed important differences of the HT oxygen uptake of $SrFeO_{2.5}$ single crystal compared to the EC oxygen intercalation at ambient in terms of the intermediate phase sequence. In HT reaction we did not observe the formation of $SrFeO_{2.75}$. The system directly pass from $SrFeO_{2.5}$ to $SrFeO_{2.875}$ while in EC we have observed the phase sequence $SrFeO_{2.5} \rightarrow SrFeO_{2.75} \rightarrow SrFeO_{2.875}$.

Also we have discussed the difference in the defect structure as obtained from HT oxidation compared to EC. The $SrFeO_{2.875}$ obtained from EC show huge 1D diffuse scattering showing long range correlation problem related to the oxygen ordering while in contrary the $SrFeO_{2.875}$ phase obtained from HT oxidation does not show any such defect structure. This importantly show low temperature synthesis gives the possibility to synthesize metastable phases with long range oxygen order which is very difficult to obtain from HT synthesis.

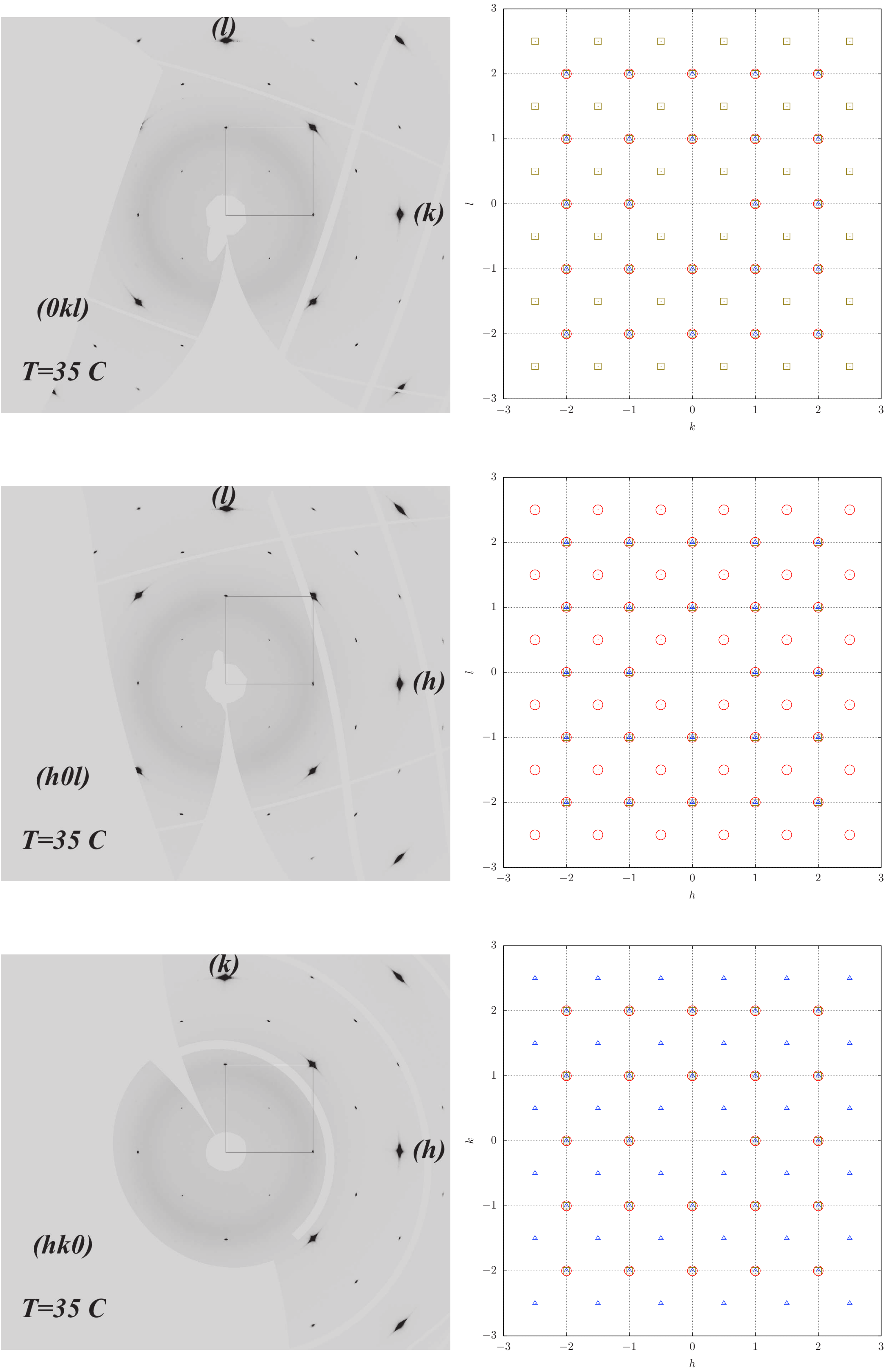

Figure 7.14: (left) The principle planes (*0kl*), (*h0l*) and (*hk0*) of SrFeO$_{2.75}$ reconstructed in the pseudocubic cell from the diffraction data obtained at T=35 °C on the course of cooling. (right) Simulated patterns for SrFeO$_{2.75}$ with 3 variants. Reflection related to V2 in olive squares, V1 in red circles and V3 in blue triangles.

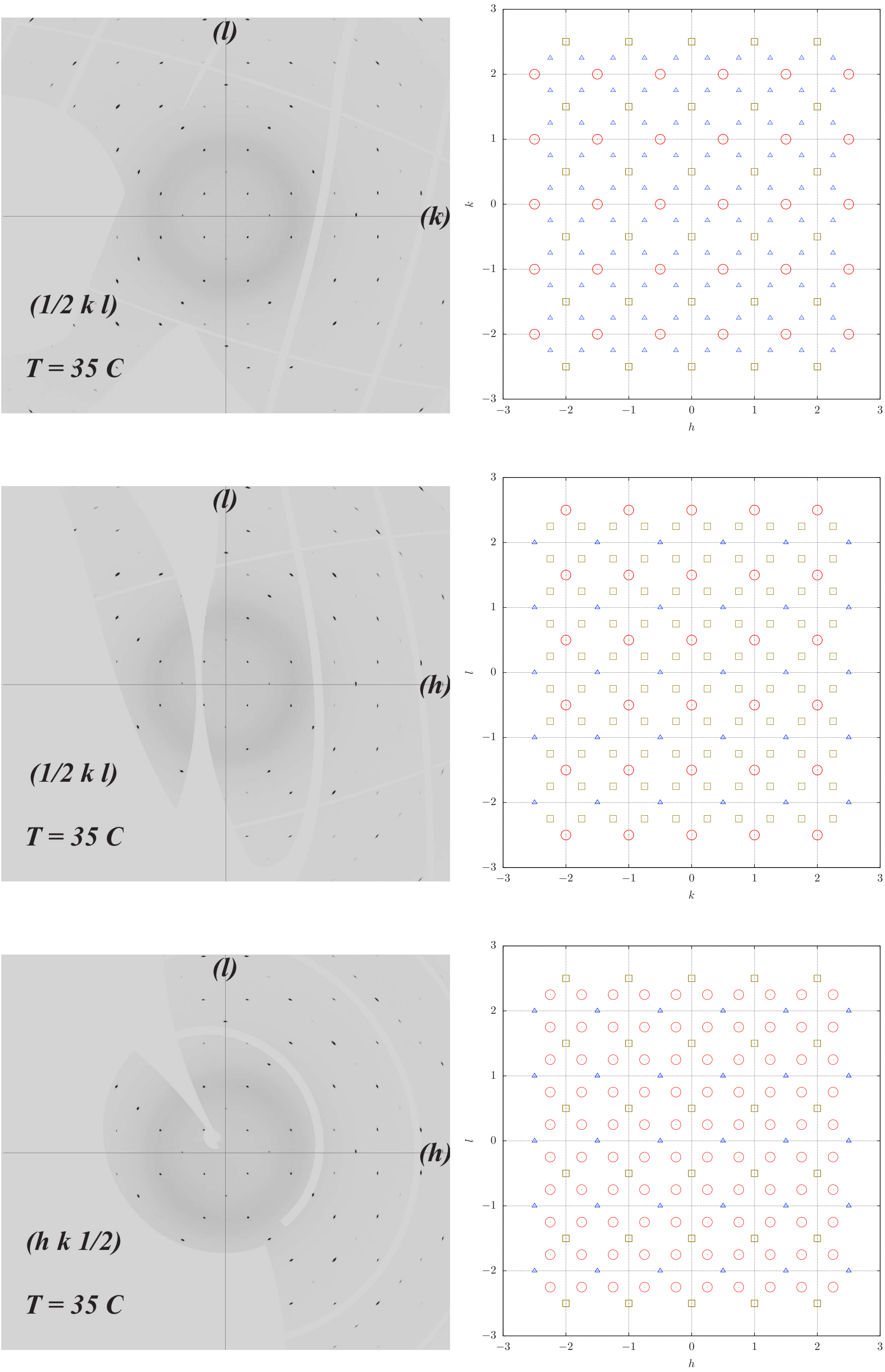

Figure 7.15: (left) The HALF planes $(1/2\,k\,l)$, $(h\,1/2\,l)$ and $(h\,k\,1/2)$ of $SrFeO_{2.75}$ reconstructed in the pseudocubic cell from the diffraction data obtained at T=35 °C on the course of cooling. (right) Simulated patterns for $SrFeO_{2.75}$ with 3 variants. Reflection related to V2 in olive squares, V1 in red circles and V3 in blue triangles.

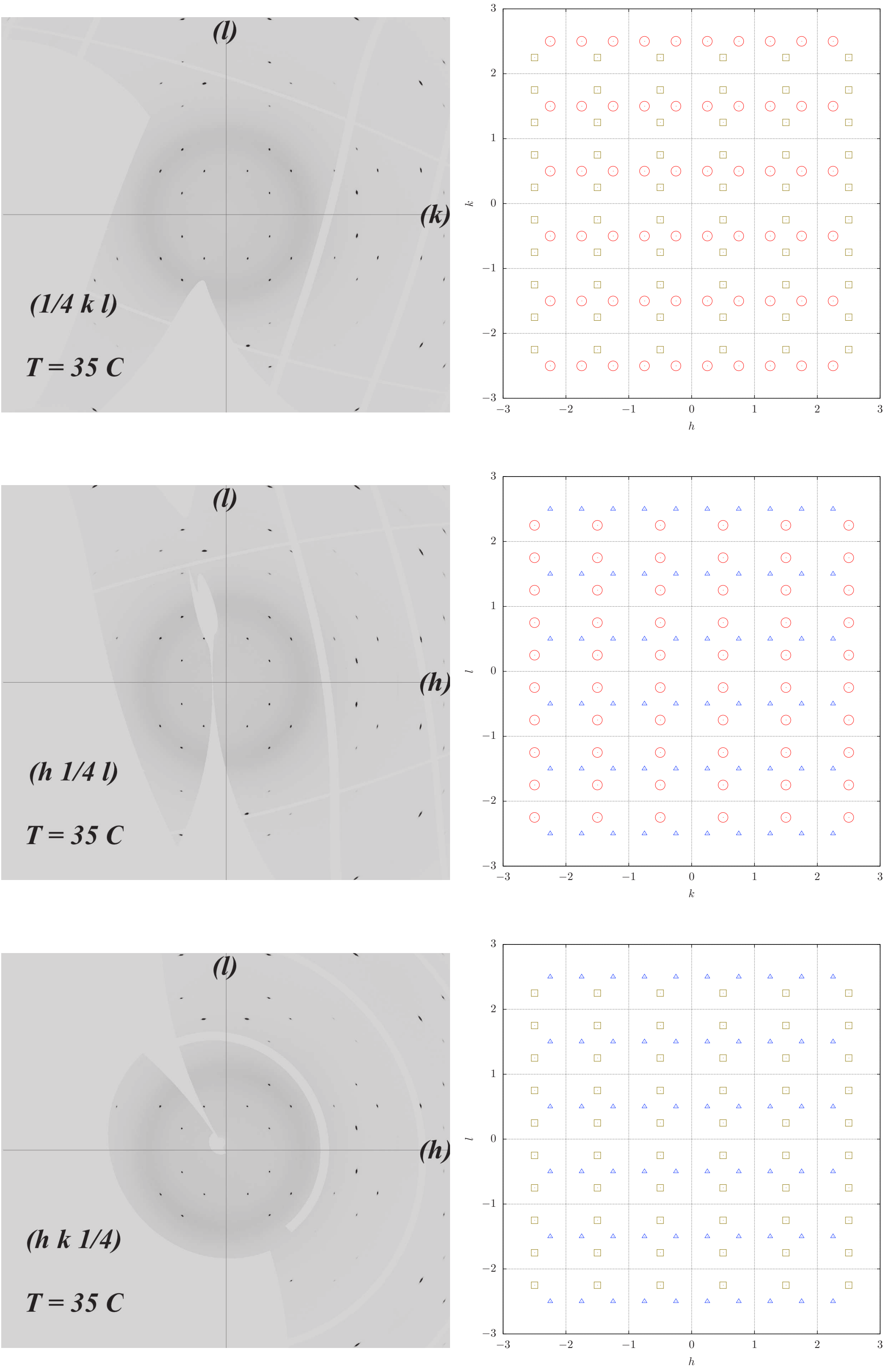

Figure 7.16: (left) The QUARTER planes $(^1/_4 k l)$, $(h\, ^1/_4 l)$ and $(h k\, ^1/_4)$ of $SrFeO_{2.75}$ reconstructed in the pseudocubic cell from the diffraction data obtained at **T=35 °C** on the course of cooling. (right) Simulated patterns for $SrFeO_{2.75}$ with 3 variants. Reflection related to V2 in olive squares, V1 in red circles and V3 in blue triangles.

Chapter 8

The $Pr_2NiO_{4+\delta}$ system

$Pr_2NiO_{4+\delta}$ belongs to the K_2NiF_4 family of oxides. Scince the discovery of high temperature superconductivity in $La_2CuO_{4+\delta}$ [106], there has been intensive investigation on the structures and physical properties of cuprates as well as nickelates and cobabltates. Although no evidence of superconductivity has been found in the related nickelates *e.g.* $Pr_2NiO_{4+\delta}$, still more and more interest is growing in these compounds with time because of their high scientific impact, such as diversity in the physical properties and structural complexities related to charge-spin and excess oxygen. The other aspect is the low temperature oxygen mobility in theses compounds related to special lattice dynamics in the presence of interstitial oxygen which has drawn a lot of attention towards R&D technology for devoloping SOFC devices [18,19]. In a wide range of oxygen non-stoichiometry ($0 \leq \delta \leq 0.25$), oxygen can be intercalated and de-intercalated in $Pr_2NiO_{4+\delta}$ in a reversible manner even at ambient by electrochemisty (EC) while the structural stability remains intact [26].

$Pr_2NiO_{4+\delta}$ represents a perfect model system belonging to K_2NiF_4 family to investigate the fundamental scientific aspect regarding its complex structure and properties while its also serves as a model system to design new generation SOFC cathode material through the understanding of underline diffusion mechanism at low temperature.

The phase diagram of this compound is very complicated as it is very sensitive to the oxygen stoichiometry. The structure and physical properties changes quite drastically as a function of oxygen stoichiometry. The phase diagram of $Pr_2NiO_{4+\delta}$ has been investigated at high temperature by controlling oxygen partial as well as at low temperature by EC oxidation and reduction. In this chapter we will discuss the high temperature phase diagram as established until now in literature followed by the phase diagram at low temperature and also the complexity that arises from the interstitial oxygen ordering.

8.1 Established HT phase diagram of $Pr_2NO_{4+\delta}$

The structure of the stoichiometric ternary oxide Pr_2NiO_4 can be described as a succession of NiO_2 and Pr_2O_2 layers (Fig. 8.1). At high temperature the structure of the stoichiometric Pr_2NiO_4 is tetragonal *I4/mmm* where Ni^{2+} ions are in octahedral coordination. With the decrease of temperature, the increased differences of the in plane lattice parameters (*l.p.*) of these two different layers (*l.p.* NiO_2 > *l.p.* Pr_2O_2) generate stress inside the structure.

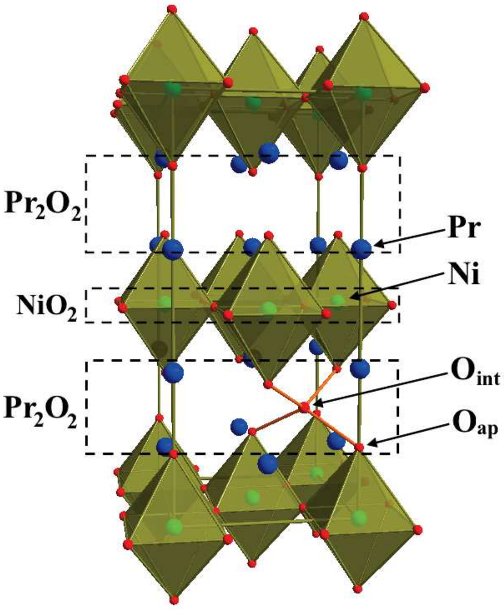

Figure 8.1: Structure of $Pr_2NiO_{4+\delta}$, described as a succession of NiO_2 and Pr_2O_2 layers. Excess oxygen (O_{int}) stays in the interstitial position inside the Pr_2O_2 layer coordinated by 4 apical oxygen atoms (O_{ap}).

In the absence of the oxygen atmosphere during cooling the stress in the structure is released by rotation of the NiO_6 octahedra. Thus the system goes through a phase transition from High Temperature Tetragonal (HTT) phase to low temperature orthorhombic (LTO) phase. For Pr_2NiO_4, the estimated transition temperatures of the phase transition in the absence of the oxidising atmosphere is around 1500 K[107]. At even lower temperature, the system pass through a first order transition from LTO to a new low temperature tetragonal (LTT) phase *P4₂/ncm* due to the change of the rotation axes of the octahedra[108,109].

In the presence of oxidising atmosphere the stress is reduced by different mechanism. The structure gets relaxed by incorporating oxygen as interstitial defects. The interstitial oxygen occupy the ($^1/_4{}^1/_4z$) with $z \sim 0.25$ position in the supercell of the HTT [$\sqrt{2}a_t \times \sqrt{2}b_t \times c_t$] inside the bilayer Pr_2O_2 as was suggested by the study of Chaillout *et al.*[110]

and Jorgensen *et al.*[111] for the homologous $La_2(Cu/Ni)O_{4+\delta}$ systems. By the insertion of the interstitial oxygen, two effects play important role in relaxing the stress[112]. First, the oxygen atoms increase the in plane lattice parameters in Pr_2O_2 layer therefore decrease the compression in the NiO_2 layers. Secondly, the smaller size of the oxidised Ni ions ($Ni^{2+} \rightarrow Ni^{3+}$) for electro neutrality makes the Ni-O bond shorter which acts in the same way to realease the stress in the structure. The maximum amount interstitial oxygen which the sysytem accommodates inside the structure in order to release the stress depends on the size of the RE (*e.g.* La, Pr, Nd etc.) atoms. The smaller size of the Pr-atom in $Pr_2NiO_{4+\delta}$ requires larger oxygen excess to stabilize the $Pr_2NiO_{4+\delta}$ compared the homologous ($La_2NiO_{4+\delta}$) when lowering the temperature in the oxidised atmosphere[112]. The possibility of accommodating higher amount of excess oxygen in the $Pr_2NiO_{4+\delta}$ with high diffusivity even down to room temperature[19,113] makes these compound very special and promising material for SOFC electrode.

The structure of $Pr_2NiO_{4+\delta}$ was first investigated by Willer and Daire in the 70's[114]. The structure of stoichiometric Pr_2NiO_4 was reported to be monoclinically distorted variant of the K_2NiF_4 structure with $a = b$ though Singh *et al.* reported a monoclinic symmetry with $a \neq b$[115]. Buttray *et al.*[116] and Sullivan *et al.*[63] studied more systematically the phase diagram of $Pr_2NiO_{4+\delta}$ as a function of oxygen non-stoichiometry by complimentary neutron and synchrotron diffractions on the single crystals as well as on powder.

As established in the literature untill now, above $\geq$1500 K the stoichiometric parent structure have an ideal tetragonal (HTT) symmetry in *I4/mmm*. While cooling the structure pass through different lower symmetric phases. The symmetries of the new phases on the course of cooling are expected to belong to its landau subgroups symmetries *e.g. Bmab*, *P4$_2$/ncm*, *Pccn* and *Fmmm*. These subgroups represent the various possible type of octahedral rotation due to continuous phase transition from HTT phase.

The distortion associated with these subspace groups, in the supercell of the HTT phase [$\sqrt{2}a_t \times \sqrt{2}b_t \times c_t$], are related to the systematic rotation of the NiO_6 octahedra around the particular sets of axes which are parallel to the Pr_2O_2/NiO_2 layers. In the *Bmab* structure, the NiO_6 octahedra rotate around [100] direction in the supercell of the HTT phase. While the neighbouring octahedras along *a*-direction are co-rotated in the same NiO_2 plane, they are contra-rotated in the alternative NiO_2 planes (Fig. 8.2(a)). The LTT phase in *P4$_2$/ncm* structure characterized by the octahedral rotation about [110] direction in the basal plane such that the nearest neighbours are contra-rotated. The rotation axes changes from [110] to [$1\bar{1}0$] in the consecutive layers (Fig. 8.2(b)). The *Pcnn* can be understood by visualising the rotation of the NiO_6 octahedra along a particular pair of direction [*hk0*] and [$h\bar{k}0$] which are the vector sum of the [100] to [110] weighted by proper coefficients. In fact, *h* and *k* are fixed such a way that the canting angle lies in between 0° in *Bmab* and 45° in *P4₂/ncm*.

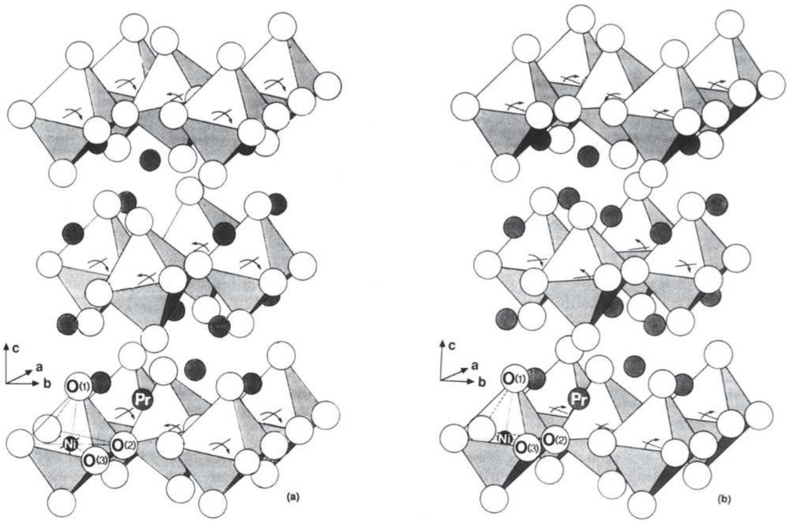

Figure 8.2: Clinographic projections of the (a) *Bmab* structure and the (b) *P4₂/ncm* structure for $Pr_2NiO_{4+\delta}$. **Reproduced from FIG. 3. of ref[116].**

The study by Sullivan *et al.*[63] reported the phase diagram obtained from different $Pr_2NiO_{4+\delta}$ samples with different oxygen stoichiometry which were prepared with in the stability field of $Pr_2NiO_{4+\delta}$ in terms of oxygen fugacity and temperature (Fig. 8.4). The phase diagram as suggested by the study from the high resolution synchrotron diffraction is presented in the Fig. 8.3. As can be seen from the phase diagram at the stoichiometric limit with $\delta \leq 0.02$ the structure is orthorhombic *Bmab* as studied by the syncrotron X-ray diffraction though the neutron diffraction on single crystal study by neutron show *Pccn* structure with the presence of very weak superlattice reflections[63,116].

In the non-stoichiometric range $0.058 \leq \delta \leq 0.065$, $Pr_2NiO_{4+\delta}$ reported to be tetragonal. The phase separation range between *P4₂/ncm* & *Bmab* was estimated to be $0.005 \leq \delta \leq 0.058$. The next phase separation region between the tetragonal *P4₂/ncm* and the next orthorhombic *Fmmm* phase at higher oxygen stoichiometry is estimated to be in the range $0.065 \leq \delta \leq 0.17$. The excess oxygen gets accommodated inside the structure as interstitial defects. As discussed above the symmetry of the structure is determined by the the tilting patterns of the octahedras in long range order. At higher oxygen content the disorder incorporated in the form of interstitial oxygen affects the octahedral tilting pattern in short range and the average structure can be best described by *Fmmm* space group without assigning weak commensurate or incommensurate superstructure intensities. In addition, the study reports at higher stoichiometric range two phases can coexist with different oxygen stoichiometry $\delta = 0.162$ *i.e. Fmmm(1)* and

$\delta = 0.195$ *i.e. Fmmm(1)* but with same average symmetry *Fmmm* as shown in Fig. 8.3.

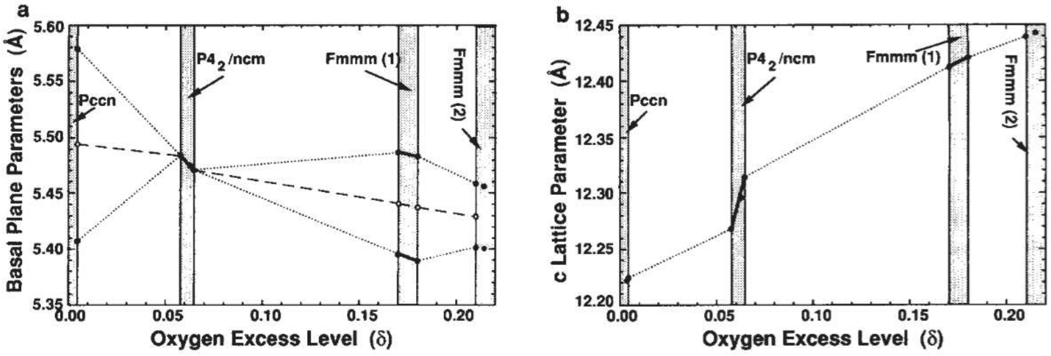

Figure 8.3: Lattice parameters dependence on excess oxygen in $Pr_2NiO_{4+\delta}$ synthesized at high temperature. Dotted lines connect parameters across two-phase regions, dashed lines represent the average basal plane lattice parameter for each phase. **Reproduced from FIG. 13 of ref.[63].**

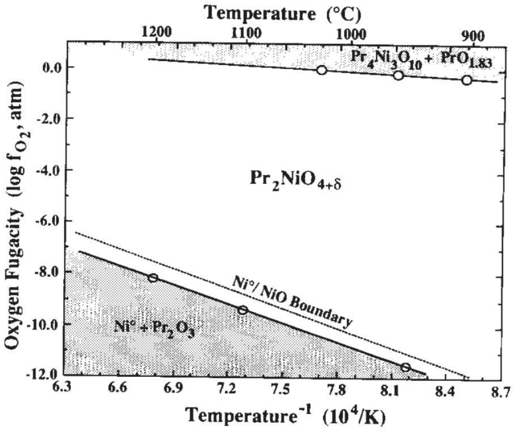

Figure 8.4: Stability field for $Pr_2NiO_{4+\delta}$, showing the f_{O_2}-temperature dependence of the reduction and oxidation boundaries, as well as the reduction boundary of NiO/Ni° for reference. **Taken from FIG. 1 of ref.[63]**

Thermal stability of $Pr_2NiO_{4+\delta}$

Thermal stability of the compound is an important issue while working at high temperature. Sullivan *et al.*[63] characterized the $(f_{O_2} - T)$ dependence for the overall stability field of $Pr_2NiO_{4+\delta}$ with conventional X-ray diffraction techniques as shown in the Fig. 8.4. The oxidation boundary of the overall stability field was determined by annealing single crystals under increasingly oxidizing atmospheres until the formation of oxidation products were observed. The study reported, below 1303 K under pure oxygen atmosphere, the crystal was oxidized to $PrO_{1.83}$ and the multilayered perovskite $Pr_4Ni_3O_{10}$ [PrO*(PrNiO3)$_n$, where n = 3], while no evidence of other layered phases such as

$Pr_3Ni_2O_7$ [PrO*(PrNiO3)$_n$, where $n = 2$]. Odier *et al.* also studied the behaviour of the polycrystalline samples during heating and cooling under pure oxygen atmosphere[117]. Similarly the sample was oxidised to PrO_{2-y} and $Pr_4Ni_3O_{10}$ beyond 1000 °C showing non-reversibility while cooling (Fig. 8.5). This non-reversibility behaviour can be the biggest disadvantage for any high temperature application as oxygen membrane despite its exceptional performance as oxygen ion conductor.

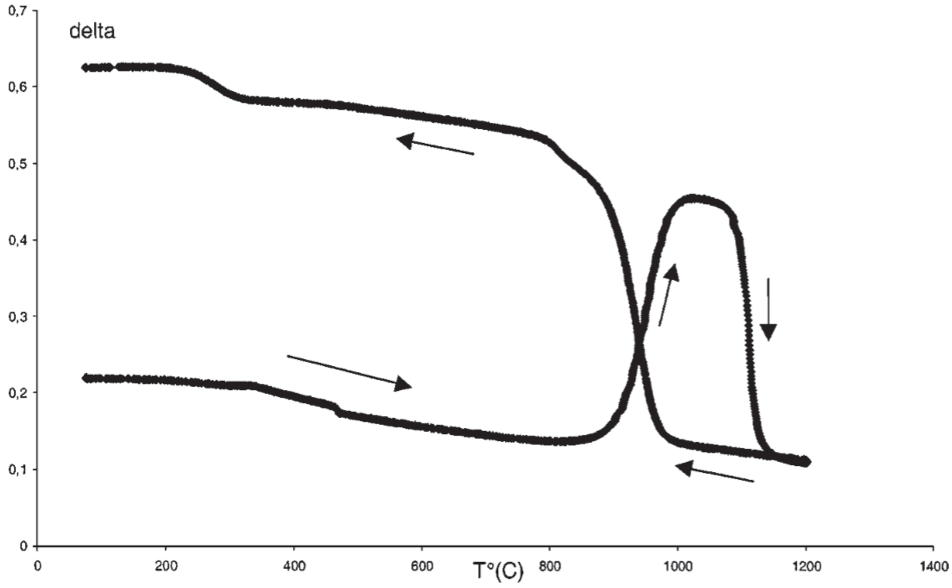

Figure 8.5: Oxygen stoichiometry versus temperature in $Pr_2NiO_{4+\delta}$ under pure oxygen flow (ambient pressure; oxygen flow, 20 l/h; heating and cooling ramp, 300 °C/h). **Taken from FIG. 1 of ref.[117].**

While the synthesis of polycrystalline $Pr_2NiO_{4+\delta}$ phases can be seemingly reproducible, the synthesis of monophasic single crystal was long time a challenge. Prabhakaran *et al.*[118] reported the $Pr_2NiO_{4+\delta}$ single crystals obtained by the floating zone method start to disintegrate after one week, even when stored under vacuum. Although stable crystals have been reported to be obtained under flowing oxygen by Wahyudi *et al.*[76]. However a microscopic formation of NiO has been evidenced, especially for slight deviations from a perfect cation stoichiometry of the feed rods. Since NiO is volatile at high temperatures, it permanently leaves the system under crystal growth conditions. This makes the crystal growth very challenging and its success strongly depending on the applied growth conditions. This might be also a source of non-reproducible results when discussing the formation of extremely weak superstructure reflections as is the case in terms of charge, spin or orbital ordering.

8.2 Phase diagram obtained by EC oxidation/reduction

In contrary to the high temperature phase diagram, the phase diagram of $Pr_2NiO_{4+\delta}$ has been also investigated at ambient by EC oxygen intercalation and deintercalation. The homologous series of compounds (*e.g.* $La_2CuO_{4+\delta}$[33,61,119] $(La/Nd)_2NiO_{4+\delta}$[120,121] and $Nd_2CoO_{4+\delta}$[21]) are very well known to undergo reversible *topotactic* oxygen intercalation by EC. The oxygen intercalation/deintercalation reaction in $Pr_2NiO_{4+\delta}$ can be described by the following equation.

$$Pr_2NiO_{4+\delta} + 2\delta e^- \Longleftrightarrow Pr_2NiO_{4.00} + \delta O^{2-} \tag{8.1}$$

In the thesis work by Olivia Wahyudi[26], the electrochemical reduction on polycrystalline $Pr_2NiO_{4+\delta}$ have been studied by *in situ* neutron powder diffraction. The electrochemical reduction was performed on the dense pallet of polycrystalline $Pr_2NiO_{4+\delta}$ inside a quartz made EC cell in an aquas solution of 1N KOD. The reaction was done in galvanostatic mode by applying appropriate current according to sample weight needed to reduce the sample to stoichiometric $Pr_2NiO_{4.00}$. In a galvanostatic (constant current) process the number of electrons (n) transfer into the sample can be correlated to the number of oxygen (2δ) following the electrochemical equation Eq. 8.1 [$n = 2\delta$].

Contrary to the high temperature phase diagram, the EC intercalation proceeding at ambient reveals complex phase sequence as a function of the oxygen stoichiometry. The phase diagram and the related lattice parameter as a function of charge transfer is shown in the Fig. 8.6(bottom). The diffraction data show three principle line phases appeared during the course of oxygen deintercalation. The starting phase with highest oxygen non-stoichiometry ($\delta \sim 0.25$) show an average orthorhombic structure with *Fmmm* space though detail analysis reveals the presence of incommensurate reflections[26]. The second phase with tetragonal symmetry $P4_2/ncm$ which was observed in the non-stoichiometry range ($0.115 \le \delta \le 0.126$) shows the presence of very weak P-type reflection identified by the neutron diffraction while almost impossible to identify from normal laboratory X-ray. The oxygen non-stoichiometry range for the tetragonal phase was found to be much narrower compared to the biphasic region of ($Fmmm + P4_2/ncm$). The final phase which appears in the stoichiometric limit in the range $\delta \le 0.06$ show orthorhombic symmetry in *Bmab* space group. In between the tetragonal and the final orthorhombic phase the system pass through a biphasic region ($Fmmm + P4_2/ncm$) in the non-stoichiometric oxygen range ($0.06 \le \delta \le 0.115$). The changes in the volume fractions of the different phases can be understood from the refined scale factor as shown in Fig. 8.6(top).

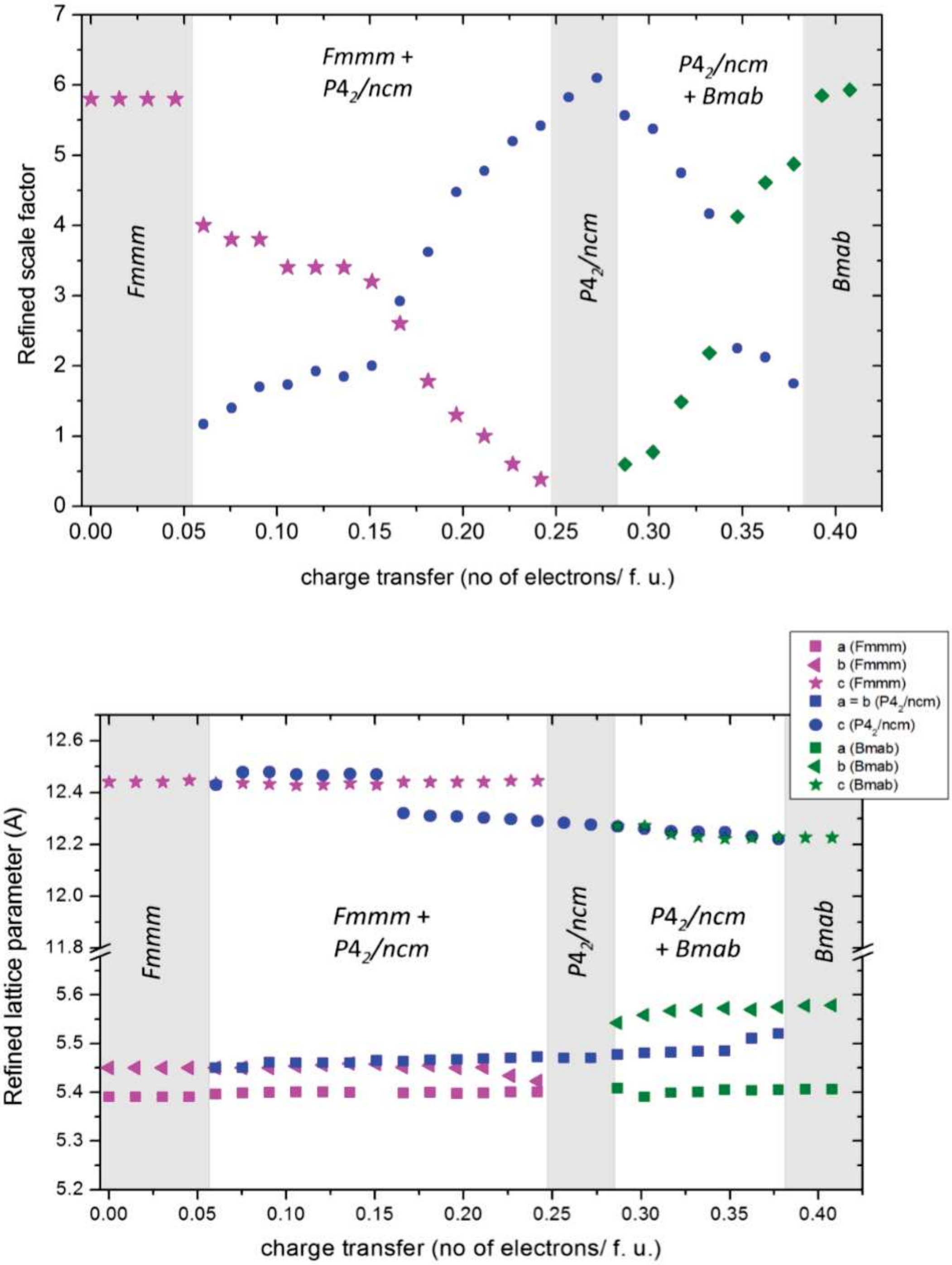

Figure 8.6: Refined scale factor (top) and lattice parameters (bottom) as a function of the charge transfer from *in situ* neutron powder diffraction. Regions in grey represent single phase regions while white represent biphasic regions. **Taken from thesis of Olivia Wahyudi[26].**

8.3 Effect of interstitial oxygen in $Pr_2NiO_{4+\delta}$

8.3.1 Impact on structure

In the above section we have discussed only the average structure of $Pr_2NiO_{4+\delta}$-system. However the real structure of $Pr_2NiO_{4+\delta}$ is much more complex compared to the average structure. The complexity is related to the ordering of the excess oxygen in commensurate or incommensurate superlattice. The neutron powder diffraction study by Fernández-Díaz *et al.*[107] very distinctively showed the appearance of the superstructure reflections in the nickelates (Fig. 8.7). The study reported presence of extra low intensity peaks appearing for $Pr_2NiO_{4+\delta}$ and homologous $Nd_2NiO_{4+\delta}$ while they were absent in the case for $La_2NiO_{4+\delta}$. The reason behind such particular sample dependent behaviour was related to the amount of excess oxygen incorporated to releases the structural stress. As discussed previously, the stability of this kind of structure mainly depends on the different size of the NiO_2 and R_2O_2 layer. Since the bond lengths in Pr_2O_2 and Nd_2O_2 are shorter compared to La_2O_2, $Pr_2NiO_{4+\delta}$ and $Nd_2NiO_{4+\delta}$ incorporate extra amount of interstitial oxygen which might be able to establish long range order and can be identified even by the macroscopic diffraction technique *i.e.* X-ray and neutron diffraction. As shown in the Fig. 8.7 the arrow headed peaks are the result of such long range ordering.

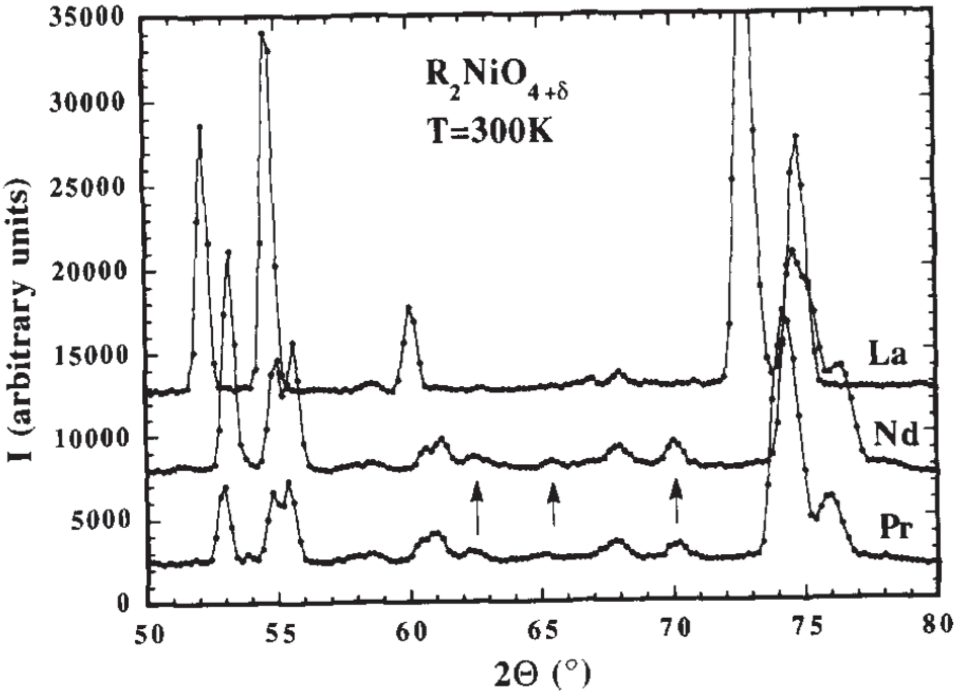

Figure 8.7: Portion of the diffraction pattern for $R_2NiO_{4+\delta}$ (R = La, Pr and Nd). Arrows indicate the main differences between the different patterns. **Taken from FIG. 2 of ref.[107]**

Superstructure reflections resulting from the ordered oxygen interstitials may be seen clearly around the main Bragg reflections. In fact, the superstructure reflections in the diffraction patterns can be extremely complex to index and sometimes multiple commensurate or incommesurate propagation vectors needed. Taking the simplest case of the presence of only one superlattice, the diffraction patterns may be described by one modulation vector. In such case the superstructure reflections can be written in the form $\mathbf{G} \pm m\,\mathbf{q}$, where **G** corresponds to basis vector to span all the main Bragg reflections and $\mathbf{q} = \alpha\,\mathbf{a^*} + \beta\,\mathbf{b^*} + \gamma\,\mathbf{c^*}$ or $\mathbf{q} = (\alpha, \beta, \gamma)$ is the primary modulation vector on the top of **G** vector to span all the superstructure reflections.

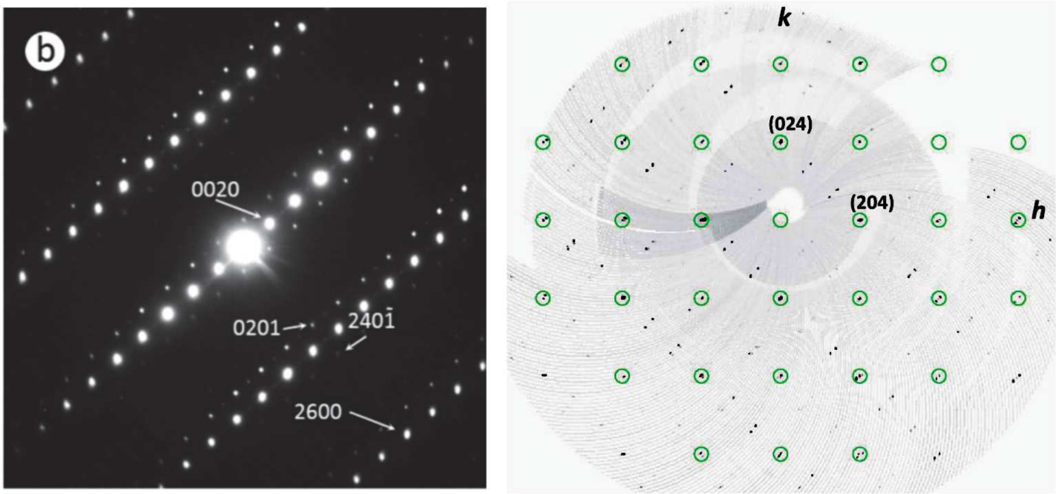

Figure 8.8: (Left) Electron diffraction pattern along the [210] zone axis $Pr_2NiO_{4+\delta}$. **Taken from FIG. 8(b) of ref.[76]**. (Right) Reconstructed *(hk4)*-plane, obtained by neutron diffraction on $Nd_2NiO_{4.25}$ two times twinned single crystal. Strong incommensurate reflections are observed in addition to the basic reflections (green circles) **Taken from FIG. 1 of ref.[18]**.

The TEM study by Wahyudi *et al.*[76] on the single crystal of $Pr_2NiO_{4+\delta}$ show presence of incommensurate reflection as shown in the Fig. 8.8. The whole pattern can then be indexed in (3 + 1) dimension with an incommensurate modulation vector $\mathbf{q} = 0.73\,\mathbf{a^*} + 0.53\,\mathbf{b^*}$ of order $m = 2$. The superstructure are highly dependent on the oxygen quantity. In that regard the problem arising from electron microscopy is related measurement condition of UHV and strong reducing e^- beam as it puts evidently some doubts on the real oxygen stoichiometry of the sample. The single crystal neutron diffraction by Ceretti *et al.*[18] on the homologous compound $Nd_2NiO_{4.25}$ show similar incommensurate superstructure which can be indexed with the modulation vector $\mathbf{q} = 0.4378\,\mathbf{a^*} \pm 0.2302\,\mathbf{b^*}$.

8.3.2 Impact on electronic structure

Beside structural complexity in $Pr_2NiO_{4+\delta}$ the interstitial oxygen also modify the electronic state of Ni ($Ni^{2+} \rightarrow Ni^{3+}$) in order to make the whole compound electronically neutral. This is atleast equivalent electronically to the hole doping in the Pr_2NiO_4 system by replacing the RE atom by alkali metal i,e $Pr_{2-x}Sr_xNiO_4$ for $x = 2\delta$. The total hole concentration in the very general case of non-stoichiometric Sr doped sample $Pr_{2-x}Sr_xNiO_{4+\delta}$ is $\epsilon = x + 2\delta$. While Sr-doping is obtained at high temperatures only, oxygen intercalation is a fully equivalent method to introduce holes into these non-stoichiometric oxides but instead can be done at ambient. Such hole doping induces very fascinating phenomena of charge or spin ordering in terms of phase separation of Ni^{2+} and Ni^{3+} in the shape of a stripe or checkerboard (CB). $Pr_2NiO_{4+\delta}$ and its hole doped analogue $Pr_{2-x}Sr_xNiO_4$ show a complex phase diagram with several electronically or structurally driven phase transitions. Hücker and Tranquada *et al.*[122] studied intensively the interplay between crystal symmetry and stripe order in $Pr_{2-x}Sr_xNiO_4$ as a function of temperature. These ordering phenomena arise in addition to the already complex phase diagram.

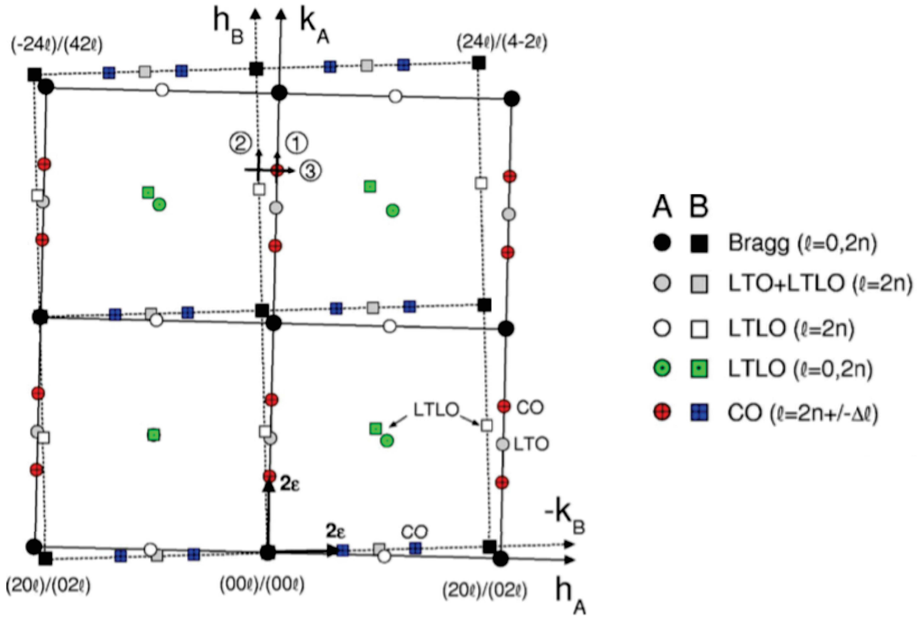

Figure 8.9: Scheme of the unidirectional charge ordering scheme as proposed Hücker *et al.*[122] from the syncrotron diffraction of twin single crystal of $Pr_{1.75}Sr_{0.25}NiO_4$. Projection along l of the *h,k* zone. Domain A: round symbols. Domain B: quadratic symbols. Tilt between the two domains exaggerated. Fundamental reflections are black, LTO superlattice peaks grey, LTLO superlattice peaks green (with dot) and white. The charge stripe peaks (CO) are red and blue (with cross), and appear at incommensurate positions, displaced by 2ϵ along k from Bragg peaks. Reflection conditions for l are indicated in the legend (right). l depends on the stacking order. **Taken from Fig.2 of ref.[122]**

Recent synchrotron X-ray diffraction study by Hücker *et al.* on $Pr_{1.75}Sr_{0.25}NiO_4$ suggest a tendency of unidirectional and 3D ordering of charge stripes[122] compared to other $RE_{2-x}Sr_xNiO_4$ system which is related to the presence of more orthorhombic strain in the NiO_2 layer for the small size of the Pr^{3+}. The incommensurate superstructure reflections always had a tendency to appear along the [010] direction of the orthorhombic cell in the $k \pm \epsilon$ positions (Fig. 8.9). The charge ordering temperature found to be $T_{co} \sim$ 240 K. The study also report from the temperature dependent investigation that around the charge ordering temperature $T_{co} \sim 240$ K the system show a lock-in transition towards the commensurate $\epsilon = 1/3$ modulation.

While very importantly Ishizaka *et al.*[123] studied the effect of heavy doping of Sr in the homologous $Nd_{2-x}Sr_xNiO_4$ ($0.33 \leq x \leq 0.77$). The study reveals the presence of commensurate checkerboard (CB)-type charge ordering for the composition $x \geq 0.5$ at much higher temperature ~ 480 K (210 °C) compared to the stripe ordering temperature ~ 180 K for lower Sr-doping. In fact the study report the CB charge ordering eventually taken over by an incommensurate type ($\epsilon = 0.44$) stripe order when cooling down from 480 K at around 180 K. The linear relation between the modulation and the hole concentration ($x \propto \epsilon$) does not hold any more beyond the doping limit $x \geq 0.5$. In this regard the most interesting system to investigate will be $Pr_2NiO_{4.25}$ which are electronically equivalent to $Pr_{1.5}Sr_{0.5}NiO_4$.

8.3.3 Impact on lattice dynamics

Lattice dynamics is becoming more and more acknowledged to play an important role for high diffusion of oxygen in $Pr_2NiO_{4+\delta}$ and related homologous series of compounds. The effect of interstitial oxygen has been investigated theoretically and experimentally. The study by Perrichon *et al.*[19] show lattice dynamics gets activated only in the presence of the interstitial oxygen and diffusion becomes more and more pronounce with the presence of more and more interstitial oxygen. Recently high resolution neutron diffraction study by Ceretti *et al.*[18] combined with Maximum Entropy (MEM) analysis revealed a direct observation of the complex situation of the local oxygen structure. The introduction of extra oxygen atoms (O_{int}) in the interstitial site (1/4, 1/4, 1/4) induces strong deviations to the apical oxygen atoms (O_{ap}) from their average position. The $O_{int}(O_{ap})_4$ tetrahedron is symmetrically increased, while the respective apical oxygen atoms are pushes into the [110]-directions with respect to the crystallographic F-cell, *i.e.* towards the next vacant interstitial lattice sites (see for more details in chapter 1). The large anisotropic displacement factors of the O_{ap} have been interpreted to be at least partially of dynamic origin leading to a phonon assisted fast diffusion of oxygen through the Pr_2O_2 rock salt layer as reported by the studies.

Also it becomes evident that the presence of higher amount of interstitial oxygen should provide a higher probability for oxygen diffusion by increasing the number of O_{ap} which are deviated towards the interstitial vacancy positions. Estimating the smaller size of Pr^{3+} with respect to the other RE *e.g.* La^{3+}, one might expect that the lattice mismatch and specifically the RE-O_{ap} distance does not favour the oxygen uptake limiting the oxygen uptake δ in $Pr_2NiO_{4+\delta}$ to be smaller. Despite $Pr_2NiO_{4+\delta}$ is reported to accommodate a maximum value of about $\delta \sim 0.25$ of interstitial oxygen. Compared to other $(RE)_2MO_{4+\delta}$ type compounds, $Pr_2NiO_{4+\delta}$ shows higher values of δ even at elevated temperatures. The study by Grimaud *et al.*[124] reported $Pr_2NiO_{4+\delta}$ to have $\delta \sim 0.1$ even at 1000 °C as shown in the Fig. 8.10. This might also be the reason for strongly enhanced oxygen mobility in $Pr_2NiO_{4+\delta}$ compared to the other La-based $(RE)_2MO_{4+\delta}$ compounds.

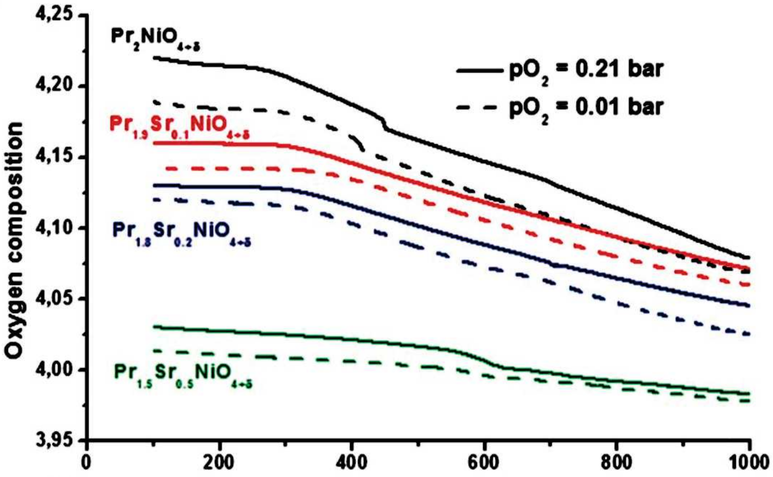

Figure 8.10: Thermal dependence of the oxygen non-stoichiometry under air (solid lines) and under $p^{O_2} = 10^{-2}$ bar (dashed lines). **Taken from Fig. 3 of ref.[124]**.

Theoretical lattice dynamics studies of $Pr_2NiO_{4+\delta}$ clearly evidences a push-pull diffusion mechanism between the apical and interstitial oxygen sites, which is activated due to the presence of interstitial oxygen[19,125]. Stoichiometric $Pr_2NiO_{4.00}$ does not show any oxygen diffusion even when coming to elevated temperatures. Similar study has been done on the homologous compound $Nd_2NiO_{4+\delta}$. For the latter compound a significant oxygen diffusion has been evidenced down to ambient temperature. The simulated values as activation energy barrier calculated by Benedek *et al.*[125] for different $RE_2NiO_{4.00}$ (Fig. 8.11) does not correspond to the experimental values where migration barriers for $Nd_2NiO_{4.00}$ found to be higher compared to $Pr_2NiO_{4.00}$[19].

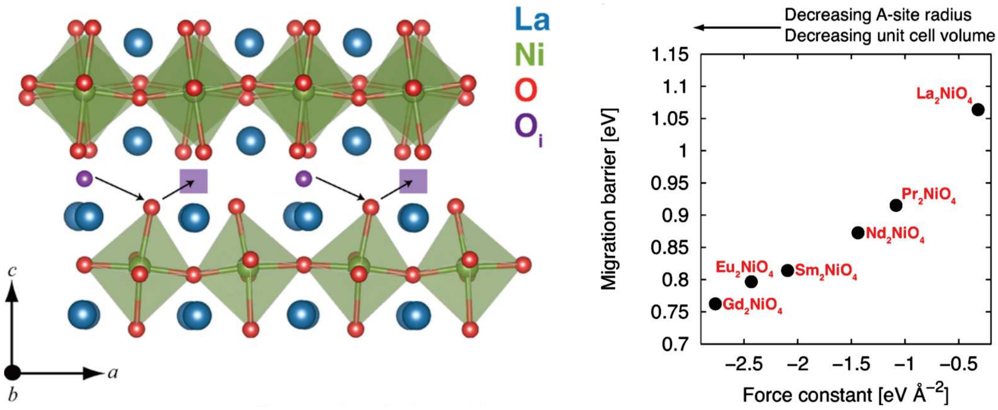

Figure 8.11: (Right) Migration barrier for oxygen diffusion via the interstitialcy pathway (as shown in the left figure) as a function of the force constant of the octahedral rotation mode. The migrating oxide ion O_i is depicted as a purple sphere, and the arrows show the direction of travel. The migrating oxide ion will displace the apical oxygen of the NiO_6 octahedron, which will move into the interstitial site denoted by the purple square. Note the tilting of the octahedra away from the interstitial.**Taken from Fig. 1 of ref.**[125].

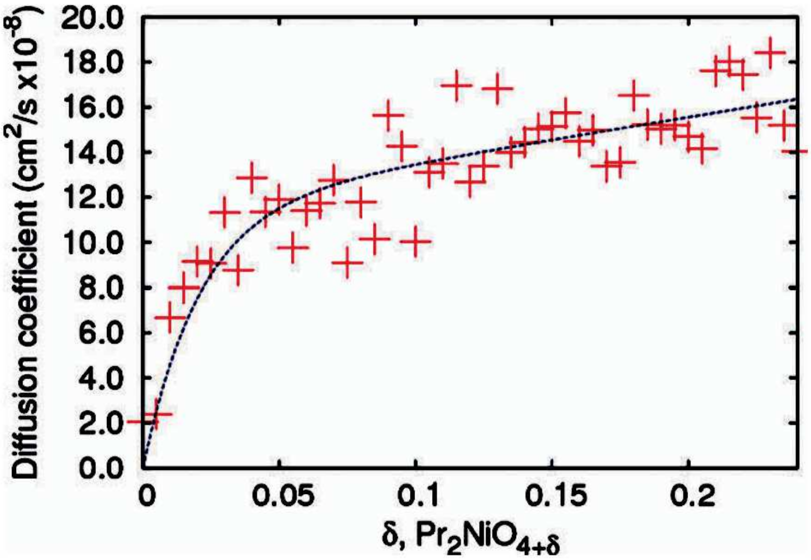

Figure 8.12: Calculated diffusion coefficient plotted as a function of delta for a series of simulations at 1100 K. The oxygen diffusivity, D, at a temperature T is given by, $D = [O_i] f exp(E_m/k_B T)$. Where $[O_i]$ is the concentration of oxygen interstitials, f is the correlation factor which in the study has been assumed to be constant, E_m is the energy barrier of migration and k_B is Boltzmann's constant.**Taken from Fig. 2 of ref.**[126].

The lattice dynamical study by Perrichon *et al.*[19] on $Nd_2NiO_{4+\delta}$ reveals one of the most intriguing issue is the presence of oxygen mobility down to ambient temperature which has been discussed to be affected as a function of the *c*-axis parameter (for more details see chapter 1). The increase of *c*-lattice parameter leads to a significant amplification of the O_{int} diffusion around its equilibrium value. The *c*-axis parameter becomes somehow important as it defines the thickness of the Pr_2O_2 rock salt layer, defining the potential of diffusion of the oxygen atoms. The phase diagrams discussed earlier show the *c*-lattice parameter increases with the increase of oxygen non-stoichiometry implying with the incrase of interstitial oxygen the oxygen diffusion must enhance. While the study by Parfitt *et al.*[126] show almost no effect of oxygen interstitial on diffusion as shown in the Fig. 8.12.

In order to better understand the oxygen diffusion pathways and associated structural changes, a study to follow up the oxygen intercalation/deintercalation reaction by *in situ* diffraction methods is mandatory. We therefore decided to investigate the electrochemical oxygen deintercalation reaction of as grown $Pr_2NiO_{4+\delta}$ single crystals with synchrotron diffraction, in order to analyze possible reaction intermediate phases and possible changes of the oxygen ordering in real time while the system stays under applied electrochemical potential and will be described in details in chapter 9. As already shown for $SrFeO_{3-x}$, The data collection on the single crystals using 2D detector as available in synchrotron source is very fast and allows to obtain an almost complete scanning of the reciprocal space. The single crystal was optimized in the shape of needles and *c*-axis was oriented along the axis of the needle to maximize the oxygen diffusion as much faster diffusion occurs in the (*a,b*)-plane, yielding optimized reactivity as a whole. The principal idea behind the experiment was not only explore the underlying reaction mechanism but also to follow the formation and changes in the oxygen ordering phases as well as to investigate changes in the microstructure on the course of reduction. The title compound is in this way a key system as it changes its symmetry from incommensurate orthorhombic ($Pr_2NiO_{4.25}$) to tetragonal ($Pr_2NiO_{4.12\pm\delta}$) and again orthorhombic for the stoichiometric $Pr_2NiO_{4.0}$ phase. Since almost all $Pr_2NiO_{4.25}$ crystals are twinned, we follow up of each volume fraction of the respective twin individuals with time. This gives important information regarding how the domain structure changes and also gives important indication regarding macro- or micro twinning. A permanently homogeneous distribution of all individuals would give a hint to micro-twinning. Such information on twinning behaviour also helps to conclude on possible importance or necessity of a huge amount of anti-phase boundaries for oxygen diffusion as discussed by Nemudry *et al.*[127].

8.4 Summary

In this chapter we have discussed in details the phase diagram of $Pr_2NiO_{4+\delta}$ from high temperature synthesis. At the stoichiometric limit $\delta = 0$, the structure is described in *Bmab* while at the highest non-stoichiometric limit $\delta \geq 0.16$ it shows the average orthorhombic structure model *Fmmm* and in between $0.058 \leq \delta \leq 0.065$ the structure is tetragonal $P4_2/ncm$. Preparation of $Pr_2NiO_{4+\delta}$ is extremely difficult as slight deviation from the stability filed (in terms of $P(O_2)$ & T) of this compound lead to the unwanted products like $Pr_4Ni_3O_{10}$, $Pr_2Ni_3O_7$ and $PrO_{2-\delta}$. Electrochemical reduction at ambient temperature give similar phase diagram as we will be discussed in more details in chapter 9.

The excess interstitial oxygen not only modifies the structure but also modify the electronic states and the lattice dynamics. The interstitial oxygen gets ordered on a commensurate or incommensurate superlattice. Besides the structural modifications the interstitial oxygen modifies the electronic states of Ni ($Ni^{2+} \rightarrow Ni^{2+}$) to make the whole compound electronically neutral and induces charge and spin ordering. The interstitial oxygen also influence the lattice dynamics of the system. We have discussed the phonon assisted oxygen diffusion at room temperature which makes them promising oxygen ion conductor and which gets only activated in the presence of interstitial oxygen.

Chapter 9

In situ electrochemical reduction: From $Pr_2NiO_{4.25}$ to $Pr_2NiO_{4.00}$

$Pr_2NiO_{4+\delta}$ is one of the model compounds to understand the low temperature oxygen mobility. In order to better understand the oxygen diffusion pathways and associated structural changes we have investigated oxygen intercalation/deintercalation reaction on single crystal of $Pr_2NiO_{4.25}$ by *in situ* synchrotron X-ray diffraction methods, in order to identify possible reaction intermediates and possible changes of the oxygen ordering in real time, while the system stays under applied electrochemical potential. The advantage of data collection on the single crystals over powder sample using 2D detector as available in synchrotron source is the possibility to obtain an almost complete reciprocal space. Also the fast data collection at synchrotron gives a huge potential to follow up changes in the whole reciprocal space almost continuously throughout the reaction.

The principal idea behind the experiment was not only to explore the underlying reaction mechanism but also to follow the formation and changes in the oxygen ordered phases. Also the superstructure intensities in this system related to commensurate or incommensurate modulation of oxygen/charge-spin discussed in chapter 8 are weaker by 10^{-4} to 10^{-5} times compared to the average structure intensities. From powder diffraction it is very difficult to work with such weak commensurate/incommensurate modulated intensities[26]. In this regard single crystal is much more convenient especially today with the availability of high resolution low noise area detectors as the reflections from single crystals appear separately in reciprocal space.

The other very important aspect was to investigate the changes in the underlying microstructure while intercalating (or deintercalating) the oxygen into (or from) the structure. Such knowledge is specially necessary for developing the new generation electrode materials for SOFC and also similar information are very important for battery materials. The single crystal gives the possibility to have such information much more conveniently compared to powder. Almost all the single crystals of $Pr_2NiO_{4.25}$ are twinned. They can have at maximum four twin individuals. The single crystal which was used for EC was four times twinned. We have followed the behaviour of the twin domain evolution on the course of EC reduction as will be discussed later in details. Also it was very astonishing to see that the single crystal could withstand the orthorhombic strain during the reduction reaction while it pass from a less orthorhombic *Fmmm* phase (orthorhombicity $\Delta_{Fmmm} = 0.74°$) to a high orthorhombic *Bmab* phase (orthorhombicity $\Delta_{Bmab} = 1.87°$) via tetragonal phase representing very high structural stability in terms of oxygen intercalation and deintercalation.

9.1 Experimental Strategies

The EC reduction was performed on a 50 μm size cylindrical shaped single crystal. The axis of the cylinder was aligned to be the *c*-axis of the unit cell by Laue diffraction. The reason to align the crystal in this way was to optimize oxygen diffusion in the (*a,b*)-plane where diffusion occurs almost 10^3 times faster compared to the diffusion along *c*-direction[18,66] and also the cylindrical shape helps to optimize the X-ray absorption problem. The electrochemical reduction was performed in a dedicated electrochemical cell specially adapted for the BM01A diffractometer in ESRF. The single crystal was used as cathode in the cell.

Diffraction was performed with a beam orientation perpendicular to the axis of the cylindrical crystal using wavelength 0.6631 Å. For each rotation of 0.1° of the single crystal around its axis, the diffraction pattern was framed using the high resolution Pilatus 2M area detector. Each frame was collected with an exposure time of 0.5 s. In total 2000 frames were collected for 200° rotation in ~17 min for each data set implying that the changes in the structure during the electrochemical reduction has been temporarily averaged over a time window of 17 min. The detail of the experimental set up for the data collection on BM01A diffractometer at The European Synchrotron has been described in chapter 2.

For electrochemistry 1N KOH was used. In principle the current required to reduce such small crystal in two days is about ~10 nA . But we noticed the sample even does not start reacting with such a small current. This could be related to a considerable amount of parasitic reactions. The sample starts reacting only with a current load of $\gtrsim 10$ μA which is almost 3 orders of magnitude higher than the calculated current. In that context the reaction is no longer galvanostatic but governed by its self controlled kinetics which does not correspond any longer on the current once activated. This was one of the draw backs to work with such a tiny single crystal as the structural evolution what has been investigated can not be particularly related to the electron transfer by following the equation below Eq. 9.1, hence oxygen stoichiometry but rather it will be described in terms of the reaction time.

$$Pr_2NiO_{4+\delta} + 2\delta e^- \Longleftrightarrow Pr_2NiO_{4.00} + \delta O^{2-} \tag{9.1}$$

9.2 Results and discussion

The electrochemistry was performed on the as grown single crystal of $Pr_2NO_{4.25}$. Before discussing the results of the EC reduction performed, we need the detail knowledge of the as grown single crystal regarding the structure and microstructure which we want to follow throughout the reaction. We will discuss first in details the structure and microstructure as obtained from synchrotron X-ray diffraction of the crystal. These information will be useful to understand how the structure evolves on the course of EC reduction.

9.2.1 Analysis of the $Pr_2NO_{4.25}$ single crystal used for EC

9.2.1.1 Analysis of the average structure

The diffraction pattern obtained on the as grown single crystal of $Pr_2NiO_{4.25}$ is shown in Fig. 9.1. All the strong reflection can be indexed in the orthorhombic *Fmmm* cell. Careful observation in the (*hk0*) plane shows splitting of all the main reflections which becomes clear at higher 2θ value (*i.e.* (-600) reflection). During the crystal growth while the $Pr_2NO_{4+\delta}$ pass through the phase transition from HTT phase in *I4/mmm* to the LTO in *Fmmm*, in order to minimize the energy of related to the stress in the system, the system forms twin domains. The number of twin domains formed depends on the crystal growth condition and also the quenching rate. In the present diffraction patterns in (*hk0*), the four splittings indicate the presence of four twin individuals. The reflections related to each twin domains have been indicated by the different color in the simulated (*hk0*) plane. All the strong reflection follow the extinction for *Fmmm* space group with *h, k, l* are all odd or all even. The basic reflections in the (*0kl*) and (*h0l*) planes, except (*00l*) type, are also four times splitted but they appear to be two times splitted because of the perpendicular projection.

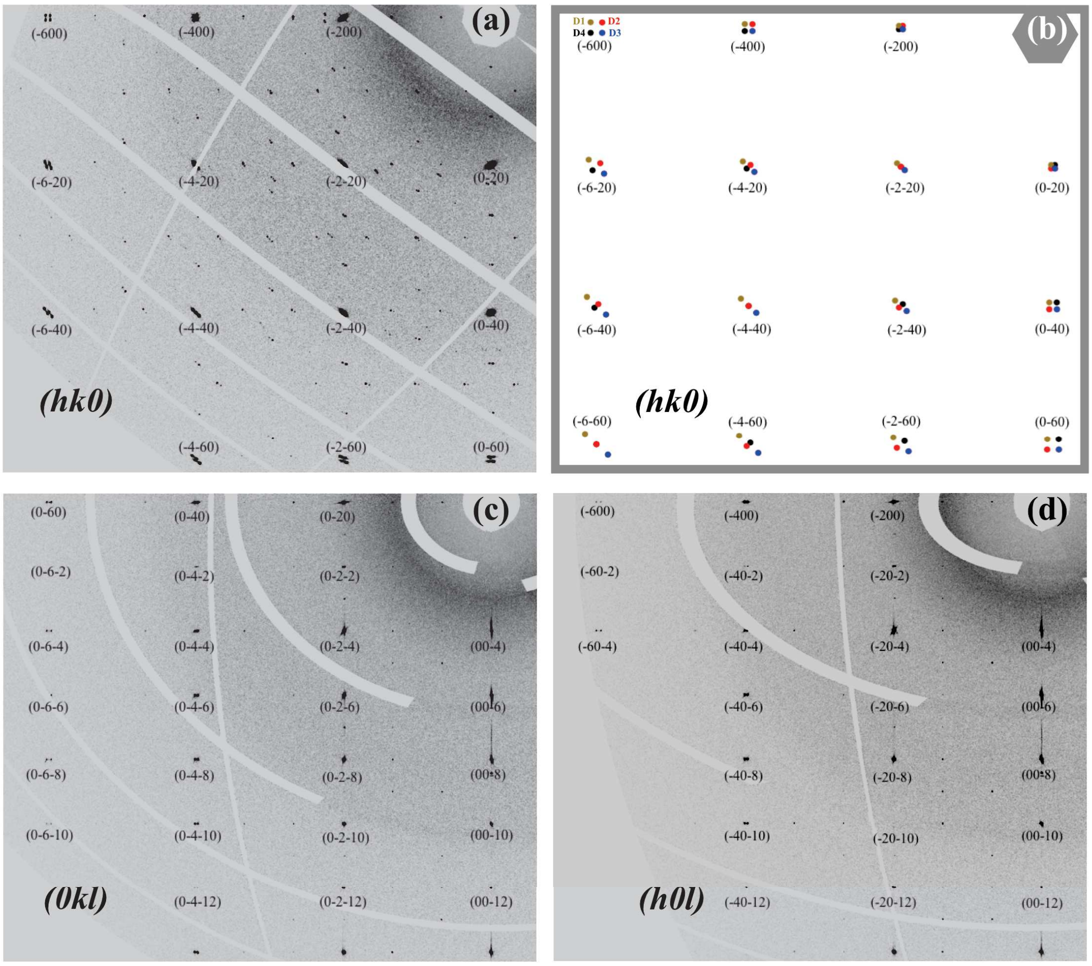

Figure 9.1: (a,c,d) Reconstructed principle planes (*hk0*),(*0kl*) and (*h0l*) as obtained from the synchrotron diffraction data of $Pr_2NO_{4.25}$ as grown single crystal indexed in the orthorhombic *Fmmm* cell . The splitting of the reflections in all the three planes are related to the twin domains. From (*hk0*) the presence of four twin individuals is recognizable. All reflections corresponding to four twins have been shown in different colors in the simulated (*hk0*) pattern (b). The splitting has been exaggerated for visibility. Olive ● and blue ● reflection are from domain D1 and D3 with common mirror plane [-*hh0*]. While black ● and red ● reflection are from domain D2 and D4 with common mirror plane [*hh0*].

9.2.1.2 Analysis of the superstructure

Though all the strongest reflections could be indexed in terms of the average orthorhombic *Fmmm* cell, there are a lot of weak reflections which could not be indexed with the average lattice. The proper origin of such individual superstructure reflection are very complex to assign as they can be from oxygen ordering and also from charge ordering of the Ni^{2+} and Ni^{3+} as we have discussed such example in chapter 8 as an effect of interstitial oxygen in structure. Both oxygen and charge ordering manifest themselves as a subtle distortion of the octahedra orientation. The correlation of such tilt in a long range give rise to such weak super structure reflections. This is the reason it can be very difficult to deconvolute the effect of oxygen and charge ordering. While for example the Sr-doping in $Pr_{1.5}Sr_{0.5}NiO_{4.0}$ creates electronically same situation for Ni, but in that scenario the Sr atoms do not necessarily need to order on a superlattice as the oxygen atoms do in case of $Pr_2NO_{4.25}$. In such case it would be interesting to observe the charge ordering in $Pr_{1.5}Sr_{0.5}NiO_{4.0}$ which is beyond the scope of this thesis.

We tried to index all the superstructure reflection positions and simulated corresponding diffraction patterns. All the superstructure reflections present in the (*hk0*) and (*hk1*) planes (see Fig. 9.2(top panel)) can be indexed in the (3+1) dimension superspace with the modulation vector $\mathbf{q}_1 = (\pm 5/6, 1/2, 0)$ of order $m_1 = 6$. The careful observation shows in the (*hk0*) plane the odd orders (m_1 = 1, 3, 5) are absent while there is no such extinction in the (*hk1*) plane. For better understanding we have also simulated the superstructure reflection positions in the (*hk0*) and (*hk1*) planes taking care of the contribution from all four twin domains. The different superstructure reflections corresponding to different twin domains are presented in different colors as shown in Fig. 9.2 (Bottom panel). Twin convention has been followed as earlier in Fig. 9.1. The D1 and D3 have common [-*hh0*] mirror plane and D2 and D4 have [*hh0*] as common mirror plane. The list of modulation vectors and lattice parameter used is given below:

Lattice parameters:
$a = 5.3968$
$b = 5.4532$
$c = 12.4422$
Modulation vectors used for each domain to simulate the (*hk0*) and (*hk1*) planes:
$q_{1a} = (+5/6, 1/2, 0); -q_{1a} = -(+5/6, 1/2, 0)$
$q_{1b} = (-5/6, 1/2, 0); -q_{1b} = -(-5/6, 1/2, 0)$

To index the superstructure reflections in the ($hk1/2$) plane a second modulation vector was necessary $\mathbf{q}_2$, *i.e.* the reflections can be indexed in the (3+2) superspace. As in this plane the main reflections are forbidden the superstructure reflections must be indexed with respect to the reflections present in the (*hk0*) and (*hk1*) planes. With respect to the (*hk0*) plane the second vector needed to the index the superstructure reflections in the ($hk1/2$) plane is $\mathbf{q}_2 = (\mp 1/4, 1/4, 1/2)$ of order $m_2 = 1$ while to index the superstructure reflections in the ($hk1/2$) plane with respect to (*hk1*) plane we need $\mathbf{q}_2 = (\mp 1/4, 1/4, -1/2)$. Both the (*hk0*) and (*hk1*) planes contribute to the ($hk1/2$) plane. The reconstructed ($hk1/2$) plane as obtained from the diffraction pattern is shown in Fig. 9.3. Corresponding reflection pattern has been simulated using two modulation vectors $\mathbf{q}_1 = (\pm 1/2, 1/6, 0)$ and $\mathbf{q}_2 = (\mp 1/4, 1/4, \pm 1/2)$ for four twin individuals and shown in Fig. 9.4.

Modulation vectors used for each domain to simulate the $(hk\,{}^1\!/\!_2)$ plane:

$$[q_{1a}+q_{2a}] = (+{}^5\!/\!_6, {}^1\!/\!_2, 0) + (-{}^1\!/\!_4, {}^1\!/\!_4, \pm{}^1\!/\!_2);\ -[q_{1a}+q_{2a}] = -[(+{}^5\!/\!_6, {}^1\!/\!_2, 0) + (-{}^1\!/\!_4, {}^1\!/\!_4, \pm{}^1\!/\!_2)]$$

$$[q_{1b}+q_{2b}] = (-{}^5\!/\!_6, {}^1\!/\!_2, 0) + (+{}^1\!/\!_4, {}^1\!/\!_4, \pm{}^1\!/\!_2);\ -[q_{1b}+q_{2b}] = -[(-{}^5\!/\!_6, {}^1\!/\!_2, 0) + (+{}^1\!/\!_4, {}^1\!/\!_4, \pm{}^1\!/\!_2)]$$

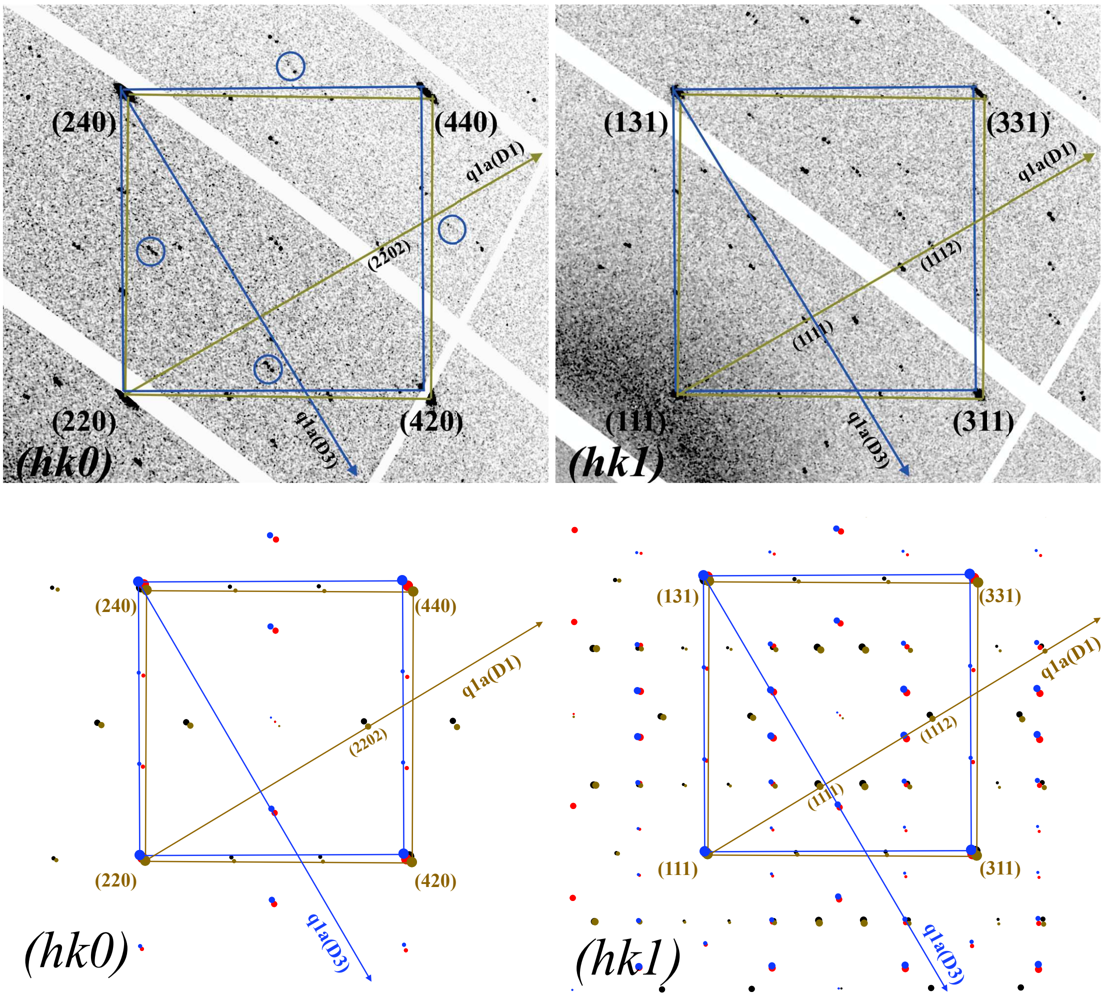

Figure 9.2: (Top panel) Reconstructed (*hk0*) and (*hk1*) planes obtained from synchrotron diffraction. The *Fmmm* cell for two twin domains out of four are denoted by the squares. All the superstructures (except the blue circled reflections which are related to intergrowth) can be indexed with commensurate modulation vector $\mathbf{q}_1 = (\pm{}^5\!/\!_6, {}^1\!/\!_2, 0)$ of order $m_1 = 6$. The odd orders $m_1 = 1, 3, 5$ are extinct in the (*hk0*) plane. In this figure q_{1a} is $(+{}^5\!/\!_6, {}^1\!/\!_2, 0)$. D1 and D3 denote two of the four twin domains present in the crystal as discussed earlier in this chapter. D1 and D3 are related by one mirror plane [-*hh0*]. The q_{1a} for the other two domains (D2 and D4) have not been presented for maintaining the simplicity of the figure. Indexation of reflections has been shown with respect to q_{1a}(D1) in the $(hklm_1)$ format where m_1 is the order of q_{1a}(D1). **(Bottom panel)** Simulated patterns corresponding to (*hk0*) and (*hk1*) taking into account all the four twin domains present. same twin convention followed as earlier in this chapter in Fig. 9.1. The D1 and D3 have common [-*hh0*] mirror plane and D2 and D4 have [*hh0*] has common mirror plane.

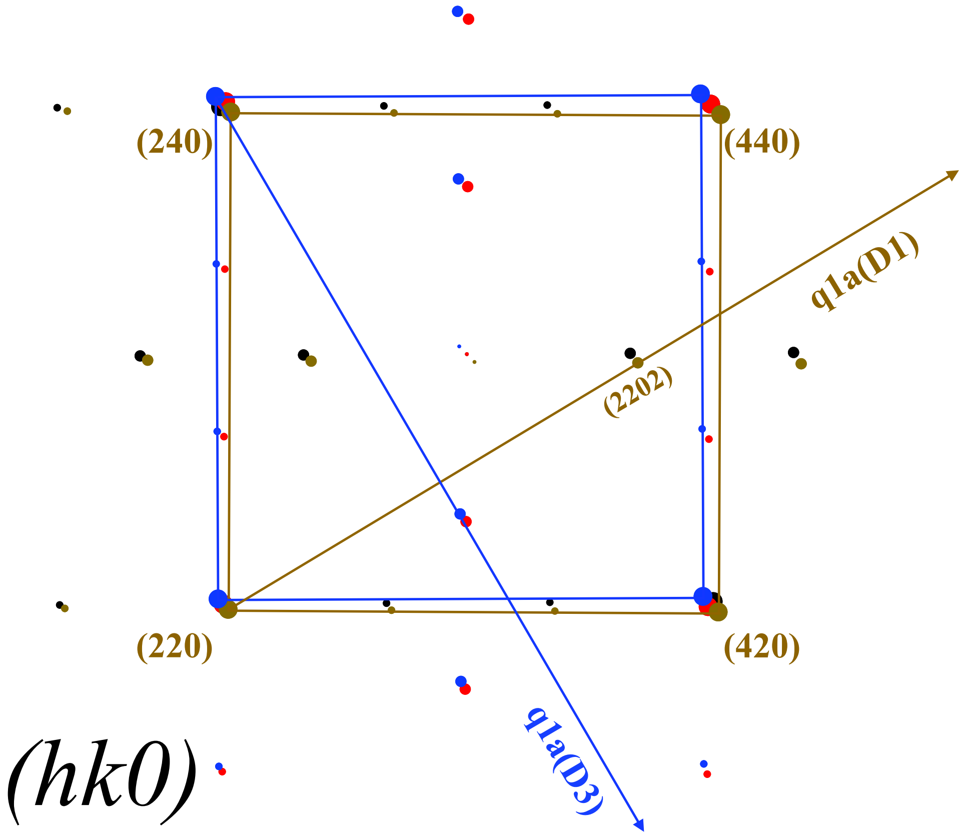
(240)
(440)
q1a(D1)
(2202)
(220)
(420)
(hk0)
q1a(D3)

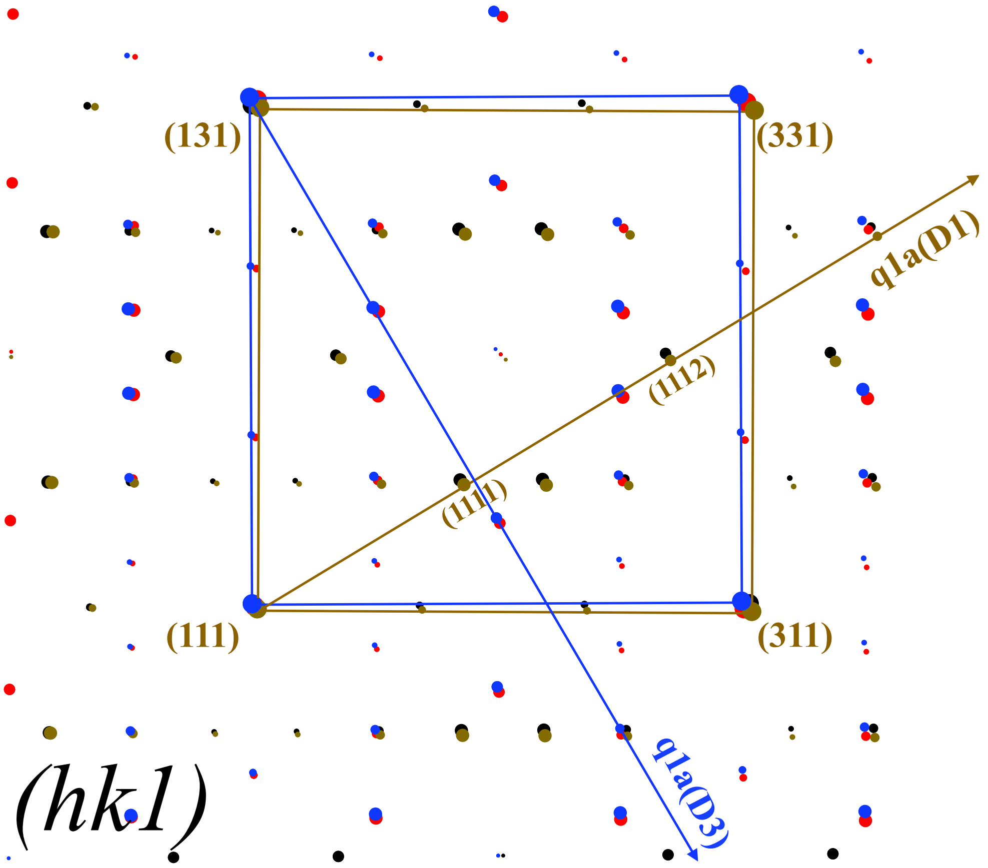
(131)
(331)
q1a(D1)
(1112)
(1111)
(111)
(311)
(hk1)
q1a(D3)

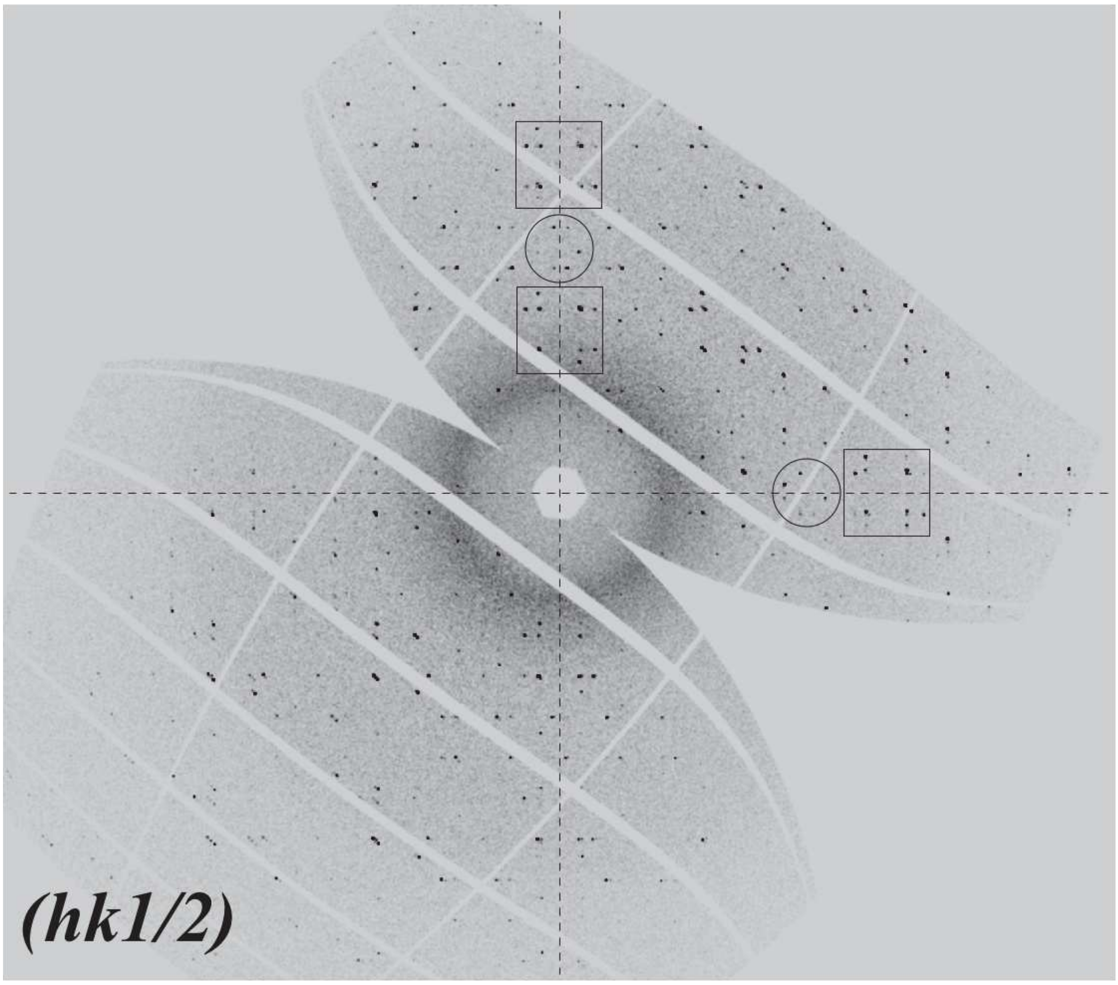

Figure 9.3: Reconstructed $(hk\,{}^1\!/_2)$ plane as obtained from the diffraction data. The super structure intensities are too feeble which is almost invisible in the centre of the diffraction pattern because of heavy background from quartz capillary and the electrolyte used for the electrochemistry. The circles and the boxes are used to guide the readers to compare the simulated reflection pattern $(hk\,{}^1\!/_2)$ using the two modulation vectors $\mathbf{q}_1 = (\pm{}^1\!/_2, {}^1\!/_6, 0)$ and $\mathbf{q}_2 = (\mp{}^1\!/_4, {}^1\!/_4, \pm{}^1\!/_2)$ for four twin individuals in Fig. 9.4

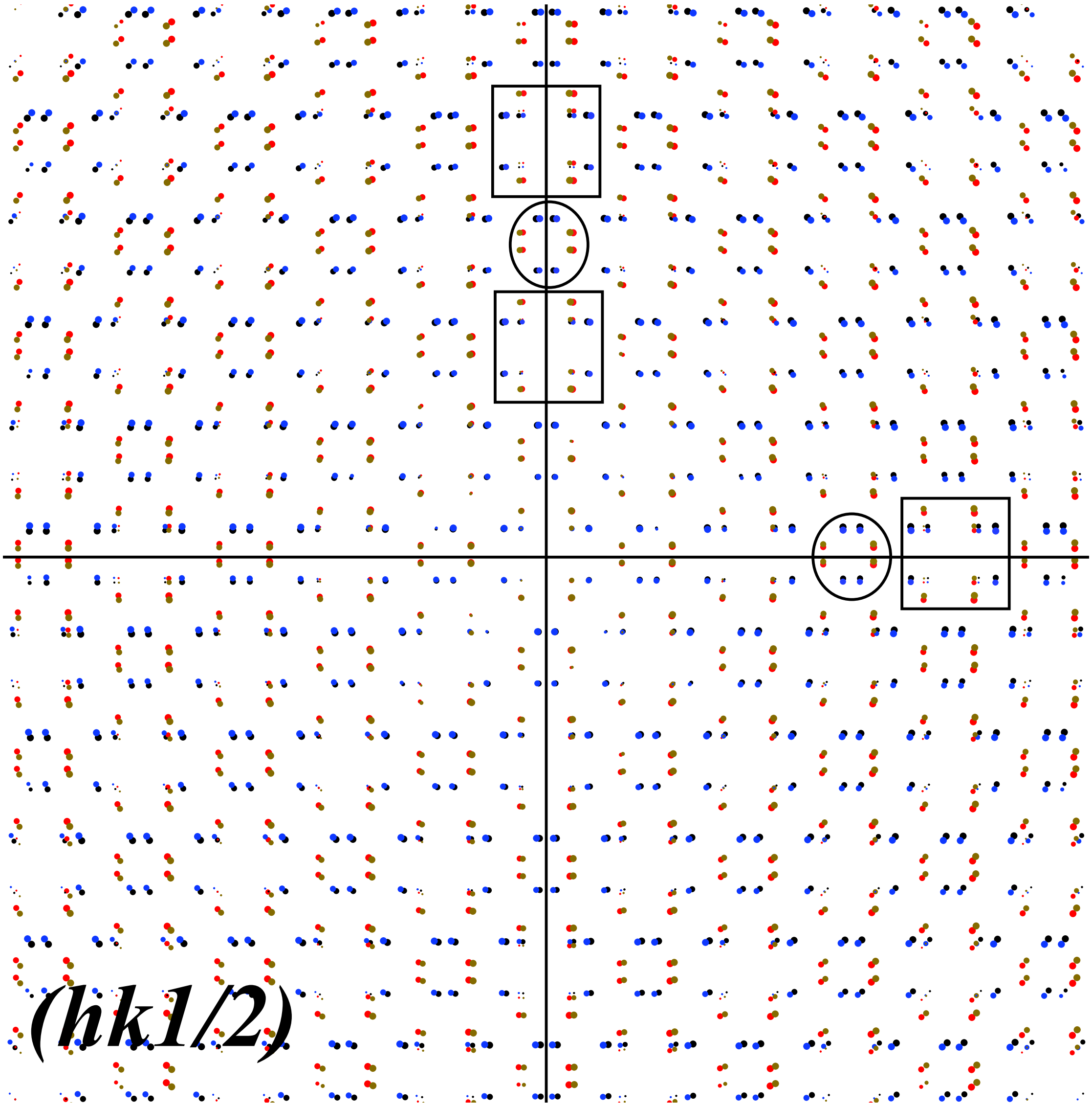

Figure 9.4: Simulated $(hk\,^1/_2)$ diffraction pattern. The circles and the boxes are used to guide the eye to compare the reconstructed plane pattern $(hk\,^1/_2)$ as shown in Fig. 9.3. Simulation is done using combinations of two modulation vectors $\mathbf{q}_1 = (\pm^1/_2, ^1/_6, 0)$ and $\mathbf{q}_2 = (\mp^1/_4, ^1/_4, \pm^1/_2)$ for four twin individuals.

$[q_{1a} + q_{2a}] = (+^5/_6, ^1/_2, 0) + (-^1/_4, ^1/_4, \pm^1/_2)$; $-[q_{1a} + q_{2a}] = -[(+^5/_6, ^1/_2, 0) + (-^1/_4, ^1/_4, \pm^1/_2)]$

$[q_{1b} + q_{2b}] = (-^5/_6, ^1/_2, 0) + (+^1/_4, ^1/_4, \pm^1/_2)$; $-[q_{1b} + q_{2b}] = -[(-^5/_6, ^1/_2, 0) + (+^1/_4, ^1/_4, \pm^1/_2)]$

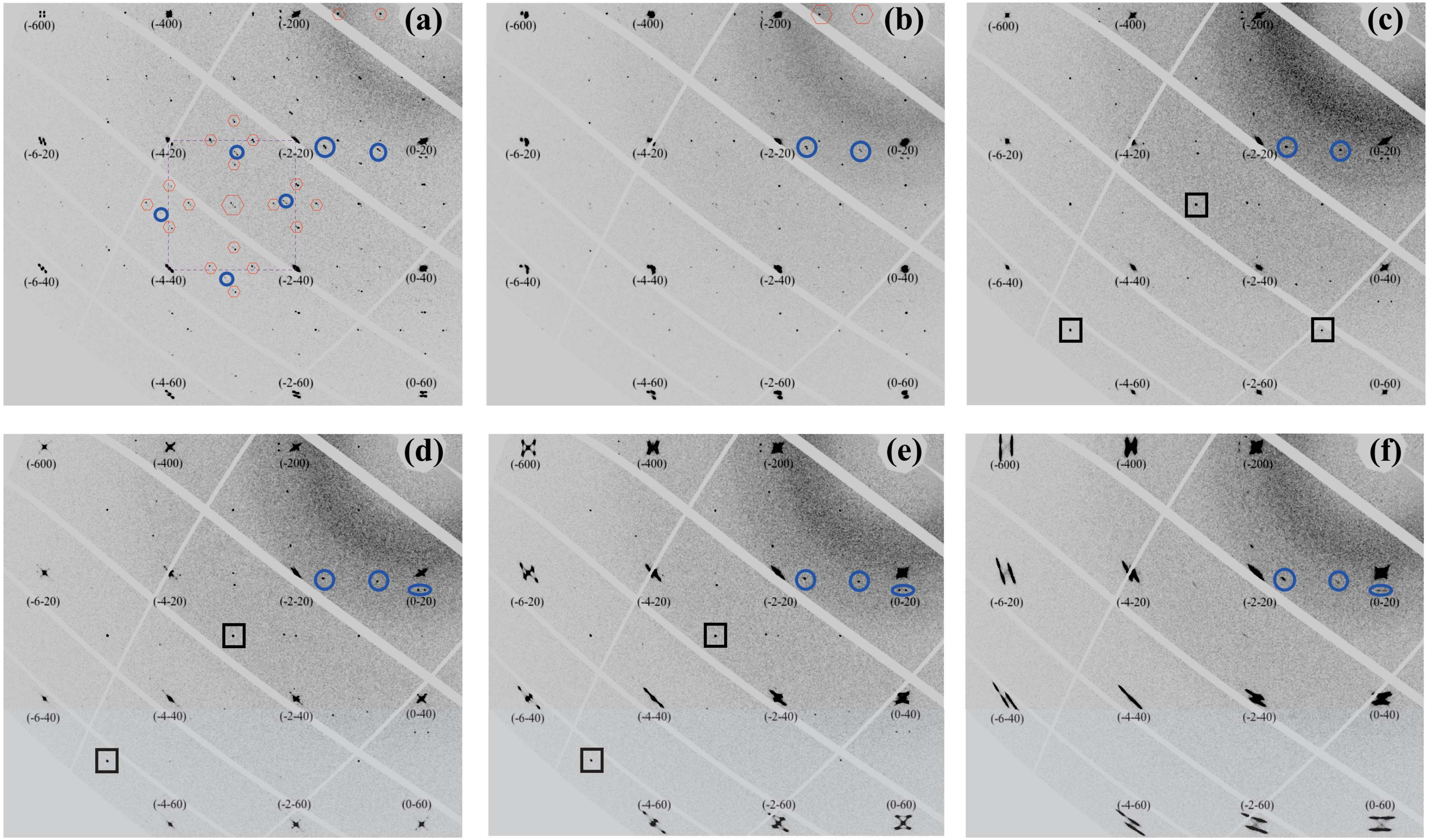

Figure 9.5: Evolution of the (*hk0*) diffraction pattern on the course of electrochemical reduction of $Pr_2NiO_{4+\delta}$. (a) starting orthorhombic phase in *Fmmm* with $\delta \sim 0.25$, (b) biphasic region *Fmmm* + *P4*$_2$*/ncm*, (c) the tetragonal pahse in *P4*$_2$*/ncm* for $\delta \sim 0.12$, (d-e) biphasic region *P4*$_2$*/ncm* + *Bmab* and (f) end orthorhombic phase in *Bmab* with $\delta \leq 0.05$. The basic *Fmmm* cell outlined by the dashed square in violet in (a). The reflection enclosed in the red hexagon in (a) represents the commensurate superstructures as discussed above. The *P*-type reflections of the tetragonal phase are enclosed in the black square. The blue circles show the reflections from intergrowth.

9.2.2 Analysis of *In situ* electrochemical reduction

The structural evolution of the $Pr_2NiO_{4+\delta}$ has been followed on the course of oxygen deintercalation. As discussed earlier the reaction was self controlled by its kinetics once it was activated by applying a constant current which was almost 3 orders of magnitude higher compared to calculated current. The phase transitions involve the structural and micro-structural modification and will be described as a function of reaction time.

9.2.2.1 Structural evolution

The structural evolution was investigated by following the changes in the (*hk0*) plane during the EC reduction. Fig. 9.5 summerizes all the principle changes occur during the oxygen deintercalation. Fig. 9.5(a) shows the diffraction pattern of the starting phase $Pr_2NiO_{4.25}$. All the reflections could be indexed in the *Fmmm* space group. The splitting of the basic reflections are related to four twin domains. The diffraction patterns also show plenty of superstructure reflections related to the excess oxygen or charge ordering and can be indexed in a (3+2) dimensional superspace as described earlier in this chapter.

Fig.9.5(c) represents the diffraction patterns corresponding to the tertragonal phase in $P4_2/ncm$ for $Pr_2NiO_{4.12\pm\delta}$. As can be seen from the diffraction pattern all the splitting vanishes due to transition from the orthorhombic phase to tetragonal phase. The appearance of the *P*-type reflection was very clearly visible confirming the tetragonal phase $P4_2/ncm$ in the *P*-lattice. These *P*-type reflections are related to the correlated tilt pattern of the octahedra in the diagonal direction as discussed in chapter 8 and in general very feeble compared to the basic reflections related to HTT phase. The important changes was observed on the disappearance of the superstructure reflections. In the course of the reduction the commensurate superstructure reflections vanish without changing the reflection positions which indicate that the commensurate modulation vector as discussed before did not change with the change of the oxygen content during the electrochemistry.

We followed the intensity of such commensurate superstructure reflection *e.g.* (-0.667, 0, 0) (chosen for its convenient position for intensity integration) to investigate how the intensity drops in relation to the appearance of the *P*-type reflection *e.g.* (-5 -5 0) (chosen for the convenience of intensity integration) of the intermediate tetragonal phase as a function of the reaction time and has been shown in Fig. 9.6. The figure shows the superstructure intensity vanishes almost simultaneously with the appearance of the tetragonal phase. At the beginning the relatively lower intensity of the superstructure as can be seen in Fig. 9.6 is related to the crystal mosaicity. As the synchrotron X-ray flux was normalized for integrating the intensity which rules out the possibilities of the changes in the flux of the synchrotron X-ray beam. The other possible reason can be the

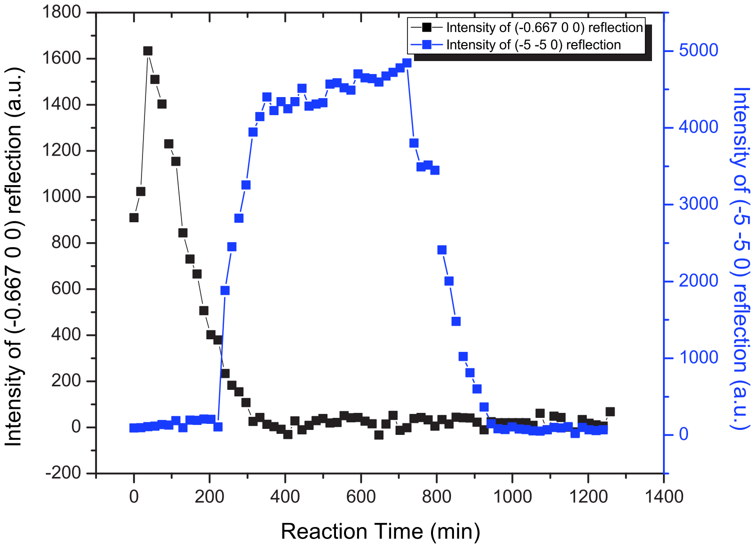

Figure 9.6: Intensity evolution of the superstructure reflection (-0.667 0 0) related and of the *P*-type reflection (-5 -5 0) belonging to the tetragonal intermediate phase.

perfectness of the crystal. Before starting the electrochemical oxygen deintercalation the crystal was too perfect and the lower intensity is related to the multiple reflection extinction. The degree of perfectness of the crystal diminishes immediately after applying the current with increase of mosaicity due to oxygen removal. The other aspect which is very important as can be seen from the plateau on the intensity profile for *P*-type (-5-50) reflection. Such plateau indicates the existence of the tetragonal phase for wide range of oxygen stoichiometry. As the reaction was not galvanostatically controlled, it was not possible to assign the non-stoiciometry range instead it has been indicated as $Pr_2NiO_{4.12\pm\delta}$. There were certain reflections encircled in blue in the figure which remains almost inert throughout the electrochemical reduction. These reflection were related to the intergrowth phases.

Fig.9.5(b) represents the biphasic region *Fmmm* + *P4₂/ncm*. As can be observed from the diffraction pattern some of the twin domains already started disappearing. Also the intensity of the superstructure reflections dropped. Fig. 9.5(d,e) represents the second biphasic region *P4₂/ncm* + *Bmam* before the appearance of the final orthorhombic line phase *Bmab*. All the reflections splits again due to the appearance of the new orthorhombic phase with much higher orthorhomicity. As can be seen from Fig. 9.5(e), in the (-600) reflection, the central intensity is related to the reminiscent tetragonal phase while the outer four reflection are related to the appearance of the new the orthorhombic phase in *Bmab*. The newly appeared orthorhombic phase have also four twin domains. The diffuse intensities in (-600) reflection spot between the central peak (belonging to the tetragonal phases) to the outer four peaks (belonging to the newly appeared orthorhombic phases) can be related to a coherence length problem of synchrotron X-ray used with length scale of the microscopic changes in the domains or can be an effect of structural strain due to the change in orthorhombicity. Fig. 9.5(f) shwos the diffraction pattern of the final orthorhombic *Bmab* phase with $\delta \lesssim 0.05$. All the *P*-type reflections related to the tetragonal phase disappeared. The crystal goes though a huge structural strain due to the change of othorhombicity almost three times of the starting orthorhombic phase $\Delta_{Bmab} \sim 3 \times \Delta_{Fmmm}$. It was surprising to see that even after passing through such huge structural strain, the crystal was intact until the end of the reduction. In any case we want to underline that a quantitative interpretation of the intensity data is difficult, as the absorption of $Pr_2NiO_{4+\delta}$ at $\lambda = 6631$ Å is rather high ($\mu_{im} = 26.14\ \text{cm}^{-1}$) yielding a transmission of about 29% for a crystal of 50 μm diameter. This also concerns quantitative analysis of the volume fractions of the twin domains, as one needs to know the locations of the corresponding twin domains inside the crystal, which are almost impossible to determine.

9.2.2.2 Microstructural evolution

During the EC reduction of the $Pr_2NiO_{4.25}$ single crystal, the crystal pass through the phase transitions from less orthorhombic *Fmmm* to tetragonal *P4$_2$/ncm* followed by the next orthorhombic phase in *Bmab* with much higher orthorhombicity. The identification of such phases were very evident just by looking at the $(\pm h00)$ or $(0 \pm k0)$ type reflections where the reflections are four times splitted (Fig.9.5(a)). At higher 2θ value the splitting is clearly visible (*i.e.* (-600) reflection). The intensities corresponding to each of four splitted reflections are proportional to the volume fractions of the four twin domains. Over the EC reduction the intensity of such reflection evolves and during the phase transition to the tetragonal phase all of the reflections vanished and the reflections related to the tetragonal phase appear. Further reduction towards the final orthorhombic phase leads to the splitting of the reflections again into four corresponding to the new orthorhombic phase.

We have followed intensities of four splitted reflections at (-600) reflection position to see how the relative volume fractions of the twin domains evolve during EC reductions and summarized in Fig. 9.7. Fig. 9.8 shows semi-quantitative analysis of how the (-600) reflection evolves along with the oxygen deintercalation. The twin domains we assigned with respect to their connecting mirror planes and followed in the same setting through out the reduction. Twin domains D1 and D3 are related by the mirror plane (*-hh0*) where as the domains D2 and D4 are related by the mirror plane (*hh0*). Fig. 9.8(b) shows that in the starting phase the twin domains D1 and D3 are stronger compared to the D2 and

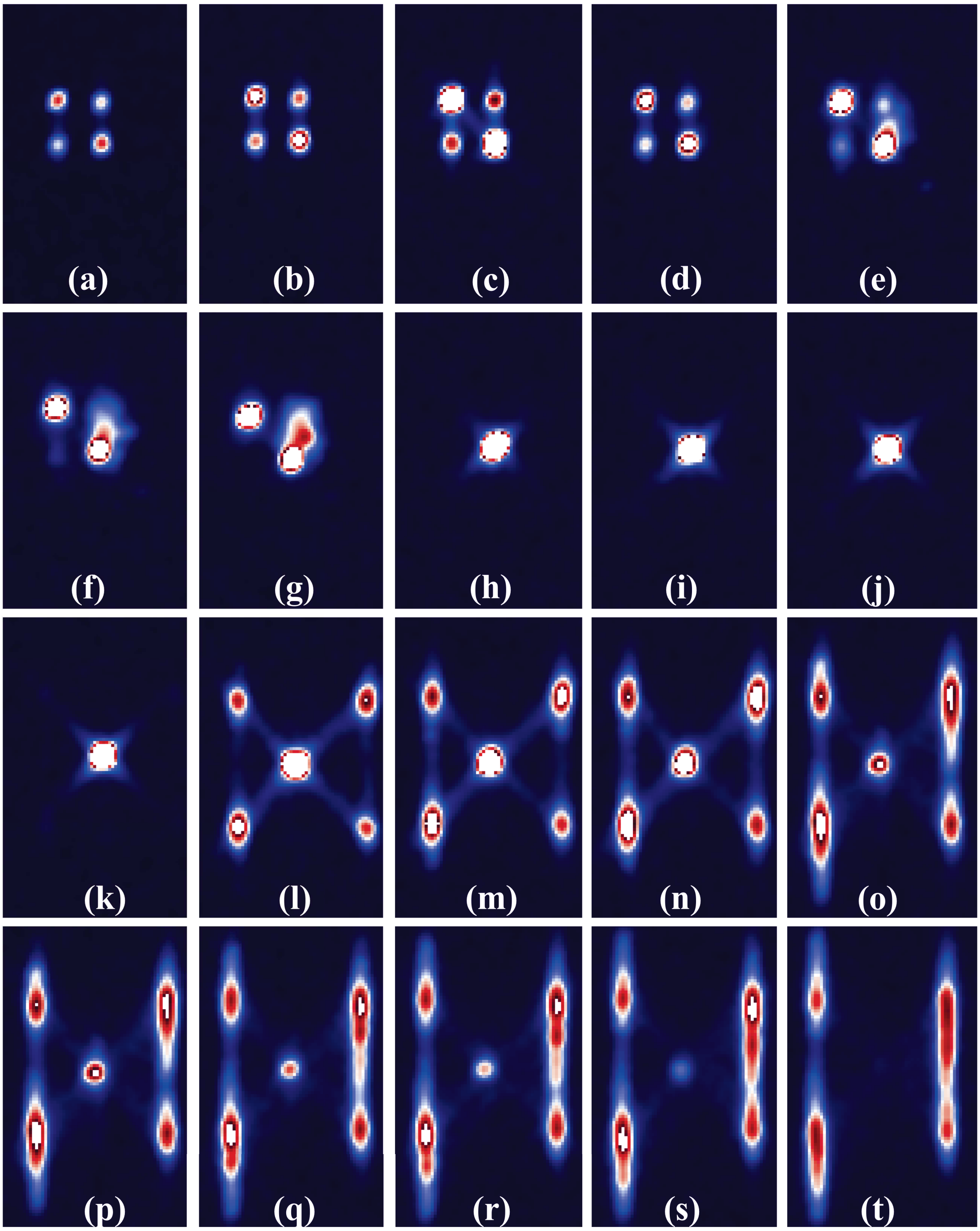

Figure 9.7: Evolution of the twin domains investigated via the observation of (-600) reflection. ((a)-(e)) correspond to orthorhombic *Fmmm* phase; ((f),(g)) correspond to the biphasic region of *Fmmm* + $P4_2/ncm$; ((h)-(k)) correspond to $P4_2/ncm$; ((l)-(s)) correspond to next biphasic region $P4_2/ncm$ + *Bmam* and (t) corresponds to the final *Bmab* phase.

D4. The weaker domains (D2 and D4) disappeared immediately with the appearance of the tetragonal phase while the stronger domains (D1 and D3) were still present. The time scale of the appearance of the tetragonal phase is very close to what has been found

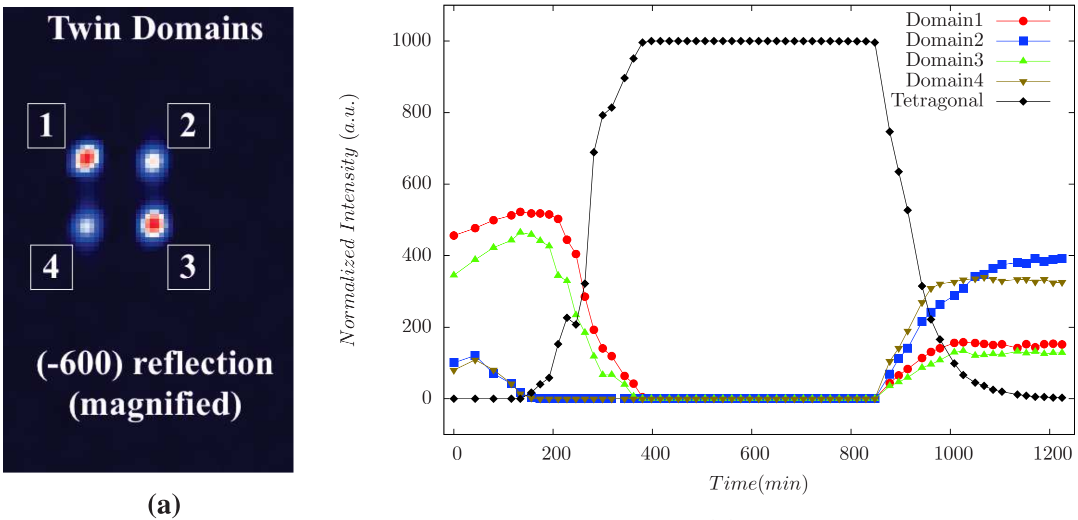

(a)

(b)

Figure 9.8: (a) Enlarged (-600) reflection from the diffraction pattern of $Pr_2NiO_{4.25}$ in *Fmmm* phase showing how the twin domains are assigned. D1, D2, D3 and D4 represent the four twin domains. D1 and D3 are related by the [-*hh0*] mirror plane where as D2 and D4 are related by the [*hh0*] mirror plane; (b) shows the evolution of the relative volume fractions ($\propto$ intensities) of the twin domains corresponding to orthorhombic phases and the tetragonal phase.

by following the appearance of the *P*-type (-5-50) reflection in Fig. 9.6. The anomaly related to the slight increase in the intensities in the range of first ~200 min is related to the change of the mosaicity of the crystal from a very perfect (less mosaic) to less perfect (more mosaic) due to oxygen deintercalation and have been discussed earlier in this chapter while discussing the evolution of the superstructure reflection in Fig. 9.6. Due to extinction from multiple reflection inside the perfect crystal the intensities were low at the beginning. On the course the of EC reduction during the oxygen deintercalation as the crystal mosaicity increases the intensities of the all reflections also increased but immediately after it went down due to the decrease of the volume fractions of the different domains.

The final orthorhombic phase appears almost at the same time while the intensity related to the tetragonal phase went down. The upcoming orthorhombic phase also had a domain structure with four individuals. Keeping the same reference of the twins related to the two mirror planes *i.e.* D1 and D3 having the common (-*hh0*) mirror plane and D2 and D4 having common (*hh0*) mirror plane, we have noticed some astonishing behaviour regarding the evolution of the volume fractions of different domains. The strong twin domains D1 and D3 with bigger volume fractions in the starting orthorhombic *Fmmm* phase became weaker (less volume fraction) in the final orthorhombic phase *Bmab* while the weaker domains D2 and D4 with less volume fractions in the starting orthorhombic *Fmmm* phase became stronger (bigger volume fractions) in the end. It apparently indicates that the system lost its all past memory regarding the domain structure while passing through the tetragonal phase and the microstructure changed considerably.

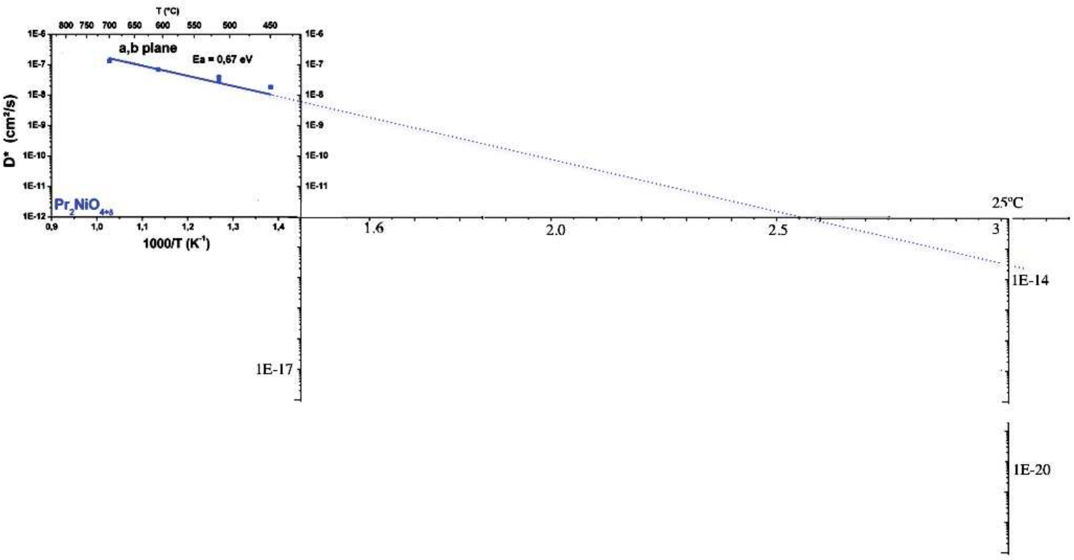

Figure 9.9: Linear extrapolation of the oxygen diffusion coefficient to RT measure on single crystal $Pr_2NiO_{4.25}$ in high temperature range (solid blue line). The dotted line represent the extrapolation to room temperature. **Figure is taken from the ref.[66] and modified according to the necessity.**

9.2.2.3 Estimation of diffusion coefficient

The whole reaction was completed in less than 20 hours in a [50 μm × 50 μm × 400 μm] which was considerably very fast diffusion. The anisotropic oxygen diffusion study by Bassat *et al.* on the single crystal of $Pr_2NiO_{4+\delta}$ at high temperature range showed that the diffusion coefficient is 10^{-8} cm^2s^{-1} at 450 °C in the (*a*,*b*)-plane. Linear extrapolation of such measurement to room temperature expects the diffusion coefficient to be 10^{-14} cm^2s^{-1} (see Fig. 9.9)[66]. While very approximate estimation of the diffusion coefficient in the (*a*,*b*)-plane for the single crystal (oriented along *c* direction) used for EC by using Einstein's Diffusion equation and taking the mean free path for the oxygen diffusion to be similar to the 25 μm (radius of the cylindrical crystal used) would give a diffusion coefficient of 10^{-11} cm^2s^{-1}, already 3 orders of magnitude higher compared to the extrapolated value. Which gives a hint that at low temperature the lattice dynamics plays an impotant role. The sallow level lattice modes are responsible for fast diffusion through the lattice via push-pull mechanism. In the presence of such high oxygen diffusion in the oriented single crystal even at room temperature, one can easily anticipate potential use of the thin film of such materials as SOFC electrode, oxygen membrane where the nanometer size thin film of can be reduced or oxidised in almost no time.

9.3 Summary

In this chapter we have discussed the *in situ* elctrochemical reduction of the $Pr_2NiO_{4.25}$ single crystal. The structure pass through clearly three distinct line phases from average *Fmmm* to the tetragonal $P4_2/ncm$ to the final orthorhombic phase *Bmab* at the stochiometric limit. The phase transitions have been verified by looking at the splitting and the calculated orthorhombicity of the (*h00*) and (*hh0*) type reflections. Even after passing from a low orthorhombic *Fmmm* phase to the final orthorhombic *Bmam* phase with orthorhombicity 3 times higher, the crystal stability was remarkable. We have also investigated the super structure in the *Fmmm* phase related to the oxygen ordering which found to be commensurately modulated for the present single crystal with 4 twin individuals. In the course of electrochemical reduction the commensurate modulation vector **q** did not change but the intensity drops down quickly as the intermediate tetragonal phase $P4_2/ncm$ starts to grow. The intensity evolution of the *P*-type reflection corresponding to the tetragonal phase reveals that the tetragonal phase exists over a wide range of oxygen stoichiometry. The domain structure followed from the 4 splittings of the (-600) reflection shows surprising behaviour of the domain evolution. The two out of the 4 twin domains present in the crystal and related to a common mirror plane, which were weak in the in the *Fmmm* phase, become stronger at the final orthorhombic phase after the eletrochemical reduction. The system undergo a complete memory loss regarding the volume fractions of the domains during the phase transition via tetragonal phase and the underlying microstructure gets modified. Finally we have estimated the fast diffusion coefficientin $Pr_2NiO_{4+\delta}$ which is almost 3 orders of magnitude higher compared to what one would expect from classical Arrhenious theory at RT. This gives a hint to the important role of lattice dynamics for oxygen diffusion at low temperature.

General conclusion

The principal aim of this thesis was to investigate reaction mechanisms of the oxygen uptake and release in transition metal oxides, namely $SrFeO_{3-x}$ and $Pr_2NiO_{4+\delta}$. Both systems have already been investigated intensively, related to their interesting physical properties, but also as they have been shown to intercalate oxygen reversibly in important stoichiometric quantities at already ambient temperature, controlled by electrochemical methods. This makes them as a perfect object to investigate the underlying reaction mechanism in order to explore the respective underlying phase diagram and phase stabilities, especially concerning reaction intermediates under applied electrochemical potential, but also in terms of changes of the microstructure. To this end the original aspect here was to investigate these reactions on oriented single crystals in an especially designed electrochemical cell, allowing to follow up under *in situ* conditions the intercalation/deintercalation process, while scanning the whole reciprocal space in good resolution and sufficient scattering intensity to allow detection of even diffuse scattering. In order to avoid complications related to reaction kinetics, very tiny single crystals down to 30 μm thickness needed to be used for all electrochemical experiments.

A huge experimental effort was thus devoted to optimize the experimental conditions in terms of crystal preparation, *i.e.* their orientation and down shaping to the required size and gluing with a conductive paste on a 50 μm thick gold wire. The as prepared crystals were then put into the electrochemical cell and many tests were necessary to optimize the reaction conditions. The electrochemical cell allowed to explore the reciprocal space by carrying out oscillations of 360° around the direction of the crystal/capillary, which turned out to be fully sufficient for the information needed. The cell as optimized is the first one which was reported to follow up a complete chemical solid state reaction by *in situ* diffraction methods.

Although known since more than 5 decades, the phase diagram of $SrFeO_{3-x}$ is still under debate. One reason for this is that for the four phases with $x = 0$, 0.125, 0.25 and 0.5 reported in the literature, those with $x = 0.125$ and 0.25 are difficult to adjust for the oxygen content. Another point which was of special interest here is also to find out whether oxygen vacancy ordering occurs during the oxygen intercalation at ambient temperature, as was reported for the synthesis under controlled oxygen partial pressure at elevated temperatures. Since Nemudry *et al.* were able to identify the two intermediate phases by Mössbauer spectroscopy but not by diffraction methods (laboratory powder X-ray), the challenge here was to clarify if oxygen vacancy ordering is obtained instantly on a long range scale or it is limited to local dimensions only. For all $SrFeO_{3-x}$ phases we described for the first time a complete relation of the different twin individuals of the pseudo-merohedral twinning of $SrFeO_{2.5}$ and $SrFeO_{2.75}$ related to its orthorhombic symmetry, as well as the merohedral twinning of $SrFeO_{2.875}$ showing tetragonal symmetry. The related consequences due to the overlap of different twin individuals crystal have been analysed with a self-written program which was indispensable to treat the complex attribution of reflection overlap.

During the electrochemical oxidation of $SrFeO_{2.5}$ towards $SrFeO_3$ the two reaction intermediates $SrFeO_{2.75}$ and $SrFeO_{2.875}$ could be unambiguously identified as different phases showing 3D oxygen vacancy ordering. The identification of both phases was difficult due to the twinning, possible changes of the twin individuals in the course of the reaction and related reflection overlap of different twin individuals. It could also be demonstrated that the number of the number of twin individuals changed, as four out of possible twelve individuals were found for the $SrFeO_{2.5}$ starting phase, and which were kept to four individuals for the $SrFeO_{2.75}$ phase, while for the $SrFeO_{2.875}$ phase only two twin individuals were expected consequently. From the reconstruction of the three equivalent $(hk\,^1\!/_4)$ type planes of the tetragonal $SrFeO_{2.875}$ phase, the appearance of a new $(hk\,^1\!/_4)$ plane, not expected for the underlying twin structure of the starting phase could have been clearly identified. This is an important issue, not because it can not obtained by powder diffraction methods, but as it clearly shows that these type of microstructural changes allow to conclude up to which extent the reaction mechanism is pure *topotactic* or not. In this case it could be shown that the important rearrangements of the apical and equatorial oxygen atoms induced during the *topotactic* oxidation from $SrFeO_{2.5}$ towards $SrFeO_{2.75}$, imply important structural changes, which in fine lead upon further oxygen uptake to the change of the number of twin domains in a *non-topotactic* reaction.

On the other hand the real structure of $SrFeO_{2.5}$ has been demonstrated to adapt on an average scale the *Imma* space group and not, as recently proposed, a *Pbma* symmetry. The important detail related to this fact is that the *Pbma* symmetry implies an ordered tetrahedral $(FeO_4)_\infty$-chain arrangement, while in *Imma* a statistical disorder of these chains is found, with split positions of the equatorial oxygen atoms and the Fe atoms. These results confirm what has been observed by high resolution TEM investigations. The differentiation between the two space groups becomes evident from the appearance of characteristic diffuse rods in the ($hk\frac{1}{4}$) planes, which transform into defined reflections for the $SrFeO_{2.75}$ and $SrFeO_{2.875}$ phase respectively upon electrochemical oxidation.

While the oxygen uptake at ambient temperature reveals the existence of two distinct intermediate phases, namely $SrFeO_{2.75}$ and $SrFeO_{2.875}$, the oxygen uptake at elevated temperature yields spontaneously at around 300 °C the $SrFeO_{2.875}$ phase without passing through the $SrFeO_{2.75}$ phase. This is most probably due to kinetical reasons, while under the performed heating conditions in air, the fast data collection on beamline BM01A can be excluded to be the limiting factor to eventually having overseen the $SrFeO_{2.75}$ intermediate. Surprisingly the $SrFeO_{2.75}$ appeared upon cooling from the high temperature cubic Perovskite $SrFeO_{3-x}$. Probably both phases, $SrFeO_{2.75}$ and $SrFeO_{2.875}$, lie energetically very close and phase transitions related to temperature and simultaneous oxygen uptake/release might also be influenced by the temperature sequence, *i.e.* heating or cooling condition, associated by induced strain related to the twin structure and respective symmetry.

Finally we can confirm that oxygen vacancy ordering is observed during the electrochemical oxidation reaction to take place instantly at ambient temperature undergoing the same phase sequence as already obtained at elevated temperatures under different oxygen partial pressure. This is at first sight not obvious as some of the transitions completely modify the underlying microstructure and must be, to a certain extent, considered to have a reconstructive character. The stacking disorder in $SrFeO_{2.5}$, as indicated by the 1D diffuse rods of the octahedral/tetrahedral layers heals completely out with the oxygen intercalation, leading to well-defined $SrFeO_{2.75}$ and further $SrFeO_{2.875}$ oxygen vacancy ordered phases.

Diffuse rods have also been observed for the formation of $SrFeO_{2.875}$ and its further oxidation to the cubic $SrFeO_3$. This important issue goes along with the idea of a non-topotactic oxygen uptake, resulting in a more complex twin domain structure, although the overall twin domains appear macroscopically to three only. It becomes clear that extended defects in terms of phase boundaries are likely at the origin to observe diffuse lines for the (*h00*) type reflections indexed for the cubic Perovskite unit cell. This might also be a hint to explain the helimagnetic ordering below 130 K in nominally $SrFeO_3$ still with cubic symmetry, which is contradictory, and require a non-cubic space group.

The electrochemical reduction of as grown nominally $Pr_2NiO_{4.25}$ single crystals, observed by *in situ* diffraction with synchrotron radiation on BM01A had two main aspects: (i) to follow up the microstructural changes in terms of volume fractions of the different twin individuals for the orthorhombic → tetragonal → orthorhombic phase sequence while reducing to the stoichiometric $Pr_2NiO_{4.00}$, and (ii) to investigate to which extent the modulation of the incommensurate reflections of the starting phase are modified by the oxygen stoichiometry under the applied reaction conditions. Also in this case four twin individuals have been evidenced, but since all twin individuals have a common zone axis, their relation is much easier to analyse. The high brilliance of the BM01A beamline, together with its "zero" contamination by harmonics and very high resolution of the primary beam made a very detailed analysis of the symmetry changes and possible changes in the positions of the incommensurate reflections possible. It became clear that, in discrepancy with theoretical predictions of a series of phase sequences with different charge ordering, no change in the incommensurability has been observed during the reduction. This clearly indicated a two phase reaction mechanism towards the tetragonal $Pr_2NiO_{4.12}$ phase, having a small non-stoichiometric phase width. The four twin individuals of the orthorhombic starting phase contract all together into one individual for the $P4_2/ncm$ symmetry, which upon further oxidation results into the orthorhombic and stoichiometric $Pr_2NiO_{4.00}$ phase with *Bmab* symmetry. It turned out that the volume fractions of the twin individuals for the final reaction product show a completely reversed situation compared to the respective twin orientations for the starting phase. This on one hand underlines that the symmetry of the intermediate $Pr_2NiO_{4.12}$ is truly tetragonal, without this such a change in the twin behaviour could not be possible. From the absolute values of the twin volume fractions is also becomes clear that it does not correspond to an equal distribution of $1/4$ for each fraction, clearly excluding a microtwinning behaviour. This also indicates that the quantitative amount of twin boundaries is certainly reduced compared to the formation of small but numerous amount of twin domains. This is also an indicator that twin boundaries may play a less important role to amplify oxygen mobility in the low temperature range as often reported in literature.

An important and surprising fact is that the entire electrochemical reduction of $Pr_2NiO_{4.25}$ was observed to proceed perfectly homogeneous in terms of phase definition, as turned out from the reconstructed (*hkl*) planes, always showing only one defined phase without contamination related to a heterogeneous phase equilibrium as a consequence of the relatively high current applied. The whole reduction of a single crystal with 50 μm diameter has been observed to proceed in less than 24 h. The related underlying chemical diffusion coefficient has been analysed to be in the order of 1×10^{-11} cm^2 s^{-1}. This is very surprising from its absolute value, but strong anharmonic lattice dynamics resulting in a phonon assisted diffusion mechanism has been discussed for $Pr_2NiO_{4+\delta}$ following neutron scattering experiments. It implies that also on single crystals oxygen diffusion is still high at ambient temperature and probably following a similar diffusion mechanism, essentially involving lattice dynamics. Also the less amount of grain boundaries in a single crystal might contribute positively to the increased oxygen diffusion. The experimentally found diffusion coefficient during the oxygen intercalation reaction is especially surprising, when extrapolating the chemical diffusion coefficients obtained from isotope exchange depth profile method (IEDP), with subsequent secondary ion mass spectrometry (SIMS) analysis – to ambient temperature, where it yields 1×10^{-14} cm^2 s^{-1}. The difference of 3 orders of magnitude thus presents a strong variation of the Arrhenius equation and confirms that another mechanism, as already suggested by phonon assisted diffusion in $Pr_2NiO_{4+\delta}$, gains importance. This result is specifically interesting for the development of SOFCs, based on membranes realized as epitaxially grown thin films, as the increased amount of grain boundaries found in polycrystalline electrodes reduce importantly all oxygen permeability.

Last not least we want to underline that following up oxygen intercalation/deintercalation on single crystals is a very powerful tool to explore not only phase diagrams and related oxygen vacancy ordering, but also gives an important insight in possible changes of the microstructure, which are decisive to understand oxygen diffusion pathways also on a more mesoscopic scale. The related data analysis is today not at all standard and necessits a profound understanding of possible twin domains and the respective orientations in terms of reflection overlap. It is anyway the only technique giving relatively “easy” access to microstructural changes, not accessible at all by powder diffraction techniques. From this point of view this new technique to follow chemical reaction by *in situ* diffraction on single crystals is supposed to develop and especially for materials for energy storage and transformation, *i.e.* batteries and fuel cells.

Bibliography

[1] C. Almasan and M. Maple, “Electron doped high T_c cuprate superconductors. In C. N. R. Rao (ed.),” *Chemistry of High-Temperature Superconductors (World Scientific, Singapore)*, pp. 205–242, 1991.

[2] K. Yamada, M. Matsuda, Y. Endoh, B. Keimer, R. J. Birgeneau, S. Onodera, J. Mizusaki, T. Matsuura, and G. Shirane, “Successive antiferromagnetic phase transitions in single-crystal La_2CoO_4,” *Physical Review B*, vol. 39, pp. 2336–2343, 1989.

[3] M. Cwik, M. Benomar, T. Finger, Y. Sidis, D. Senff, M. Reuther, T. Lorenz, and M. Braden, “Magnetic Correlations in $La_{2-x}Sr_xCoO_4$ Studied by Neutron Scattering:Possible Evidence for Stripe Phases,” *Physical Review Letter*, vol. 102, pp. 057201–057204, 2009.

[4] H. Asano, J. Hayakawa, , and M. Matsui, “Two-dimensional ferromagnetic ordering and magnetoresistance in the layered perovskite $La_{2-2x}Ca_{1+2x}Mn_2O_7$,” *Physical Review B*, vol. 56, no. 9, pp. 5395–5403, 1997.

[5] J. Burgy, M. Mayr, V. Martin-Mayor, A. Moreo, and E. Dagotto, “Colossal Effects in Transition Metal Oxides Caused by Intrinsic Inhomogeneities,” *Physical Review Letter*, vol. 87, no. 27, pp. 277202–277204, 2001.

[6] K. Aryanpour, E. Dagotto, M. Mayr, T. Paiva, W. Pickett, and R. Scalettar, “Effect of inhomogeneity on s-wave superconductivity in the attractive Hubbard model,” *Physical Review B*, vol. 73, pp. 104518–104522, 2006.

[7] V. J. Emery, S. A. Kivelson, and J. M. Tranquada, “Stripe phases in high-temperature superconductors,” *Proc. Natl. Acad. Sci. USA*, vol. 96, no. 26, pp. 8814–8817, 1999.

[8] J. Zaanen, “Stripes defeat the Fermi liquid,” *Nature*, vol. 404, pp. 714–715, 2000.

[9] J. Tranquada, H. Woo, T. G. Perring, H. Goka, G. D. Gu, G. Xu, F. M., and Y. K., “Quantum magnetic excitations from stripes in copper oxide superconductors,” *Nature*, vol. 429, pp. 534–538, 2004.

[10] S. M. Hayden, H. A. Mook, P. Dai, T. G. Perring, and F. Doğan, “The structure of the high-energy spin excitations in a high-transition-temperature superconductor,” *Nature*, vol. 429, pp. 531–534, 2004.

[11] S. Anissimova, D. Parshall, G. Gu, K. Marty, M. Lumsden, S. Chi, J. Fernandez-Baca, D. Abernathy, D. Lamago, J. Tranquada, and D. Reznik, “Direct observation of dynamic charge stripes in $La_{2x}Sr_xNiO_4$,” *Nature Communications*, vol. 5, pp. 1–9, 2014.

[12] E. Dagotto, “Complexity in Strongly Correlated Electronic Systems,” *Science*, vol. 309, pp. 257–262, 2005.

[13] R. Caciuffo, D. Rinaldi, G. Barucca, J. Mira, J. Rivas, M. Señarís Rodríguez, P. Radaelli, D. Fiorani, and J. Goodenough, “Structural details and magnetic order of $La_{1-x}Sr_xCoO_3$ ($x \leq 0.3$),” *Physical Review B*, vol. 59, no. 2, pp. 1068–1078, 1999.

[14] E. Dagotto, “Nanoscale phase seperation and colossal magnetoresistance,” *Springer-Verlag Berlin Heidelberg GmbH*, 2003.

[15] A. Dagotto, T. Hottab, and A. Moreoa, “Colossal magnetoresistant materials: the key role of phase separation,” *Physical Reports*, vol. 344, pp. 1–153, 2001.

[16] L. Rademaker, Y. Pramudya, J. Zaanen, and V. Dobrosavljevic, “Influence of long-range interactions on charge ordering phenomena on a square lattice,” *Physical Review E*, vol. 88, pp. 032121–032121, 2013.

[17] W. Paulus, H. Schober, S. Eibl, M. Johnson, T. Berthier, O. Hernandez, C. M., M. Plazanet, K. Conder, and C. Lamberti, “Lattice Dynamics To Trigger Low Temperature Oxygen Mobility in Solid Oxide Ion Conductors,” *J. Am. Chem. Soc.*, vol. 130, pp. 16080–16085, 2008.

[18] M. Ceretti, O. Wahyudi, A. Cousson, A. Villesuzanne, M. Meven, B. Pedersen, J. M. Bassat, and W. Paulus, “Low temperature oxygen diffusion mechanisms in $Nd_2NiO_{4+\delta}$ and $Pr_2NiO_{4+\delta}$ via large anharmonic displacements, explored by single crystal neutron diffraction,” *J. Mater. Chem. A*, vol. 3, no. 42, pp. 21140–21148, 2015.

[19] A. Perrichon, A. Piovano, M. Boehm, M. Zbiri, M. Johnson, H. Schober, M. Ceretti, and W. Paulus, “Lattice Dynamics Modified by Excess Oxygen in $Nd_2NiO_{4+\delta}$: Triggering Low-Temperature Oxygen Diffusion,” *The Journal of Physical Chemistry C*, vol. 119, no. 3, pp. 1557–1564, 2015.

[20] A. Wattiaux, L. Fournès, A. Demourgues, N. Bernaben, J. Grenier, and M. Pouchard, “A Novel Preperation Method of the $SrFeO_3$ Cubic Perovskite by Electrochemical Means,” *Solid State Communications*, vol. 77, no. 7, pp. 489–493, 1991.

[21] A. Nemudry, M. Weiss, I. Gainutdinov, V. Boldyrev, and R. Schöllhorn, “Room Temperature Electrochemical Redox Reactions of the Defect Perovskite $SrFeO_{2.5+x}$,” *Chem. Mater.*, vol. 10, pp. 2403–2411, 1998.

[22] M. Schmidt and S. J. Campbell, “Crystal and Magnetic Structures of $Sr_2Fe_2O_5$ at Elevated Temperature,” *Journal of Solid State Chemistry*, vol. 156, pp. 292–304, 2001.

[23] M. Reehuis, C. Ulrich, A. Maljuk, C. Niedermayer, B. Ouladdiaf, A. Hoser, T. Hofmann, and B. Keimer, “Neutron diffraction study of spin and charge ordering in $SrFeO_{3\delta}$,” *Physical review B*, vol. 85, pp. 184109–184123, 2012.

[24] V. Dyadkin, P. Pattison, V. Dmitriev, and D. Chernyshov, “A new multipurpose diffractometer PILATUS @ SNBL,” *J. Synchrotron Rad.*, vol. 23, pp. 825–829, 2016.

[25] J. Auckett, A. Studer, N. Sharma, and C. Ling, “Floating-zone growth of brownmillerite $Sr_2Fe_2O_5$ and the observation of a chain-ordered superstructure by single-crystal neutron diffraction,” *Solid State Ionics*, vol. 225, pp. 432–436, 2012.

[26] O. Wahyudi, “Thesis on Exploring oxygen mobility in $(Pr/Nd)_2NiO_{4+\delta}$: single crystal growth, isotopic exchange depth profiling and structural characterization by X-ray, neutron and electron diffraction,” 2011.

[27] H. Mehrer, “Difusions in Solids,” *Springer-Verlag Berlin Heidelberg*, 2007.

[28] J. Goodenough, “Oxide-Ion Electrolytes,” *Annual Review of Materials Research*, vol. 33, pp. 91–128, 2003.

[29] B. Steele and A. Heinzel, “Materials for fuel-cell technologie,” *Nature*, vol. 414, pp. 345–352, 2001.

[30] S. Adler, “Mechanism and kinetics of oxygen reduction on porous $La_{1-x}Sr_xCoO_{3-\delta}$ electrodes,” *Solid State Ionics*, vol. 111, pp. 125–134, 1998.

[31] S. Adler, “Limitations of charge-transfer models for mixed-conducting oxygen electrodes,” *Solid State Ionics*, vol. 135, pp. 603–612, 2000.

[32] S. Adler, X. Chen, and J. Wilson, “Mechanisms and rate laws for oxygen exchange on mixed-conducting oxide surfaces,” *Journal of Catalysis*, vol. 245, pp. 91–109, 2007.

[33] P. Rudolf, W. Paulus, and R. Schöllhorn, “Electron/Proton Transfer Reactions and Superconductivity: The Role of Hydrogen in Lanthanum Copper Oxide,” *Adv. Mater.*, vol. 3, no. 9, pp. 438–440, 1991.

[34] T. Kudo, H. Obayashi, and T. Gejo, “Electrochemical Behavior of the Perovskite-Type $Nd_{1-x}Sr_xCoO_3$ in an Aqueous Alkaline Solution ,” *Journal of The Electrochemical Society*, vol. 122, no. 2, pp. 159–163, 1975.

[35] R. Toquin, W. Paulus, A. Cousson, C. Prestipino, and C. Lamberti, “Time-Resolved in Situ Studies of Oxygen Intercalation into $SrCoO_{2.5}$, Performed by Neutron Diffraction and X-ray Absorption Spectroscopy,” *J. Am. Chem. Soc.*, vol. 128, pp. 13161–13174, 2006.

[36] A. Chroneos, B. Yildiz, A. Tarancon, D. Parfitt, and J. A. Kilner, “Oxygen diffusion in solid oxide fuel cell cathode and electrolyte materials: mechanistic insights from atomistic simulations,” *Energy Environ. Sci*, vol. 4, pp. 2774–2789, 2011.

[37] R. Krishnamurthy, Y. Yoon, D. Srolovitz, and R. Car, “Oxygen Diffusion in Yttria-Stabilized Zirconia: A New Simulation Model,” *Journal of American Ceramic Society*, vol. 87, pp. 1821–1830, 2004.

[38] S. Skinner and J. Kilner, “Oxygen ion conductors,” *materialstoday*, vol. 6, pp. 30–37, 2003.

[39] V. Butler, C. Catlow, B. Fender, and J. Harding, “Dopant Ion Radius and Ionic Conductivity in Cerium Oxide,” *Solid State Ionics*, vol. 8, pp. 109–113, 1983.

[40] L. Minervini, M. Zacate, and R. Grimes, “Defect cluster formation in M_2O_3-doped CeO_2,” *Solid State Ionics*, vol. 116, pp. 339–349, 1999.

[41] I. Kosacki, H. Andersona, Y. Mizutanib, and K. Ukai, “Nonstoichiometry and electrical transport in Sc-doped zirconia,” *Solid State Ionics*, vol. 152-153, pp. 431–438, 2002.

[42] F. Esch, S. Fabris, L. Zhou, T. Montini, C. Africh, P. Fornasiero, and R. Comelli, G .and Rosei, “Electron Localization Determines Defect Formation on Ceria Substrates,” *Science*, vol. 309, pp. 752–755, 2005.

[43] E. Shoko, M. Smith, and R. McKenzie, “Charge distribution near bulk oxygen vacancies in cerium oxides,” *J. Phys.: Condens. Matter*, vol. 22, no. 22, pp. 223201–223218, 2010.

[44] M. Nakayama, H. Ohshima, M. Nogami, and M. Martin, “A concerted migration mechanism of mixed oxide ion and electron conduction in reduced ceria studied by first-principles density functional theory,” *Phys. Chem. Chem. Phys.*, vol. 14, pp. 6079–6084, 2012.

[45] J. Kilner, “Fast oxygen transport in acceptor doped oxides,” *Solid State Ionics*, vol. 129, pp. 13–23, 2000.

[46] M. Feng and J. B. Goodenough, “A superior oxide-ion electrolyte,” *European Journal of Solid State and Inorganic Chemistry*, vol. 31, pp. 663–672, 1994.

[47] T. Ishihara, H. Matsuda, and Y. Takita, “Doped $LaGa0_3$ Perovskite Type Oxide as a New Oxide Ionic Conductor,” *J. Am. Chem. Soc.*, vol. 116, pp. 3801–3803, 1994.

[48] T. Ishihara, T. Shibayama, H. Nishiguchi, and Y. Takita, “Oxide ion conductivity in $La_{0.8}Sr_{0.2}Ga_{0.8}Mg_{0.2-x}Ni_xO_3$ perovskite oxide and application for the electrolyte of solid oxide fuel cells,” *Journal Of Materials Science*, vol. 36, pp. 1125–1131, 2001.

[49] A. Tarancćn, M. Burriel, J. Santiso, S. Skinner, and J. Kilner, “Advances in layered oxide cathodes for intermediate temperature solid oxide fuel cells,” *Journal of Materials Chemistry*, vol. 20, pp. 3799–3813, 2009.

[50] A. Taskin, A. N. Lavrov, and Y. Ando, “Achieving fast oxygen diffusion in perovskites by cation ordering,” *Applied Physics Letters*, vol. 86, pp. 091910–091912, 2005.

[51] A. Taskin, A. N. Lavrov, and Y. Ando, “Transport and magnetic properties of $GdBaCo_2O_{5+x}$ single crystals: A cobalt oxide with square-lattice CoO_2 planes over a wide range of electron and hole doping,” *Physical Review B*, vol. 71, 2005.

[52] G. Kim, S. Wang, A. Jacobson, Z. Yuan, W. Donner, C. L. Chen, L. Reimus, P. Brodersen, and C. A. Mims, “Oxygen exchange kinetics of epitaxial $PrBaCo_2O_{5+\delta}$ thin films,” *Appl. Phys. Lett.*, vol. 88, 2006.

[53] G. Kim, S. Wang, A. Jacobson, L. Reimus, P. Brodersen, and C. A. Mims, “Rapid oxygen ion diffusion and surface exchange kinetics in $PrBaCo_2O_{5+x}$ with a perovskite related structure and ordered A cations,” *J. Mater. Chem.*, vol. 17, pp. 2500–2505, 2007.

[54] P. Lacorre, F. Goutenoire, O. Bohnke, R. Retoux, and Y. Laligant, “Designing fast oxide-ion conductors based on $La_2Mo_2O_9$,” *Nature*, vol. 404, pp. 856–858, 2000.

[55] F. Goutenoire, O. Isnard, R. Retoux, and P. Lacorre, “Crystal Structure of $La_2Mo_2O_9$, a New Fast Oxide-Ion Conductor,” *Chem. Mater.*, vol. 12, pp. 2575–2580, 2000.

[56] A. Abakumov, A. Kalyuzhnaya, M. Rozova, E. Antipov, J. Hadermann, and G. Tendeloo, “Compositionally induced phase transition in the $Ca_2MnGa_{1-x}Al_xO_5$ solid solutions: Ordering of tetrahedral chains in brownmillerite structure,” *Solid State Sciences*, vol. 7, pp. 801–811, 2005.

[57] A. Nemudry, P. Rudolf, and R. Schöllhorn, “Topotactic Electrochemical Redox Reactions of the Defect Perovskite $SrCoO_{2.5+x}$,” *Chem . Mater.*, vol. 8, pp. 2232–2238, 1996.

[58] J. Grenier, A. Wattiaux, L. Fournes, M. Pouchard, and M. Etourneau, “The Electrochemical Oxidation : a New Way for Preparing Highly Oxidized Ferrites,” *Journal de Physique IV Colloque*, vol. 07, pp. C1–49–C1–52, 1997.

[59] K. Gupta, S. Singh, M. Ceretti, M. Rao, and W. Paulus, “Scaling of extended defects in nano-sized Brownmillerite $CaFeO_{2.5}$,” *Physica Status Solidi a*, vol. 210, pp. 1771–1777, 2013.

[60] S. Corallini, M. Ceretti, G. Silly, A. Piovano, S. Singh, J. Stern, C. Ritter, J. Ren, H. Eckert, K. Conder, W.-T. Chen, F.-C. Chou, N. Ichikawam, Y. Shimakawa, and W. Paulus, “One-Dimensional Oxygen Diffusion Mechanism in Sr2ScGaO5 Electrolyte Explored by Neutron and Synchrotron Diffraction, 17O NMR, and Density Functional Theory Calculations,” *J. Phys. Chem. C*, vol. 119, pp. 11447–11458, 2015.

[61] P. Rudolf and R. Schöllhorn, "Semiconductor/Superconductor Transition of La_2Cu0_4 via Chemical Oxidation at Ambient Temperature," *J. Chem. Soc. Commun.*, pp. 1158–1160, 1992.

[62] W. W. Paulus, G. Heger, P. Rudolf, and R. Schöllhorn, "In situ neutron diffraction studies on the electrochemical oxidation of polycrystalline La_2CuO_4," *Physica C: Superconductivity*, vol. 235-240, pp. 861–862, 1994.

[63] J. D. Sullivan, D. Buttrey, D. Cox, and J. Hriljac, "A conventional and High-Resolution Synchrotron X-Ray Diffraction Study of Phase Separations in $Pr_2NiO_{4+\delta}$," vol. 351, pp. 337–351, 1991.

[64] A. Villesuzanne, W. Paulus, A. Cousson, S. Hosoya, L. Dréau, O. Hernandez, M. Prestipino, C.and Houchati, and J. Schefer, "On the role of lattice dynamics on low-temperature oxygen mobility in solid oxides: a neutron diffraction and first-principles investigation of $La_2CuO_{4+\delta}$," *Journal of Solid State Electrochemistry*, vol. 15, pp. 357–366, 2011.

[65] L. Dréau, C. Prestipino, O. Hernandez, J. Schefer, G. Vaughan, S. Paofai, J. Perez-Mato, S. Hosoya, and W. Paulus, "Structural Modulation and Phase Transitions in $La_2CoO_{4.14}$ Investigated by Synchrotron XâĂŚray and Neutron Single-Crystal Diffraction," *Inorg. Chem.*, vol. 51, pp. 9789–9798, 2012.

[66] J. Bassat, M. Burriel, O. Wahyudi, R. Castaing, M. Ceretti, P. Veber, I. Weill, A. Villesuzanne, J. Grenier, W. Paulus, and J. Kilner, "Anisotropic Oxygen Diffusion Properties in $Pr_2NiO_{4+\delta}$ and $Nd_2NiO_{4+\delta}$ Single Crystals," *J. Phys. Chem. C*, vol. 117, pp. 26466–26472, 2013.

[67] A. Piovano, A. Perrichon, M. Boehm, M. Johnson, and W. Paulus, "Positional recurrence maps, a powerful tool to de-correlate static and dynamical disorder in distribution maps from molecular dynamics simulations: the case of $Nd_2NiO_{4+\delta}$," *Phys. Chem. Chem. Phys.*, vol. 18, pp. 17398–17403, 2016.

[68] H. A. Susumu Nakayama, Tatsuya Kageyama and Y. Sadaoka, "Ionic conductivity of lanthanoid silicates, Ln10(SiO4)6O3(Ln = La, Nd, Sm, Gd, Dy, Y, Ho, Er and Yb)," *J. Mater. Chem.*, vol. 5, pp. 1801–1805, 1995.

[69] M. Islam, J. Tolchard, and P. Slater, "An apatite for fast oxide ion conduction," *Chemical. Commun.*, pp. 1486–1487, 2003.

[70] A. Jones, P. Slater, and M. Islam, "Local Defect Structures and Ion Transport Mechanisms in the Oxygen-Excess Apatite $La_{9.67}(SiO_4)_6O_{2.5}$," *Chem. Mater.*, vol. 20, pp. 5055–5060, 2008.

[71] E. Kendrick, M. Islam, and P. Slater, "Developing apatites for solid oxide fuel cells: insight into structural, transport and doping properties," *Journal of Materials Chemistry*, vol. 17, pp. 3104–3111, 2007.

[72] J. Sansom, D. Richings, and P. Slater, "A powder neutron diffraction study of the oxide-ion-conducting apatite-type phases, $La_{9.33}Si_6O_{26}$ and $La_8Sr_2Si_6O_{26}$," *Solid State Ionics*, vol. 139, pp. 205–210, 2001.

[73] L. Reina, E. Losilla, M. Martínez-Lara, S. Bruque, and M. Aranda, “Interstitial oxygen conduction in lanthanum oxy-apatite electrolytes,” *J. Mater. Chem.*, vol. 14, pp. 1142–1149, 2004.

[74] L. Reina, J. Porras-Vázquez, E. Losilla, and M. Aranda, “Phase transition and mixed oxide-proton conductivity in germanium oxy-apatite,” *Journal of Solid State Chemistry*, vol. 180, pp. 1250–1258, 2007.

[75] J. Tolchard, M. Islam, and P. Slater, “Defect chemistry and oxygen ion migration in the apatite-type materials $La_{9.33}Si_6O_{26}$ and $La_8Sr_2Si_6O_{26}$,” *J. Mater. Chem.*, vol. 2003, pp. 1956–1961, 13.

[76] O. Wahyudi, M. Ceretti, I. Weill, A. Cousson, F. Weill, M. Meven, M. Guerre, A. Villesuzanne, J.-M. Bassat, and W. Paulus, “Growth of high quality single crystals of strontium doped (Nd,Pr)-nickelates, $Nd_{2-x}Sr_xNiO_{4+\delta}$ and $Pr_{2-x}Sr_xNiO_{4+\delta}$,” *CrystEngComm*, vol. 17, pp. 6278–6285, 2015.

[77] G. J. Halder and C. J. Kepert, “In Situ Single-Crystal X-ray Diffraction Studies of Desorption and Sorption in a Flexible Nanoporous Molecular Framework Material, journal = Journal of the American Chemical Society,” vol. 127, no. 21, pp. 7891–7900, 2005.

[78] S. R. Miller, P. A. Wright, T. Devic, C. Serre, G. Férey, P. L. Llewellyn, R. Denoyel, L. Gaberova, and Y. Filinchuk, “Single Crystal X-ray Diffraction Studies of Carbon Dioxide and Fuel-Related Gases Adsorbed on the Small Pore Scandium Terephthalate Metal Organic Framework, $Sc_2(O_2CC_6H_4CO_2)_3$,” *Langmuir*, vol. 25, no. 6, pp. 3618–3626, 2009.

[79] “Web reference of BM01A,” *http://www.esrf.eu/home/UsersAndScience /Experiments/Beamlines/content/content/bm01a.html*.

[80] “Web reference for CrysAlis^{pro},” *http://www.rigaku.com/en/products/smc/crysalis*.

[81] P. Batti, “The equilibrium diagram of the system SrO–Fe_2O_3 (in Italian),” *Ann. Chim. (Rome)*, vol. 52, pp. 941–961, 1962.

[82] P. K. Gallagher, J. B. MacChesney, and D. N. E. Buchanan, “Mössbauer Effect in the System $SrFeO_{2.5-3.0}$,” *J. Chem. Phys.*, vol. 41, p. 2429, 1964.

[83] J. B. MacChesney, S. R. C., and J. F. Potter, “Electric and Magnetic Properties of the Strontium Ferrates,” *J. Chem. Phys.*, vol. 43, pp. 1907–1913, 1965.

[84] B. C. Tofield, C. Greaves, and B. E. F. Fender, “The $SrFeO_{2.5}$ | $SrFeO_{3.0}$ system. evidence of a new phase $Sr_4Fe_4O_{11}$ ($SrFeO_{2.75}$),” *Mater. Res. Bull. 10*, vol. 10, pp. 737–745, 1975.

[85] C. Greaves, A. J. Jacobson, B. C. Tofield, and B. E. F. Fender, “ A powder neutron diffraction investigation of the nuclear and magnetic structure of $Sr_2Fe_2O_5$,” *Acta Crystallogr. B*, vol. 31, pp. 641–646, 1975.

[86] G. T. C, “Magnetic exchange interactions in perovskite solid solutions. Part 5. The unusual defect structure of $SrFeO_{3-y}$,” *J. Chem. Soc. Dalt. Trans.*, vol. 7, pp. 1455–1470, 1985.

[87] Y. Takeda, K. Kanno, T. Takada, O. Yamamoto, M. Takano, N. Nakayama, and Y. Bando, “Phase relation in the oxygen nonstoichiometric system, SrFeOx (2.5 ≤ x ≤ 3.0),” *J. Solid State Chem.*, vol. 63, pp. 237–249, 1986.

[88] M. Takano, T. Okita, N. Nakayama, Y. Bando, Y. Takeda, O. Yamamoto, and J. B. Goodenough, “Dependence of the structure and electronic state of $SrFeO_x$ (2.5 ≤ x ≤ 3) on composition and temperature,” *J. Solid State Chem.*, vol. 73, pp. 140–150, 1988.

[89] J. P. Hodges, S. Short, J. D. Jorgensen, X. Xiong, B. Dabrowski, S. M. Mini, and C. W. Kimball, “Evolution of Oxygen–Vacancy Ordered Crystal Structures in the Perovskite Series $Sr_nFe_nO_{(3n-1)}$ ($n = 2, 4, 8 and \infty$), and the Relationship to Electronic and Magnetic Properties,” *Journal of Solid State Chemistry*, vol. 151, pp. 190–209, 2000.

[90] P. Adler, A. Lebon, V. Damljanović, C. Ulrich, C. Bernhard, A. V. Boris, A. Maljuk, C. T. Lin, and B. Keimer, “Magnetoresistance effects in $SrFeO_{3-\delta}$: Dependence on phase composition and relation to magnetic and charge order,” *Physical Review B*, vol. 73, pp. 094451–094466, 2006.

[91] Y. Y. Takeda T and W. H, “Magnetic structure of SrFeO3,” *J. Phys. Soc. Japan*, vol. 33, pp. 967–69, 1972.

[92] P. M. Woodward, D. E. Cox, E. Moshopoulou, A. W. Sleight, and S. Morimoto, “Structural studies of charge disproportionation and magnetic order in $CaFeO_3$,” *Physical Review B*, vol. 62, pp. 844–855, 2000.

[93] M. Schmidt, M. Hofmann, and S. J. Campbell, “Magnetic structure of strontium ferrite $Sr_4Fe_4O_{11}$,” *J. Phys.: Condens. Matter*, vol. 15, pp. 8691–8701, 2003.

[94] J. C. Grenier, N. Ea, M. Pouchard, and P. Hagenmuller, “Structural Transition at High Temperature in $Sr_2Fe_2O_5$,” *Journal of Solid State Chemistry*, vol. 58, pp. 243–252, 1985.

[95] S. Parsons, “Introduction to Twinning,” *Acta Cryst. D*, vol. 59, pp. 1995–2003, 2003.

[96] L. Le Dréau, “Thesis on Phase transitions and oxygen ordering in $La_2CoO_{4+\delta}$ and (T, T’)- La_2CoO_4: single crystal growth and structural studies using synchrotron and neutron diffraction methods,” 2011.

[97] A. J.E., A. Studer, E. Pellegrini, J. Ollivier, M. Johnson, H. Schober, W. Miiller, and C. Ling, “Combined Experimental and Computational Study of Oxide Ion Conduction Dynamics in $Sr_2Fe_2O_5$ Brownmillerite,” *Chemistry of Materials*, vol. 25, pp. 3080–3087, 2013.

[98] "Web reference of FullProf," *https://www.ill.eu/sites/fullprof/php/programs.html*.

[99] H. D'Hondt, A. M. Abakumov, J. Hadermann, A. S. Kalyuzhnaya, M. G. Rozova, E. V. Antipov, and G. V. Tendeloo, "Tetrahedral Chain Order in the $Sr_2Fe_2O_5$ Brownmillerite," *Chem. Mater.*, vol. 20, pp. 7188–7194, 2008.

[100] T. Takeda, Y. Yamaguchi, and S. Tomiyoshi, "Magnetic Structure of $Ca_2Fe_2O_5$," *J. Phys. Soc. Japan*, vol. 24, pp. 446–452, 1968.

[101] J. J.C. Waerenborgh, E. Tsipis, J. Auckett, C. Ling, and V. Kharton, "Magnetic structure of $Sr_2Fe_2O_5$ brownmillerite by single-crystal Moössbauer spectroscopy," *Journal of Solid State Chemistry*, vol. 205, pp. 5–9, 2013.

[102] T. Berthier, "Thesis on Oxygen mobility in solid oxides at moderate temperature: Crystal Growth, Structure Analysis, Lattice Dynamics and Chemical Reactivity of (Ca,Sr)$FeO_{2.5+x}$ $0 \leq x \leq 0.5$," 2007.

[103] M. W. Schmidt, "Thesis on Phase Formation and Structural Transformation of Strontium Ferrite $SrFeO_x$," 2001.

[104] J. Mizusaki, M. Okayasu, S. Yamaguchi, and K. Fueki, "Nonstoichiometry and Phase Relationship of the $SrFeO_{2.5}$–$SrFeO_3$ System at High Temperature," *J. Solid State Chem.*, vol. 99, pp. 166–172, 1992.

[105] S. Wissmann and K. D. Becker, "Localization of Electrons in Nonstoichiometric $SrFeO_{3-\delta}$.," *Solid State Ionics,*, vol. 85, pp. 279–283, 1996.

[106] J. Bednorz and K. Müller, "Possible High T_c Superconductivity in the Ba–La–Cu–O System," *Z. Phys. B – Condensed Matter*, vol. 64, pp. 189–193, 1986.

[107] M. Fernández-Díaz, J. Martínez, and J. Rodríguez-Carvajal, "High-temperature phase transformation of oxidized $R_2NiO_{4+\delta}$ (R = La, Pr, Nd) under vaccum," *Solid State Ionics*, vol. 63–65, pp. 902–906, 1993.

[108] M. Fernández-Díaz, J. Rodríguez-Carvajal, J. Martínez, G. Fillion, F. Fernández, and R. Saez-Puche, "Structural and magnetic phase transitions in Pr_2NiO_4 ," *Z. Phys. B – Condensed Matter*, vol. 82, pp. 275–282, 1991.

[109] J. Martínez, M. Fernández-Díaz, J. Rodríguez-Carvajal, and P. Odier, "Lattice instability and low-temperature phase transitions in Pr_2NiO_4 ," *Physical Review B*, vol. 43, pp. 13766–13769, 1991.

[110] C. Chaillout, S. Cheong, Z. Fisk, M. Lehmann, M. Marezio, B. Morosin, and J. SCHIRBER, "The Crystal Structure of Superconduction $La_2CuO_{4.032}$ by Neutron Diffraction," *Physica C*, vol. 158, pp. 183–191, 1989.

[111] J. D. Jorgensen, B. Dabrowski, S. Pei, D. G. Hinks, and L. Soderholm, "Snpercondncting phase of $La_2CuO_{4+\delta}$: A snpercondncting composition resulting from phase separation," *Physical Review B*, vol. 38, no. 16, pp. 11337–11345, 1988.

[112] C. Allançon, J. Bassat, J. Riflet, J. Loup, and P. Odier *Proceeding ECRS european ceramic society 3rd conference*, vol. 2, pp. 335–340, 1993.

[113] C. Allançon, J. Rodríguez-Carvajal, M. Fernández-Díaz, P. Odier, J. Bassat, and J. Loup, “Crystal Structure of High Temperature Phase of Oxidised $Pr_2NiO_{4+\delta}$,” *Z. Phys. B*, vol. 100, pp. 85–90, 1996.

[114] P. Willer and M. Daire *CR Acad Science paris*, vol. 267, p. 1482, 1968.

[115] K. K. Singh, P. Ganguly, and J. B. Goodenough, “Unusual Effects of Anisotropic Bonding in Cu(II) and Ni(II) Oxides with K_2NiF_4 Structure,” *Journal of Solid State Chemistry*, vol. 52, pp. 254–273, 1984.

[116] D. Buttrey, J. Sullivan, G. Shirane, and K. Yamada, “Influence of oxygen Nonstoichiometry on structure and magnetism in $Pr_2NiO_{4+\delta}$,” *Physical Review B*, vol. 42, no. 7, pp. 3944–3951, 1990.

[117] P. Odier, C. Allançon, and J. Bassat, “Oxygen Exchange in Pr_2NiO_4 at High Temperature and Direct Formation of $Pr_4Ni_3O_{10-x}$,” *Journal of Solid State Chemistry*, vol. 153, pp. 381–385, 2000.

[118] D. Prabhakaran, A. T. Boothroyd, and J. Gonzalez *J. Mater. Sci.: Mater. Electron.*, vol. 14, pp. 583–586, 2003.

[119] R. Schöllhorn, “From Electronic/Ionic Conductors to Superconductors: Control of Materials Properties,” *Angew.Chem.lnt. Ed. Engl.*, vol. 27, no. 10, pp. 1392–1400, 1988.

[120] S. Bhavaraju, D. DiCarlo, D. Scarfe, I. Yazdi, and A. Jacobson, “Electrochemical Intercalation of Oxygen in Nd_2Ni0_{4+x} ($0 \leq x \leq 0.18$) at 298 K,” *Chem. Mater.*, vol. 6, pp. 2172–2176, 1994.

[121] S. Bhavaraju, D. DiCarlo, D. Scarfe, A. Jacobson, and D. Buttrey, “Electrochemical oxygen intercalation in $La_2Ni0_{4+\delta}$ crystals,” *Solid State Ionics*, vol. 86–88, pp. 825–831, 1996.

[122] M. Hücker, M. v. Zimmermann, R. Klingeler, S. Kiele, J. Geck, S. N. Bakehe, J. Z. Zhang, J. P. Hill, A. Revcolevschi, D. J. Buttrey, B. Buüchner, and J. M. Tranquada, “Unidirectional diagonal order and three-dimensional stacking of charge stripes in orthorhombic $Pr_{1.67}Sr_{0.33}NiO_4$ and $Nd_{1.67}Sr_{0.33}NiO_4$,” *Physical Review B*, vol. 74, pp. 085112–085123, 2006.

[123] K. Ishizaka, Y. Taguchi, R. Kajimoto, H. Yoshizawa, and Y. Tokura, “Charge ordering and charge dynamics in $Nd_{2-x}Sr_xNiO_4$ ($0.33 \leq x \leq 0.7$),” *Physical Review B*, vol. 67, p. 184418, May 2003.

[124] A. Alexis Grimaud, F. Mauvy, J. Bassat, S. Fourcade, M. Marronyb, and J. Grenier, “Hydration and transport properties of the $Pr_{2-x}Sr_xNiO_{4+\delta}$ compounds as H^+-SOFC cathodes,” *J. Mater. Chem.*, vol. 22, pp. 16017–16025, 2012.

[125] X. Li and N. Benedek, “Enhancement of Ionic Transport in Complex Oxides through Soft Lattice Modes and Epitaxial Strain,” *Chemistry of Materials*, vol. 27, pp. 2647–2652, 2015.

[126] D. Parfitt, A. Chroneos, J. Kilner, , and R. Grimes, “Molecular dynamics study of oxygen diffusion in $Pr_2NiO_{4+\delta}$,” *Physical Chemistry Chemical Physics*, vol. 12, pp. 6834–6836, 2010.

[127] A. Nemudry, E. Goldberg, M. Aguirre, and M. Alario-Franco, “Electrochemical topotactic oxidation of nonstoichiometric perovskites at ambient temperature,” *Solid State Sciences*, vol. 4, pp. 677–690, 2002.

Acknowledgement

After an intensive period of thesis writing today is the day I am writing this note of thanks to the people without whose contributions this thesis would not be the same. It has been a period of intensive learning not only in the scientific arena but also on a personal level. Writing this thesis has had a big impact on me.

Foremost, I would like to thank my supervisor Professor Werner Paulus for giving me the opportunity to work in this thesis, and also for introducing me to the fascinating world of diffraction. His immense knowledge and constant supervision throughout my PhD research helped me to enlarge my periphery of scientific knowledge, and also taught me how to act independently and think critically on a scientific problem. I would also like to thank my co-supervisor Dr. Angélique Letrouit-Lebranchu for her continuous support, scientific advices and constructive discussions throughout this thesis process. I am extremely thankful to Dr. Monica Ceretti for her expertise and extraordinary advices for high quality single crystal growth which was very important for the success of this thesis work, and also I want to thank her for helping me with powder diffraction data treatment. I greatly appreciate the help from Antonio Vieira-E-Silva for optimizing the electrochemical cell. I also thank Dr. Bernard Fraisse, Julien Fullerwarth, Dominique Granier for their technical support in X-ray diffraction, Pierre Sans for computer and IT support, Veronique Sidoux and Francois Blanc for scientific purchase and travel arrangements. Above all I sincerely thank also Prof. Philippe Papet for giving me the opportunity to work in the ICGM C2M group.

Beside the people from Montpellier university, I greatly appreciate the help and support provided by the beamline scientists during the *in situ* synchrotron diffraction experiments. I would like to acknowledge people from BM01A, ESRF: Dr. Dmitry Chernyshov and Dr. Vadim Dyadkin for their great support throughout the *in situ* experiments and afterwards in data analysis. My sincere thanks also goes to Prof. Georg Roth from RWTH Aachen University and Dr. Martin Meven from FRM-II for their active participation and insightful comments and encouragement during the *in situ* experiments at ESRF. I would also like to thank all the jury members for accepting to be in my PhD dissertation committee and for taking the burden of going through my thesis. I heartily appreciate their insightful comments and suggestions.

I thank my fellow labmates Rajesh, Bartosz, Adrien, Oles for the stimulating and fruitful discussions we had, for the sleepless nights we were working during the *in situ* experiments at the synchrotron, and for all the scientific adventure we have done in the last years. Also I thank my other colleagues from Montpellier university Elizabeth, Rocio, Padmini, Renjith, Wahid for the nice company and pleasant time we share.

Last but not least, my special thanks go to my parents Asoke and Mala, and my sister Arpita, and to the rest of my family for their unwavering support in every step of my life.

14th Nov. 2016, Montpellier
Avishek Maity

This thesis is financed by
Ministry of Research and Technology, France

Abstract

Understanding fundamental aspects of oxygen diffusion in solid oxides at moderate temperatures, down to ambient, is an important issue for the development of a variety of technological devices in the near future. This concerns *e.g.* the progress and invention of next generation solid oxygen ion electrolytes and oxygen electrodes for solid oxide fuel cells (SOFC) as well as membrane based air separators, oxygen sensors and catalytic converters to transform *e.g.* NO_x or CO from exhaust emissions into N_2 and CO_2. On the other hand oxygen intercalation reactions carried out at low temperatures present a powerful tool to control hole doping, *i.e.* the oxygen stoichiometry, in electronically correlated transition metal oxides. In this aspect oxides with Brownmillerite ($A_2BB'O_5$) and K_2NiF_4-type frameworks, have attracted much attention, as they surprisingly show oxygen mobility down to ambient temperature.

In this thesis we investigated oxygen intercalation mechanisms in $SrFeO_{2.5+x}$ as well as $Pr_2NiO_{4+\delta}$ by *in situ* diffraction methods, carried out on single crystals in especially designed electrochemical cells, mainly exploring by synchrotron radiation. Following up oxygen intercalation reactions on single crystals is challenging, as it allows to scan the whole reciprocal lattice, enabling to obtain valuable information as diffuse scattering, weak superstructure reflections, as well as information of the volume fractions of different domains during the reaction, to highlight a few examples, difficult or impossible to access by powder diffraction.

Both title systems are able to take up an important amount of oxygen on regular or interstitial lattice sites, inducing structural changes accompanied by long range oxygen ordering. For $SrFeO_{2.5+x}$ the uptake of oxygen carried out by electrochemical oxidation yields $SrFeO_3$ as the final reaction product. The as grown $SrFeO_{2.5}$ single crystals we found to show a complex defect structure, related to the stacking disorder of the octahedral and tetrahedral layers. During the oxygen intercalation we evidenced the formation of two reaction intermediates, $SrFeO_{2.75}$ and $SrFeO_{2.875}$, showing complex and instantly formed long range oxygen vacancies. Due to the specific twinning with up to totally twelve possible twin individuals, we directly followed up the formation and changes of the specific domain and related microstructure. We thus observed a topotactic reaction mechanism from $SrFeO_{2.5}$ to $SrFeO_{2.75}$, while further oxidation lead to important rearrangements in the dimensionality of the oxygen defects in $SrFeO_{2.875}$, implying the formation of an additional twin domain in course of the reaction.

The electrochemical reduction of orthorhombic $Pr_2NiO_{4.25}$ yields stoichiometric $Pr_2NiO_{4.0}$ as the final reaction product with the same symmetry, while tetragonal $Pr_2NiO_{4.12\pm\delta}$ appears as a non-stoichiometric intermediate phase. Using a single crystal with 50 μm diameter, the reaction proceeded under equilibrium conditions in slightly less than 24 h, implying an unusually high oxygen ion diffusion coefficient of $\geq 10^{-11}$ cm^2s^{-1} at already ambient temperature. From the changes of the associated twin domain structure during the reduction reaction, the formation of macro twin domains was evidenced.

Beside exploring the complex phase diagrams of $SrFeO_{2.5+x}$ and $Pr_2NiO_{4+\delta}$ we were able to investigate detailed changes in the microstructure using *in situ* single crystal diffraction techniques, impossible to access by classical powder diffraction methods. The importance of changes in the domain structure goes far beyond the investigated title compounds and has utmost importance of the performance, stability and lifetime of e.g. battery materials.

Résumé

La compréhension des aspects fondamentaux de la diffusion de l'oxygène dans les oxydes solides à des températures modérées, jusqu'à température ambiante, est un enjeu majeur pour le développement d'une variété de dispositifs technologiques dans un avenir proche. Cela concerne, par exemple, le développement de la prochaine génération d'électrolytes et membranes solides d'oxygène pour les piles à combustible de type SOFC. De plus, les réactions d'intercalation de l'oxygène réalisées à basse température présentent un outil puissant pour contrôler le dopage en oxygène ainsi que des propriétés physiques. Dans ce contexte, les oxydes ayant une structure type brownmillérite ($A_2BB'O_5$) ou type K_2NiF_4, ont attiré beaucoup d'attention, car ils montrent une mobilité de l'oxygène déjà à température ambiante.

Dans cette thèse, nous avons étudié les mécanismes d'intercalation d'oxygène dans $SrFeO_{2.5+x}$, ainsi que $Pr_2NiO_{4+\delta}$ par des méthodes de diffraction *in situ*, réalisées sur des monocristaux dans une cellule électrochimique spécifiquement conçue, explorant principalement le rayonnement synchrotron. Ceci a permis d'explorer en 3D tout le réseau réciproque, et d'obtenir des informations précieuses sur la diffusion diffuse, sur les faibles intensités des raies de surstructure, ainsi que des informations sur la fraction volumique des différents domaines de maclage au cours de la réaction, impossibles à obtainir par diffraction de poudre.

Les deux systèmes montrent des changements structuraux complexes, accompagnés par une mise en ordre de l'oxygène à longue distance. Au cours de l'intercalation d'oxygène nous avons mis en évidence deux phases intermédiaires, $SrFeO_{2.75}$ et $SrFeO_{2.875}$, possédant des lacunes en oxygène ordonnées à longue échelle. En raison du maclage, et avec jusqu'à douze individus possibles, nous avons suivi directement la formation et l'évolution des domaines de maclage ainsi que leur microstructure apparentée. Nous avons ainsi observé un mécanisme de réaction topotactique pour $SrFeO_{2.5}$ vers $SrFeO_{2.75}$, tandis que l'oxydation de $SrFeO_{2.875}$ conduit à d'importants réarrangements de l'oxygène, associés à un changement de nombre de domaines de maclage.

La réduction électrochimique de la phase orthorhombique $Pr_2NiO_{4.25}$ donne $Pr_2NiO_{4.0}$ comme produit final, ayant la même symétrie, tandis que la phase tétragonale $Pr_2NiO_{4.12\pm\delta}$ apparaît comme phase intermédiaire. Utilisant un monocristal d'un diamètre de 50 microns, la réaction se déroule dans des conditions d'équilibre en moins de 24 heures, ce qui implique un coefficient de diffusion de l'oxygène anormalement élevé, supérieur à 10^{-11} cm^2s^{-1} à température ambiante. Grâce aux changements de la structure associés aux domaines mâclés pendant la réaction de réduction, la formation de domaines mâclés macroscopiques a été mise en évidence.

Outre l'exploration des diagrammes de phases complexes de $SrFeO_{2.5+x}$ et $Pr_2NiO_{4+\delta}$, nous avons pu étudier les changements détaillés concernant la microstructure à l'aide de la diffraction sur monocristaux *in situ*, impossible à accéder par des méthodes de diffraction de poudre classique. Les changements de la micro-structure des domaines va bien au-delà des composés étudiés ici et est tres importante pour extrapoler sur la performance, la stabilité et la durée de vie par exemple des matériaux utilisés pour le stockage de l'énergie.